

## REPORT DOCUMENTATION PAGE

Form Approved  
OMB No. 0704-0188

The public reporting burden for this collection of information is estimated to average 1 hour per response, including the time for reviewing instructions, searching existing data sources, gathering and maintaining the data needed, and completing and reviewing the collection of information. Send comments regarding this burden estimate or any other aspect of this collection of information, including suggestions for reducing the burden, to Department of Defense, Washington Headquarters Services, Directorate for Information Operations and Reports (0704-0188), 1215 Jefferson Davis Highway, Suite 1204, Arlington, VA 22202-4302. Respondents should be aware that notwithstanding any other provision of law, no person shall be subject to any penalty for failing to comply with a collection of information if it does not display a currently valid OMB control number.

PLEASE DO NOT RETURN YOUR FORM TO THE ABOVE ADDRESS.

1. REPORT DATE (DD-MM-YYYY)  
17/Sep/20012. REPORT TYPE  
DISSERTATION

3. DATES COVERED (From - To)

4. TITLE AND SUBTITLE  
THE MESOSCALE EVOLUTION OF EXPLOSIVE CYCLOGENESIS: A  
NUMERICAL STUDY OF MARCH 1993 STORM OF THE CENTURY

5a. CONTRACT NUMBER

5b. GRANT NUMBER

5c. PROGRAM ELEMENT NUMBER

6. AUTHOR(S)  
MAJ PFEIFFER KARL D

5d. PROJECT NUMBER

5e. TASK NUMBER

5f. WORK UNIT NUMBER

7. PERFORMING ORGANIZATION NAME(S) AND ADDRESS(ES)  
NORTH CAROLINA STATE UNIVERSITY8. PERFORMING ORGANIZATION  
REPORT NUMBER  
CI01-2369. SPONSORING/MONITORING AGENCY NAME(S) AND ADDRESS(ES)  
THE DEPARTMENT OF THE AIR FORCE  
AFIT/CIA, BLDG 125  
2950 P STREET  
WPAFB OH 45433

10. SPONSOR/MONITOR'S ACRONYM(S)

11. SPONSOR/MONITOR'S REPORT  
NUMBER(S)12. DISTRIBUTION/AVAILABILITY STATEMENT  
Unlimited distribution  
In Accordance With AFI 35-205/AFIT Sup 1

13. SUPPLEMENTARY NOTES

14. ABSTRACT

DISTRIBUTION STATEMENT A  
Approved for Public Release  
Distribution Unlimited

20011016 178

15. SUBJECT TERMS

16. SECURITY CLASSIFICATION OF:

a. REPORT b. ABSTRACT c. THIS PAGE

17. LIMITATION OF  
ABSTRACT18. NUMBER  
OF  
PAGES  
206

19a. NAME OF RESPONSIBLE PERSON

19b. TELEPHONE NUMBER (Include area code)

## ABSTRACT

PFEIFFER, KARL D. The mesoscale evolution of explosive cyclogenesis: A numerical study of the March 1993 Storm of the Century. (Under the direction of Yuh-Lang Lin.)

The early, overwater cyclogenesis of the March 12–14 1993 Storm of the Century (SOC93) is investigated using mesoscale simulation datasets. Numerical results indicate that the convective available potential energy for initial development is supplied by a mid-level cold pool that develops in western Texas through evaporative cooling and convective overturning in the elevated mixed layer (EML). The EML and mountain-plains solenoid (MPS) endemic to the Mexican plateau interact with a terrain-induced low-level moist flow to sustain shallow convection in this layer; the resulting cold pool propagates to the Texas Gulf Coast early on 12 March. These results clarify previous studies that have speculated that the cold pool was a product of coastal frontogenesis, possibly enhanced by sea-surface temperature gradients. Deep, organized convection is triggered along this boundary under mid-tropospheric divergence at the junction of opposing ageostrophic circulations induced by the unbalanced exit region of a synoptic jet streak perturbed by plateau heating and the southwesterly upper branch of the MPS. This finding departs from previous studies by demonstrating the importance of the Mexican plateau to the initiation of convection; the initial ascent was previously attributed largely to low-level warm advection in advance of an upper-level potential vorticity (PV) anomaly. The early surface cyclone, organized around the mesoscale convective complex initiated early on 12 March, develops over the open water of the western Gulf initially as a warm-core system. Warm air attendant to the MPS phases with the entrance region of a subtropical jet streak and propagates ahead of the surface cyclone, becoming the locus for a secondary cyclogenesis that resembles the initial warm core cyclone. Synoptic-scale cold air advancing southward along the Mexican plateau triggers an eastward cold surge that propagates quickly into rear flank of the secondary development, producing a hybrid warm-core and cold-core structure in the now-dominant secondary cyclone. Both primary and secondary development are demonstrated to occur largely independently of the advancing upper-level PV anomaly, though the mesoscale cold surge ahead of the synoptic-scale cold air is crucial to the rapid transition to a hybrid structure.

## BIOGRAPHY

Karl D. Pfeiffer was born [redacted] Pfeiffer at Keesler AFB, Biloxi, MS. He graduated from the University of West Florida (Pensacola) in April 1988 with a Bachelor of Science in Physics, and married his high school sweetheart, the former [redacted] of Pensacola, in May 1988 (it was a very good year).

He entered Air Force Officer Training School in January 1989 and was commissioned a second lieutenant on May 4. Upon completion of the Basic Meteorology Program (BMP) at the University of Oklahoma in May 1990, Karl was assigned to the 15th Weather Squadron, 21st Air Force, Military Airlift Command, at McGuire AFB, NJ, as Assistant Chief, Weather Support Unit. This job primarily involved getting up at 0300 to prepare weather briefings on regions of interest to the 21AF commander, and tending to the occasional wayward airman. In December 1991, he was reassigned as Weather Systems Manager for the newly-formed Tanker Airlift Control Center (TACC), Air Mobility Command, Scott AFB, IL. The TACC has worldwide responsibility for Air Force airlift assets and the supporting weather unit is often called upon for short-notice weather briefings for *any* area of the world, from Thule, Greenland, to McMurdo Station, Antarctica (and warmer locations as well). His primary responsibility was to turn these diverse data requirements into hard computer system requirements for the unit, then find the resources to satisfy these requirements. He was given the opportunity to return to graduate school in May 1993 for a Master of Science in Computer Science through the Air Force Institute of Technology, School of Engineering, Wright-Patterson AFB, OH, graduating in December 1994. Karl returned to Scott AFB to the Environmental and Technical Applications Center (USAFETAC), now the Air Force Combat Climatology Center (AFCCC), in January 1995, serving as a staff scientist; as Chief, Database Administration Branch; as Assistant Chief, Systems Division and briefly as Chief, Systems Division. While at Scott AFB, he also taught evening classes in physics and computer science at McKendree College, Lebanon, IL. He was given the opportunity to pursue the PhD in Meteorology at North Carolina State University in August, 1998.

Karl was promoted to Major effective July 1, 2000. He is a Senior Meteorologist and holds the Meritorious Service Medal and the Air Force Commendation Medal (first oak leaf cluster). He and [redacted] have three beautiful children:

## ACKNOWLEDGEMENTS

I wish to express my deepest gratitude to Professors Yuh-Lang Lin, Michael L. Kaplan, Gary M. Lackmann, Allen J. Riordan and Gerald S. Janowitz for their encouragement and patient guidance through my arduous journey to become a professional scientist.

Dr. Jay Charney has been a patient reviewer and good friend over these few years, as have my colleagues in the Mesoscale Modeling Lab: Maj Jeff Cetola, Sen (Sam) Chiao, James Thurman, Darrell Ensley, Allan Huffman, Kevin Lux, and Chris Hill. Dr. Ken Waight has been of invaluable assistance with the MASS mesoscale model.

Finally, I would like to thank Air Force Combat Climatology Center, Asheville, NC, for providing additional surface and upper air data over Mexico. Phil Schumacher supplied the surface data from the Kocin et al. (1995) mesoanalysis, used in verification computations. Numerical simulations were executed on an SGI/Origin 2000 operated by the North Carolina Supercomputing Center (NCSC). This research was funded under NASA Grant NAG-5480C; the support of Dr. Ramesh Kakar, Manager, Atmospheric Dynamics and Thermodynamics Program, NASA Headquarters, Washington, D.C., is gratefully acknowledged. The views expressed in this work are those of the author and do not reflect the official policy or position of the United States Air Force, Department of Defense or U.S. Government.



# TABLE OF CONTENTS

<b>LIST OF FIGURES</b> . . . . .	vii
<b>LIST OF TABLES</b> . . . . .	xxi
<b>1 INTRODUCTION</b> . . . . .	1
1.1 State of the science in understanding the Storm of the Century . . . . .	1
1.2 Focus of this study . . . . .	4
<b>2 THE MESOSCALE EVOLUTION OF THE MARCH 1993 STORM OF THE CENTURY. PART I: ORIGIN OF THE PRECURSOR CONVECTIVE AVAILABLE POTENTIAL ENERGY</b> . . . . .	10
2.1 Introduction . . . . .	10
2.2 Data and methodology . . . . .	13
2.2.1 Model initialization . . . . .	13
2.2.2 Numerical experiments . . . . .	13
2.3 Model verification and synoptic situation . . . . .	14
2.4 Observations and simulations of the mid-tropospheric baroclinic zone . . . . .	16
2.4.1 Overview . . . . .	16
2.4.2 Initiation of the cold pool . . . . .	17
2.4.3 Frontogenesis and jetogenesis . . . . .	24
2.4.4 Sensitivity analysis . . . . .	28
2.5 Concluding discussion . . . . .	30
<b>3 THE MESOSCALE EVOLUTION OF THE MARCH 1993 STORM OF THE CENTURY. PART II: INITIATION AND MAINTENANCE OF ANTECEDENT CONVECTION</b> . . . . .	66
3.1 Introduction . . . . .	66
3.2 Methodology and model verification . . . . .	68
3.2.1 Observation and simulation datasets . . . . .	68
3.2.2 Model verification . . . . .	69
3.3 Initiation and maintenance of the Stage I SOC93 . . . . .	69
3.3.1 Overview . . . . .	69
3.3.2 Initiation of convection . . . . .	70
3.3.3 Jetogenesis in the supporting environment . . . . .	73
3.3.4 Transition to surface cyclogenesis . . . . .	77
3.3.5 Sensitivity analysis . . . . .	81

3.4	Summary and concluding discussion . . . . .	83
<b>4</b>	<b>THE MESOSCALE EVOLUTION OF THE MARCH 1993 STORM OF THE CENTURY. PART III: TRANSITION FROM WARM- CORE TO COLD-CORE CYCLOGENESIS . . . . .</b>	<b>116</b>
4.1	Introduction . . . . .	116
4.2	Methodology . . . . .	118
4.3	Evolution of the surface cyclone . . . . .	119
4.4	Early warm-core development . . . . .	121
4.4.1	Warm-core characteristics and mid-tropospheric structure . . . . .	121
4.4.2	Local jet structure . . . . .	123
4.4.3	Summary . . . . .	125
4.5	Secondary cyclogenesis . . . . .	125
4.5.1	Pre-cyclogenesis environment . . . . .	126
4.5.2	Early convection and jetogenesis . . . . .	127
4.5.3	Rapid frontogenesis . . . . .	131
4.5.4	Summary . . . . .	134
4.6	Transition to dominant cold-core development . . . . .	134
4.6.1	Precipitation and surface development . . . . .	135
4.6.2	Frontal evolution . . . . .	135
4.6.3	Mid and upper-tropospheric development . . . . .	136
4.6.4	Summary . . . . .	137
4.7	Potential vorticity structure . . . . .	138
4.8	Concluding discussion . . . . .	140
<b>5</b>	<b>SUMMARY AND CONCLUSIONS . . . . .</b>	<b>195</b>
5.1	Stage I: Conditioning of environment . . . . .	195
5.2	Stage I: Initiation of organized convection . . . . .	196
5.3	Stage II: Overwater development . . . . .	198
5.4	Future research . . . . .	199
<b>A</b>	<b>COMPUTATION OF DIABATIC FORCING . . . . .</b>	<b>200</b>
	<b>REFERENCES . . . . .</b>	<b>201</b>

## LIST OF FIGURES

1.1	Storm track of SOC93 with selected snowfall amounts (cm). Central pressures (in hPa) follow the NMC surface analyses. From Fig. 2 of Uccellini et al., 1995.	7
1.2	Composite surface analysis from Kocin et al. (1995), Fig. 2. Three-hourly evolution of the surface low pressure center (marked with L, central pressures in hPa), surface cold front (solid black line), the squall line (shaded) on 12–13 March 1993. Inset map marks location and depth (m) of the storm surge and approximate location of tornado outbreaks. . . . .	8
1.3	Tracks and 12-h positions (UTC/day; March 1993) of PV anomalies A, C, and D, marked with long dash, dotted and dash-dot paths, respectively. Solid line denotes track of SOC93 (12-h positions as above), with central pressures in hPa. The PV analysis is adapted from Bosart et al. (1996) and Dickinson et al. (1997), while the storm central pressures are taken from the mesoscale analysis of Kocin et al. (1995). . . . .	9
2.1	GOES-7 IR imagery valid (a) 0600 UTC, (b) 0900 UTC, and (c) 1200 UTC 12 March. Position of the surface low from the Kocin et al. (1995) mesoanalysis is indicated. . . . .	33
2.2	Tracks and 12-h positions (UTC/day; March 1993) of PV anomalies A, C, and D, marked with long dash, dotted and dash-dot paths, respectively. Solid line denotes track of SOC93 (12-h positions as above), with central pressures in hPa. The PV analysis is adapted from Bosart et al. (1996) and Dickinson et al. (1997), while the storm central pressures are taken from the mesoscale analysis of Kocin et al. (1995). . . . .	34
2.3	Sea-surface temperature fields contoured every 1 C for (a) synthesized from buoy, satellite and NHC analysis, used in the control simulation and (b) the original 9 March NHC analysis (Gilhousen, 1994). . . . .	35
2.4	Map depicting topography at 500 m intervals, contoured and shaded. Stations referenced in the text are also plotted. The Edwards Plateau and Altiplanicie Mexicana (Mexican High Plains) are indicated. . . . .	36

2.5	Grid boundaries for the 12-km resolution simulations (inner box) and 96 km simulation (outer box). For clarity, every third grid point for the 96 km simulation is displayed, while every sixth grid point is displayed for the 12 km simulations. . . . .	37
2.6	Initialization terrain fields for the (a) CONTROL and (b) SMOOTH simulations. . . . .	37
2.7	Track of the SOC93 surface cyclone in the mesoanalysis of Kocin et al. (1995), the CONTROL simulation and the ECMWF analysis. Depicted are comparisons of (a) storm central pressures and (b) storm position, where the mesoanalysis is indicated by a filled diamond, the CONTROL simulation is indicated by a hollow diamond, and the ECMWF analysis is indicated by the hollow triangle. Times in (b) are of the form <i>DDHH</i> (e.g. 1218 = 1800 UTC 12 March). . . . .	38
2.8	300 hPa winds and geopotential heights from (a) the NMC upper air analysis and (b) control simulation. Heights are contoured every 120 dm, winds are plotted in kt following standard convention. . . . .	39
2.9	ECMWF isentropic potential vorticity in the column from 336 K to 316 K, contoured every 0.5 PVU. Valid (a) 1800 UTC 11 March, (b) 0000 UTC 12 March, (c) 0600 UTC 12 March and (d) 1200 UTC 12 March. Positions of Bosart et al. (1996) PV anomaly D are indicated by a filled octagon, while positions of PV anomaly C are indicated by a filled box. . . . .	40
2.10	CONTROL isentropic potential vorticity, as in Fig. 2.9. . . . .	41
2.11	ECMWF analysis (a) 700 hPa potential temperature field at 0000 UTC 12 March contoured every 1 K, with standard wind vectors in $\text{m s}^{-1}$ . and (b) time-series plot of ECMWF-derived CAPE (in $\text{J kg}^{-1}$ ) at Brownsville (BRO), Texas, from 1200 UTC 10 March to 1200 UTC 13 March, with observed BRO CAPE values plotted with filled squares. The cold trough is denoted by the dashed line in (a). . . . .	42
2.12	Observed data at 0600 UTC 11 March. (a) NCEP (NMC) surface analysis; (b) ECMWF 850 hPa standard wind vectors ( $\text{m s}^{-1}$ ), isentropes contoured every 2 K, warm advection ( $-\mathbf{V} \bullet \nabla_p \theta$ ) shaded every $0.1 \text{ K h}^{-1}$ , and hot conveyor belt indicated by the arrow; and (c) ECMWF 700 hPa isentropes contoured every 1 K, standard wind vectors on GOES-7 IR satellite, and initial cold pool indicated by the dashed line southwest of DRT; the northwest branch of the active MPS outflow is indicated by a solid arrow northwest of DRT, and the previous MPS is indicated by a dashed-dotted arrow southeast of DRT. . .	43

2.13	CONTROL 700 hPa standard wind vectors ( $\text{m s}^{-1}$ ), and isentropes contoured every 1 K, with surface precipitation (shaded in $\text{mm h}^{-1}$ ) valid 11 March at (a) 0300 UTC, (b) 0600 UTC, (c) 0900 UTC, and (d) 1200 UTC. Positions of cross-sections in Fig. 2.15 are indicated. . . . .	44
2.14	CONTROL 700 hPa standard wind vectors ( $\text{m s}^{-1}$ ), isentropes contoured every 1 K, and vertical velocity (shaded in $\mu\text{bar s}^{-1}$ , ascent outlined in dashed contours) valid 11 March at (a) 0300 UTC, (b) 0600 UTC, (c) 0900 UTC, and (d) 1200 UTC. . . . .	45
2.15	CONTROL simulation cross-sections along the path of the 700 hPa cold pool, depicting ageostrophic circulation vectors, isentropes contoured every 2 K, and rainwater mixing ratio shaded every $0.1 \text{ g kg}^{-1}$ , valid (a) 0300 UTC, (b) 0600 UTC, (c) 0900 UTC, and (d) 1200 UTC. Plane is indicated in Fig. 2.13b. . . . .	46
2.15	<i>Continued.</i> . . . .	47
2.16	CONTROL diagnosis of the hot conveyor belt at 0300 UTC 11 March. Depicted are (a) 800 hPa standard wind vectors ( $\text{m s}^{-1}$ ), isentropes contoured every 2 K, shaded in the range 304 to 308 K; and (b) cross-section along the major axis of the 700 hPa cold pool, depicting ageostrophic circulation vectors, isentropes contoured every 2 K, and precipitation mixing ratio shaded every $0.1 \text{ g kg}^{-1}$ . Point of impact of the hot conveyor belt in the plane of the cross-section is depicted with a dashed line in (b). . . . .	48
2.17	CONTROL diagnosis of the hot conveyor belt at 0600 UTC 11 March, as in Fig. 2.16. . . . .	49
2.18	CONTROL simulation cross-section along the hot conveyor. Depicted are ageostrophic circulation vectors, equivalent potential temperature ( $\theta_e$ ) contoured every 4 K, and relative humidity shaded at 70% and 90%, valid (a) 0300 UTC and (b) 0600 UTC 11 March. Plane is indicated in Fig. 2.17a; horizontal position of the cold pool is indicated in (b) by the dashed vertical line. . . . .	50
2.19	CONTROL diagnosis of the hot conveyor belt at 0900 UTC 11 March, as in Fig. 2.16. . . . .	51
2.20	CONTROL simulation cross-section along the major axis of the 700 hPa cold pool at 0900 UTC 11 March, depicting ageostrophic circulation vectors, isentropes contoured every 2 K, and Richardson number ( $Ri$ ) shaded for $Ri \leq 0.25$ . Plane is indicated in Fig. 2.13c. . . . .	52

2.21	CONTROL diagnosis of the hot conveyor belt at 1200 UTC 11 March, as in Fig. 2.16. . . . .	53
2.22	ECMWF 700 hPa isentropes contoured every 1 K and standard wind vectors ( $\text{m s}^{-1}$ ) on GOES-7 IR imagery from 1200 UTC 11 March. Position of the major axis of the 700 hPa cold pool is indicated by the dashed line. . . . .	54
2.23	Observed soundings at Del Rio (DRT), TX, 0000 and 1200 UTC 11 March. Depicted are temperature (solid line) and dewpoint (dashed line) in K, with standard wind vectors in $\text{m s}^{-1}$ . The 0000 UTC sounding parameters are depicted in black, the 1200 UTC sounding in dark gray. The MPS layer and the inversion at its base are indicated, as is the cold pool, discussed in the text. . . . .	55
2.24	CONTROL simulation time series over Del Rio (DRT), TX, from 0000 to 1200 UTC 11 March, parameters (a) potential temperature and (b) relative humidity for levels 850 hPa (solid), 800 hPa (short dashed), 750 hPa (long dashed) and 700 hPa (dash-dotted). Observed potential temperatures are plotted in dark gray in (a), though these represent only two data points in time (0000 and 1200 UTC). . . . .	56
2.25	CONTROL simulation 700 hPa isentropes, contoured every 1 K, and frontogenesis shaded every 1 K $(100 \text{ km})^{-1} (3 \text{ h})^{-1}$ , valid 11 March at (a) 1500 UTC, (b) 1800 UTC, (c) 2100 UTC, and (d) 0000 UTC 12 March. Position of Bosart et al. (1996) PV anomaly D is indicated by a filled octagon in (b), (c) and (d). . . . .	57
2.26	CONTROL simulation 700 hPa isentropes, contoured every 1 K, simulated precipitation shaded in $\text{mm h}^{-1}$ , and 300 hPa ageostrophic wind vectors (reference vector in lower right of figure), valid 11 March at (a) 1500 UTC, (b) 1800 UTC, (c) 2100 UTC, and (d) 0000 UTC 12 March. . . . .	58
2.27	CONTROL simulation 300 hPa wind vectors ( $\text{m s}^{-1}$ ), total wind isotachs shaded above $30 \text{ m s}^{-1}$ , and divergence contoured every $0.5 \times 10^{-4} \text{ s}^{-1}$ (thick lines), valid 11 March at (a) 1500 UTC, (b) 1800 UTC, (c) 2100 UTC, and (d) 0000 UTC 12 March. The position of Bosart et al. (1996) PV anomaly D is indicated by a filled octagon in (b), (c) and (d). . . . .	59
2.28	ECMWF 300 hPa standard wind vectors ( $\text{m s}^{-1}$ ) and isotachs contoured every $5 \text{ m s}^{-1}$ at 0000 UTC 12 March. Verifying position of jetlet J1 is indicated, with simulated position indicated in Fig. 2.27d. Positions of Bosart et al. (1996) PV anomalies C (filled square) and D (filled octagon) are indicated. . . . .	60

2.29	Comparison of control and sensitivity experiments at 1200 UTC 11 March at 700 hPa. Potential temperature difference fields, contoured every 1 K (negative dashed) for (a) <i>CONTROL – ADIAB</i> , (b) <i>CONTROL – NOSFLX</i> , (c) <i>CONTROL – NOLATENT</i> , and (d) <i>CONTROL – SMOOTH</i> . . . .	61
2.30	NOLATENT 700 hPa frontogenesis at 1500 UTC 11 March, as in Fig. 2.25. .	62
2.31	Comparison of control and sensitivity experiments at 0000 UTC 12 March at 700 hPa. Potential temperature difference fields, contoured every 1 K (negative dashed) for (a) <i>CONTROL – ADIAB</i> , (b) <i>CONTROL – NOSFLX</i> , (c) <i>CONTROL – NOLATENT</i> , and (d) <i>CONTROL – SMOOTH</i> . Position of Bosart et al. (1996) PV anomaly D is indicated by the filled octagon. . .	63
2.32	SMOOTH simulation 700 hPa standard wind vectors ( $\text{m s}^{-1}$ ), isentropes contoured every 1 K, and 800 hPa isentropes shaded from 302 to 304 K (light gray) and 304 to 306 K (dark gray), valid 11 March at (a) 0300 UTC, (b) 0600 UTC, (c) 0900 UTC, and (d) 1200 UTC. . . . .	64
2.33	Summary of the development of the mid-level cold pool that is the locus of development early on 12 March. Schematics depict (a) initiation of the cold pool in the upper Rio Grande Valley early on 11 March, (b) frontogenesis and jetogenesis that condition the environment along the Gulf Coast for deep convection and (c) a cross-section view of the cold pool initiation with the plane indicated in (a). . . . .	65
3.1	GOES-7 IR imagery with superimposed storm positions from the mesoanalysis of Kocin et al. (1995), valid (a) 1200 UTC 12 March (1000 hPa), (b) 1800 UTC 12 March (992 hPa), (c) 0000 UTC 13 March (984 hPa), and (d) 0600 UTC 13 March (979 hPa). Position of Bosart et al. (1996) PV anomaly C, discussed in the text, is indicated by the filled square. . . . .	87
3.2	Track of the SOC93 surface cyclone in the mesoanalysis of Kocin et al. (1995), the CONTROL simulation and the ECMWF analysis. Depicted are comparisons of (a) storm central pressures and (b) storm position, where the mesoanalysis is indicated by a filled diamond, the CONTROL simulation is indicated by a hollow diamond, and the ECMWF analysis is indicated by the hollow triangle. Times in (b) are of the form <i>DDHH</i> (e.g. 1218 = 1800 UTC 12 March). . . . .	88

3.3	Observation analyses valid 0000 UTC 12 March, depicted are (a) ECMWF 700 hPa analysis, potential temperature contoured every 2 K and standard wind vectors in $\text{m s}^{-1}$ , with GOES-7 IR imagery, and (b) ECMWF 300 hPa analysis, ageostrophic wind vectors (reference vector in lower right) and total wind isotachs contoured and shaded over $35 \text{ m s}^{-1}$ ; horizontal divergence contoured every $0.5 \times 10^{-4} \text{ s}^{-1}$ with heavy lines. . . . .	89
3.4	As in Fig. 3.3 except for 0600 UTC 12 March. . . . .	90
3.5	CONTROL simulation fields valid 0000 UTC 12 March. Depicted are (a) Mean sea-level pressure (PMSL) contoured every 2 hPa, surface wind vectors ( $\text{m s}^{-1}$ ) and simulated hourly precipitation ( $\text{mm h}^{-1}$ ); (b) 700 hPa potential temperature contoured every 2 K and ageostrophic wind vectors; (c) 500 hPa potential temperature contoured every 2 K, ageostrophic wind vectors, and terrain shaded every 500 m; (d) 300 hPa isotachs (shaded $> 35 \text{ m s}^{-1}$ ), geopotential height contoured with dashed lines every 30 m, horizontal divergence contoured in heavy black lines contoured at $0.5 \times 10^{-4} \text{ s}^{-1}$ and every $1.0 \times 10^{-4} \text{ s}^{-1}$ thereafter. Reference vectors for ageostrophic wind plots are in the lower right corner of the respective panels. . . . .	91
3.6	CONTROL simulation cross-sections valid 0000 UTC 12 March oriented (a) approximately parallel to the Sierra Madres (along MPS) and (b) normal to the Sierra Madres. Depicted are isentropes contoured every 2 K, ageostrophic circulation vectors, and vertical velocity shaded every $-5 \mu\text{bar s}^{-1}$ . Planes of the cross-sections are indicated in Fig. 3.5d, and 3.7d. . . . .	92
3.7	As in Fig. 3.5, except for 0300 UTC 12 March. . . . .	93
3.8	CONTROL simulation cross-sections valid 0300 UTC 12 March oriented (a) approximately parallel to the Sierra Madres (along MPS) and (b) normal to the Sierra Madres, parameters as in Fig. 3.6. Planes of the cross-sections are indicated in Fig. 3.7d. . . . .	94
3.9	As in Fig. 3.5, except for 0600 UTC 12 March. . . . .	95
3.10	CONTROL simulation cross-sections valid 0600 UTC 12 March oriented (a) approximately parallel to the Sierra Madres (along MPS) and (b) normal to the Sierra Madres, parameters as in Fig. 3.6. Planes of the cross-sections are indicated in Fig. 3.7d and 3.9d. . . . .	96
3.11	Same as Fig. 3.3 except for 1200 UTC 12 March. . . . .	97



3.12	ECMWF 300 hPa analysis of vertical velocity, contoured every $1 \mu\text{bar s}^{-1}$ (negative or ascent is dashed), valid 1200 UTC 12 March. Also depicted are standard wind vectors in $\text{m s}^{-1}$ . . . . .	98
3.13	Comparison of 300 hPa simulation results, valid 0600 UTC 12 March. Depicted are standard wind vectors ( $\text{m s}^{-1}$ ), isotachs (shaded $> 35 \text{ m s}^{-1}$ ), and divergence (thick solid lines at $0.5 \times 10^{-4} \text{ s}^{-1}$ and every $1.0 \times 10^{-4} \text{ s}^{-1}$ thereafter), from the (a) CONTROL, (b) ADIABATIC, (c) NOLATENT, and (d) NOSFLX simulations. . . . .	99
3.14	NOSFLX simulation at 0600 UTC 12 March, mean sea-level pressure (PMSL) contoured every 2 hPa, surface wind vectors ( $\text{m s}^{-1}$ ) and simulated hourly precipitation ( $\text{mm h}^{-1}$ ). . . . .	100
3.15	As in Fig. 3.5, except for 0900 UTC 12 March. . . . .	101
3.16	0900 UTC 12 March 300 hPa difference fields between the CONTROL simulation and (a) ADIABATIC simulation, (b) NOLATENT simulation, and (c) NOSFLX simulation. Depicted are the vector difference in the total wind field (reference vector lower right corner of each panel) and difference in geopotential height field contoured every 10 m (negative dashed). . . . .	102
3.17	0900 UTC 12 March 700 hPa difference fields between the CONTROL simulation and (a) ADIABATIC simulation, (b) NOLATENT simulation, and (c) NOSFLX simulation. Depicted are the vector difference in the total wind field (reference vector lower right corner of each panel) and difference in geopotential height field contoured every 5 m (negative dashed). . . . .	103
3.18	Isentropic potential vorticity difference fields, CONTROL - ADIABATIC, in the column from 336 K to 316 K, contoured every 0.25 PVU; and Lagrangian Rossby number ( $Ro$ ) from the CONTROL simulation at 326 K, valid (a) 0600 UTC, (b) 0900 UTC, and (c) 1200 UTC 12 March. Also shown are surface pressure centers from the CONTROL PMSL field. Positions of Bosart et al. (1996) PV anomaly C are indicated by the filled square. . . . .	104
3.19	Isentropic potential vorticity difference fields, in the column from 336 K to 316 K, contoured every 0.25 PVU; and Lagrangian Rossby number ( $Ro$ ) from the CONTROL simulation at 326 K, valid 0600 UTC 12 March for the (a) CONTROL - NOSFLX and (b) CONTROL - NOLATENT. Also shown are surface pressure centers from the CONTROL PMSL field. Positions of Bosart et al. (1996) PV anomaly C are indicated by the filled square. . . . .	105
3.20	NCEP surface analysis valid 0900 UTC 12 March. . . . .	106

- 3.21 GOES-7 satellite imagery and a Barnes objective analysis of available PMSL (contoured every 2 hPa) and wind data (standard wind vectors in  $\text{m s}^{-1}$ ), valid (a) 0900, (b) 1000, (c) 1100, and (d) 1200 UTC 12 March. . . . . 107
- 3.22 CONTROL simulation cross-sections at 0900 UTC 12 March, (a) west to east, plane indicated in Fig. 3.7d, depicting isentropes contoured every 2 K, ageostrophic circulation vectors, and vertical velocity shaded every  $-5 \mu\text{bar s}^{-1}$ , (b) south to north, plane indicated in Fig. 3.15d, depicting isentropes and circulation vectors as in (a), with rain water mixing ratio (shaded in  $\text{g kg}^{-1}$ ). Positions of MTY and BRO are indicated; for (b), MTY and BRO are projected into the same position in the south-north plane. . . . . 108
- 3.23 CONTROL simulation fields, as in Fig. 3.5, valid 1200 UTC 12 March. . . . 109
- 3.24 CONTROL simulation cross-sections at 1200 UTC 12 March, as in Fig. 3.22. Plane of (a) is indicated in Fig. 3.7d, and plane of (b) is indicated in Fig. 3.23d. The positions of MTY and BRO relative to the plane of the cross-section are indicated. . . . . 110
- 3.25 SMOOTH simulation comparisons at 0900 UTC 12 March, (a) 700 hPa potential temperature contoured every 2 K and ageostrophic wind vectors; (b) 500 hPa potential temperature contoured every 2 K, ageostrophic wind vectors, and terrain shaded every 500 m; and (c) 300 hPa isotachs (shaded  $> 35 \text{ m s}^{-1}$ ), geopotential height contoured with dashed lines every 30 m, horizontal divergence contoured in heavy black lines contoured at  $0.5 \times 10^{-4} \text{ s}^{-1}$  and every  $1.0 \times 10^{-4} \text{ s}^{-1}$  thereafter. Reference vectors for ageostrophic wind plots are in the lower right corner of the respective panels. . . . . 111
- 3.26 Verification of the SMOOTH simulation against the mesoanalysis of Kocin et al. (1995). Depicted are (a) storm central pressures and (b) storm track, indicating times (e.g. 1215 = 1500 UTC 12 March) and positions, observed track in normal black type, SMOOTH track in italicized dark gray type. . . . . 112
- 3.27 NHCSST simulation results, valid (a) 0900 UTC and (b) 1200 UTC 12 March. Depicted are PMSL contoured every 2 hPa and surface wind vectors in  $\text{m s}^{-1}$ . 113
- 3.28 Verification of the NHCSST simulation against the mesoanalysis of Kocin et al. (1995), as in Fig. 3.26. . . . . 114
- 3.29 Schematic summarizing the sequence of events on 12 March that (a) initiates deep convection and (b) organizes the convection and upper-level flow, triggering surface cyclogenesis. . . . . 115

4.1	GOES-7 IR imagery with superimposed storm positions from the mesoanalysis of Kocin et al. (1995), valid (a) 1200 UTC 12 March (1000 hPa), (b) 2100 UTC 12 March (988 hPa), (c) 0600 UTC 13 March (979 hPa), and (d) 1200 UTC 13 March (971 hPa). The position of PV anomaly C (Bosart et al., 1996), discussed in the text, is indicated by the filled square. South Marsh Island, LA (7R8) is indicated by the star in (b). . . . .	143
4.2	Grid boundaries for the 12 km simulations; every sixth grid point is displayed.	144
4.3	Track of the SOC93 surface cyclone in the mesoanalysis of Kocin et al. (1995), the CONTROL simulation and the ECMWF analysis. Depicted are comparisons of (a) storm central pressures and (b) storm position, where the mesoanalysis is indicated by a filled diamond, the CONTROL simulation is indicated by a hollow diamond, and the ECMWF analysis is indicated by the hollow triangle. Times in (b) are of the form <i>DDHH</i> (e.g. 1218 = 1800 UTC 12 March). . . . .	145
4.4	Observed and simulated surface fields at 1200 UTC 12 March. (a) NCEP surface analysis and (b) CONTROL surface fields on GOES-7 IR imagery, depicting PMSL (solid every 4 hPa), surface temperature (dashed every 5 C), and total wind vectors (in $\text{m s}^{-1}$ ). . . . .	146
4.5	Observed and simulated surface fields at 1500 UTC 12 March. (a) NCEP surface analysis and (b) CONTROL surface fields on GOES-7 IR imagery, depicting PMSL (solid every 4 hPa), surface temperature (dashed every 5 C), and total wind vectors (in $\text{m s}^{-1}$ ). . . . .	147
4.6	Observed and simulated surface fields at 1800 UTC 12 March, as in Fig. 4.4.	148
4.7	Observed and simulated surface fields at 2100 UTC 12 March, as in Fig. 4.4.	149
4.8	Observed and simulated surface fields at 0000 UTC 13 March, as in Fig. 4.4.	150
4.9	Observed and simulated surface fields at 0600 UTC 13 March, as in Fig. 4.4.	151
4.10	CONTROL simulation at 1500 UTC 12 March. Vertically integrated instantaneous diabatic heating from 336 K (350 hPa) to 316 K (650 hPa) contoured at 1, 4, 10, 16, and 22 $\text{K h}^{-1}$ , and layer-averaged wind field in the column 336:316 K, superimposed on GOES-7 IR. . . . .	152
4.11	CONTROL 500 hPa fields at 1500 UTC 12 March. Depicted are geopotential height (contoured every 30 m), isentropes (contoured every 3 K), standard wind vectors (in $\text{m s}^{-1}$ ), and vertical velocity (shaded in $\mu\text{bar s}^{-1}$ ). Surface low pressure centers are indicated. . . . .	153

- 4.12 CONTROL parcel trajectories crossing the storm center at 1500 UTC 12 March. Depicted are (a) a composite of four representative trajectories, with arrows representing wind speed; and (b)-(e), individual trajectories following the plot model: standard wind vector in  $\text{m s}^{-1}$ , DDHH (e.g. 1215 = 1500 UTC 12 March) in the upper left, parcel pressure (hPa) in the upper right and equivalent potential temperature ( $\theta_e$ , in K) in the lower right. . . . . 154
- 4.13 CONTROL cross-sections along the path of the storm at 1500 UTC 12 March, depicting (a) potential temperature (contoured every 2 K), ageostrophic circulation vectors, and vertical velocity (shaded in  $\mu\text{bar s}^{-1}$ , ascent only shown); and (b) equivalent potential temperature (contoured every 4 K) and relative humidity (shaded at 70% and 90%). Plane of the cross-section is indicated in Fig. 4.11. . . . . 155
- 4.14 CONTROL 800 hPa fields at 1500 UTC 12 March. Depicted are equivalent potential temperature ( $\theta_e$ ) contoured every 4 K, divergence shaded and contoured every  $1 \times 10^{-4} \text{ s}^{-1}$  (negative dashed contour), and standard wind vectors in  $\text{m s}^{-1}$ . Surface low pressure centers and the plane of the cross-section in Fig. 4.13 are indicated. . . . . 156
- 4.15 ECMWF 250 hPa jet analysis at 1200 UTC 12 March. Depicted are standard wind vectors (in  $\text{m s}^{-1}$ ) and isotachs (shaded  $> 35 \text{ m s}^{-1}$ ). . . . . 157
- 4.16 CONTROL 250 hPa fields at 1500 UTC 12 March. Depicted are total wind speed ( $> 35 \text{ m s}^{-1}$  shaded), ageostrophic wind vectors (reference vector in lower right of panel) and horizontal divergence (contoured every  $1 \times 10^{-4} \text{ s}^{-1}$ ). 158
- 4.17 ADIABATIC comparisons at 250 hPa, 1500 UTC 12 March. (a) total wind speed ( $> 35 \text{ m s}^{-1}$  shaded), ageostrophic wind vectors (reference vector in lower right of panel) and horizontal divergence (contoured every  $1 \times 10^{-4} \text{ s}^{-1}$ ); and (b) vector subtraction of total wind ( $\mathbf{V}_{\text{CNTL}} - \mathbf{V}_{\text{ADIA}}$ ), reference vector in lower right of panel. Surface low pressure centers from the ADIABATIC simulation are indicated in (a); centers from the CONTROL simulation are indicated in (b). . . . . 159
- 4.18 CONTROL surface fields, depicting PMSL (contoured every 4 K), surface wind vectors (in  $\text{m s}^{-1}$ ), and total precipitation (shaded in  $\text{mm h}^{-1}$ ), valid (a) 1600 UTC, (b) 1800 UTC, (c) 2100 UTC, and (d) 2300 UTC 12 March. . 160

- 4.19 CONTROL parcel trajectories crossing the secondary storm at 1600 UTC 12 March. Depicted are (a) a composite of four representative trajectories, with arrows representing wind speed; and (b)-(e), individual trajectories following the plot model: standard wind vector in  $\text{m s}^{-1}$ , DDHH (e.g. 1215 = 1500 UTC 12 March) in the upper left, parcel pressure (hPa) at upper right and equivalent potential temperature ( $\theta_e$ , in K) at lower right. . . . . 161
- 4.20 CONTROL analysis at 1200 UTC 12 March, depicting (a) 700 hPa geopotential height (solid every 30 m), potential temperature (dashed every 3 K), standard wind vectors (in  $\text{m s}^{-1}$ ), and vertical velocity (shaded in  $\mu\text{bar s}^{-1}$ ); and (b) 250 hPa isotachs ( $> 35 \text{ m s}^{-1}$  shaded), ageostrophic wind vectors (reference vector in lower right of panel) and horizontal divergence (contoured every  $1 \times 10^{-4} \text{ s}^{-1}$ ). . . . . 162
- 4.21 CONTROL cross-section at 1200 UTC 12 March along the plane indicated in Fig. 4.20, depicting equivalent potential temperature contoured every 4 K, ageostrophic circulation vectors, and isotachs (shaded  $> 30 \text{ m s}^{-1}$ ). . . . . 163
- 4.22 CONTROL analysis at 1400 UTC 12 March, as in Fig. 4.20. . . . . 164
- 4.23 CONTROL cross-section at 1400 UTC 12 March along the plane indicated in Fig. 4.22, parameters as in Fig. 4.21. . . . . 165
- 4.24 CONTROL 800 hPa fields at 1600 UTC 12 March, depicting equivalent potential temperature ( $\theta_e$ ) contoured every 4 K, standard wind vectors (in  $\text{m s}^{-1}$ ) and divergence (shaded every  $1 \times 10^{-4}$ , negative dashed). Positions of surface lows are indicated. . . . . 166
- 4.25 CONTROL 500 hPa fields at 1600 UTC 12 March. Depicted are potential temperature ( $\theta$ ) contoured every 3 K, standard wind vectors (in  $\text{m s}^{-1}$ ) and vertical velocity (shaded in  $\mu\text{bar s}^{-1}$ ). The position of PV anomaly C (Bosart et al., 1996) is indicated. . . . . 167
- 4.26 CONTROL cross-sections through the secondary cyclone at 1600 UTC 12 March, depicting (a) potential temperature (contoured every 4 K), ageostrophic circulation vectors, and vertical velocity (shaded in  $\mu\text{bar s}^{-1}$ , ascent only shown); and (b) equivalent potential temperature (contoured every 4 K) and relative humidity (shaded at 70% and 90%). Plane of the cross-section is indicated in Fig. 4.24. . . . . 168

4.27	CONTROL jet structure at 1600 UTC 12 March, depicting (a) 250 hPa ageostrophic wind vectors (reference vector in lower right of panel), divergence (contoured every $1 \times 10^{-4}$ ), and total isotachs (shaded $> 35 \text{ m s}^{-1}$ ); and (b) cross-section through the PFJ and STJ entrance regions; ageostrophic circulation vectors, isotachs (shaded $> 35 \text{ m s}^{-1}$ ), and equivalent potential temperature (contoured every 4 K). Plane of the cross-section is indicated in (a). Positions of the primary ( <b>Lp</b> ) and secondary ( <b>Ls</b> ) low are indicated relative to the plane of the cross-section. . . . .	169
4.28	CONTROL jet structure at 1800 UTC 12 March, depicting (a) 400 hPa ageostrophic wind vectors (reference vector in lower right of panel), isotachs (shaded $> 30 \text{ m s}^{-1}$ ), geopotential height (contoured every 60 m), and potential temperature (contoured every 3 K); and (b) 250 hPa ageostrophic wind vectors (reference vector in lower right of panel), isotachs (shaded $> 30 \text{ m s}^{-1}$ ), and divergence (contoured at $1 \times 10^{-4} \text{ s}^{-1}$ ). . . . .	170
4.29	CONTROL cross-section at 1800 UTC 12 March along the plane indicated in Fig. 4.28, parameters as in Fig. 4.21. . . . .	171
4.30	ECMWF 250 hPa jet structure at 1800 UTC 12 March, depicting ageostrophic wind vectors (reference vector in lower right of panel), isotachs (shaded $> 30 \text{ m s}^{-1}$ ), and divergence (contoured at $1 \times 10^{-4} \text{ s}^{-1}$ ). . . . .	172
4.31	CONTROL jet structure at 2100 UTC 12 March, as in Fig. 4.28. . . . .	173
4.32	CONTROL cross-section at 2100 UTC 12 March along the plane indicated in Fig. 4.31, parameters as in Fig. 4.21. . . . .	174
4.33	CONTROL jet structure at 2300 UTC 12 March, as in Fig. 4.28. . . . .	175
4.34	CONTROL cross-section at 2300 UTC 12 March along the plane indicated in Fig. 4.33, parameters as in Fig. 4.21. . . . .	176
4.35	ADIABATIC jet structure at 2300 UTC 12 March, as in Fig. 4.28. . . . .	177
4.36	CONTROL 800 hPa fields at 1800 UTC 12 March, depicting equivalent potential temperature ( $\theta_e$ ) contoured every 4 K, standard wind vectors (in $\text{m s}^{-1}$ ), and horizontal frontogenesis on $\theta_e$ (shaded $> 1 \text{ K } 100 \text{ km}^{-1} \text{ } 3 \text{ h}^{-1}$ ). Positions of surface lows are indicated. . . . .	178

4.37	CONTROL cross-sections through the secondary cyclone at 1800 UTC 12 March, depicting (a) potential temperature (contoured every 4 K), ageostrophic circulation vectors, and vertical velocity (shaded in $\mu\text{bar s}^{-1}$ , ascent only shown); and (b) equivalent potential temperature (contoured every 4 K) and relative humidity (shaded at 70% and 90%). Plane of the cross-section is indicated in Fig. 4.36. . . . .	179
4.38	CONTROL 800 hPa fields at 2100 UTC 12 March, as in Fig. 4.36. . . . .	180
4.39	CONTROL cross-sections through the secondary cyclone at 2100 UTC 12 March, as in Fig. 4.37. . . . .	181
4.40	CONTROL 800 hPa fields at 2300 UTC 12 March, as in Fig. 4.36. . . . .	182
4.41	CONTROL cross-sections through the secondary cyclone at 2300 UTC 12 March, as in Fig. 4.37. . . . .	183
4.42	CONTROL absolute vorticity profile through center of secondary cyclone, at 1800, 2100 and 2300 UTC 12 March. Vorticity is scaled by $10^{-5} \text{ s}^{-1}$ , and wind vectors (in $\text{m s}^{-1}$ ) are depicted at right. . . . .	184
4.43	CONTROL surface fields, depicting PMSL (contoured every 4 K), surface wind vectors (in $\text{m s}^{-1}$ ), and total precipitation (shaded in $\text{mm h}^{-1}$ ), valid (a) 0000 UTC, (b) 0300 UTC, and (c) 0600 UTC 13 March. . . . .	185
4.44	CONTROL 800 hPa fields at 0300 UTC 13 March. Depicted are equivalent potential temperature ( $\theta_e$ ) contoured every 4 K, divergence shaded and contoured every $1 \times 10^{-4} \text{ s}^{-1}$ (negative dashed contour), and standard wind vectors in $\text{m s}^{-1}$ . Surface low pressure centers and the plane of the cross-section in Fig. 4.45 are indicated. . . . .	186
4.45	CONTROL cross-sections through the secondary cyclone at 0300 UTC 13 March, depicting (a) potential temperature (contoured every 2 K), ageostrophic circulation vectors, and vertical velocity (shaded in $\mu\text{bar s}^{-1}$ , ascent only shown); and (b) equivalent potential temperature (contoured every 4 K) and relative humidity (shaded at 70% and 90%). Plane of the cross-section is indicated in Fig. 4.44. . . . .	187
4.46	CONTROL 800 hPa fields at 0600 UTC 13 March, as in Fig. 4.44. . . . .	188
4.47	CONTROL cross-sections through the secondary cyclone at 0600 UTC 13 March, as in Fig. 4.45. . . . .	189

4.48	CONTROL jet structure at 0300 UTC 13 March, depicting (a) 400 hPa ageostrophic wind vectors (reference vector in lower right of panel), isotachs (shaded $> 30 \text{ m s}^{-1}$ ), and geopotential height (contoured every 60 m); and (b) 250 hPa ageostrophic wind vectors (reference vector in lower right of panel), isotachs (shaded $> 30 \text{ m s}^{-1}$ ), and divergence (contoured at $1 \times 10^{-4} \text{ s}^{-1}$ ). . . . .	190
4.49	CONTROL jet structure at 0600 UTC 13 March, as in Fig. 4.48. . . . .	191
4.50	CONTROL 250 hPa Lagrangian Rossby number (shaded) and total wind vectors (in $\text{m s}^{-1}$ ), valid (a) 0300 UTC and (b) 0600 UTC 13 March. . . . .	192
4.51	CONTROL IPV analysis in the column from 336 K to 316 K, with IPV contoured at 0.5 PVU and every 1.0 PVU thereafter, IPV advection ( $-\mathbf{V} \bullet \nabla \text{IPV}$ ) shaded at $5 \text{ PVU day}^{-1}$ and every $10 \text{ PVU day}^{-1}$ thereafter (negative dashed contour outline), and layer-averaged wind vectors (in $\text{m s}^{-1}$ ). Valid (a) 1200 UTC 12 March, (b) 1800 UTC 12 March, (c) 0000 UTC 13 March, and (d) 0600 UTC 13 March. . . . .	193
4.51	<i>Continued.</i> . . . . .	194



## LIST OF TABLES

2.1	Summary of the SOC93 three-stage evolution. . . . .	32
2.2	Numerical experiments. All simulations initialized at 1200 UTC 10 March. .	32
3.1	Summary of the SOC93 three-stage evolution. . . . .	86
3.2	Numerical experiments. All simulations initialized at 1200 UTC 10 March. .	86
4.1	Summary of the SOC93 three-stage evolution. . . . .	142
4.2	Numerical experiments. All simulations initialized at 1200 UTC 10 March. .	142

# Chapter 1

## Introduction

### 1.1 State of the science in understanding the Storm of the Century

The March 1993 Storm of the Century (SOC93) has been a recurring subject of study in the literature in large part because of its human impact: property damage in excess of \$2.7 billion and 79 deaths directly attributable to the storm, and a virtual shutdown of commercial aviation along the eastern United States (NWS, 1994). More significant meteorologically, however, is that major operational forecast models initialized as early as 8 March predicted a strong extratropical cyclone moving up the east coast in the period of 13–14 March (Caplan, 1995). Although considered largely a forecasting success, much of the life-cycle of SOC93 was not captured in operational models (Uccellini *et al.*, 1995). The initial cyclogenesis in the western Gulf of Mexico was consistently poorly forecast, resulting in a significant underestimation of storm impact as it made landfall in Florida (Uccellini *et al.*, 1995; Huo *et al.*, 1995; Dickinson *et al.*, 1997). A coastal flood watch for Apalachee Bay (northwest Florida) was not upgraded to a warning until a 4-m storm surge was in progress; 10 people died in this flooding (Gilhousen, 1994). Fig. 1.1 (from Uccellini *et al.*, 1995), presents a brief overview of the storm path with selected snowfall amounts.

While unusual for its intensity, SOC93 developed in a region considered climatologically favored for winter cyclogenesis (Hsu, 1993). In an early study of Texas-West Gulf cyclones, Saucier (1949) analyzed 388 storms in the period 1899–1938, for a mean of 9.7 winter cyclones

per year. In a more recent study, Johnson *et al.* (1984) analyzed extratropical cyclogenesis in the western Gulf over a control period of 1972–1982, finding an average of 10.4 winter cyclones per year. Dickinson *et al.* (1997) present a brief study of cool-season (November–April) storms in the Gulf of Mexico from 1957–1989, finding 206 deep storms (storms with central pressures  $\leq 1000$  hPa). While Dickinson *et al.* (1997) imply that deep storms are unusual for the western Gulf, an estimate from their study suggests an annual mean of 6.4 storms in this category. When compared to the Saucier (1949) and Johnson *et al.* (1984) studies showing an average of about 10 winter cyclones per season, we could conclude that about 60% of these storms have a central pressure  $\leq 1000$  hPa. Although this is a rough number, we can at least infer that *deep cyclogenesis in the western Gulf of Mexico is not a rare event.*

Kocin *et al.* (1995) present a comprehensive analysis of the synoptic-scale development over the life of the storm (12–14 March 1993), with a detailed mesoscale analysis covering the early, rapid cyclogenesis over the Gulf of Mexico from 12–13 March. Fig. 1.2 (from Kocin *et al.*, 1995), presents a composite of the mesoscale analyses of storm central surface pressure. Through this early phase of development, SOC93 deepened from 1000 hPa (1200 UTC 12 March) to 971 hPa (1200 UTC 13 March), or 29 hPa in 24 h. In their classic paper on explosive extratropical cyclogenesis, Sanders and Gyakum (1980) proposed a classification for a meteorological “bomb” as having a deepening rate of  $1 \text{ hPa h}^{-1}$  at  $60^\circ \text{ N}$  (for Northern Hemisphere storms). This measure, dubbed the Bergeron, is computed as

$$\left(\frac{\partial p}{\partial t}\right)_{\text{Bergeron}} = \left(\frac{\sin 60^\circ}{\sin \phi}\right) \frac{\overline{\delta p}}{24 \text{ h}} \quad (1.1.1)$$

which corrects the 24 h deepening ( $\overline{\delta p}$ ) for latitude ( $\phi$ ). By this measure, SOC93 had a deepening rate of 2.3 Bergerons (using a mean  $\phi = 27^\circ \text{ N}$ ). For comparison, the 1979 *Queen Elizabeth II* storm represented an extreme value in the Sanders and Gyakum (1980) study at 2.8 Bergerons; in their study of 288 “bombs”, fewer than 0.7 % of these storms deepened at greater than 2.0 bergerons.

Much of the published research on SOC93 has focused on diagnosing this early rapid cyclogenesis in the western Gulf, seeking to address the fundamental paradox of this extraordinary storm: *why did operational models that identified a major cyclone as early as five days in advance perform so poorly in simulating the initial cyclogenesis in the western*

*Gulf of Mexico?* From a broad perspective, a poor numerical weather forecast always has three suspects: a deficient initial state, poor model physics, or inadequate resolution. In an extensive study of the planetary, synoptic and sub-synoptic flow, Bosart *et al.* (1996) and Dickinson *et al.* (1997) investigated, among other issues, the quality of model physics in the National Centers for Environmental Prediction (NCEP) Medium Range Forecast (MRF). Bosart *et al.* (1996) performed a dynamical tropopause (DT) analysis over the Northern Hemisphere from 18 February to 15 March 1993, identifying long-lived potential vorticity (PV) anomalies that appear to participate in the initial cyclogenesis in the western Gulf. In this context, the dynamical tropopause was defined as the surface of 1.5 potential vorticity units ( $1 \text{ PVU} = 10^{-6} \text{ K m}^{-2} \text{ kg}^{-1} \text{ s}^{-1}$ ). Quasi-geostrophic potential vorticity (QGPV) was used as a tractable surrogate for Ertel's potential vorticity (EPV), and anomalies were identified in a subjective analysis of potential temperature ( $\theta_T$ ) and pressure ( $p_T$ ) on the DT in addition to analyses of the QGPV structure; these anomalies represent the potential for deep tropospheric ascent. Bosart *et al.* (1996) hypothesize that three anomalies (identified as PV anomaly A, C and D, see Fig. 1.3) interact to initiate and sustain the cyclogenesis of SOC93. Specifically, these investigators suggest that the initial, rapid cyclogenesis in the western Gulf grew from the destabilization of the surface environment by the dissipation of PV anomaly D over central Texas coupled to the approaching PV anomaly C descending along the front range of the Rocky Mountains into northeastern Mexico. While the body of analysis in this study demonstrates the extraordinary synoptic-scale signal of cyclogenesis, particularly after 0000 UTC 13 March, the link between the incipient cyclogenesis and the PV anomalies appears indistinct and does not give much insight to *why* the operational models failed. In a companion study to Bosart *et al.* (1996), Dickinson *et al.* (1997) further explore the DT analysis of this early period specifically addressing model predictability of the incipient cyclogenesis. Comparing the NCEP MRF initialization and forecasts to European Center for Medium-range Weather Forecasts (ECMWF) products, this study suggests that the missed forecast of early cyclogenesis is directly related to the MRF's failure to simulate the early, widespread convection from 1200 UTC 12 March to 0000 UTC 13 March. Dickinson *et al.* (1997) demonstrate that the initial state of the MRF at 1200 UTC 12 March contained sufficient instability and moisture to produce the incipient convection. These authors conclude that inadequate cumulus parameterization in the MRF resulted in the poor

simulation of this crucial period in SOC93 development. We should note that while the Dickinson *et al.* (1997) study advances the qualitative understanding of this early cyclogenesis (i.e. simulating early, organized convection is critical to a successful numerical forecast) the coarse resolution of the MRF is not suited to discerning the mesoscale phenomena associated with this development.

While the MRF forecast may have suffered from poor model physics, most operational forecast models failed to capture the incipient cyclogenesis in the Gulf of Mexico (Caplan, 1995), suggesting that other factors may have contributed to the complexity of this forecast. In an early study using a mesoscale version of the Canadian Regional Finite Element (RFE) model (50 km horizontal resolution, 23  $\sigma$ -levels in the vertical), Huo *et al.* (1995) found that the RFE could predict the synoptic-scale flow days in advance of the storm but failed to develop important mesoscale features when initialized before 0000 UTC 13 March 1993, similar to performance of the NCEP MRF (Caplan, 1995). In a follow-on study, Huo *et al.* (1998) explored the working hypothesis that poor initial conditions, particularly the low-level temperature field over the Gulf of Mexico, contributed to the RFE's inability to capture the storm prior to 0000 UTC 13 March. This hypothesis is consistent with the work of Gilhousen (1994), who found a strong mesoscale signal of early cyclogenesis in National Data Buoy Center (NDBC) data along the Texas Gulf Coast. In particular, buoy data showed a strong closed circulation with sustained 35 kt winds and a pressure center 4 to 6 hPa lower than the 12 h NCEP Nested Grid Model (NGM) forecasts verifying at 1200 UTC 12 March. The buoys also indicated a strong sea-surface temperature gradient and warmer waters that were inadequately represented in NCEP forecast products (Gilhousen, 1994). Using the PV inversion technique of Davis and Emanuel (1991), Huo *et al.* (1998) inserted a "balanced" correction to the initial 1000 hPa temperature field yielding significant improvement in the RFE forecast; much of the early cyclogenesis from 1200 UTC 12 March was well simulated with this augmented initial state.

## 1.2 Focus of this study

The work of Gilhousen (1994), Kocin *et al.* (1995), Huo *et al.* (1995, 1998) and Dickinson *et al.* (1997) all suggest that the crucial mesoscale elements of the initial storm had phased

by 1200 UTC 12 March. An open question in the literature remains: *what are the crucial mesoscale elements that initiated SOC93?* In the present study, we will use mesoscale simulations and observations to define these critical elements and document their interaction in the early cyclogenesis. We hypothesize that the March 1993 Storm of the Century evolved in three distinct stages:

- I. Early on 11 March to 1200 UTC 12 March, a sequence of mesoscale processes initiates and organizes deep convection in the western Gulf of Mexico.
- II. From 1200 UTC 12 March to early on 13 March, the storm develops initially as a warm-core system, then is transformed into a cold-core storm in the central Gulf prior to landfall in northwest Florida.
- III. 0600 UTC 13 March to late on 14 March, the storm intensifies, then matures, as a classic extratropical cyclone.

**Stage I** describes how the deep convection that supports the initial surface development is initiated and organized along the Texas Gulf Coast. Deep, organized convection requires instability, a triggering mechanism, a substantial moisture source, and a background environment capable of sustaining this convection once released. In the case of SOC93, we will demonstrate that the instability is established by the vertical juxtaposition of a mid-level cold pool over the warm, moist boundary layer of the Gulf late on 11 March. The potential energy concomitant to this arrangement is tapped for development by the triggering of deep convection in the lower Rio Grande Valley early on 12 March; we will demonstrate that sub-synoptic circulations endemic to the Mexican plateau played a significant role in initiating this convection.

**Stage II** represents the rapid deepening of SOC93 over the open waters of the Gulf of Mexico. This period is most often cited as the weakness in operational models. Published numerical studies that have shown any skill in reproducing the life cycle of SOC93 have always initialized at this point (Huo *et al.*, 1995, 1998; Schultz and Steenburgh, 1999). In the early period of Stage II, the warm-core, mesoscale convectively-generated vortex (MCV) from Stage I intensifies over the anomalously warm Gulf of Mexico. As synoptic-scale cold air is wrapped into the storm late on 12 March, the system transitions from a warm-core,

tropical-like system into an extratropical (cold-core) cyclone supported by a well-defined frontal structure.

The final period of the storm's evolution, Stage III, occurs along the east coast of the United States with the merger of PV anomalies A and C; this period is characterized by reasonably well-understood dynamics (e.g. Hakim *et al.*, 1995) and has been documented previously in the work of Bosart *et al.* (1996), among others. This research will focus on Stage I and II.

This dissertation is organized as three papers, each dealing with distinct aspects of the early cyclogenesis of SOC93. Chapter 2 documents the development of a mid-level cold pool along the Texas Gulf Coast late on 11 March that destabilizes the column and provides a source of convective available potential energy (CAPE) for the antecedent convection; this is the early period of Stage I. Chapter 3 illustrates how this CAPE is released as deep, organized convection in the lower Rio Grande Valley early on 12 March; this is the final period of Stage I. Chapter 4 describes Stage II, the overwater development of SOC93 from about 1200 UTC 12 March to landfall early on 13 March. Chapter 5 briefly summarizes the major findings in this research.

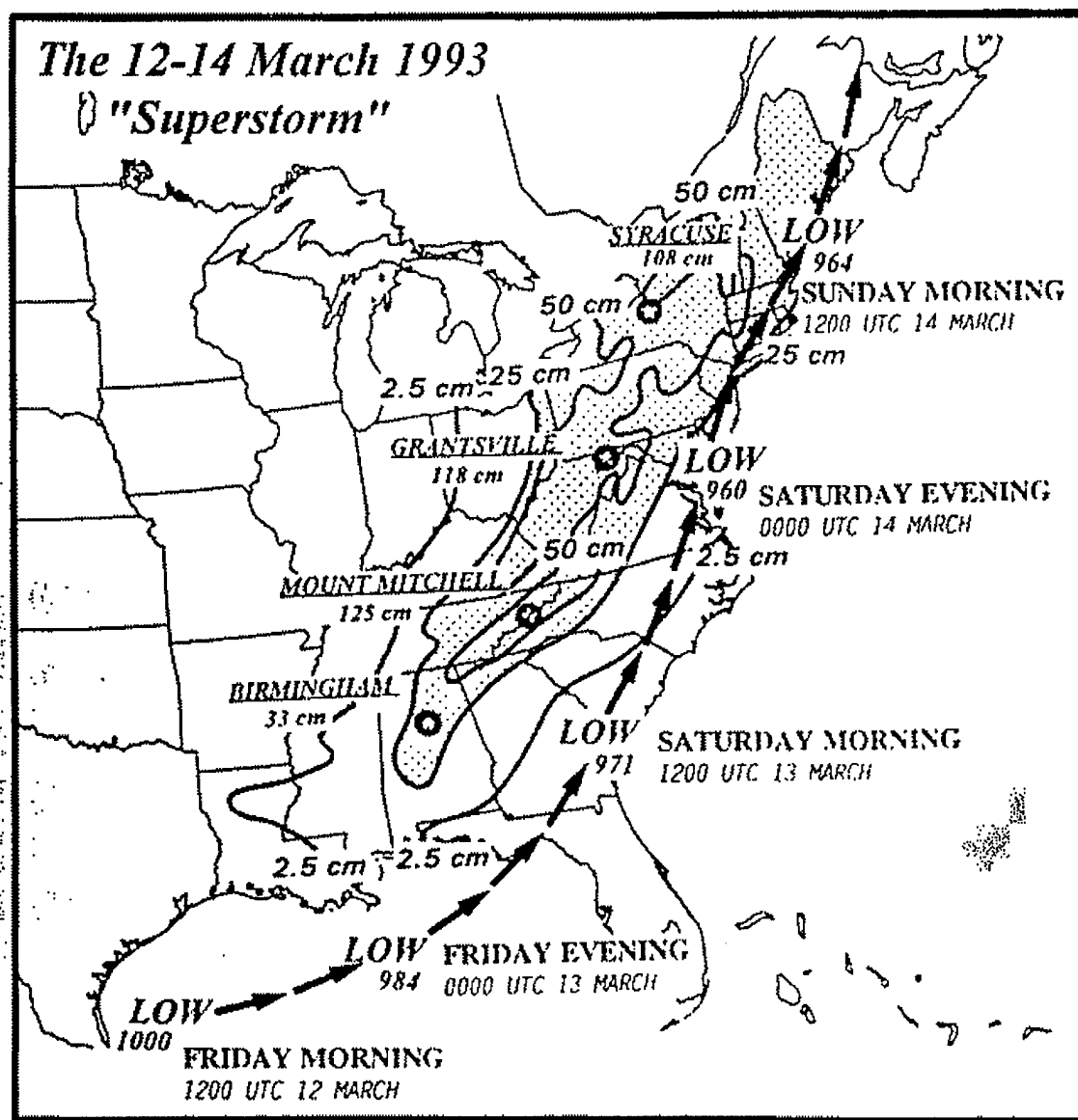


Figure 1.1: Storm track of SOC93 with selected snowfall amounts (cm). Central pressures (in hPa) follow the NMC surface analyses. From Fig. 2 of Uccellini et al., 1995.



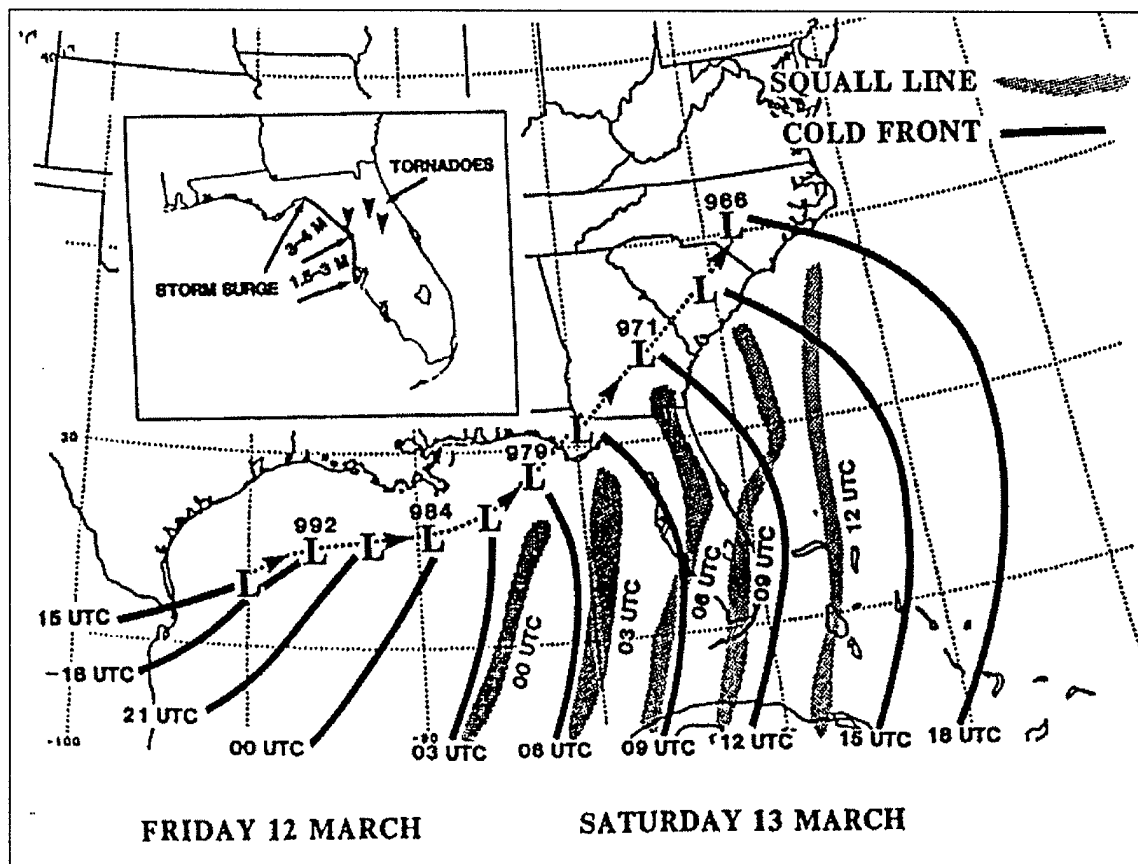


Figure 1.2: Composite surface analysis from Kocin et al. (1995), Fig. 2. Three-hourly evolution of the surface low pressure center (marked with L, central pressures in hPa), surface cold front (solid black line), the squall line (shaded) on 12–13 March 1993. Inset map marks location and depth (m) of the storm surge and approximate location of tornado outbreaks.

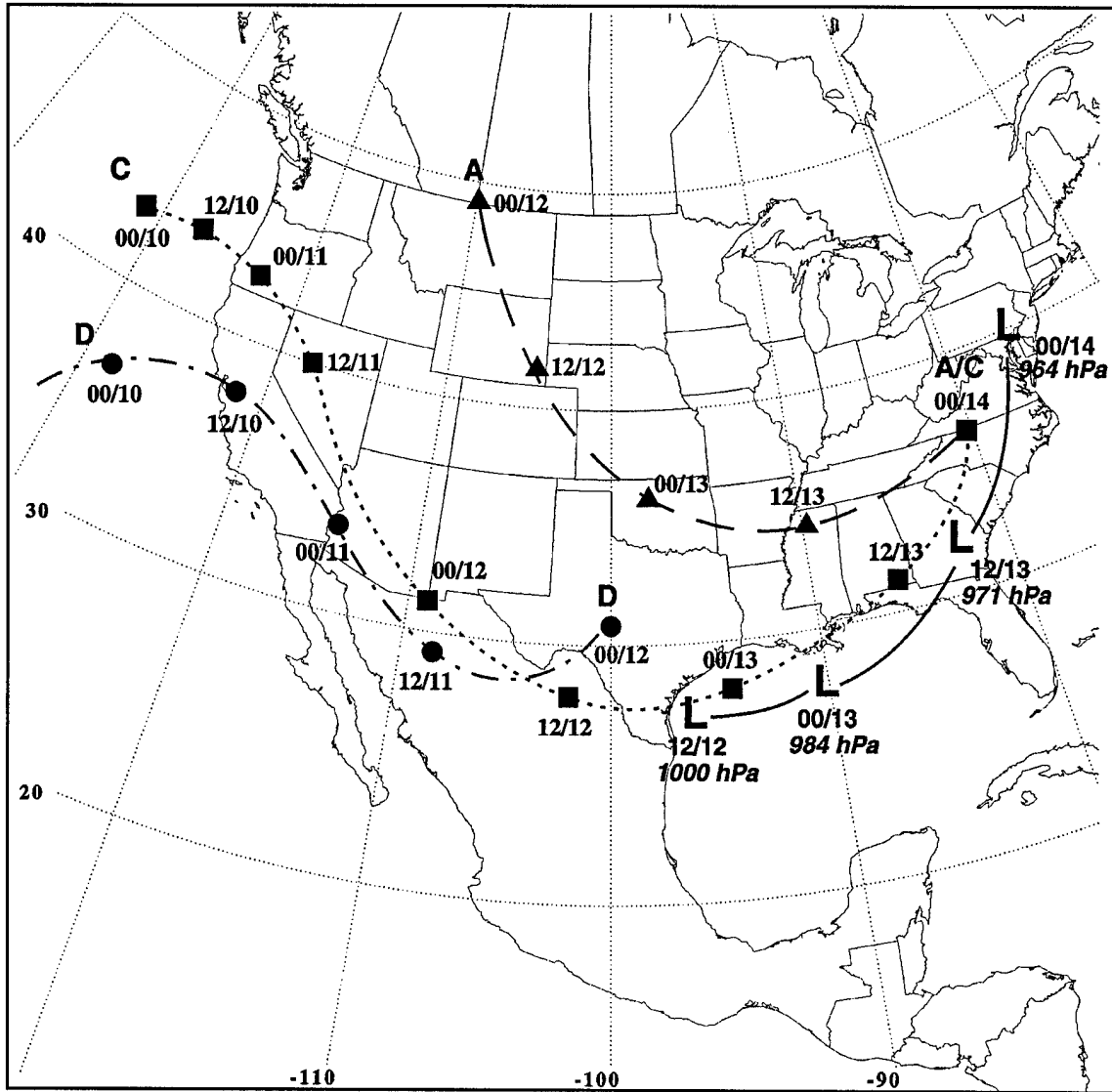


Figure 1.3: Tracks and 12-h positions (UTC/day; March 1993) of PV anomalies A, C, and D, marked with long dash, dotted and dash-dot paths, respectively. Solid line denotes track of SOC93 (12-h positions as above), with central pressures in hPa. The PV analysis is adapted from Bosart et al. (1996) and Dickinson et al. (1997), while the storm central pressures are taken from the mesoscale analysis of Kocin et al. (1995).

## Chapter 2

# The Mesoscale Evolution of the March 1993 Storm of the Century. Part I: Origin of the Precursor Convective Available Potential Energy

### 2.1 Introduction

Although considered largely a forecasting success, much of the life-cycle of SOC93 was not captured in operational models (Uccellini *et al.*, 1995). The initial surface cyclone formed early on 12 March in association with convection originating in the lower Rio Grande Valley (Fig. 2.1a). This region, extending northeastward to the central Texas Gulf Coast, appears primed for deep convection (Fig. 2.1b), though the mesoscale organization of the initial surface cyclone is first evident about 1200 UTC east of Corpus Christi, Texas (Fig. 2.1c). The surface low then deepened by 29 hPa in 24 h, making landfall in northwest Florida on 13 March between 0600 and 0900 UTC (Fig. 2.2). The initial cyclogenesis in the western Gulf of Mexico was consistently poorly forecast, resulting in a significant under estimation of storm impact as it made landfall in Florida (Uccellini *et al.*, 1995; Huo *et al.*, 1995; Dickinson *et al.*, 1997). From a broad perspective, a poor numerical weather forecast usually has three suspects: incomplete model physics, a deficient initial state, or inadequate resolution.

In an extensive study of the planetary and synoptic flow in which SOC93 developed,

Bosart *et al.* (1996) and Dickinson *et al.* (1997) investigated, among other issues, the quality of model physics in the National Centers for Environmental Prediction (NCEP) Medium Range Forecast (MRF) Model. These authors hypothesize that three potential vorticity anomalies (identified as PV anomalies **A**, **C** and **D**, see Fig. 2.2) interacted to initiate and sustain the cyclogenesis of SOC93. Specifically, they suggest that the initial, rapid cyclogenesis in the western Gulf grew from the destabilization of the surface environment by the dissipation of PV anomaly **D** over central Texas coupled to the approaching PV anomaly **C** descending along the front range of the Rocky Mountains into northeastern Mexico. While Bosart *et al.* (1996) demonstrate the extraordinary synoptic-scale signal of cyclogenesis, particularly after 0000 UTC 13 March, the role of these PV anomalies in *initiating* cyclogenesis early on 12 March cannot be clearly elucidated without mesoscale details that are not resolved in synoptic-scale datasets. Dickinson *et al.* (1997) made further progress in the qualitative understanding of these mesoscale details by examining the convection in NCEP MRF and European Center for Medium-range Weather Forecasts (ECMWF) products, concluding that inadequate cumulus parameterization in the MRF resulted in the poor simulation of the crucial period in SOC93 development. It should be noted that while these results represent progress in understanding SOC93, the coarse resolution of the MRF ( $2.5^\circ$ ) is not well suited to studying short-term explosive cyclogenesis.

Although the MRF forecast may have suffered from poor model physics, most other operational forecast models also failed to capture the initial cyclogenesis in the Gulf of Mexico (Caplan, 1995), suggesting that other factors may have contributed to the complexity of this forecast. Gilhousen (1994) found a strong mesoscale signal of early cyclogenesis in National Data Buoy Center (NDBC) data along the Texas Gulf Coast that was absent from NCEP model initial states. In particular, buoy data at 1200 UTC 12 March revealed a strong, closed circulation with sustained 35 kt winds and a pressure center 4 to 6 hPa lower than the 12 h NCEP Nested Grid Model (NGM) forecasts. The buoys also indicated a strong sea-surface temperature gradient and warmer waters that were poorly represented in NCEP forecasts (Gilhousen, 1994). Huo *et al.* (1998) employed a mesoscale version of the Canadian Regional Finite Element (RFE) model to simulate SOC93 using a modified initial state reflecting the relative warmth of the lower troposphere along the western Gulf Coast. Using the PV inversion technique of Davis and Emanuel (1991), these investigators inserted

a balanced correction to the model initial conditions yielding significant improvement in the RFE forecast over initial experiments reported in Huo *et al.* (1995).

While these studies suggest that both incomplete model physics and inadequate initialization contributed to the missed forecast in the western Gulf of Mexico, another useful insight from these studies implicates the issue of model resolution, namely: *the surface cyclogenesis of SOC93 was well underway by 1200 UTC 12 March*. The numerical studies of Huo *et al.* (1998, 1999a, 1999b) have shown considerable skill in reproducing the life cycle of SOC93 across the Gulf of Mexico only by initializing at 1200 UTC 12 March or later, at a point in time when the subsynoptic surface vortex was already well-resolved in the gridded first-guess fields. An open question in the literature remains: *what are the crucial mesoscale elements that initiated SOC93 prior to 1200 UTC 12 March?*

As implied by the observational studies of Kocin *et al.* (1995) and Bosart *et al.* (1996), convection and convective feedback are crucial to initiating SOC93. From synoptic observations and previous numerical studies, *we hypothesize that the evolution of SOC93 occurred in three stages, summarized in Table 2.1*. Stage I describes how deep convection is initiated and organized along the Texas Gulf Coast prior to 1200 UTC 12 March. Fundamentally, deep, organized convection requires instability, a triggering mechanism, a substantial moisture source, and a background environment capable of sustaining this convection once released. In this chapter, we employ observation datasets and mesoscale simulations to examine how the lower troposphere is destabilized along the Texas Gulf Coast late on 11 March and how the environment is conditioned to sustain deep convection. In a subsequent chapter, we will address how this instability is released early on 12 March.

The rest of this chapter is organized as follows: section 2.2 discusses the observation and simulation datasets used in this research; section 2.3 evaluates the overall fidelity of the control experiment; section 2.4 employs both observations and simulations to illustrate the initiation and maintenance of the mid-tropospheric baroclinic zone; and section 2.5 presents the concluding discussion.

## 2.2 Data and methodology

### 2.2.1 Model initialization

ECMWF uninitialized gridded fields were employed as initial and 6-h boundary conditions. To create the initial state, these first-guess fields were augmented with surface and upper air observations from conventional sources, supplemented with data provided by the Air Force Combat Climatology Center (AFCCC), Asheville, NC. Sea-surface temperature (SST) data and surface meteorological data were obtained from the archives of the National Data Buoy Center (NDBC) (reviewed thoroughly in Gilhousen, 1994). Gilhousen (1994) notes that the observed sea-surface temperature state was inadequately represented in operational analyses. To address this issue in the initial state of the control simulation, the National Hurricane Center (NHC) sea-surface temperature analysis (presented in Gilhousen, 1994) was used as a “first-guess” field and subjectively reanalyzed using NDBC buoy data and with Advanced Very High Resolution Radiometer (AVHRR) Pathfinder data from the Physical Oceanography Distributed Active Archive Center (PODAAC) provided by the National Aeronautics and Space Administration (NASA) Jet Propulsion Laboratory (JPL). The overall motivation of this reanalysis was to warm the analysis to realistic levels off the coast of northern Mexico and southern Texas to correct SST deficiencies noted in the literature. The subjectively reanalyzed (synthetic) SST field and the original NHC analysis appear in Fig. 2.3. Fig. 2.4 depicts the topography and observing stations referenced throughout this chapter.

### 2.2.2 Numerical experiments

All simulations were performed with the Mesoscale Atmospheric Simulation System (MASS) version 5.12, a hydrostatic, full-physics primitive equation model with fourth-order differencing (MESO Inc., 1993). As run for this study, the model used a modified Blackadar high-resolution PBL scheme (Zhang and Anthes, 1982) and the Fritsch-Chappell cumulus scheme (Fritsch and Chappell, 1980) for sub-grid scale convective processes. The control simulation was configured with a horizontal resolution of 12 km on a grid of  $260 \times 220$ , with 45  $\sigma$ -p levels in the vertical. Of the 45  $\sigma$ -p levels, approximately 31 were set below 600 hPa

to increase vertical resolution in the mid to lower troposphere. The domain of the 12 km experiments is depicted in Fig. 2.5.

Table 2.2 lists the numerical experiments used in this study. A smoothed-terrain run was conducted with resolution and physics matching the control simulation but with terrain suppressed with 50 passes through a nine-point smoother (Fig. 2.6). This reduced-terrain simulation is employed to qualitatively evaluate terrain-forced circulations in contrast to the full-terrain (full-physics) run and demonstrate the relative importance of these circulations to the initial cyclogenesis. An adiabatic simulation was also performed to quantitatively assess the role of all diabatic processes in the Stage I sequence. To separate surface diabatic processes from latent heating aloft, two additional modified physics simulation were performed. The NOLATENT simulation used full boundary layer physics but neglected all latent heating (both surface and aloft). The NOSFLX simulation used full boundary layer physics but neglected all surface sensible heat fluxes. For these modified physics runs, we should note that the time-dependent boundary conditions taken from the ECMWF gridded data do contain implicit diabatic processes; however, the introduction of coarse diabatic forcing at the perimeter should still permit qualitative assessment of the impact of these processes in the interior of the domain.

## 2.3 Model verification and synoptic situation

The CONTROL storm track and central pressures show good agreement with the Kocin *et al.* (1995) mesoanalysis (Fig. 2.7). The initial surface vortex forms off the Texas Gulf Coast just east of BRO at 1200 UTC 12 March with a central pressure of 1003 hPa (compare to 1000 hPa in Kocin *et al.*, 1995) and deepens 32 hPa over the next 24 h to 971 hPa in southeast Georgia. The control simulation deepened the initial cyclone at 2.5 Bergerons (defined in Sanders and Gyakum, 1980), in reasonable agreement with the observed deepening of 2.3 Bergerons (Kocin *et al.*, 1995). Over the period 1200 UTC 12 March to 1200 UTC 13 March, the mean error between observed and simulated sea-level pressures is approximately +3.4 hPa, in good agreement with published studies (e.g. Huo *et al.*, 1995, 1998) *that initialized at 1200 UTC 12 March*. In the present study, the simulated initial surface vortex at 1200 UTC 12 March is the product of 48 h simulation over a 96 h run ending at 1200

UTC 14 March.

To facilitate comparison with NCEP synoptic upper air analyses and ECMWF  $1.125^\circ$  gridded datasets, the control simulation dataset was smoothed with a Gaussian weighting function (Barnes, 1964) centered at  $16\Delta x$ , or  $\lambda_{max} = 192$  km. The large-scale structure of the nearly meridional subtropical jet (STJ) across western Mexico at 1200 UTC 12 March (Fig. 2.8a) is well preserved in the simulation (Fig. 2.8b), as is the more southerly branch of the STJ extending from central Mexico across the Bay of Campeche into southern Florida. For brevity, this synoptic-scale jet is referred to as the STJ though it is actually a confluence of the STJ and polar front jet (PFJ), as illustrated in Bosart *et al.* (1996). As will be demonstrated in Chapter 3, the key 300 hPa feature reproduced at 1200 UTC 12 March is the powerful divergence between Brownsville, TX (BRO) and Corpus Christi, TX (CRP), indicated by the  $90^\circ$  shift in  $25 \text{ m s}^{-1}$  (50 kt) winds along the extreme southern Texas Gulf Coast (Fig. 2.8a). This divergent signal is captured in the simulation though placed about 100 km too far south (Fig. 2.8b). This error is consistent with the placement of the simulated surface vortex at 1200 UTC 12 March; comparison of the initial positions of the simulated and observed storms (Fig. 2.7a) shows a similar 100 km discrepancy. The simulation produces an unambiguous diffluent structure over southern Texas that cannot be resolved in the NMC upper air analysis but is consistent with the strong divergence ( $10^{-4} \text{ s}^{-1}$ ) supporting explosive surface cyclogenesis.

The control simulation also reproduces the potential vorticity structure analyzed in Bosart *et al.* (1996). Isentropic potential vorticity (IPV) was calculated for both the ECMWF (observed) and CONTROL (simulated) datasets. A column-weighted average PV was analyzed from 336 K (about 375 hPa) to 316 K (about 650 hPa), to approximate the 350–675 hPa column used in the QGPV analysis of Bosart *et al.* (1996). Consistent with the dissipation of PV anomaly D at approximately 0000 UTC 12 March (Bosart *et al.*, 1996), both the observed (Fig. 2.9a) and simulated (Fig. 2.10a) fields show only a weak PV signal proximal to the position of PV anomaly D at 1800 UTC 11 March. PV anomaly C, however, is distinct in both the observed and simulation fields indicated by a 3 PVU ( $1 \text{ PVU} = \text{K m}^2 \text{ kg}^{-1} \text{ s}^{-1}$ , Hoskins *et al.*, 1985) maximum entering northern Mexico along the front range of the Sierra Madres at about 0000 UTC 12 March (Fig. 2.9b and 2.10b). The path of PV anomaly C along the western Rio Grande Valley is well-simulated (compare Fig. 2.9c–d with Fig. 2.10c–



d), and the intensity at 3 PVU is reasonably close to the ECMWF-analyzed 3.5 to 4.0 PVU. In the ECMWF dataset, the early surface low at 1200 UTC 12 March appears as an extension in the 1 PVU contour over the Gulf Coast of extreme northern Mexico and southern Texas (Fig. 2.9d). The mesoscale control simulation, however, shows a distinct 1.5 PVU maximum coincident with the simulated surface vortex (Fig. 2.10d).

We conclude that the CONTROL experiment captures the synoptic situation of SOC93 in the western Gulf of Mexico after a 48-h integration (from 1200 UTC 10 March to 1200 UTC 12 March). In the present study, we will demonstrate that this simulation reproduces SOC93 because it correctly simulates the destabilization of the lower troposphere, the sustaining background environment, and the triggering mechanism that initiates the crucial mesoscale convective complex (Fig. 2.1c). Our focus for the remainder of this chapter will be on the mechanisms that produce and maintain the source of convective available potential energy along the Texas Gulf Coast early on 12 March.

## 2.4 Observations and simulations of the mid-tropospheric baroclinic zone

### 2.4.1 Overview

The deep convection that forms the kernel of SOC93 erupts early on 12 March in an environment destabilized by a mid-level cold pool. This cold pool has been noted in previous studies (Huo *et al.*, 1995; Kocin *et al.*, 1995; Bosart *et al.*, 1996; Dickinson *et al.*, 1997) and is evident in the ECMWF analysis as a 700 hPa cold trough in the isentropes extending from central Texas to northeastern Mexico, just west of Brownsville (BRO), Texas, at 0000 UTC 12 March (Fig. 2.11a).

The impact of this cold trough on the lower troposphere can be measured with the convective available potential energy (CAPE) in the column. The propagation of this cold air down the Rio Grande Valley decreases the environmental potential temperature ( $\theta$ ) through a significant layer (800 to 400 hPa), while near-surface flow from the Gulf of Mexico provides warm and moist (high  $\theta_e$ ) air, effectively increasing the available potential energy in the column and decreasing the static stability. CAPE was calculated from ECMWF-derived

soundings at BRO for the period 1200 UTC 10 March to 1200 UTC 13 March. This time series (Fig. 2.11b) shows a peak in CAPE just after 0000 UTC 12 March of about  $1600 \text{ J kg}^{-1}$ , coincident with the approach and passage of this mid-level cold pool. Although there is a diurnal component to this maximum, we assert that it is of secondary importance to the sharp peak at 0000 UTC 12 March (Fig. 2.11b): surface temperatures at BRO on 11 March range from  $68^{\circ}\text{F}$  at midnight local to a daytime high of  $78^{\circ}\text{F}$  in the afternoon. Radiosonde data available every 12 h at BRO confirms the shape of the time series (Fig. 2.11b) though the similarity between the two is influenced in part by the incorporation of radiosonde data into the ECMWF data assimilation cycle.

We first examine how this cold pool is initiated in the upper Rio Grande Valley. We then illustrate the frontogenetical deformation of this cold pool as it propagates across central Texas on 11 March, and the upper-level jetogenesis that results as the atmosphere adjusts to this mid-tropospheric meso- $\alpha$  cold surge. We conclude with an analysis of sensitivity experiments to illustrate the relative contributions of moist and dry diabatic processes, terrain and sea-surface temperature gradients in the production of the cold feature evident at 0000 UTC 12 March (Fig. 2.11a).

## 2.4.2 Initiation of the cold pool

Early on 11 March, a cold pool forms at about 700 hPa near Del Rio (DRT), Texas, above the intersection of three very different airmasses. The near-surface environment of south central Texas is dominated by a northeasterly cold surge (Fig. 2.12a) associated with the remains of the arctic front trailing PV anomaly M (identified in Bosart *et al.*, 1996, located in the Ohio Valley at this time). Above this near-surface layer of cold air, a southeasterly flow transports warm air up the Rio Grande Valley, maximizing warm advection at 850 hPa proximal to Del Rio (DRT), Texas (Fig. 2.12b). The near-surface low pressure over central Mexico (where the mean elevation is greater than 1000 m, see Fig. 2.4) is accompanied by southwesterly flow aloft, evident in the ECMWF analysis at about 700 hPa (indicated by solid arrow in Fig. 2.12c).

The observed cold pool appears as a cold trough southwest of DRT at 700 hPa (dashed line southwest of DRT in Fig. 2.12c) and is proximal to weak convection in the upper Rio

Grande Valley. The simulated cold pool forms early on 11 March west of DRT and along the Edwards Plateau (cf. Fig. 2.4), in a region initially marked by a relatively warm pool ( $\theta > 307$  K) at 700 hPa (Fig. 2.13a). Within 3 h (by 0600 UTC) this warm pocket has become a meso- $\beta$  cool pool ( $\theta < 306$  K, Fig. 2.13b) over DRT, which verifies well with the observed feature (Fig. 2.12c). This cold pool expands in place and cools by 3 K over the next 3 h, reaching 303 K at 0900 UTC at the center of a cold ellipsoid oriented southwest to northeast along a major axis approximately 400 km in length (Fig. 2.13c). After 0900 UTC, the cold pool begins to propagate eastward, approaching the Texas Gulf Coast by 1200 UTC, with weak convection forming along the leading (eastern) edge (Fig. 2.13d).

The 700 hPa cold pool develops despite persistent warm, southwesterly flow from the Altiplanicie Mexicana. The near-surface low pressure over central Mexico (where the mean elevation is greater than 1000 m, cf. Fig. 2.4) is accompanied by an anticyclonic outflow aloft, evident just east of DRT in the ECMWF analysis (Fig. 2.12c) and in simulation fields (e.g. Fig. 2.13b). This dry convective outflow represents the upper branch of a large mountain-plains solenoid (MPS) which transports the quasi-adiabatic elevated mixed layer (EML) from the Mexican plateau northward into the Southern Plains of the U.S. (e.g. Lanicci and Warner, 1991a, 1991b, 1991c). Similar MPS signals are documented in recent studies by Kaplan *et al.* (1997) using observations and simulations west of the Rocky Mountains during the Cooperative Convective Precipitation Experiment (CCOPE). In the case of the Mexican plateau, the horizontal and temporal scale of the heating are sufficient to allow some degree of geostrophic adjustment ( $L_{circ}$  approaches the Rossby radius of deformation) hence the cyclonic near-surface inflow (Figs. 2.12a and b) and anticyclonic outflow aloft (Fig. 2.12c).

The thermally-driven MPS flow at 0300 UTC is marked by an anticyclonic arc of ascent extending from central Mexico (along the plateau) to central Texas northeast of DRT (Fig. 2.14a). This signal of ascent is interrupted by pronounced subsidence proximal to DRT in the cold pool genesis region (Fig. 2.14a). By 0600 UTC (local midnight), cooling along the plateau weakens the MPS outflow at 700 hPa with concomitant weakening of ascent along the plume and a general eastward displacement of the thermal ridge; the initial cold pool, however, is marked largely by subsidence in the upper Rio Grande Valley (Fig. 2.14b). This subsidence intensifies as the cold pool matures, and by 0900 UTC the weakened MPS and attendant plume of ascent have propagated east of the cold pool (Fig. 2.14c). By 1200

UTC, the cold pool and residual MPS signal form a meso- $\alpha$  baroclinic zone across eastern Texas oriented parallel to the coast with strong subsidence along the major axis of the cold pool and ascent on the leading (eastern) edge of the baroclinic zone (Fig. 2.14d).

The demonstrated presence of the MPS indicates that the cold pool is not a product of horizontal advection, and the strong correlation of the cooling signal and 700 hPa descent implies that adiabatic cooling (through ascent) is not the direct cause of this phenomenon. In fact, diabatic cooling through evaporation is consistent with intensification of the cold pool under meso- $\alpha$  subsidence. Weak convection is indicated near the cold pool genesis region in satellite observations (Fig. 2.12c); however, simulated precipitation fields show very little precipitation *reaching the ground* (Fig. 2.13b). Cross-sections along the mean path of the cold pool clarify the relationship between this feature and nearby precipitation.

Shallow convection is triggered between 0300 and 0600 UTC 11 March indicated by the rainwater mixing ratio ( $m_{rain} > 0.1 \text{ g kg}^{-1}$ ) in the layer from about 350 to 650 hPa (Figs. 2.15a and b). The base of this convection is elevated because of the near-surface cold air, indicated by the very cool boundary layer extending to 800 hPa over much of central Texas (Fig. 2.15a). This boundary layer is lifted mechanically to about 750 hPa over the Edwards Plateau (left or western portion of Fig. 2.15a) and this lifting is coincident with a disturbance in the quasi-adiabatic elevated mixed layer (EML) indicated from about 304 to 310 K (about 800 to 600 hPa). Once triggered, the meso- $\beta$  convection deposits evaporationally-cooled air into the top of the EML, creating a significant absolutely unstable layer between about 650 and 750 hPa; the folded 306 K isentrope in Fig. 2.15b marking this instability is coincident with the 700 hPa cold pool depicted at 0600 UTC in Fig. 2.13b. Despite the meso- $\beta$  instability created by this mechanism (about 100 hPa deep and over 100 km across) the convection persists as a *shallow* feature topping out at 400 hPa as it propagates across central Texas (Fig. 2.15c,d). At 0900 UTC, the lower portion of the cold pool is actually significantly *warmer* relative to the cool boundary layer, indicated by a sharp downfold of isentropes in Fig. 2.15c. This warming is still evident beneath the cold pool at 1200 UTC (Fig. 2.15d) though the cold pool and attendant convection have propagated slightly east of this low-level signal. Surface observations proximal to the path of this cold pool indicate little or no precipitation, which is consistent with shallow convection and evaporative cooling *above* the already-cool boundary layer. These results suggest that the

cold pool is largely a response to the shallow convection initiated in the upper Rio Grande Valley early on 11 March; to examine *how* this convection is triggered, we further investigate the signal of low-level warming attendant to the early convection.

Along the Rio Grande Valley, low-level flow brings warm air northwestward about the thermally-induced low pressure center over the Altiplanicie Mexicana (Fig. 2.12b). This hot conveyor belt operates at the interface of the cool and moist boundary layer and the bottom of the EML displaced into the valley by nocturnal cooling along the plateau. Simulated 800 hPa fields at 0300 UTC 11 March provide evidence of this flow up the valley, transporting warm air northwestward from BRO to DRT (Fig. 2.16a); the influence of outflow from the plateau is evident as this northwesterly flow is turned anticyclonically to southwesterly proximal to DRT. A cross-section along the major axis of the cold pool genesis region at this time reveals the cool and deep boundary layer (from surface to 800 hPa) capped by the EML; this layer of plateau air is indicated by the weak static stability from 600 to 800 hPa (about 304 to 310 K, Fig. 2.16b). Also evident is the strong southerly ageostrophy northeast of DRT as the MPS outflow carrying the EML accelerates over the cool boundary layer (Fig. 2.16b). By 0600 UTC, the penetration of the hot conveyor belt at this interface near DRT is indicated at 800 hPa (Fig. 2.17a shaded  $\theta > 304$  K), and the effect of this warming at the bottom of the EML is to drive an overturning in a region of weak static stability, creating the cool pool evident at 700 hPa (Fig. 2.13b). The cross-section at 0600 UTC does not indicate even shallow precipitation on the leading edge of this pool; this is not an artifact of the plane chosen for the cross-section because the west-east cross-section at this time (Fig. 2.15b) indicates precipitation on the *western* edge of this overturning. Cross-sections along the approximate path of the hot conveyor belt indicate that the southeasterly flow up the Rio Grande Valley is actually relatively dry at 0300 UTC (Fig. 2.18a); computations along this path show a mean relative humidity in the airstream of 50% to 60%. As the initial cold pool erupts about 0600 UTC, the leading edge of this southeasterly stream is quickly saturated, though significant warm and dry air continues to penetrate northwestward (Fig. 2.18b). The point of this clarification is that the cool feature is *initiated* by the penetration of the hot, *dry* conveyor belt and subsequent overturning of the EML; as previously discussed and as will be further demonstrated, this cool feature grows in scale and becomes a cold meso- $\beta$  phenomenon under evaporative cooling from shallow convection that is itself triggered by

the penetration of the hot conveyor belt.

Between 0600 and 0900 UTC, the hot conveyor belt stimulates the interface between the EML and the cool boundary layer southeast of DRT (Fig. 2.19a) as the cold pool expands and cools (Fig. 2.13c). The vertical structure indicates the hot conveyor belt as a warm depression in the isentropes immediately underneath the strongest signal of cooling (Fig. 2.19b), flanked by shallow convection of substantial ( $\sim 400$  km) horizontal scale. The combination of evaporative cooling at the top of the layer (about 600 hPa) and intense warming by the hot conveyor belt at the bottom of the layer (about 800 hPa) drives a vigorous simulated mixing that redistributes cool air into the evolving 700 hPa cold pool. This second-order process is accomplished in the simulation by the modified Blackadar PBL scheme (Zhang and Anthes, 1982).

The one-dimensional Blackadar model vertically mixes the mass and momentum fields to eliminate instability based on the local Richardson number falling below a critical value (nominally  $Ri < 0.25$ ), where

$$Ri = \frac{g}{\theta} \frac{\partial \theta}{\partial z} \left| \frac{\partial \mathbf{V}}{\partial z} \right|^{-2} \quad (2.4.1)$$

$Ri$  represents a balance between the vertical thermodynamic structure and the vertical shear where small  $Ri$  values correspond to strong vertical shear and/or low static stability and indicate a subsequent conversion of mean kinetic energy to turbulent kinetic energy (i.e. a second-order mixing of mass and momentum fields). In the case of the cold pool east of DRT, the governing factor is the absolutely unstable layer ( $[g/\theta]\partial\theta/\partial z < 0$ ) created at the penetration of the hot conveyor belt. Computation of  $Ri$  along the major axis of the cold pool at 0900 UTC verifies this assertion, indicating  $Ri \ll 0$  or significant static instability at the penetration of the hot conveyor belt (Fig. 2.20). Also evident is the destabilization induced at the top of the EML through evaporative cooling (Fig. 2.20) immediately under the shallow convection triggered by the hot conveyor belt (Fig. 2.19b).

Ascent through the mixed layer caused by the warm advection accompanying the hot conveyor belt triggers additional shallow convection, which contributes to the cooling at the top of the mixed layer as a result of latent heating-induced mass outflow. By 0900 UTC, the cold pool appears at 700 hPa as a semi-circular feature approximately 300 km along the minor axis (Fig. 2.13c). Attendant convection is oriented along and northwest of the

major axis of the cold pool (Fig. 2.13c), and a cross-section along the minor axis (mean path) shows that the scale of the convection is about 150 km compared to the cold pool characteristic width of 300 km (Fig. 2.19b). This is further support that initial mixing and deformation from the convectively-induced mass outflow are sequentially responsible for the upscale growth of the cold pool after 0600 UTC.

After 0900 UTC, the hot conveyor belt begins to weaken and retreat down the Rio Grande Valley as nocturnal cooling along the elevated plateau displaces the hot conveyor belt eastward, coincident with the eastward propagation of the cold pool. In the period from 0600 to 0900 UTC, the major axis of the cold pool moves about 30 km in 3 h or less than  $3 \text{ m s}^{-1}$ , while from 0900 UTC (Fig. 2.13c) to 1200 UTC (Fig. 2.13d) the major axis moves about 150 km in 3 h or about  $14 \text{ m s}^{-1}$ . The hot conveyor belt, indicated as a thermal ridge aligned under and along the major axis of the cold pool at 1200 UTC 11 March (Fig. 2.21a), continues to stimulate the growth of the cold pool (Fig. 2.21b) though the significant convection is displaced to the leading (eastern) edge of the cold pool along the boundary of the cold pool and the displaced warm MPS outflow (Figs. 2.13d, 2.15d). Because the convection is displaced from the hot conveyor belt, however, this does not produce the same intense mixing response characteristic of the 0600 to 0900 UTC period (compare Fig. 2.19b to Fig. 2.21b).

The simulated cold pool at 1200 UTC 11 March (Figs. 2.13d) verifies with a weak cool trough in the ECMWF 700 hPa potential temperature field (Fig. 2.22); at both times the simulated major axis is well placed with respect to the observed axis. Precipitation along the leading (eastern) edge of the cold pool (Fig. 2.13d) verifies well in the IR satellite imagery (Fig. 2.22), particularly along the Gulf Coast, and precipitation along the northern edge of the cold pool is in reasonable agreement with the simulation. Soundings from 11 March at DRT show the net effect of the passage of this cold pool and provide further corroboration of the model-produced cold pool (Fig. 2.23). The elevated mixed layer (EML) attendant to the MPS outflow appears as a nearly adiabatic region from about 800 to 500 hPa at 0000 UTC, with a characteristic inversion at the base of the layer (Lanicci and Warner, 1991a). The initiation of the cold pool at the base of the EML lifts this inversion to about 750 hPa at 1200 UTC, strengthening the cap on the lower troposphere and inhibiting widespread convection. Further inhibiting deep convection is the almost uniform cooling of the lower

troposphere below 850 hPa, though the cold pool stands out as a saturated cool layer between 850 and 750 hPa (Fig. 2.23); as discussed previously, the cold boundary layer also helps confine the convection to a shallow layer in the middle troposphere. As demonstrated with simulation results, this cool layer (Fig. 2.23) is created by evaporational cooling under shallow convection triggered by the penetration of the hot, dry conveyor belt between 800 and 850 hPa (Fig. 2.17). The initial penetration at about 0600 UTC is midnight local time in this region and is consistent with the nocturnal acceleration of the hot conveyor belt over the stable (cool) boundary layer; this result is consistent with the recent modeling and observational work of Kaplan *et al.* (2000).

We have demonstrated that the hot conveyor belt is a critical mechanism in the initiation of the cold pool. This phenomenon appears to be a less intense form of the Brownsville jet, identified by Igau and Nielsen-Gammon (1998) in their study of low-level jets of the Southern Plains. The Brownsville jet forms in summer months along the eastern boundary of the terrain of northern Mexico at the base of the EML inversion but above the marine boundary layer as nocturnal cooling along the plateau displaces the EML eastward into the Rio Grande Valley (Igau and Nielsen-Gammon, 1998). In the present, cool-season (Nov – Apr) case, the hot conveyor belt is a less-intense phenomenon than the Brownsville jet but is capable of inducing significant low-level warm advection ( $> 0.6 \text{ K h}^{-1}$ ) along the upper Rio Grande Valley resolvable within the ECMWF analysis (Fig. 2.12b).

The hot conveyor belt appears to be the triggering mechanism for the mid-level cold pool; however, this southeasterly warm airstream is actually a broad feature relative to the scale of the initial cold pool (compare the warm plume in Fig. 2.17a to the initial cold pool in Fig. 2.13b). We speculate that the region near Del Rio is the preferred point of impact because of the interaction of the local terrain and the near-surface cold air. At 0300 UTC 11 March, a cool disturbance proximal to the Edwards Plateau is evident within the mixed layer (600 to 800 hPa, southwestern or left-hand side of Fig. 2.16b, and western or left-hand side of Fig. 2.15a). The Edwards Plateau has a mean elevation of 500 m (cf. Fig. 2.4) and northeasterly, near-surface cold air is mechanically lifted or dammed against the shallow terrain, producing the cool disturbance in the EML (Fig. 2.16b, 2.15a), which appears to be the point of impact of the hot conveyor belt at about 0600 UTC (Fig. 2.17b, 2.15b).

From the evidence presented, we conclude that the mid-level cold pool is initiated by the



arrival of the hot conveyor belt along the upper Rio Grande Valley at about 0600 UTC 11 March. In a simulated time series over DRT, the penetration of this hot airstream stands out as a sharp spike in potential temperature between 0600 and 0800 UTC in the layer below 750 hPa, most pronounced at 850 hPa. (Fig. 2.24a). This peak in potential temperature is coupled with a sharp drop in relative humidity (Fig. 2.24b) characteristic of the hot, dry airstream carrying residual plateau air. Subsequent intense warm advection triggers convection that is confined to a shallow layer between the cold boundary layer and warm elevated mixed layer; overturning at the point of impact of the hot conveyor belt coupled with significant evaporative cooling at the base of this elevated convection create a distinct cold phenomena at about 700 hPa by 0900 UTC. The passage of this cold pool leaves the layer from about 800 to 850 hPa somewhat cooler and significantly more moist by 1200 UTC (Fig. 2.24b), consistent with the observed sounding at DRT (Fig. 2.23). In the next section, we will demonstrate how this cold pool is further deformed and transported to the Gulf Coast.

### 2.4.3 Frontogenesis and jetogenesis

The cold pool initiated in the upper Rio Grande Valley early on 11 March becomes a more mobile feature after about 0900 UTC as the hot conveyor belt supporting its initial development begins to retreat southeastward. This phenomenon is transported across central Texas and frontogenetically deformed at the intersection of the southwesterly MPS outflow and the synoptic-scale westerlies, transforming the initial cold pool (Fig. 2.13b) into a well-defined frontal zone along the Texas Gulf Coast by 0000 UTC 12 March. The mid-level meso- $\alpha$  scale cold air across central Texas forces an adjustment in the upper-level wind field, producing a 300 hPa jetlet that also participates in the early cyclogenesis of SOC93. We first illustrate the rapid frontogenesis across central Texas from midday on 11 March to early on 12 March, then demonstrate the upper-level adjustments that form this crucial jetlet.

Relatively strong 700 hPa frontogenesis marks the leading (eastern) edge of the cold pool when compared to the persistent frontogenesis along the mid-tropospheric boundary stretching from the Texas panhandle to central Mississippi (Fig. 2.25); this computation was performed with the quasi-horizontal, adiabatic formulation of frontogenesis (e.g. Bluestein,

1993, Eq. 2.3.8). This 700 hPa boundary across extreme northern Texas and Oklahoma is the upper-level reflection of the stationary surface front across southern Texas (Fig. 2.12a) and represents the trailing edge of the cold air associated with the Bosart *et al.* (1996) PV anomaly M. The major axis of the mobile mid-tropospheric front reaches the Gulf Coast about 1500 UTC 11 March (Fig. 2.25a) as daytime heating accelerates the southwesterly MPS outflow (1500 UTC is 0900 LST or about 3 h after sunrise). Near-surface cold air begins to move southeastward down the Rio Grande Valley and the southwest flank of cold air at 700 hPa is reinforced by a second cold pool forming midway between DRT and Brownsville (BRO), TX, between 1200 (Fig. 2.13d) and 1500 UTC (Fig. 2.25a). Intense convection forms along the northwest edge of the cold pool in the confluent region between the cold pool and the stationary boundary to the north, reinforcing the cold air along the northern portion of the cold pool between 1500 (Fig. 2.26a) and 1800 UTC (Fig. 2.26b). The result of this forcing on the extreme boundaries of the cold pool is to expand the scale of the cold pool along the major axis (parallel to the Gulf Coast) so that the cold pool extends from the southern Louisiana to extreme northeast Mexico by 2100 UTC 11 March (Fig. 2.25c). By 0000 UTC 12 March the simulated cold pool along the Gulf Coast (Fig. 2.25d) verifies well with the observed 700 hPa cold feature in the ECMWF analysis (Fig. 2.11). Cut off from near-surface cold air and with only scattered, light convection on the periphery of the feature, the cold pool remains resident along the Gulf Coast for the next 12 h (not shown).

Bosart *et al.* (1996) have suggested that the dissipation of PV anomaly D and subsequent widespread convection also enhances the baroclinicity of the lower troposphere early on 12 March. At 1800 UTC 11 March, according to Bosart *et al.* (1996) PV anomaly D is about 500 km west of Del Rio (DRT), TX, (indicated by the filled octagon in Fig. 2.25b), then arcs cyclonically across the upper Rio Grande Valley, crossing DRT between 2100 UTC (Fig. 2.25c) and 0000 UTC 12 March (Fig. 2.25d). The 700 hPa flow ahead of PV anomaly D remains relatively undisturbed through its dissipation. Vigorous convection was already in progress across north central Texas by 1500 UTC (Fig. 2.26a) and significant cold air was already in place through much of east central Texas to the Gulf Coast by 1500 UTC 11 March (Fig. 2.25a). While PV anomaly D may have made some contribution to the ongoing convection across central Texas, the dominant mechanism driving the mid-level baroclinicity was operating well before the arrival of this weak PV anomaly.

The mid-level cold air across central Texas in proximity to the warm MPS air to the southwest drives a cross-stream acceleration in the mid-upper troposphere as a result of an increasing north and northwestward-directed pressure gradient force. The subsequent acceleration of the mean flow, coupled with acceleration from convective outflow and enhanced by the mid-tropospheric latent heating, forms a 300 hPa jetlet northwest of the 700 hPa cold pool. Note, in particular, the 300 hPa ageostrophic vectors along the body of the 700 hPa cold pool in Figs. 2.26b–c which reflect the wind field adjusting to this newly-formed cross-stream temperature and, hence, deep height gradient. Away from strongly curved flow and in a friction-free environment, the ageostrophic wind makes a useful surrogate to evaluate these mesoscale accelerations.

Evidence of this acceleration is indicated by strong 300 hPa ageostrophy immediately above the 700 hPa cold pool at 1500 UTC (Fig. 2.26a) with concomitant divergence aloft (Fig. 2.27a). The extreme southwestern end of the cold pool is located along a sharp terrain gradient in the front range of the Sierra Madres just north of Monterey (MTY), MX (cf. Fig. 2.4). The exceptional 300 hPa divergence associated with this feature ( $> 2 \times 10^{-4} \text{ s}^{-1}$  in Fig. 2.27a) occurs in an environment relatively free of convection (Fig. 2.25a), from which we conclude that this signal is likely a terrain-induced forcing of cold air aloft similar to the 0300 UTC 11 March feature southwest of DRT (Fig. 2.15a, 2.16b). As the cold pool expands along the Gulf Coast between 1500 and 1800 UTC (Fig. 2.26b), the adjustment aloft forms a distinct  $40 \text{ m s}^{-1}$  jetlet north of Corpus Christi (CRP), TX (Fig. 2.27b). The ageostrophy and strong divergence along the southwest extreme of the cold pool forms the entrance region to this jetlet (Fig. 2.27b) and ascent under this signal triggers moderate convection across southern Texas and extreme northern Mexico between 1800 (Fig. 2.26b) and 2100 UTC (Fig. 2.26c) reinforcing and deforming the southwest portion of the cold pool. As noted previously, by 0000 UTC 12 March the major axis of the cold pool stretches from southern Louisiana to extreme northern Mexico (Fig. 2.26d) and the attendant jet streak (identified as **J1** in Fig. 2.27d) is aligned along the extreme northern Gulf Coast of Texas and Louisiana. Along its major axis, the simulated jet streak has an approximate length of 1500 km (Fig. 2.27d). Because of the relatively robust time and space scale of this adjustment, **J1** can be identified in the ECMWF 300 hPa wind field (Fig. 2.28) though the simulated phenomenon is about 100 km northwest of the observed feature.

The jetlet **J1** is a long-lived feature created by the pressure gradient response to meso- $\alpha$  baroclinic zone oriented along the Texas Gulf Coast formed by the the mid-level cold pool and MPS-induced warm pool. We should note, however, that there are cross-stream accelerations as a result of the increasing northward-directed pressure gradient force associated with the outflow of the mesoscale convective complex (MCC) in northern Texas (Fig. 2.26a), consistent with the classic work of Fritsch and Maddox (1981a). While strong ageostrophy characterizes both the MCC and the cold pool as early 1200 UTC 11 March (not shown), the convectively-driven outflow jet is a more transient feature that quickly becomes an extension of the entrance region to the polar front jet (PFJ) associated with the Bosart *et al.* (1996) PV anomaly M. A strong divergence signal evolves coincident with this MCC between 1500 (Figs. 2.26a and 2.27a) and 1800 UTC (Fig. 2.26b and 2.27b) building the entrance region of the PFJ associated with PV anomaly M southwestward along the Texas-Oklahoma-Arkansas border. By 2100 UTC, however, the upper-level divergence has relaxed through this region (Fig. 2.27c) as the MCC weakens (Fig. 2.26c). By 0000 UTC 12 March this extension to the PFJ has retreated into central Arkansas (Fig. 2.27d). For completeness, we should note that even though the convection directly associated with the cold pool is shallow, there is necessarily an outflow and concomitant acceleration aloft; hence, **J1** is formed in part by convective outflow, though this meso- $\beta$  outflow is overwhelmed by the long-term ( $\sim 12$  h) adjustment to the meso- $\alpha$  cold pool.

Consistent with previous studies (Huo *et al.*, 1995; Bosart *et al.*, 1996; Dickinson *et al.*, 1997), we assert that the mid-level cold pool along the Texas Gulf Coast is of critical importance to the initiation of cyclogenesis in the northwest Gulf of Mexico by providing a source of CAPE in the column. We have demonstrated the mechanisms that produce this cold pool on 11 March, and have illustrated the upper-level meso- $\alpha$  jet streak which, in turn, further enhances ascending flow as a result of the accompanying mass-flux divergence. We next examine additional numerical experiments to gain further insight into the role of individual forcing mechanisms on the overall process that initiates and maintains this cold pool.

### 2.4.4 Sensitivity analysis

To examine the relative contribution of moist and dry diabatic processes, we compare the ADIABATIC, NOSFLX, and NOLATENT runs to the CONTROL experiment through simple subtraction of the gridded fields at matching valid times. An implicit assumption in this approach is that simulation differences have a linear growth, though the technique is still useful for evaluating the qualitative or relative contribution of physical processes. At 1200 UTC 11 March, the 700 hPa cold pool stands out clearly as a cold error ( $\theta_{error} = \theta_{CONTROL} - \theta_{ADIABATIC}$ ), indicating that the ADIABATIC simulation did not produce a 700 hPa cold pool (Fig. 2.29a). With latent heating enabled but surface sensible heat fluxes disabled (NOSFLX), this error is reduced (Fig. 2.29b) but still significant; we conclude that latent heating (or in this case, evaporational cooling) *alone* is not sufficient to explain the mid-level cold pool.

With latent heating disabled (NOLATENT) the simulation is even warmer at 700 hPa than the adiabatic experiment, indicating that the sensible surface heat fluxes are not being relieved with convection and evaporation in the lower troposphere (Fig. 2.29c). We should emphasize that the shallow convection early on 11 March contributes to the expansion of the cold pool both through increased vertical mixing and increased horizontal deformation induced by the convective outflow. The NOLATENT simulation produces a weak cold trough by 1500 UTC 11 March (Fig. 2.30) with no significant frontogenesis along the leading (eastern) edge compared to the CONTROL simulation (Fig. 2.25a). We should note, however, that both simulations carry a strong signal of the southwesterly MPS outflow (band of  $15 \text{ m s}^{-1}$  winds on the western edge of the cold phenomena); this is consistent with the nature of the experiments since both the CONTROL and NOLATENT simulations include surface sensible heat fluxes. We conclude that both latent heating and cooling make significant contributions to the horizontal and vertical extent of the evolving cold pool.

Given that all the perturbations from the physics experiments are very similar in spatial extent and in magnitude (within about 1 K of each other), we conclude that both surface sensible heat fluxes and latent heat release are important to the early development of the cold pool. This is consistent with our hypothesis that the hot conveyor belt, driven by sensible heat fluxes and terrain, warms the column from below while moist convection (initiated by

the hot conveyor belt) provides evaporative cooling at the top of the column. This drives the prolonged mixing process as the  $\theta$  structure across the EML is continually nudged into instability by this mechanism. By 0000 UTC 12 March, the ADIABATIC and NOLATENT simulations show similar potential temperature structure at 700 hPa (Fig. 2.31a and c), while the NOSFLX simulation (Fig. 2.31b) more closely resembles the CONTROL simulation than either of the other two physics experiments. From this we infer that as the cold pool approaches the Gulf Coast late on 11 March, the hot conveyor belt becomes less important to maintaining the cold pool, while convection and evaporative cooling become more important to sustaining this feature.

The smoothed-terrain (SMOOTH) simulation is also presented for comparison, showing both significant warm and cold perturbations against the CONTROL simulation at 1200 UTC 11 March (Fig. 2.29d). This indicates that the SMOOTH simulation is moving the cold pool eastward more quickly than the CONTROL simulation. The smoothed terrain field (cf. Fig. 2.6b) alters the hot conveyor belt and the distribution of cold air along the upper Rio Grande Valley. In the SMOOTH simulation, extremely warm 304 K air reaches DRT at 800 hPa by 0300 UTC 11 March (Fig. 2.32a) though the hot conveyor belt weakens and retreats more quickly after 0600 UTC (compare the SMOOTH Fig. 2.32b to the CONTROL Fig. 2.17a). Note that extremely hot air never makes it northwest of DRT in the SMOOTH simulation. The resulting 0600 UTC cold pool is significantly cooler in the SMOOTH simulation (304 K in Fig. 2.32b compared to 306 K in Fig. 2.17a) but over time appears less well-organized, from which we infer that the hot conveyor belt is also an important *organizing* element to this process. The 0900 UTC cold pool in the SMOOTH simulation is more diffuse and the central cold minima not as intense (compare Fig. 2.32c to Fig. 2.19a). Consistent with the 1200 UTC 11 March error analysis (Fig. 2.29d), the SMOOTH cold pool is about 75 km southeast of the CONTROL cold pool and is not as well organized. The comparison between SMOOTH and CONTROL fields at 0000 UTC 12 March indicates that the CONTROL experiment is somewhat warmer over the Gulf of Mexico, though this is a symptom of the poorly organized SMOOTH cold pool. We conclude that the terrain-driven hot conveyor belt is important to both initiate *and* organize the critical mid-level cold pool.

The NCEP experiment (Table 2.2) was initialized with NCEP 2.5° reanalysis data as

opposed to ECMWF gridded fields and *did not produce the surface vortex at 1200 UTC 12 March*. Cursory analysis of the model fields indicate that the NCEP reanalysis data does not resolve the initial signal of the MPS. This provides additional, if anecdotal, evidence that the MPS is a crucial element in the initiation of SOC93.

Studies by Gilhousen (1994), Huo *et al.* (1995), Bosart *et al.* (1996) and Dickinson *et al.* (1997) all suggest that the strong coastal baroclinicity early on 12 March was not captured in operational models because of deficiencies in the initialized sea-surface temperature state. We have established that this coastal baroclinicity is driven largely by processes operating far inland. To examine this question further, the NHC SST field reported in Gilhousen (1994) (Fig. 2.3b) was used to initialize a numerical experiment (NHCSST). The surface track from this run (not shown) is quite similar to the control track (Fig. 2.7a). The NHCSST vortex at 1200 UTC 12 March is within 35 km (about  $3\Delta x$ ) of the CONTROL vortex and within 0.1 hPa of the central pressure. Overall the control simulation verifies better in track and central pressure, but the relative similarity of both simulations suggests that the mechanisms that form the initial surface cyclone, to include the crucial mid-level cold pool, are relatively insensitive to the sea-surface temperature gradient.

From these sensitivity analyses, we conclude that both dry and moist processes are equally significant in the initiation of the mid-level cold pool, though we have established previously that the hot conveyor belt, a relatively dry feature, triggers convection and the subsequent evaporative cooling feedback at the top of the EML, invigorating the mixing process. The smoothed-terrain experiment demonstrates that this hot conveyor belt is also an organizing feature for the mid-tropospheric front. Finally, although the sea-surface temperature field has been assumed to make an important contribution to the development of SOC93, our simulation results and sensitivity experiments suggest that the *initiation* of the surface cyclone is relatively insensitive to the sea-surface temperature field.

## 2.5 Concluding discussion

We have demonstrated that the process that conditions the environment for deep convection on 12 March is initiated early on 11 March. A substantial mid-level pool of cold air develops east of Del Rio (DRT), TX, prior to 0900 UTC at the junction of terrain-driven

circulations (the MPS aloft and hot conveyor belt below) and a low-level cold surge ahead of a synoptic-scale cold front (Fig. 2.33a). This cold pool is then frontogenetically deformed and transported across central Texas, aligned just off shore of the Texas Gulf Coast by 0000 UTC 12 March (Fig. 2.33b). In this journey across Texas, the baroclinic zone formed by mid-level cold air and MPS-induced warm air to the southwest drives a mesoscale northward-directed pressure gradient force that accelerates the upper-level flow, forming a meso- $\alpha$  scale 300 hPa jet streak (J1 in Fig. 2.33b). The mid-level cold pool conditions the environment for deep, organized convection along the Gulf Coast of southern Texas and northern Mexico by (1) directly destabilizing the lower troposphere (increasing the CAPE) and (2) creating a significant jetlet that is the focal point for explosive diabatically-induced jetogenesis early on 12 March. This explosive jetogenesis will be illustrated in a subsequent chapter.

The origin of the cold trough in the upper Rio Grande Valley sheds additional light on previous studies of SOC93. The dissipation of PV anomaly D over central Texas late on 11 March (Bosart *et al.*, 1996) occurs long after the cold pool, initiated early on 11 March, has been transported to the Gulf Coast. While PV anomaly D may have enhanced convection over central Texas late on 11 March, we have demonstrated that both this convection and the subsequent outflow jetlet at 300 hPa do not make primary contributions to the mid and upper-level structure along the Gulf Coast early on 12 March. Although the work of Gilhousen (1994), Huo *et al.* (1995), Bosart *et al.* (1996) and Dickinson *et al.* (1997) all suggest that the strong coastal baroclinicity early on 12 March was not captured in operational models because of deficiencies in the initialized sea-surface temperature state, we have demonstrated that the source of this crucial mid-level instability is a long-lived 700 hPa cold pool initiated along the terrain of western Texas. In a subsequent chapter we will address the sensitivity of the initial surface cyclogenesis to this sea-surface temperature field.

We assert that the early cyclogenesis of the March 1993 Storm of the Century challenged operational synoptic-scale models because crucial mesoscale processes could not be resolved prior to 1200 UTC 12 March. This chapter has focused on the mesoscale processes that establish a mid-level baroclinic zone along the Texas Gulf Coast late on 11 March. A subsequent chapter will employ observations and mesoscale simulations to address how this instability is realized as meso- $\alpha$  scale convection early on 12 March.



Stage	Period	Characteristics
<b>I</b>	0000 UTC 11 March to 1200 UTC 12 March	A sequence of mesoscale processes constructs a warm-core surface cyclone.
<b>II</b>	1200 UTC 12 March to 0600 UTC 13 March	The storm develops as a warm-core low then is transformed into an extratropical (cold-core) system.
<b>III</b>	0600 UTC 13 March to 0000 UTC 14 March	The storm intensifies again as PV anomalies A and C merge over the southeastern U.S. The storm then matures over the northeastern U.S.

Table 2.1: Summary of the SOC93 three-stage evolution.

Experiment ID	Horizontal Resolution	Physics	Initialization
CONTROL	12 km	Full model physics	ECMWF 1.125° Synthetic SST field
SMOOTH	12 km	Full model physics	ECMWF 1.125° Synthetic SST field Smoothed model terrain
ADIABATIC	12 km	Adiabatic physics No PBL or cumulus scheme	ECMWF 1.125° Synthetic SST field
NOLATENT	12 km	PBL physics enabled Latent heating enabled	ECMWF 1.125° Synthetic SST field
NOSFLX	12 km	Surface sensible heat flux disabled Latent heating enabled	ECMWF 1.125° Synthetic SST field
NHCSST	12 km	Full model physics	ECMWF 1.125° NHC SST field
NCEP	12 km	Full model physics	NCEP 2.5° Synthetic SST field

Table 2.2: Numerical experiments. All simulations initialized at 1200 UTC 10 March.

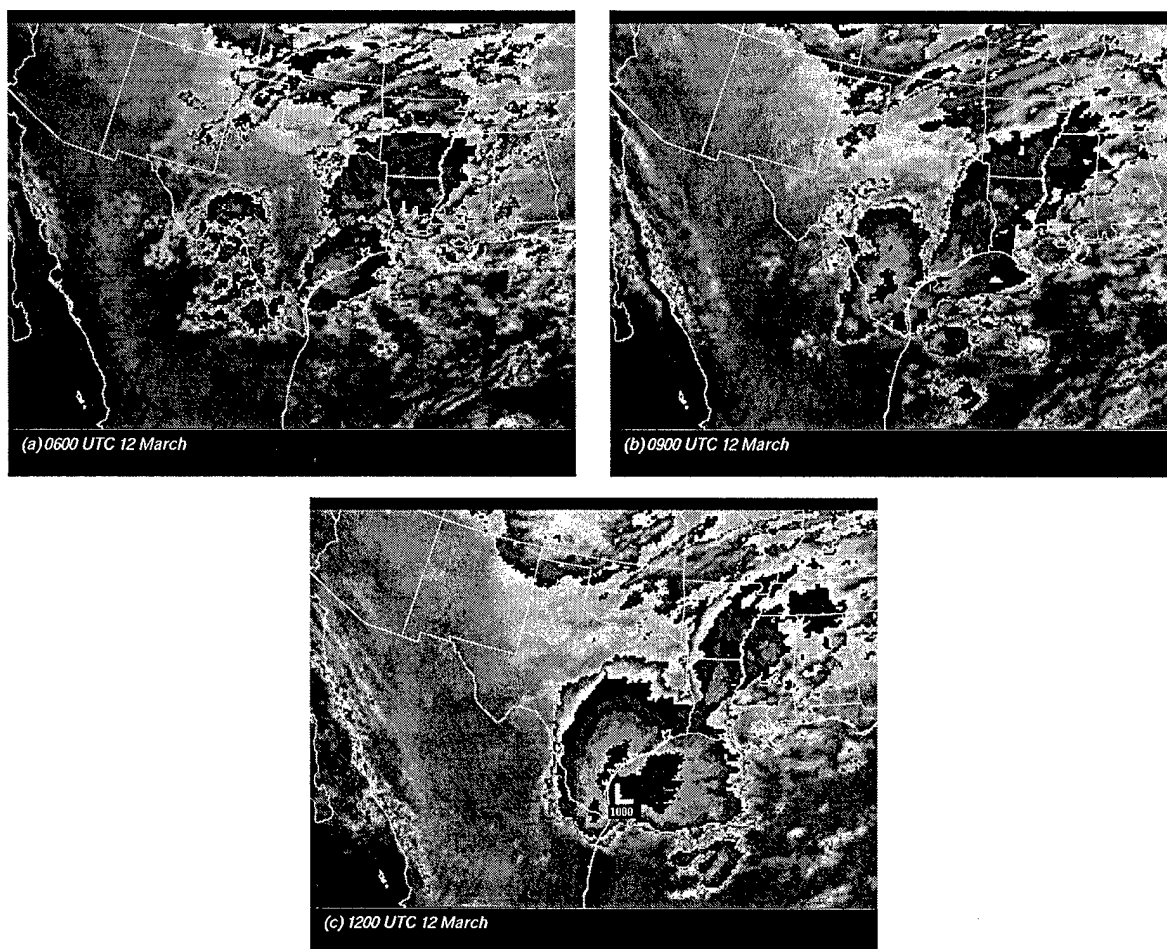


Figure 2.1: GOES-7 IR imagery valid (a) 0600 UTC, (b) 0900 UTC, and (c) 1200 UTC 12 March. Position of the surface low from the Kocin et al. (1995) mesoanalysis is indicated.

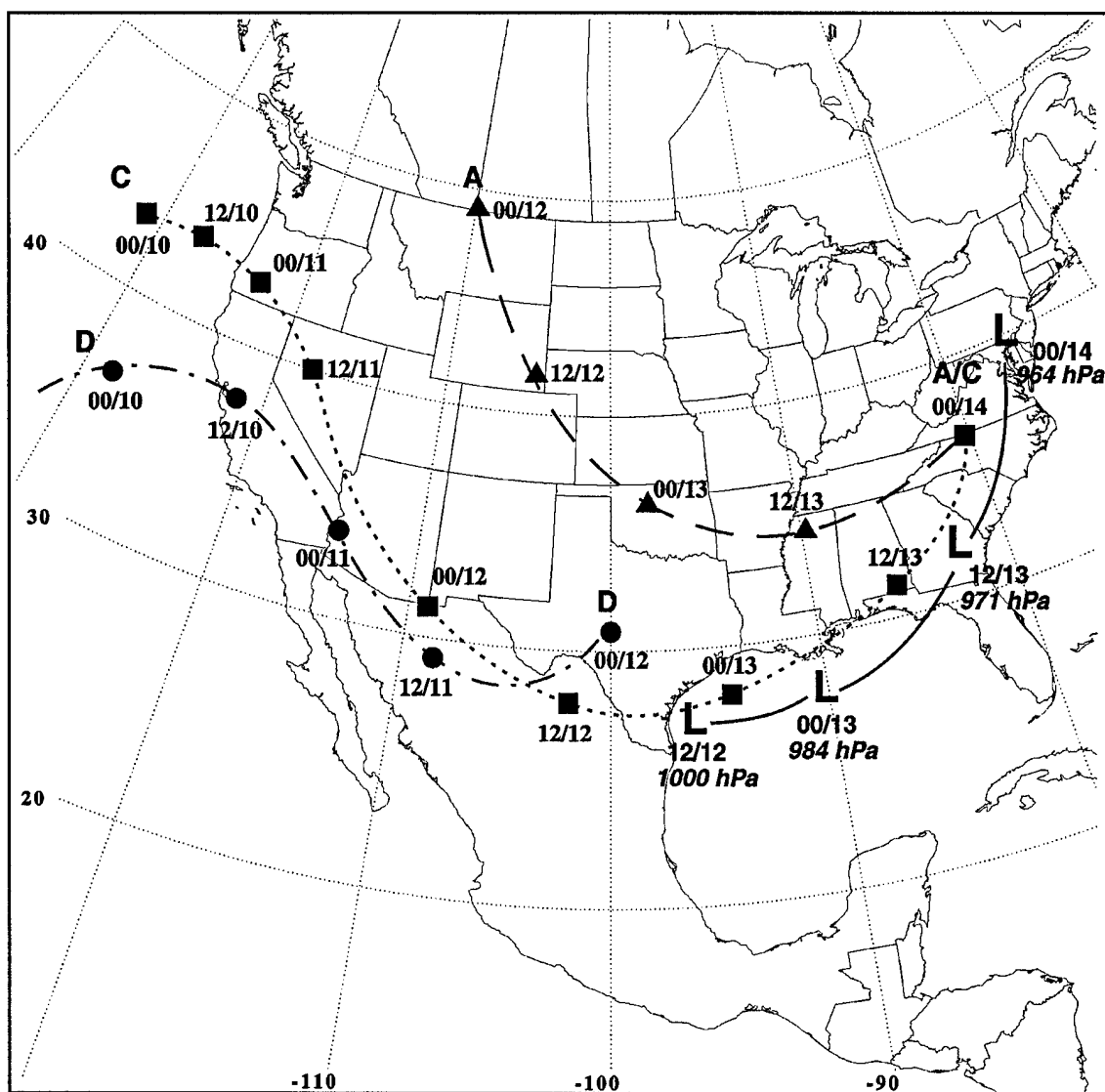


Figure 2.2: Tracks and 12-h positions (UTC/day; March 1993) of PV anomalies A, C, and D, marked with long dash, dotted and dash-dot paths, respectively. Solid line denotes track of SOC93 (12-h positions as above), with central pressures in hPa. The PV analysis is adapted from Bosart et al. (1996) and Dickinson et al. (1997), while the storm central pressures are taken from the mesoscale analysis of Kocin et al. (1995).

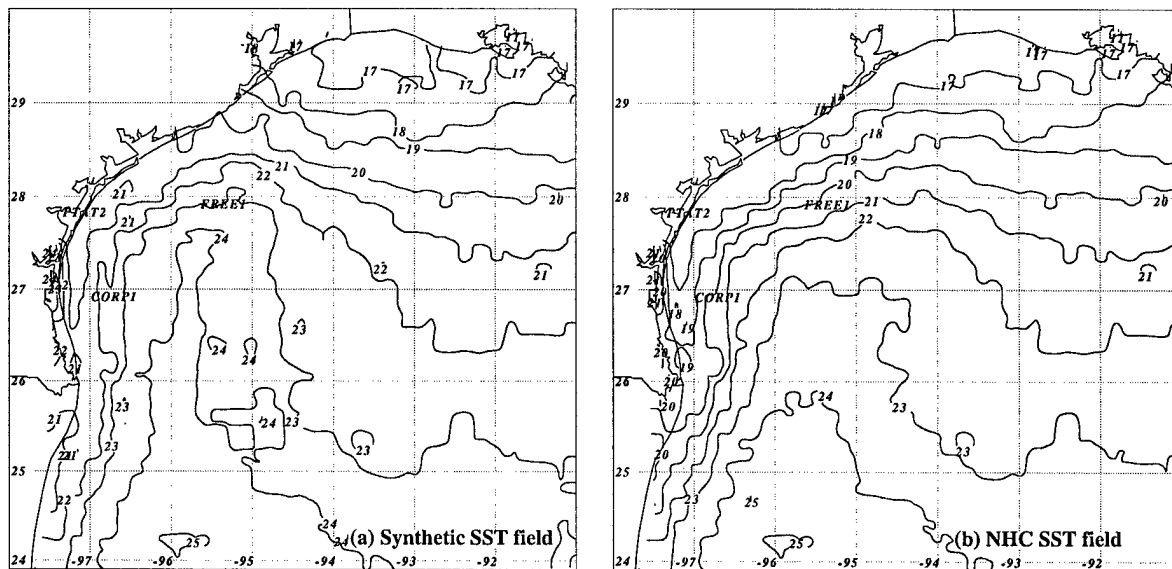


Figure 2.3: Sea-surface temperature fields contoured every 1 C for (a) synthesized from buoy, satellite and NHC analysis, used in the control simulation and (b) the original 9 March NHC analysis (Gilhousen, 1994).

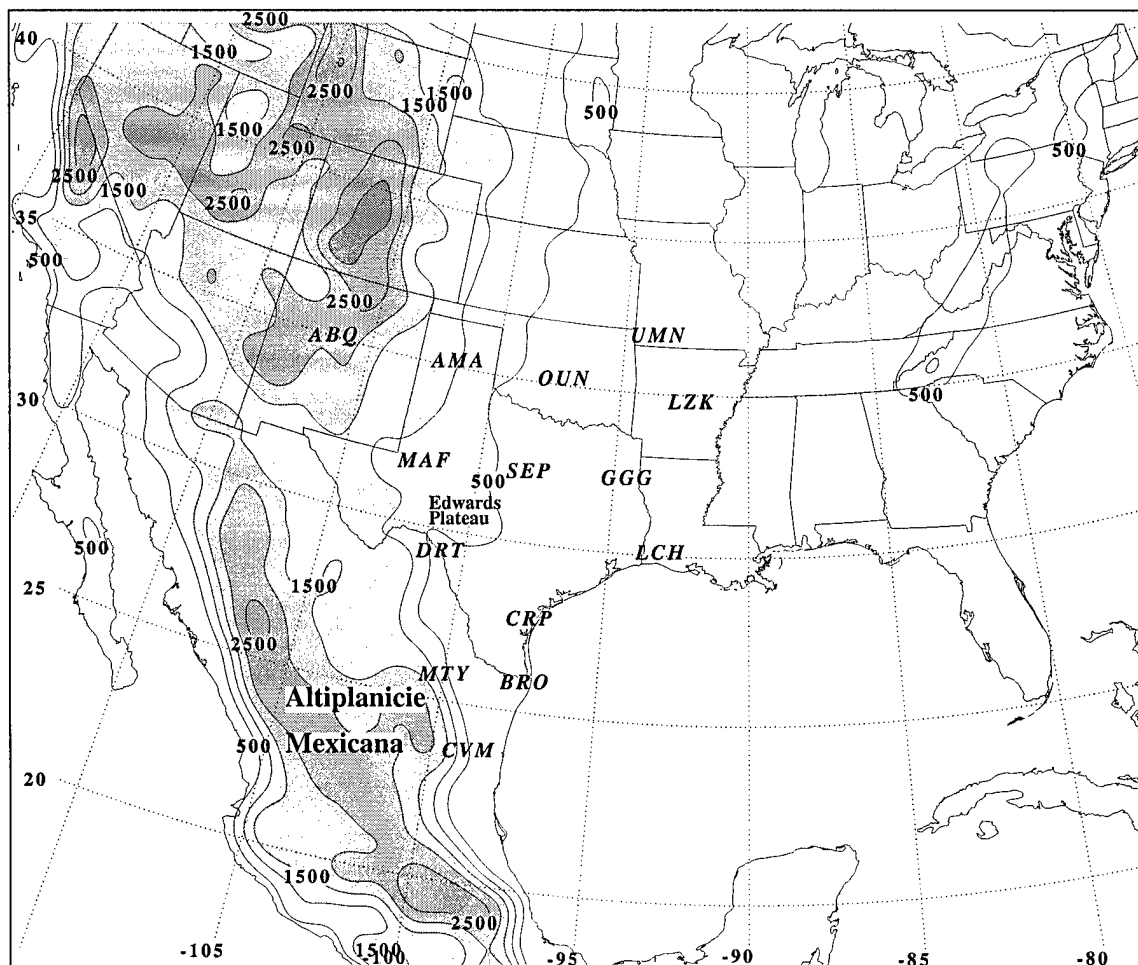


Figure 2.4: Map depicting topography at 500 m intervals, contoured and shaded. Stations referenced in the text are also plotted. The Edwards Plateau and Altiplanicie Mexicana (Mexican High Plains) are indicated.

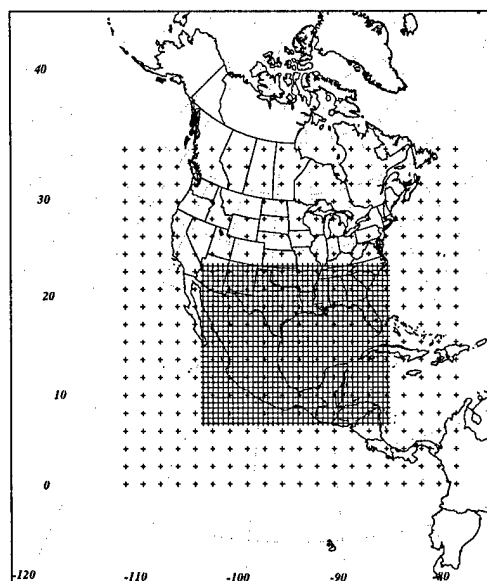


Figure 2.5: Grid boundaries for the 12-km resolution simulations (inner box) and 96 km simulation (outer box). For clarity, every third grid point for the 96 km simulation is displayed, while every sixth grid point is displayed for the 12 km simulations.

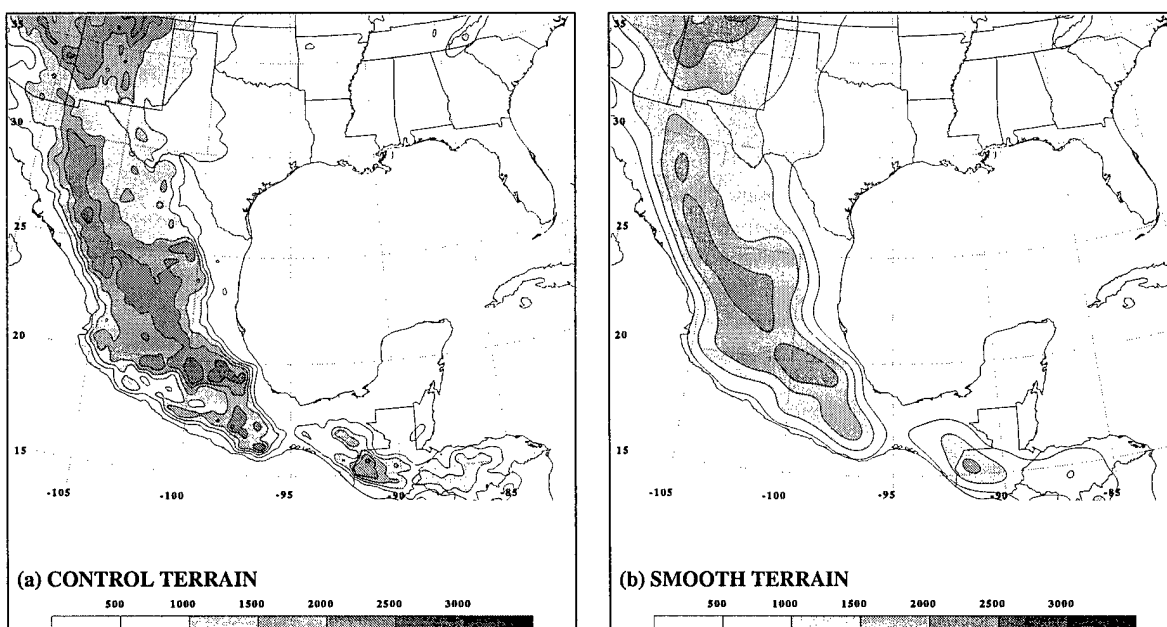


Figure 2.6: Initialization terrain fields for the (a) CONTROL and (b) SMOOTH simulations.

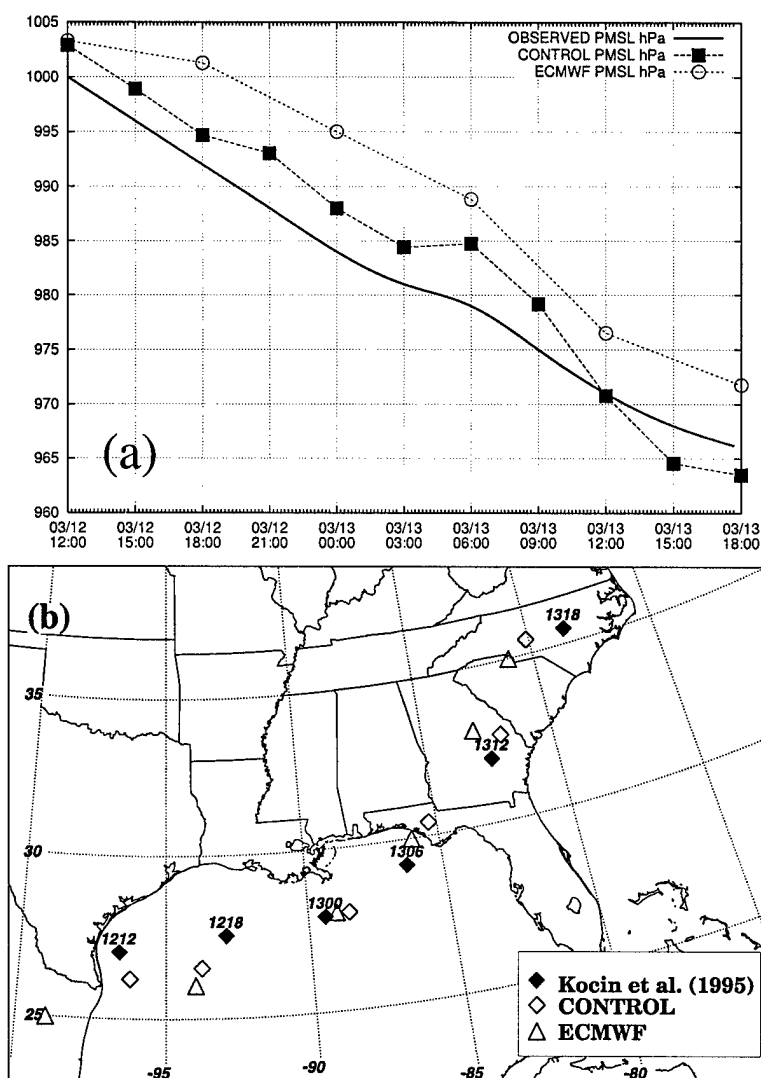


Figure 2.7: Track of the SOC93 surface cyclone in the mesoanalysis of Kocin et al. (1995), the CONTROL simulation and the ECMWF analysis. Depicted are comparisons of (a) storm central pressures and (b) storm position, where the mesoanalysis is indicated by a filled diamond, the CONTROL simulation is indicated by a hollow diamond, and the ECMWF analysis is indicated by the hollow triangle. Times in (b) are of the form DDHH (e.g. 1218 = 1800 UTC 12 March).

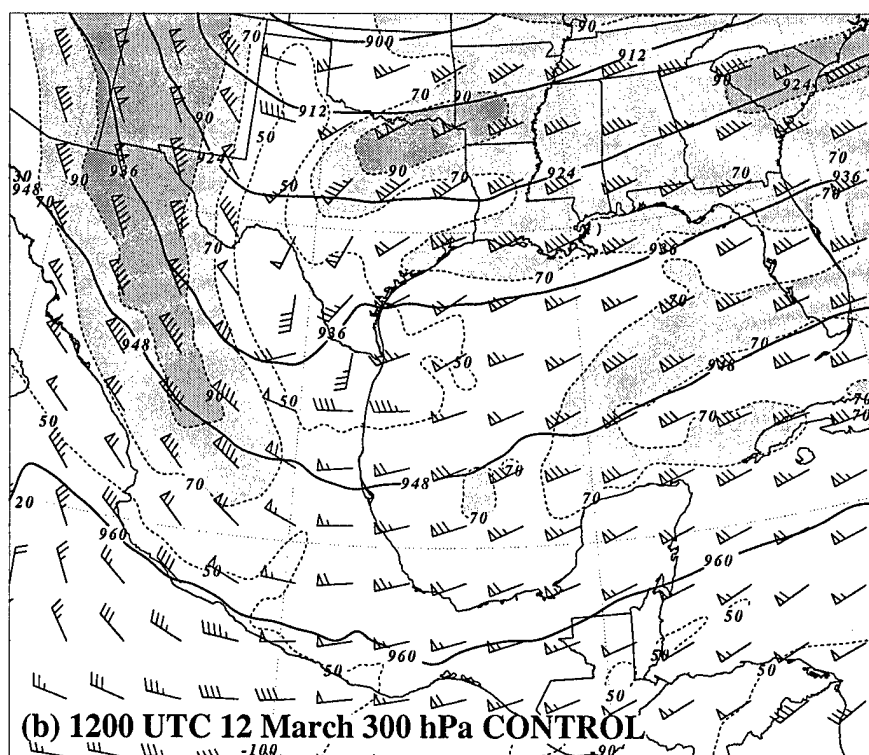
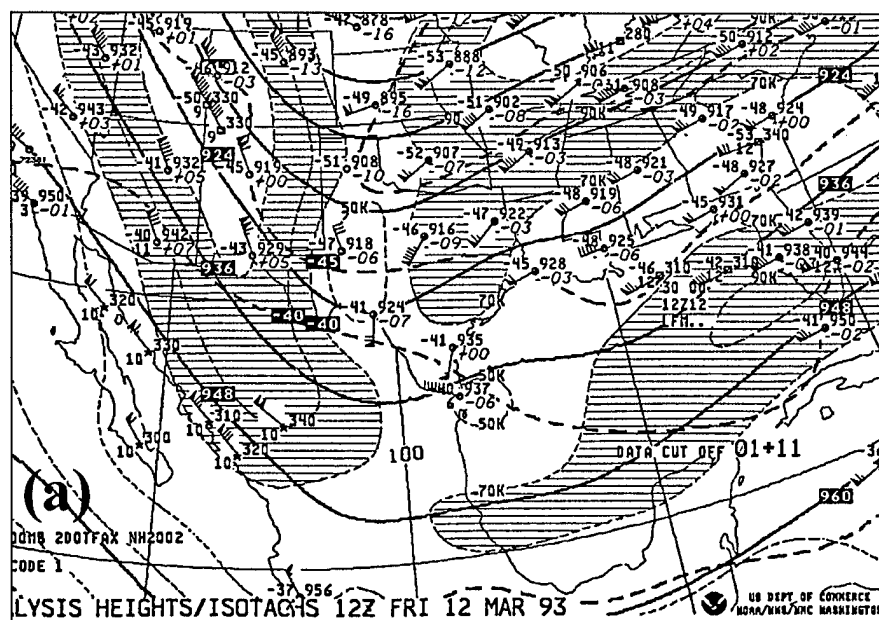


Figure 2.8: 300 hPa winds and geopotential heights from (a) the NMC upper air analysis and (b) control simulation. Heights are contoured every 120 dm, winds are plotted in kt following standard convention.



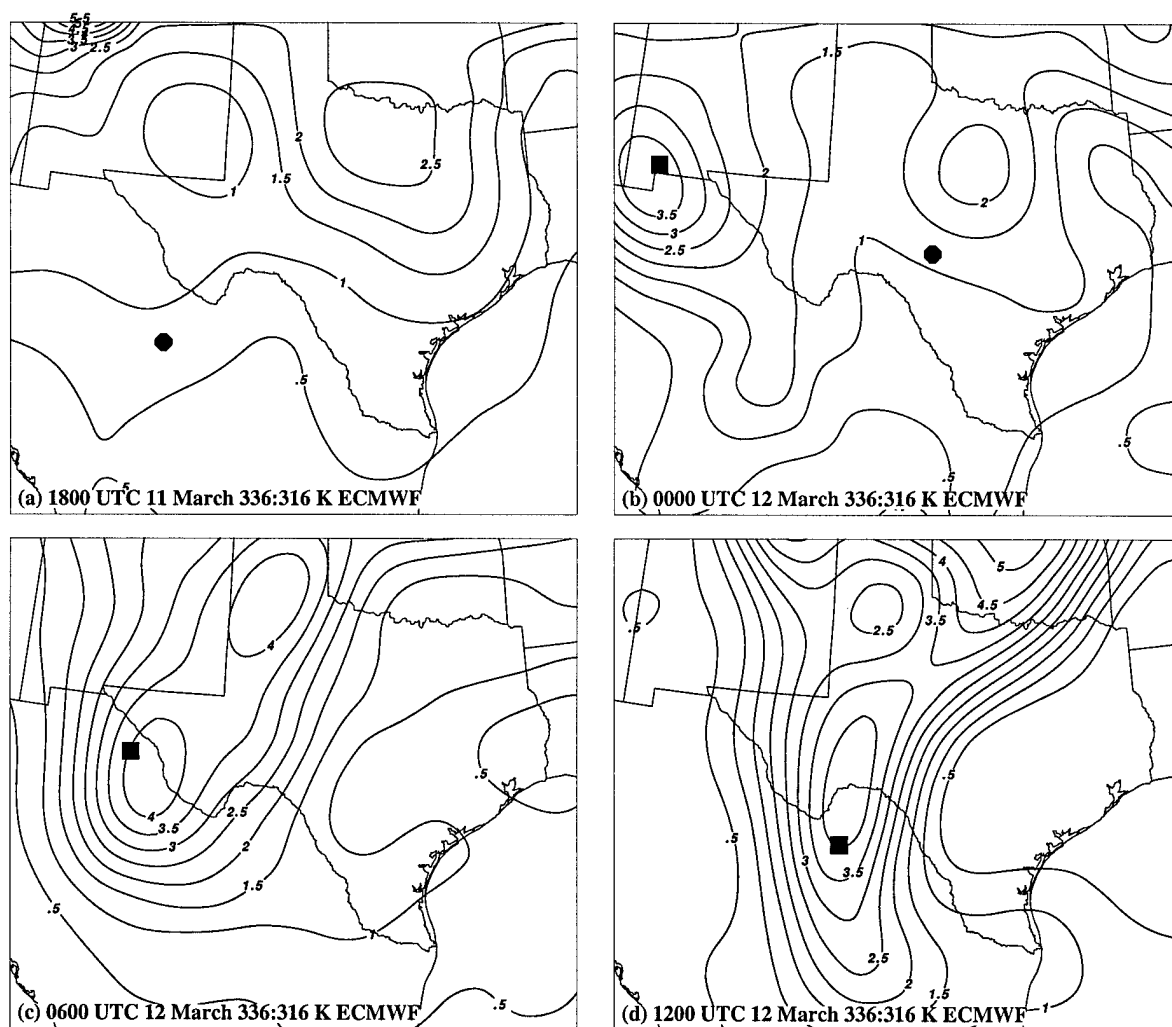


Figure 2.9: ECMWF isentropic potential vorticity in the column from 336 K to 316 K, contoured every 0.5 PVU. Valid (a) 1800 UTC 11 March, (b) 0000 UTC 12 March, (c) 0600 UTC 12 March and (d) 1200 UTC 12 March. Positions of Bosart et al. (1996) PV anomaly D are indicated by a filled octagon, while positions of PV anomaly C are indicated by a filled box.

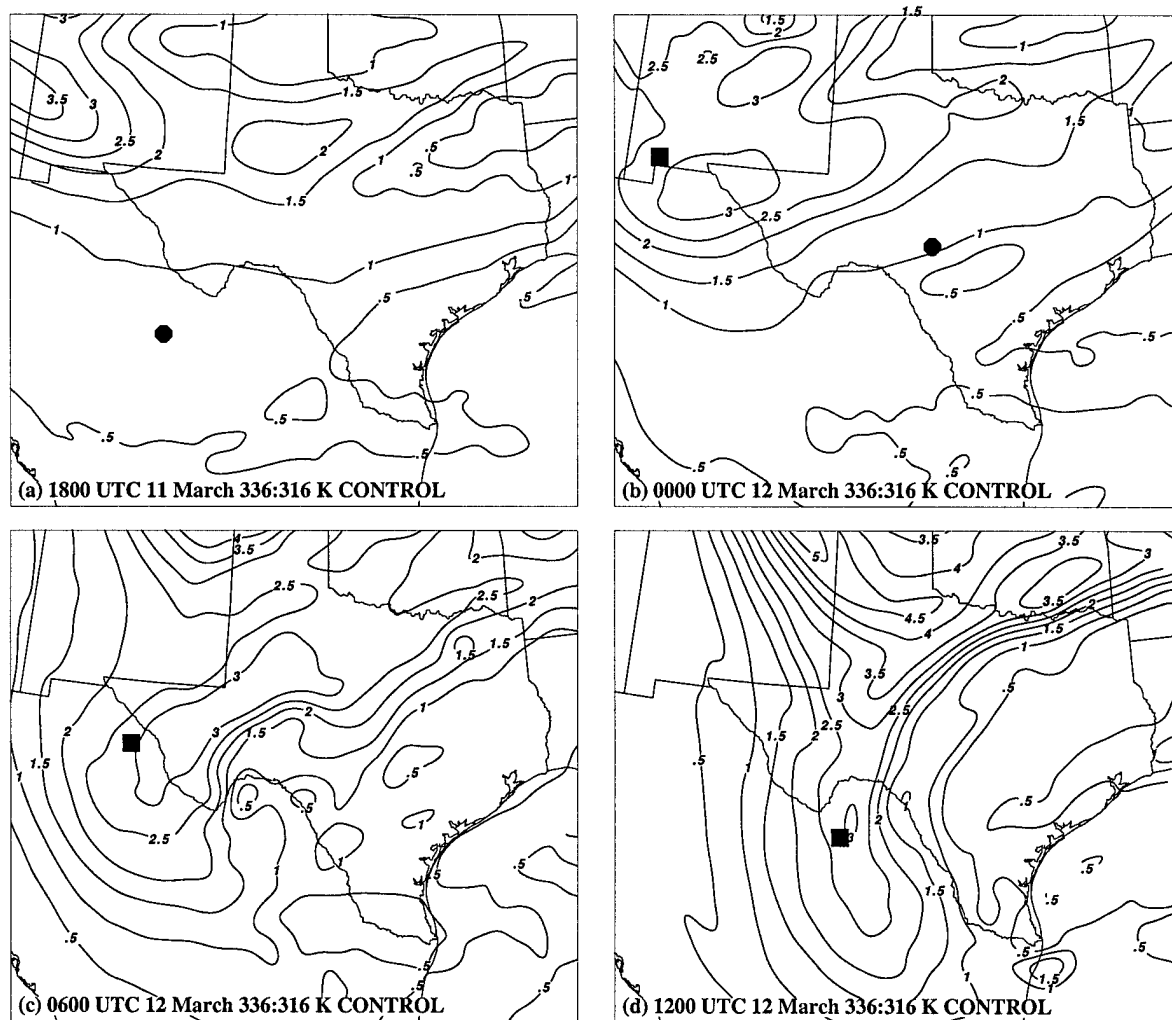


Figure 2.10: CONTROL isentropic potential vorticity, as in Fig. 2.9.

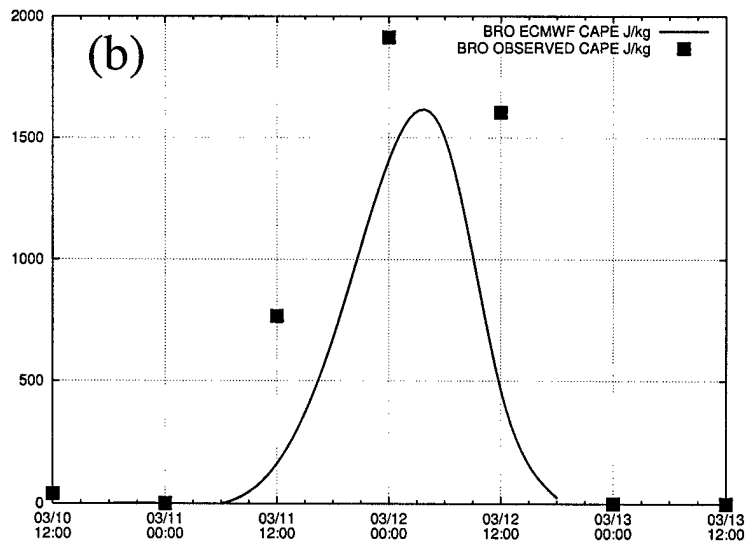
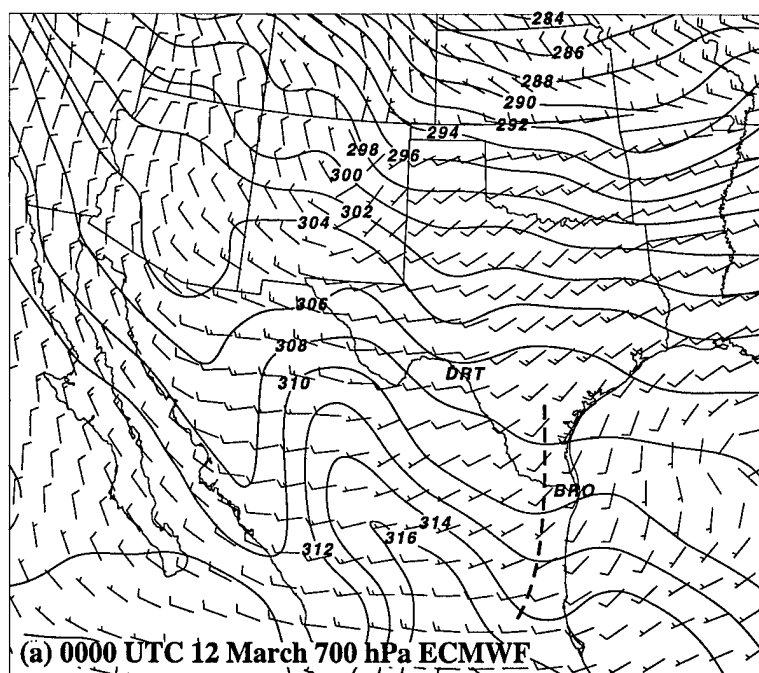


Figure 2.11: ECMWF analysis (a) 700 hPa potential temperature field at 0000 UTC 12 March contoured every 1 K, with standard wind vectors in  $\text{m s}^{-1}$ . and (b) time-series plot of ECMWF-derived CAPE (in  $\text{J kg}^{-1}$ ) at Brownsville (BRO), Texas, from 1200 UTC 10 March to 1200 UTC 13 March, with observed BRO CAPE values plotted with filled squares. The cold trough is denoted by the dashed line in (a).

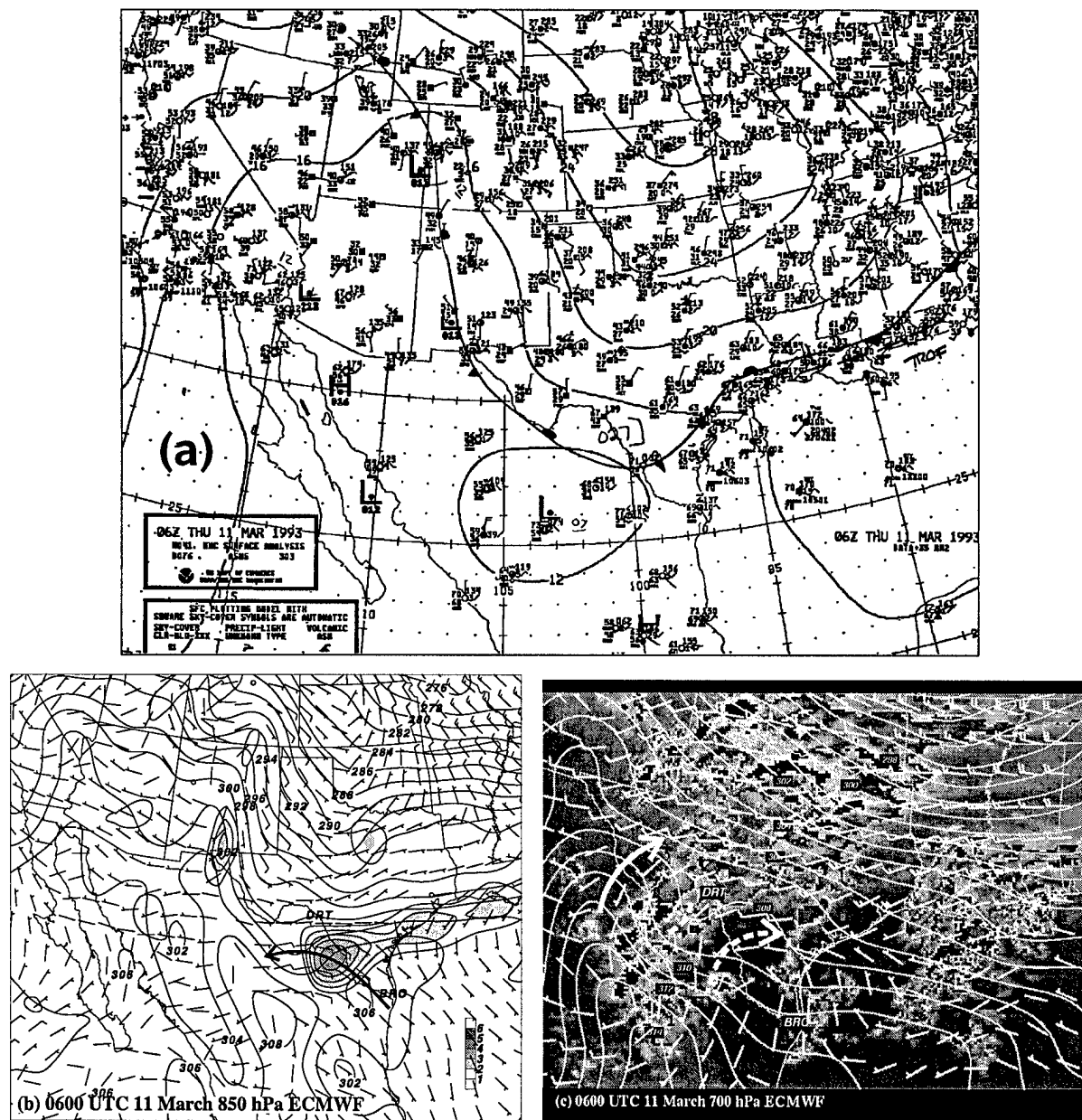


Figure 2.12: Observed data at 0600 UTC 11 March. (a) NCEP (NMC) surface analysis; (b) ECMWF 850 hPa standard wind vectors ( $\text{m s}^{-1}$ ), isentropes contoured every 2 K, warm advection ( $-\mathbf{V} \cdot \nabla_p \theta$ ) shaded every  $0.1 \text{ K h}^{-1}$ , and hot conveyor belt indicated by the arrow; and (c) ECMWF 700 hPa isentropes contoured every 1 K, standard wind vectors on GOES-7 IR satellite, and initial cold pool indicated by the dashed line southwest of DRT; the northwest branch of the active MPS outflow is indicated by a solid arrow northwest of DRT, and the previous MPS is indicated by a dashed-dotted arrow southeast of DRT.

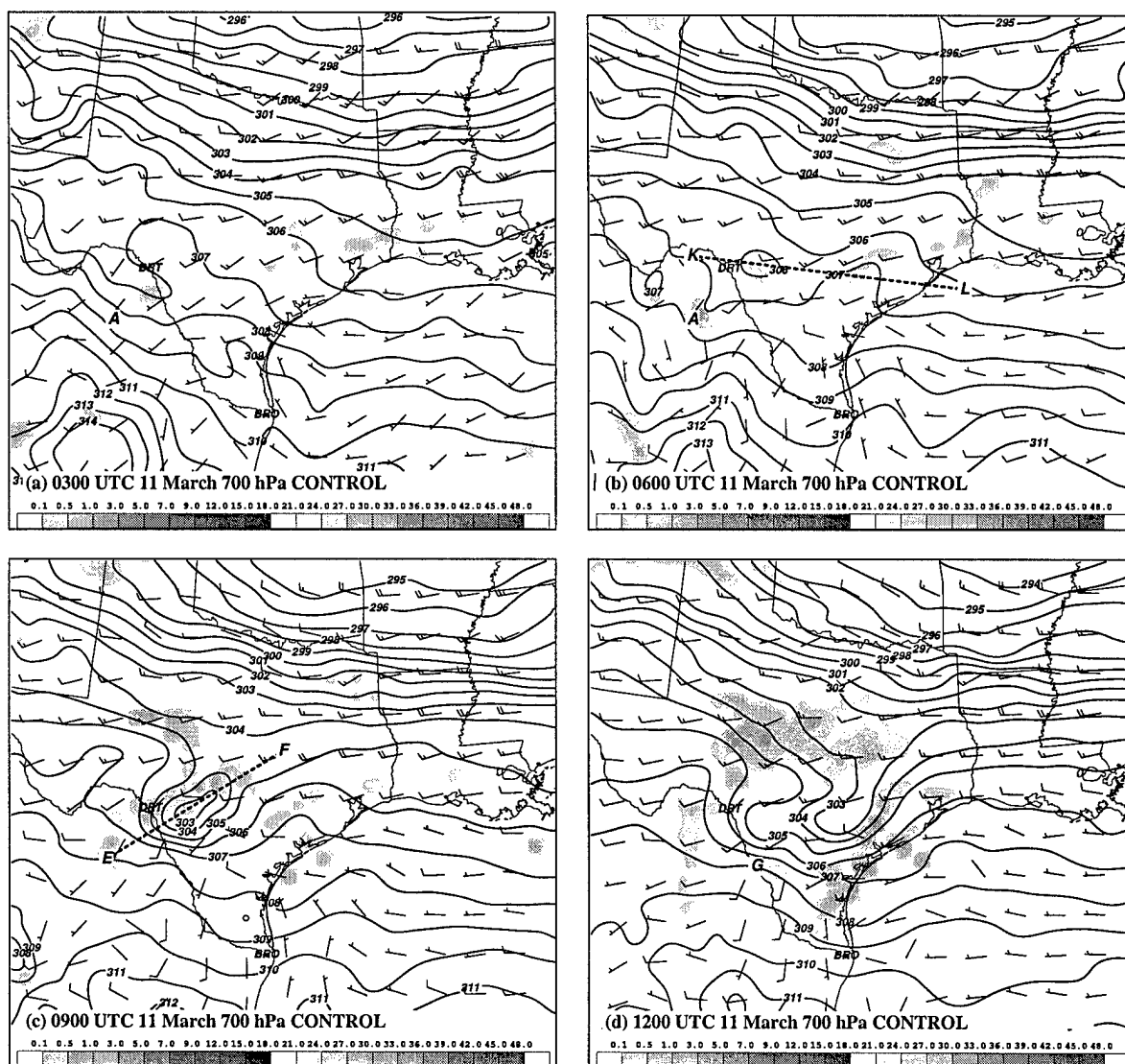


Figure 2.13: CONTROL 700 hPa standard wind vectors ( $\text{m s}^{-1}$ ), and isentropes contoured every 1 K, with surface precipitation (shaded in  $\text{mm h}^{-1}$ ) valid 11 March at (a) 0300 UTC, (b) 0600 UTC, (c) 0900 UTC, and (d) 1200 UTC. Positions of cross-sections in Fig. 2.15 are indicated.

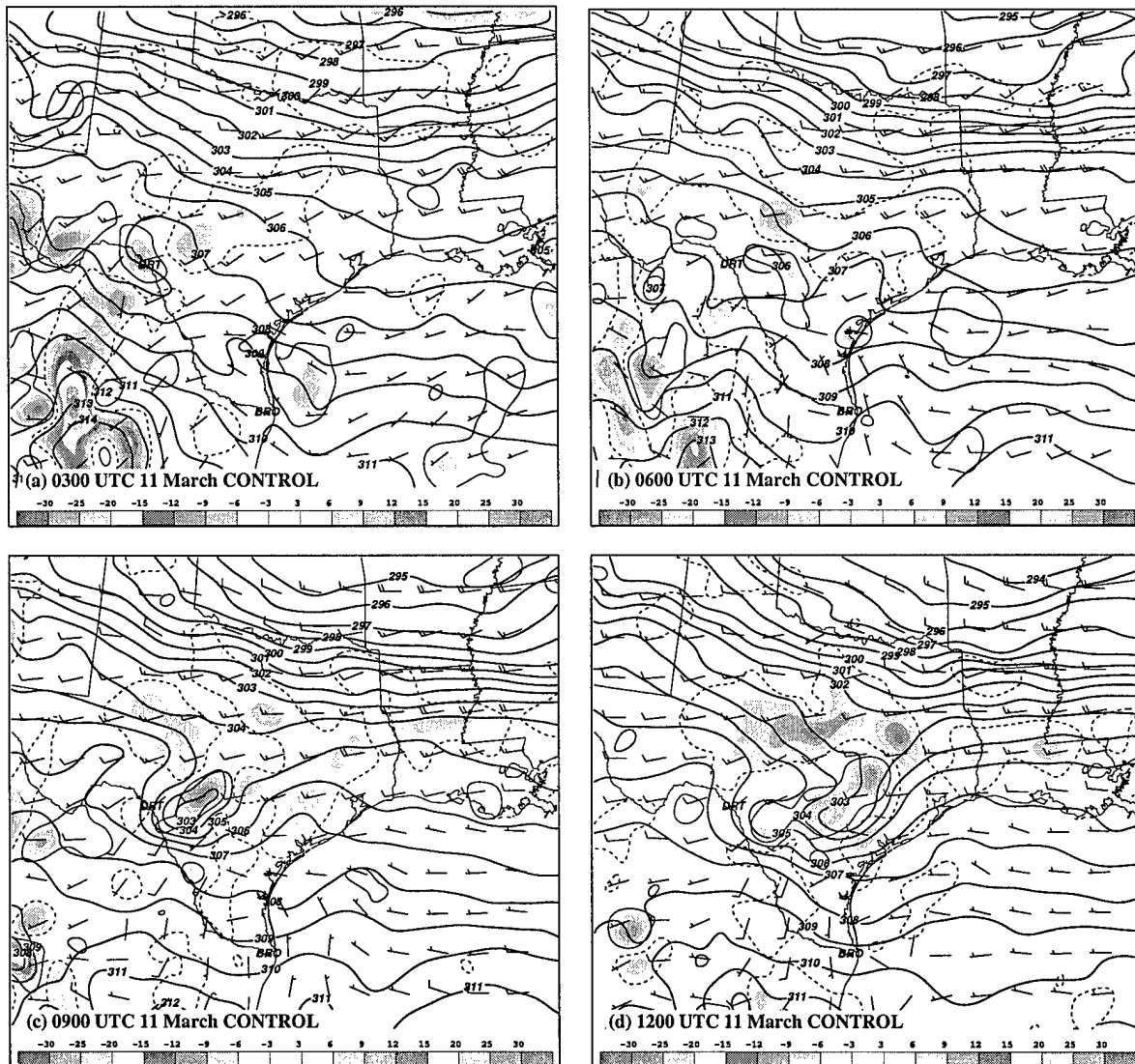


Figure 2.14: CONTROL 700 hPa standard wind vectors ( $\text{m s}^{-1}$ ), isentropes contoured every 1 K, and vertical velocity (shaded in  $\mu\text{bar s}^{-1}$ , ascent outlined in dashed contours) valid 11 March at (a) 0300 UTC, (b) 0600 UTC, (c) 0900 UTC, and (d) 1200 UTC.

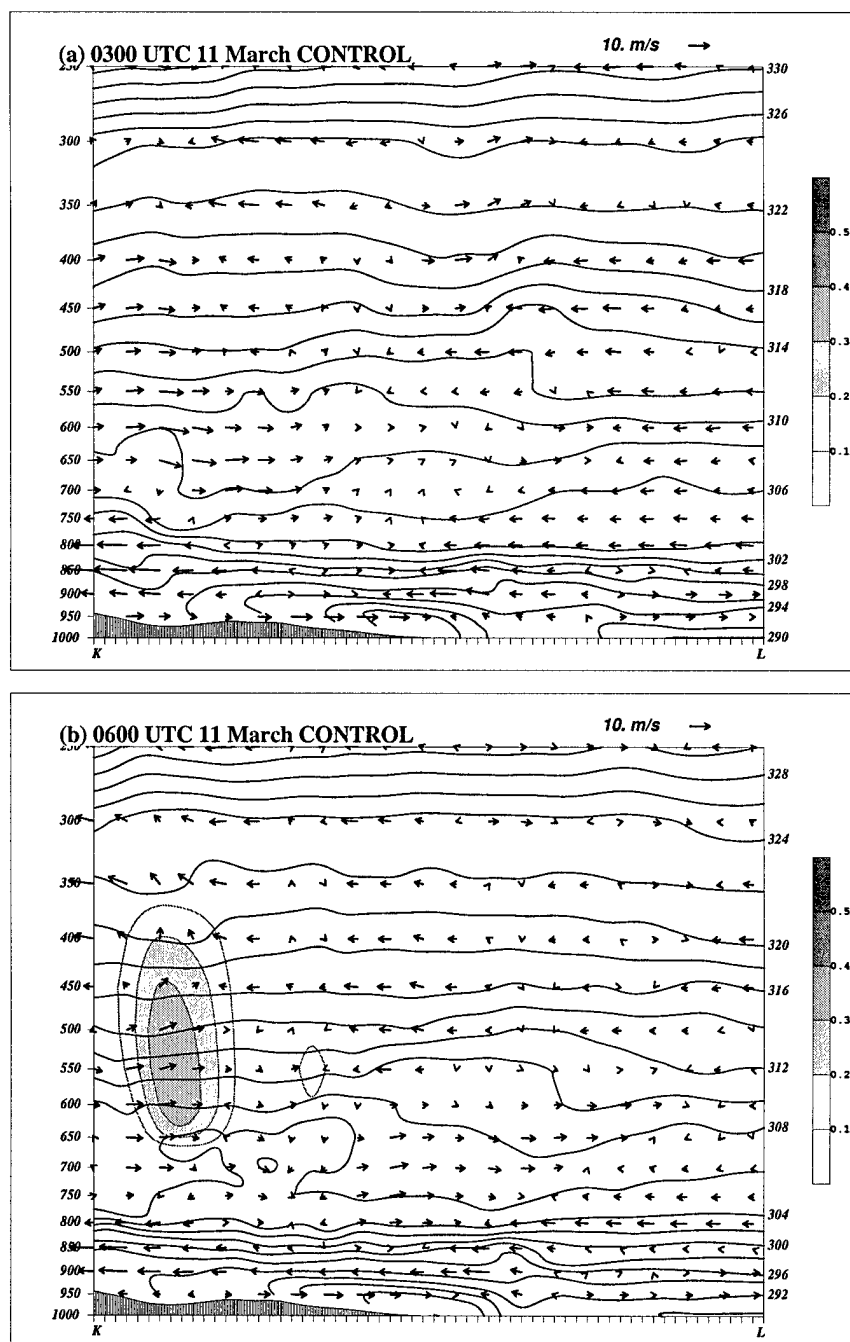
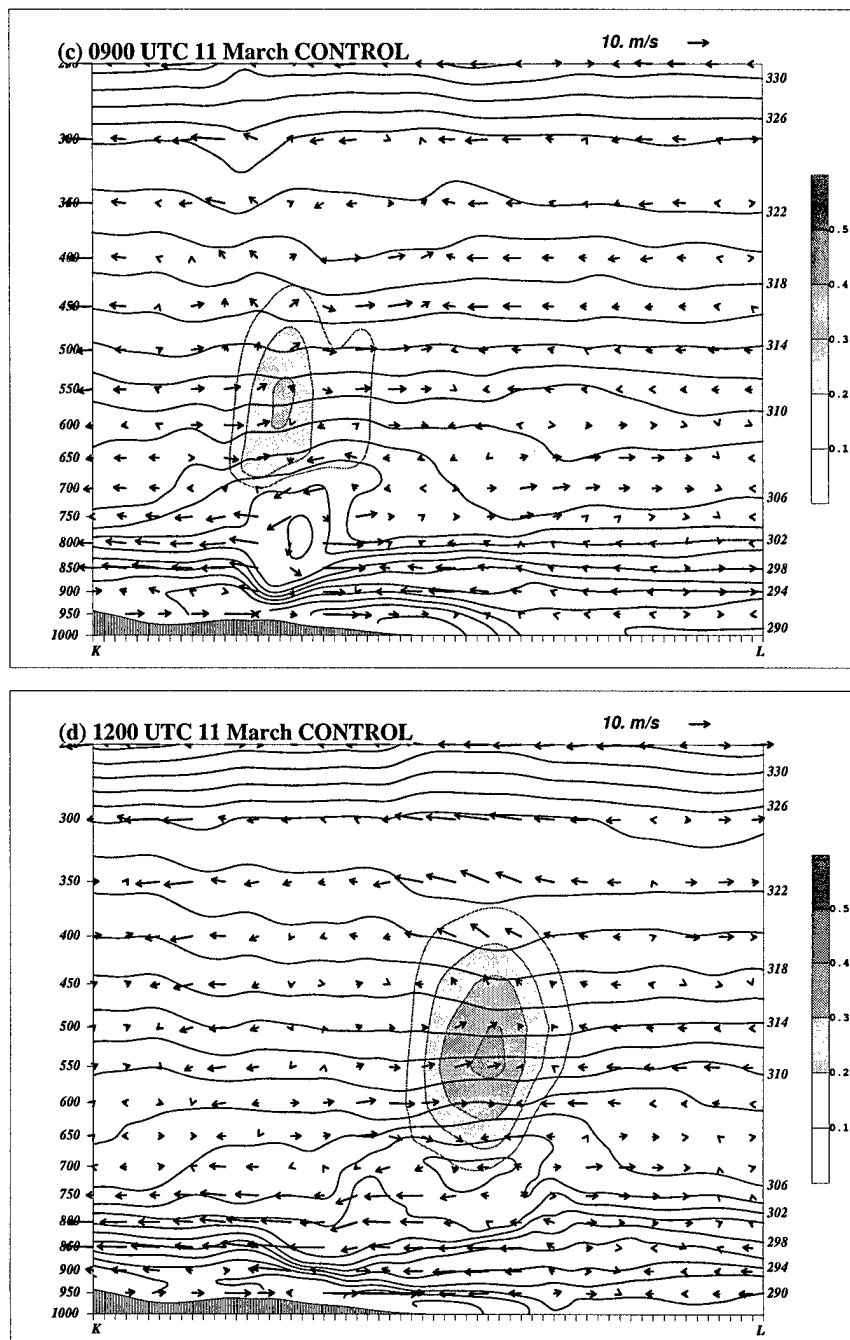


Figure 2.15: CONTROL simulation cross-sections along the path of the 700 hPa cold pool, depicting ageostrophic circulation vectors, isentropes contoured every 2 K, and rainwater mixing ratio shaded every 0.1 g kg<sup>-1</sup>, valid (a) 0300 UTC, (b) 0600 UTC, (c) 0900 UTC, and (d) 1200 UTC. Plane is indicated in Fig. 2.13b.

Figure 2.15: *Continued.*



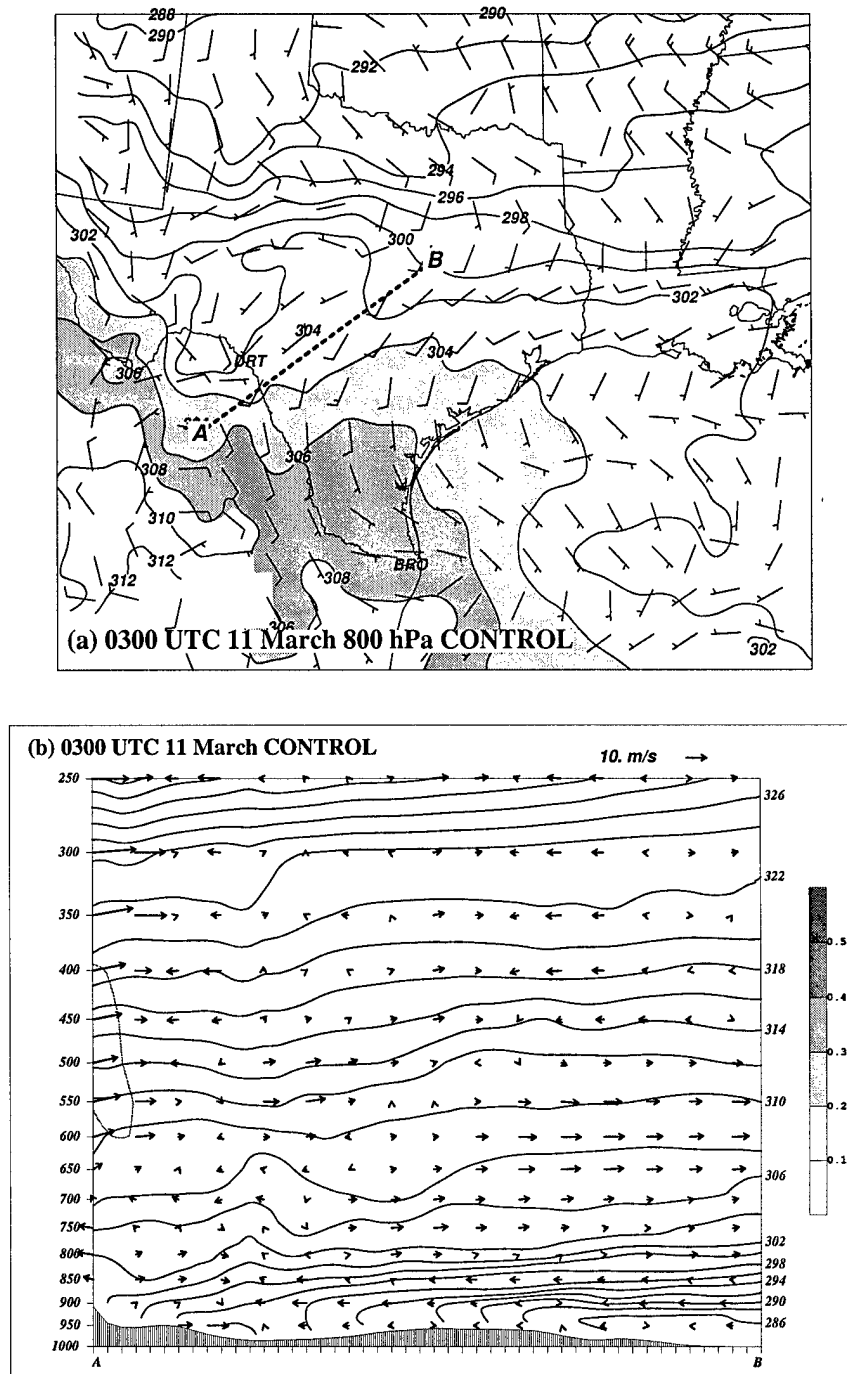


Figure 2.16: CONTROL diagnosis of the hot conveyor belt at 0300 UTC 11 March. Depicted are (a) 800 hPa standard wind vectors (m s<sup>-1</sup>), isentropes contoured every 2 K, shaded in the range 304 to 308 K; and (b) cross-section along the major axis of the 700 hPa cold pool, depicting ageostrophic circulation vectors, isentropes contoured every 2 K, and precipitation mixing ratio shaded every 0.1 g kg<sup>-1</sup>. Point of impact of the hot conveyor belt in the plane of the cross-section is depicted with a dashed line in (b).

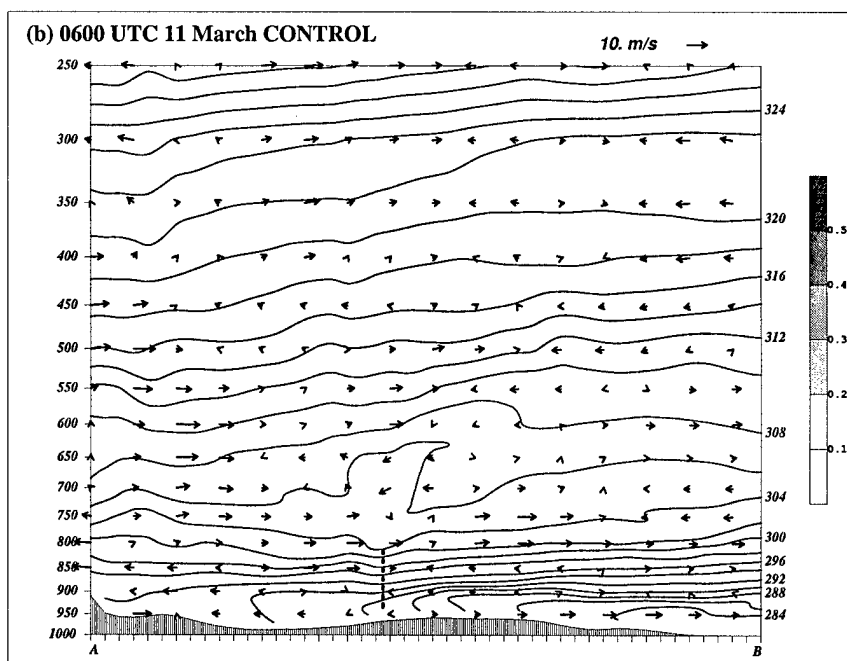
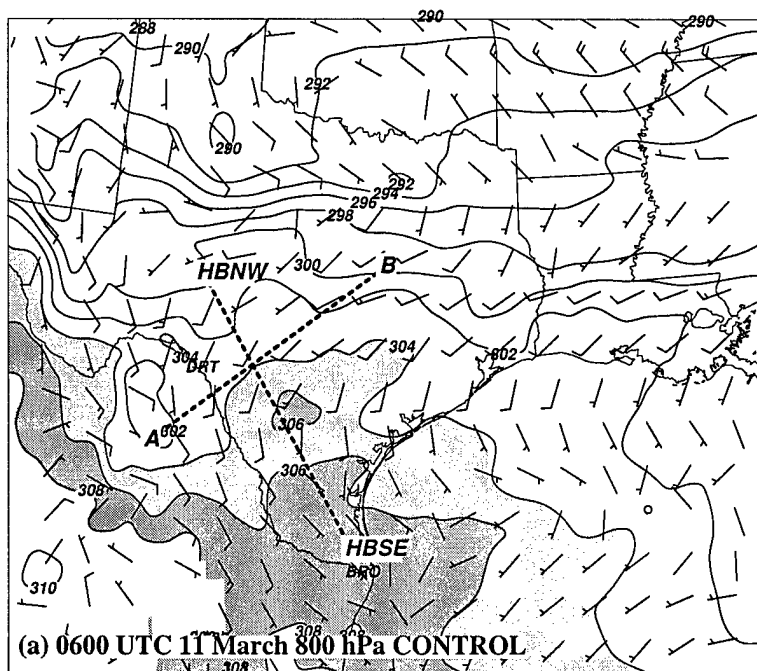


Figure 2.17: CONTROL diagnosis of the hot conveyor belt at 0600 UTC 11 March, as in Fig. 2.16.

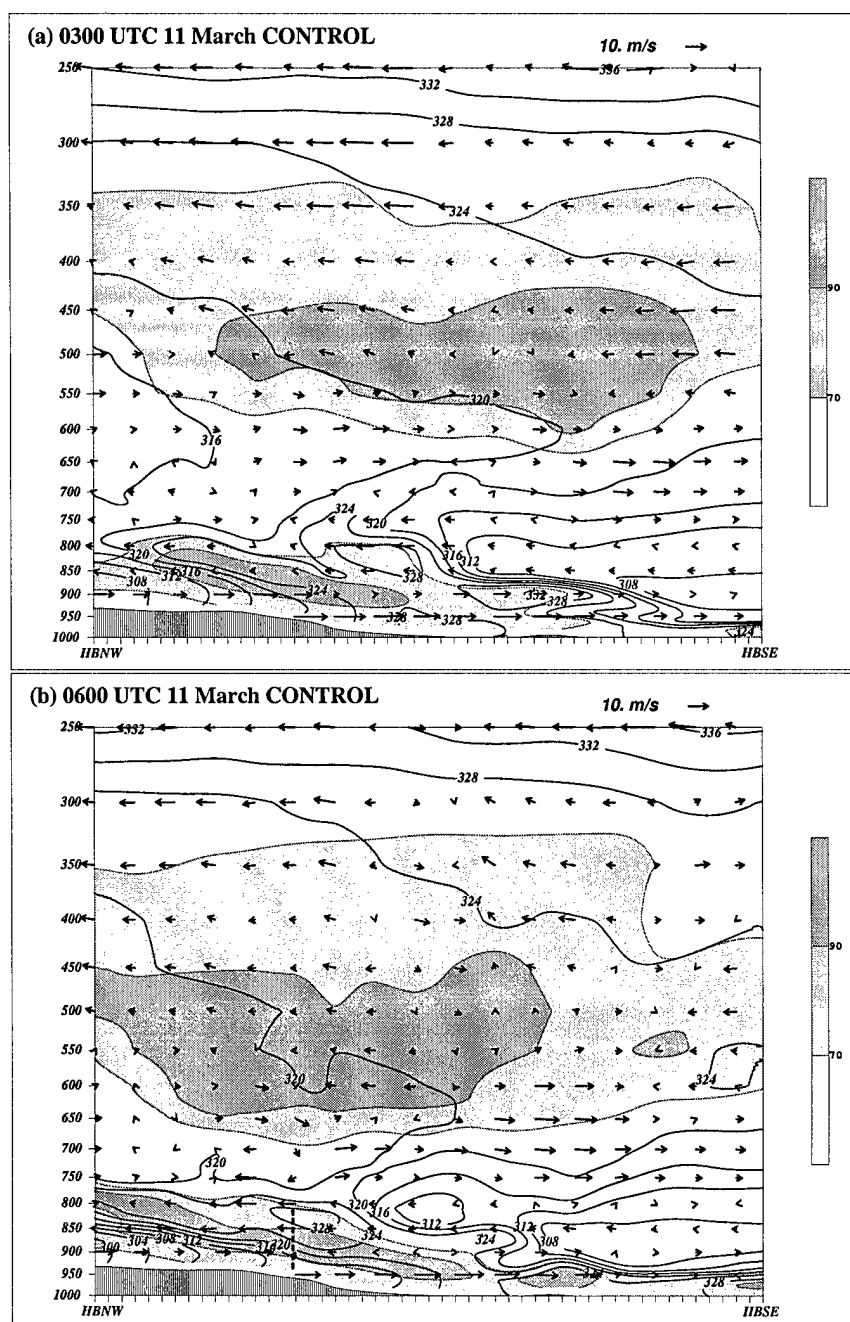


Figure 2.18: CONTROL simulation cross-section along the hot conveyor. Depicted are ageostrophic circulation vectors, equivalent potential temperature ( $\theta_e$ ) contoured every 4 K, and relative humidity shaded at 70% and 90%, valid (a) 0300 UTC and (b) 0600 UTC 11 March. Plane is indicated in Fig. 2.17a; horizontal position of the cold pool is indicated in (b) by the dashed vertical line.

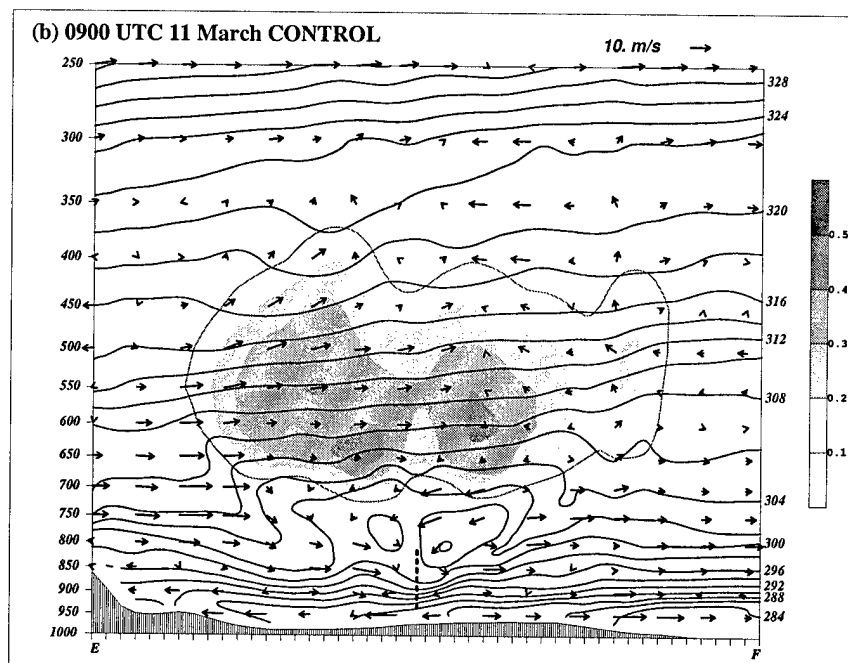
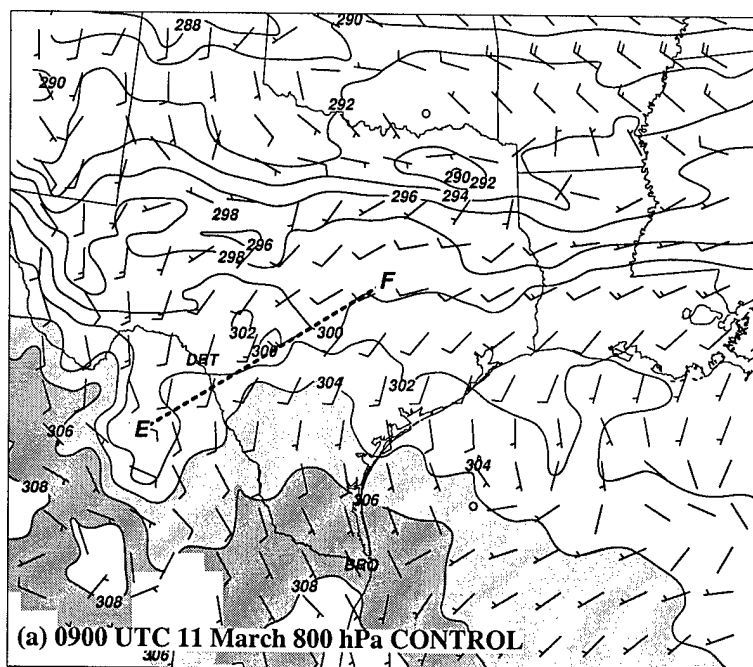


Figure 2.19: CONTROL diagnosis of the hot conveyor belt at 0900 UTC 11 March, as in Fig. 2.16.

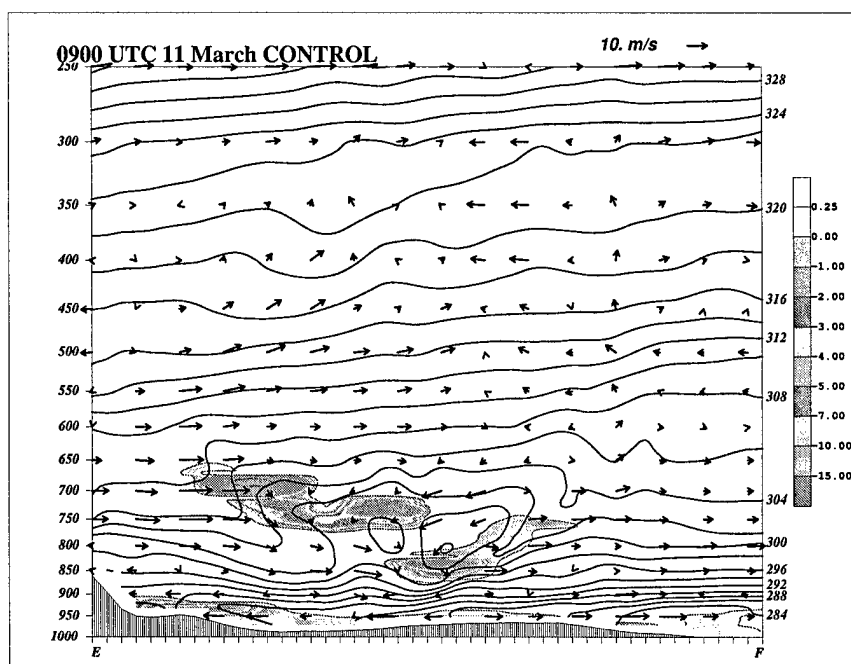


Figure 2.20: CONTROL simulation cross-section along the major axis of the 700 hPa cold pool at 0900 UTC 11 March, depicting ageostrophic circulation vectors, isentropes contoured every 2 K, and Richardson number ( $Ri$ ) shaded for  $Ri \leq 0.25$ . Plane is indicated in Fig. 2.13c.

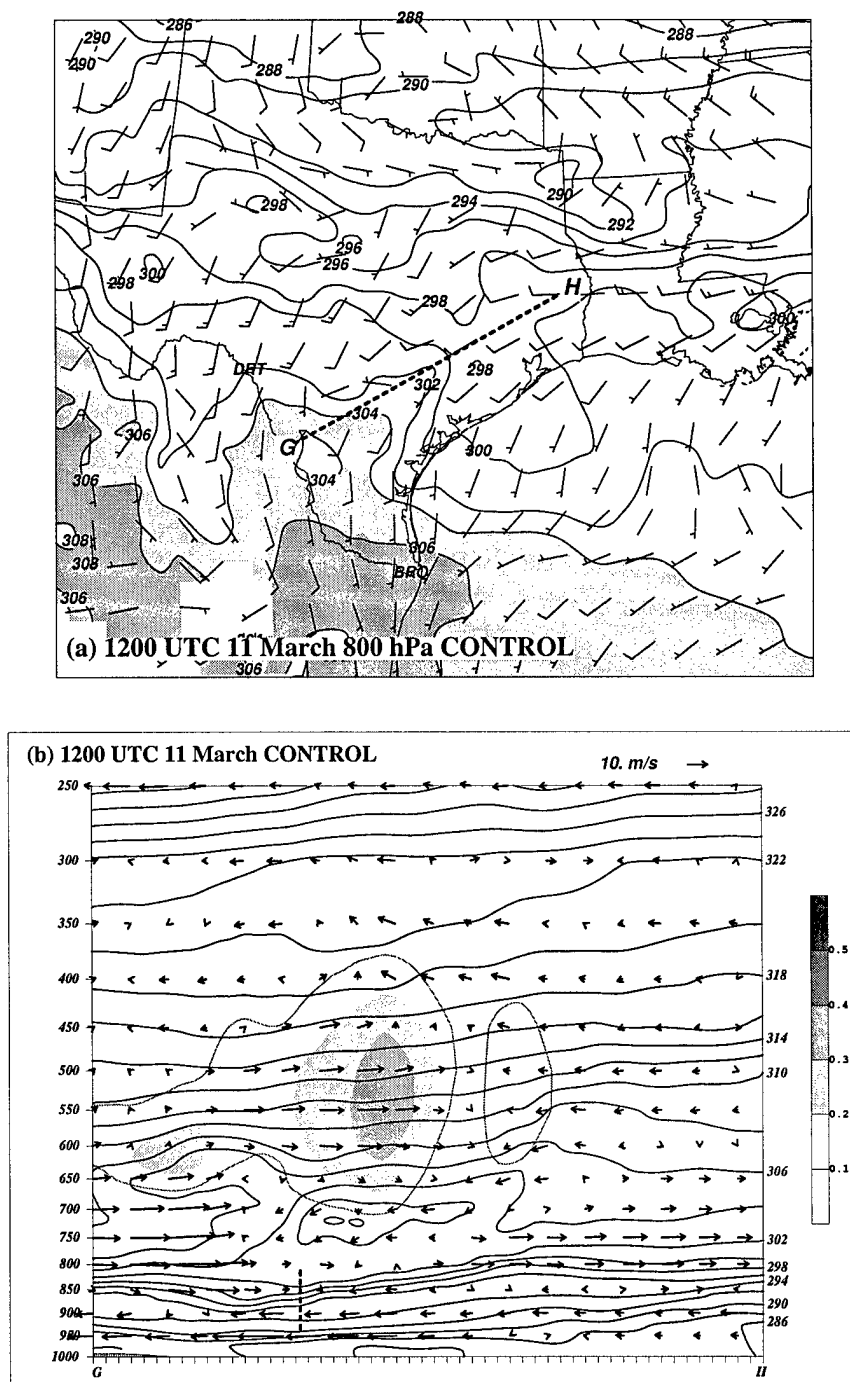


Figure 2.21: CONTROL diagnosis of the hot conveyor belt at 1200 UTC 11 March, as in Fig. 2.16.

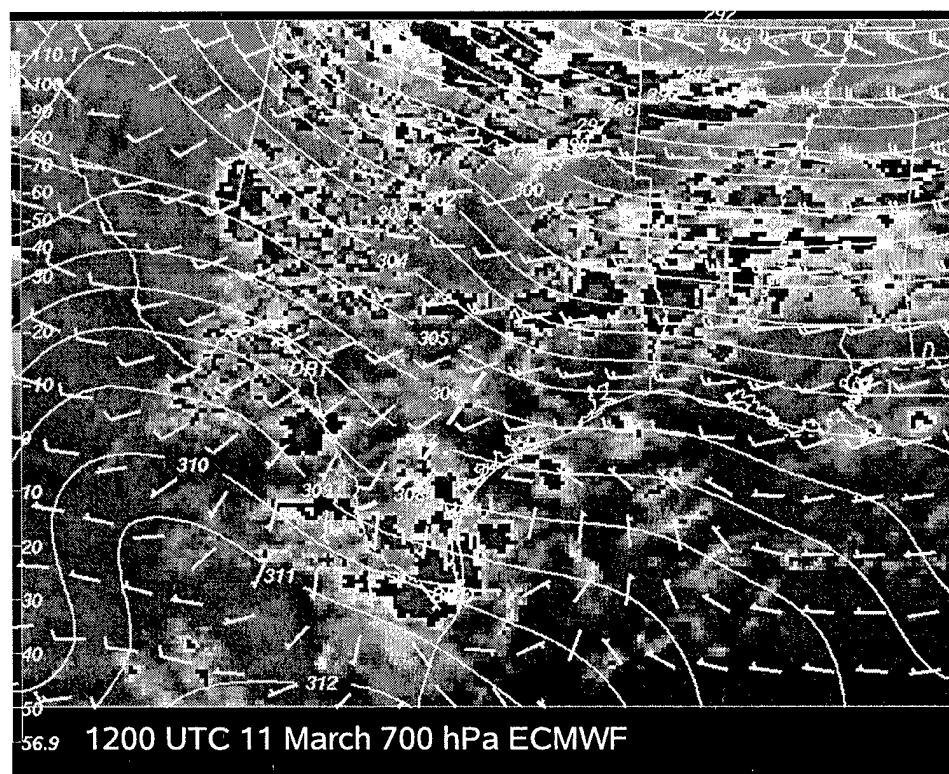


Figure 2.22: ECMWF 700 hPa isentropes contoured every 1 K and standard wind vectors ( $\text{m s}^{-1}$ ) on GOES-7 IR imagery from 1200 UTC 11 March. Position of the major axis of the 700 hPa cold pool is indicated by the dashed line.

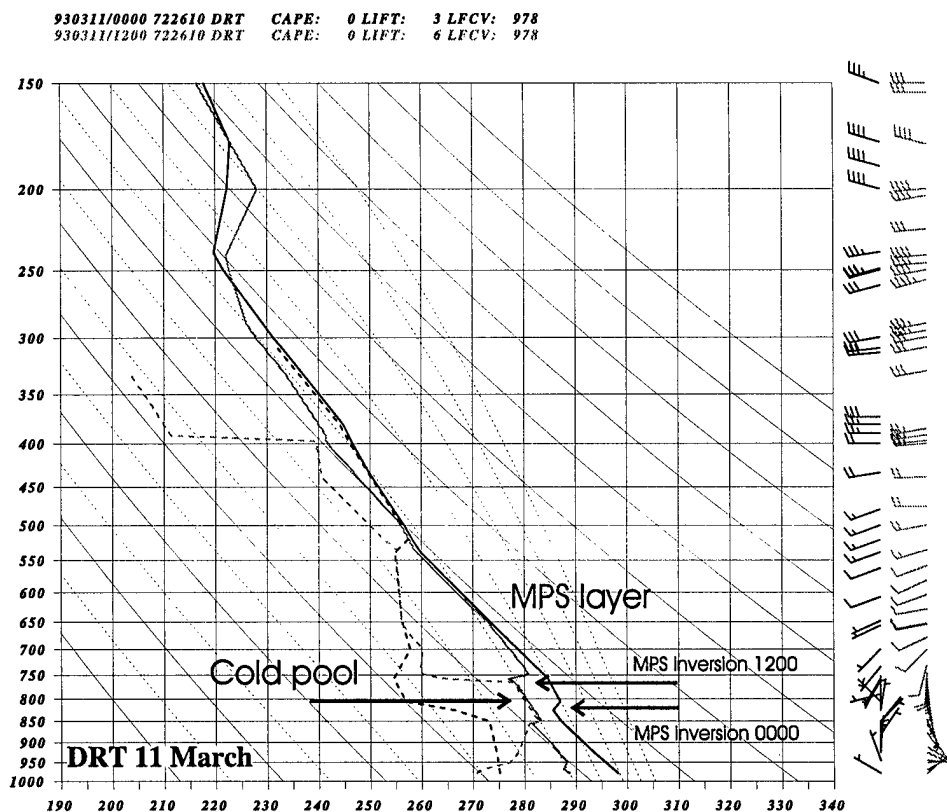


Figure 2.23: Observed soundings at Del Rio (DRT), TX, 0000 and 1200 UTC 11 March. Depicted are temperature (solid line) and dewpoint (dashed line) in K, with standard wind vectors in  $\text{m s}^{-1}$ . The 0000 UTC sounding parameters are depicted in black, the 1200 UTC sounding in dark gray. The MPS layer and the inversion at its base are indicated, as is the cold pool, discussed in the text.



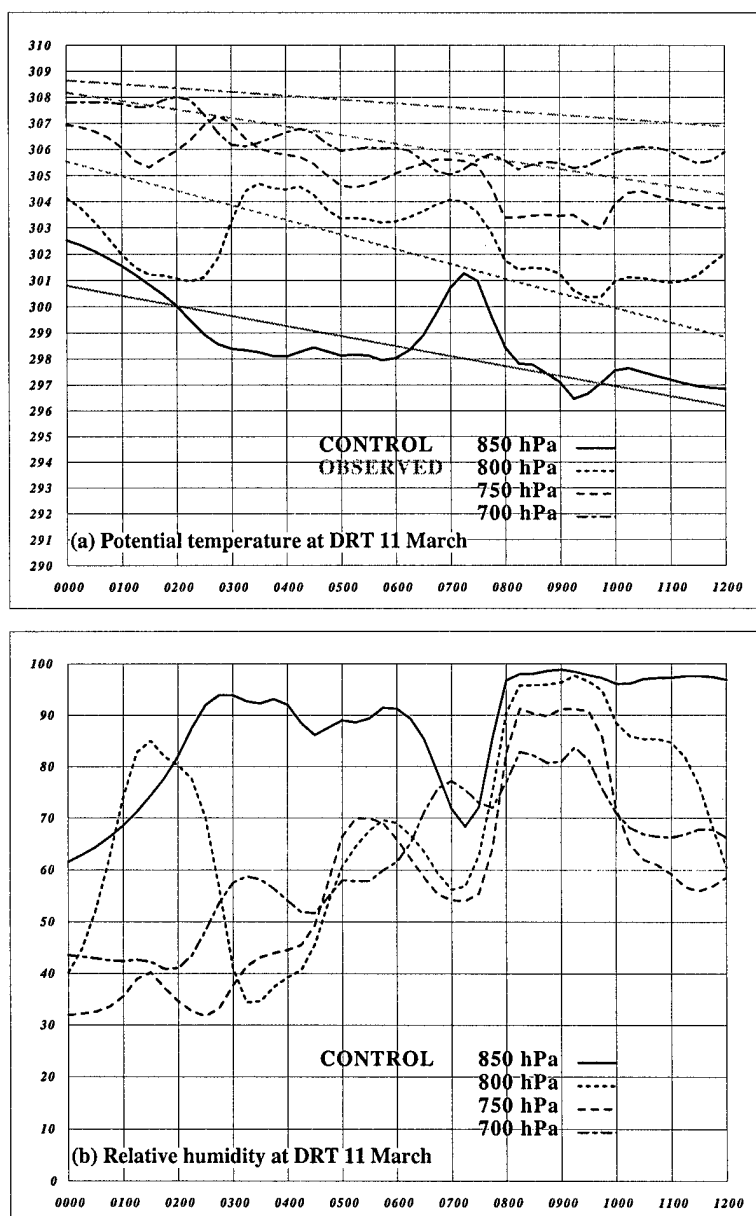


Figure 2.24: CONTROL simulation time series over Del Rio (DRT), TX, from 0000 to 1200 UTC 11 March, parameters (a) potential temperature and (b) relative humidity for levels 850 hPa (solid), 800 hPa (short dashed), 750 hPa (long dashed) and 700 hPa (dash-dotted). Observed potential temperatures are plotted in dark gray in (a), though these represent only two data points in time (0000 and 1200 UTC).

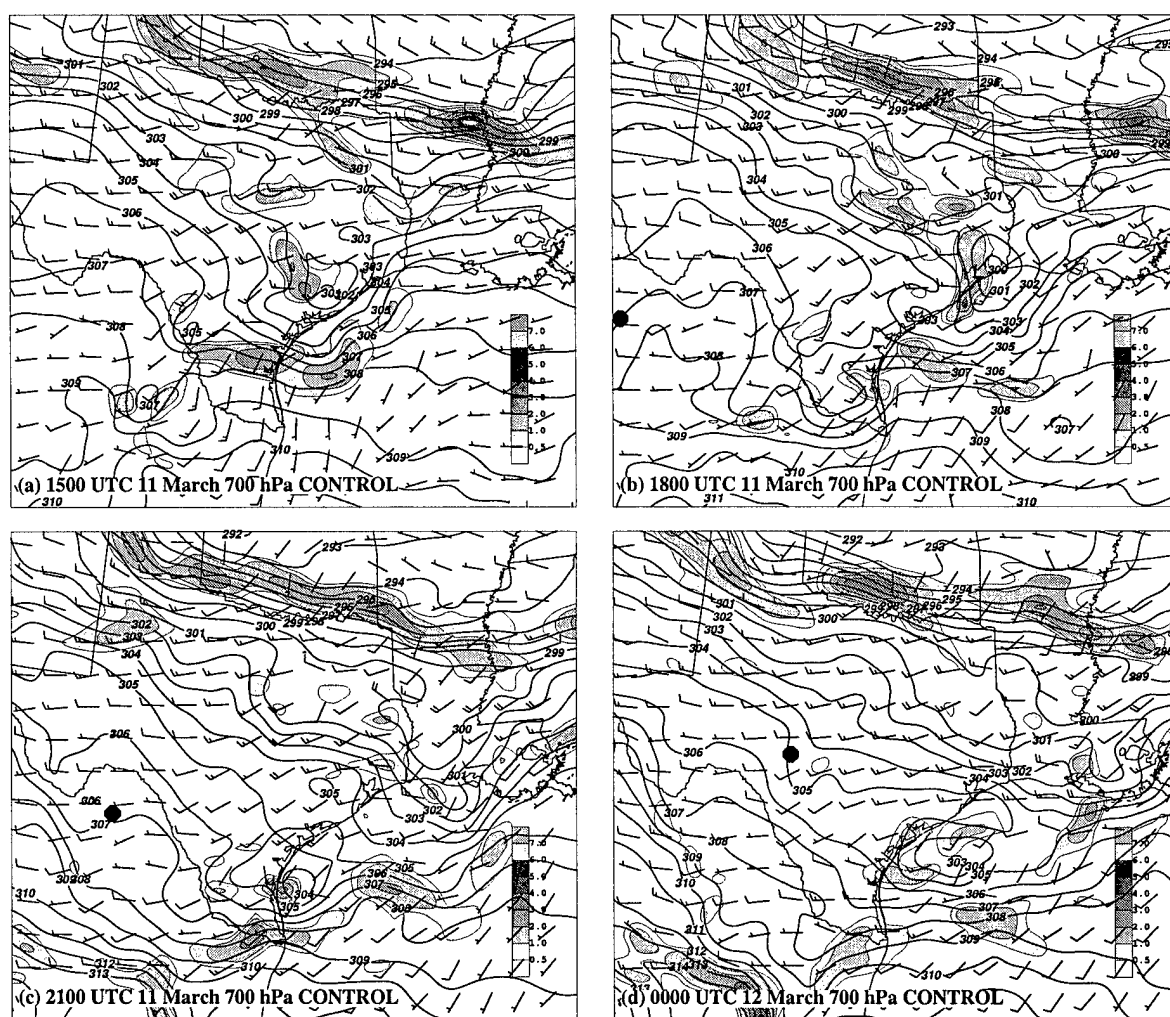


Figure 2.25: CONTROL simulation 700 hPa isentropes, contoured every 1 K, and frontogenesis shaded every 1 K  $(100 \text{ km})^{-1} (3 \text{ h})^{-1}$ , valid 11 March at (a) 1500 UTC, (b) 1800 UTC, (c) 2100 UTC, and (d) 0000 UTC 12 March. Position of Bosart et al. (1996) PV anomaly D is indicated by a filled octagon in (b), (c) and (d).

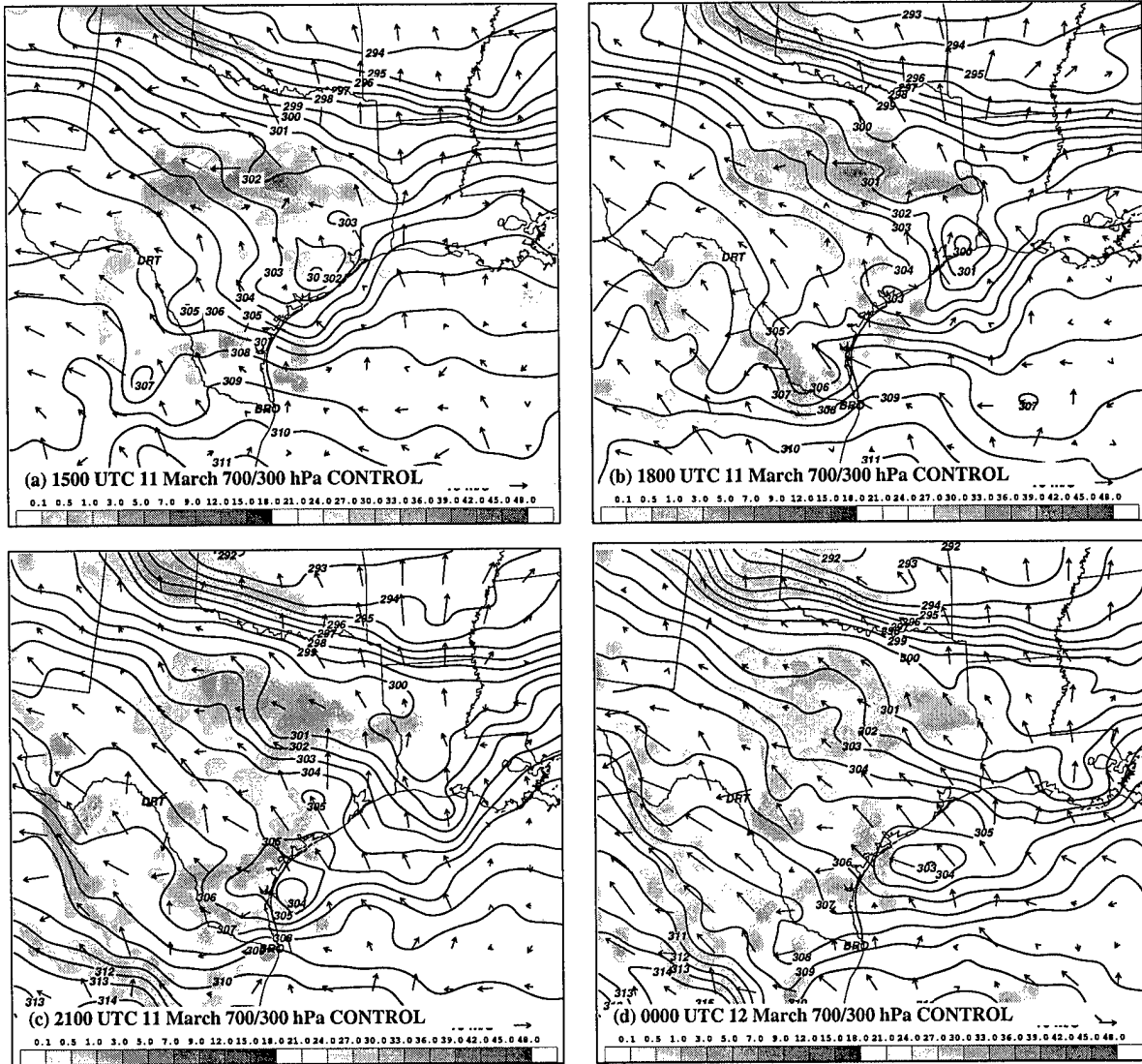


Figure 2.26: CONTROL simulation 700 hPa isentropes, contoured every 1 K, simulated precipitation shaded in mm h<sup>-1</sup>, and 300 hPa ageostrophic wind vectors (reference vector in lower right of figure), valid 11 March at (a) 1500 UTC, (b) 1800 UTC, (c) 2100 UTC, and (d) 0000 UTC 12 March.

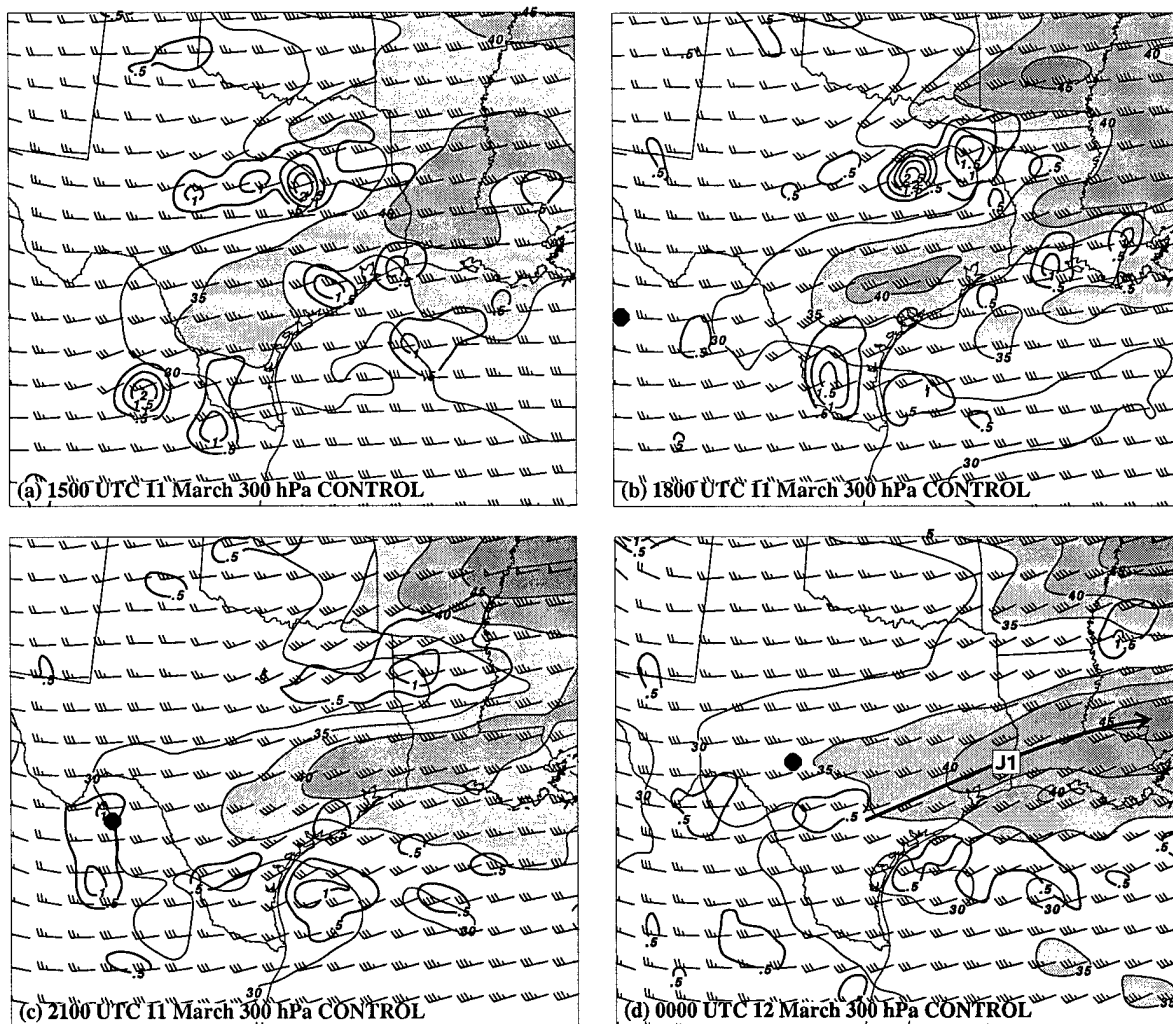


Figure 2.27: CONTROL simulation 300 hPa wind vectors ( $\text{m s}^{-1}$ ), total wind isotachs shaded above  $30 \text{ m s}^{-1}$ , and divergence contoured every  $0.5 \times 10^{-4} \text{ s}^{-1}$  (thick lines), valid 11 March at (a) 1500 UTC, (b) 1800 UTC, (c) 2100 UTC, and (d) 0000 UTC 12 March. The position of Bosart et al. (1996) PV anomaly D is indicated by a filled octagon in (b), (c) and (d).



Figure 2.28: ECMWF 300 hPa standard wind vectors ( $\text{m s}^{-1}$ ) and isotachs contoured every  $5 \text{ m s}^{-1}$  at 0000 UTC 12 March. Verifying position of jetlet **J1** is indicated, with simulated position indicated in Fig. 2.27d. Positions of Bosart et al. (1996) PV anomalies C (filled square) and D (filled octagon) are indicated.

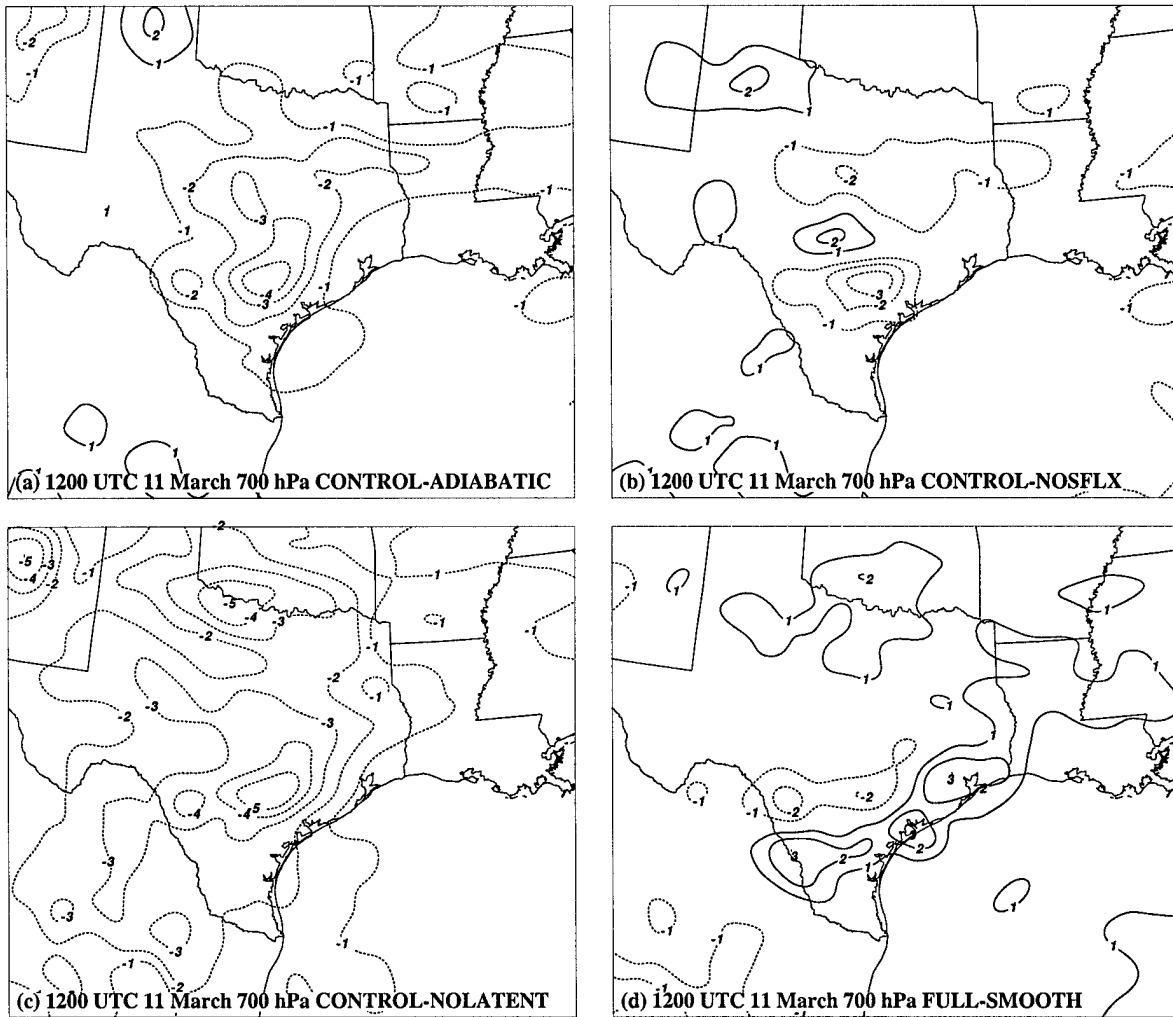


Figure 2.29: Comparison of control and sensitivity experiments at 1200 UTC 11 March at 700 hPa. Potential temperature difference fields, contoured every 1 K (negative dashed) for (a) *CONTROL-ADIAB*, (b) *CONTROL-NOSFLX*, (c) *CONTROL-NOLATENT*, and (d) *CONTROL-SMOOTH*.

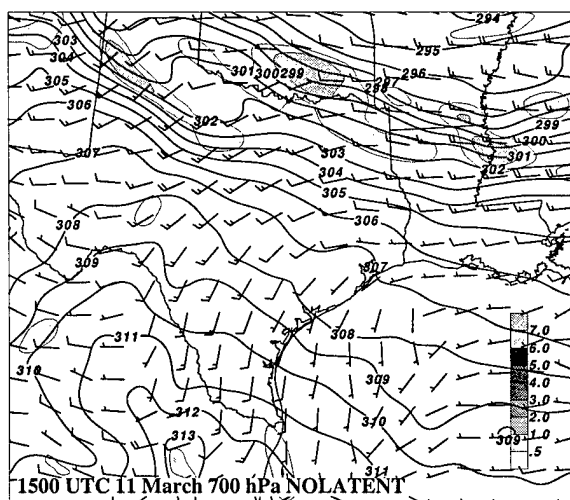


Figure 2.30: NOLATENT 700 hPa frontogenesis at 1500 UTC 11 March, as in Fig. 2.25.

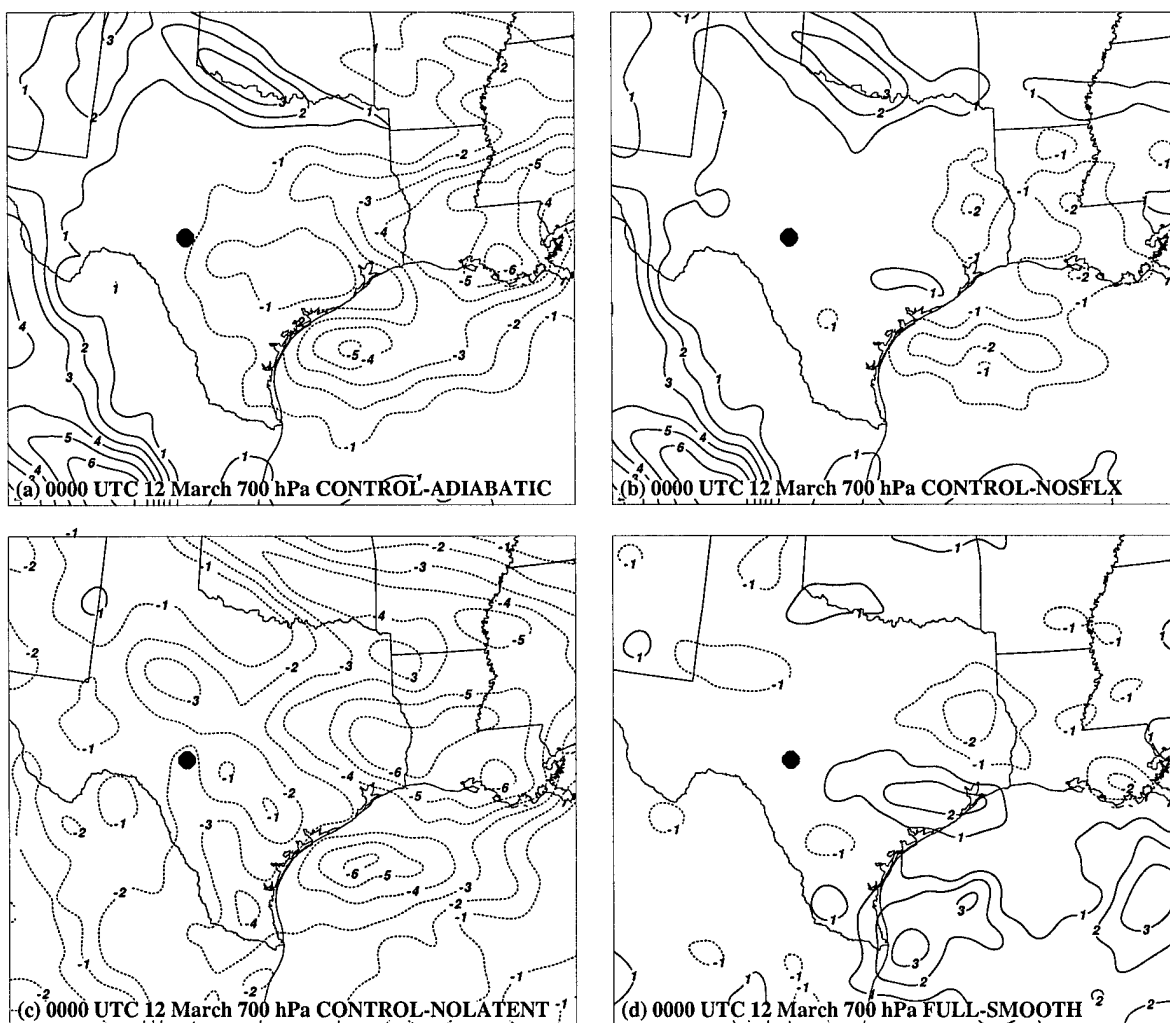


Figure 2.31: Comparison of control and sensitivity experiments at 0000 UTC 12 March at 700 hPa. Potential temperature difference fields, contoured every 1 K (negative dashed) for (a) *CONTROL-ADIAB*, (b) *CONTROL-NOSFLX*, (c) *CONTROL-NOLATENT*, and (d) *CONTROL-SMOOTH*. Position of Bosart et al. (1996) PV anomaly D is indicated by the filled octagon.



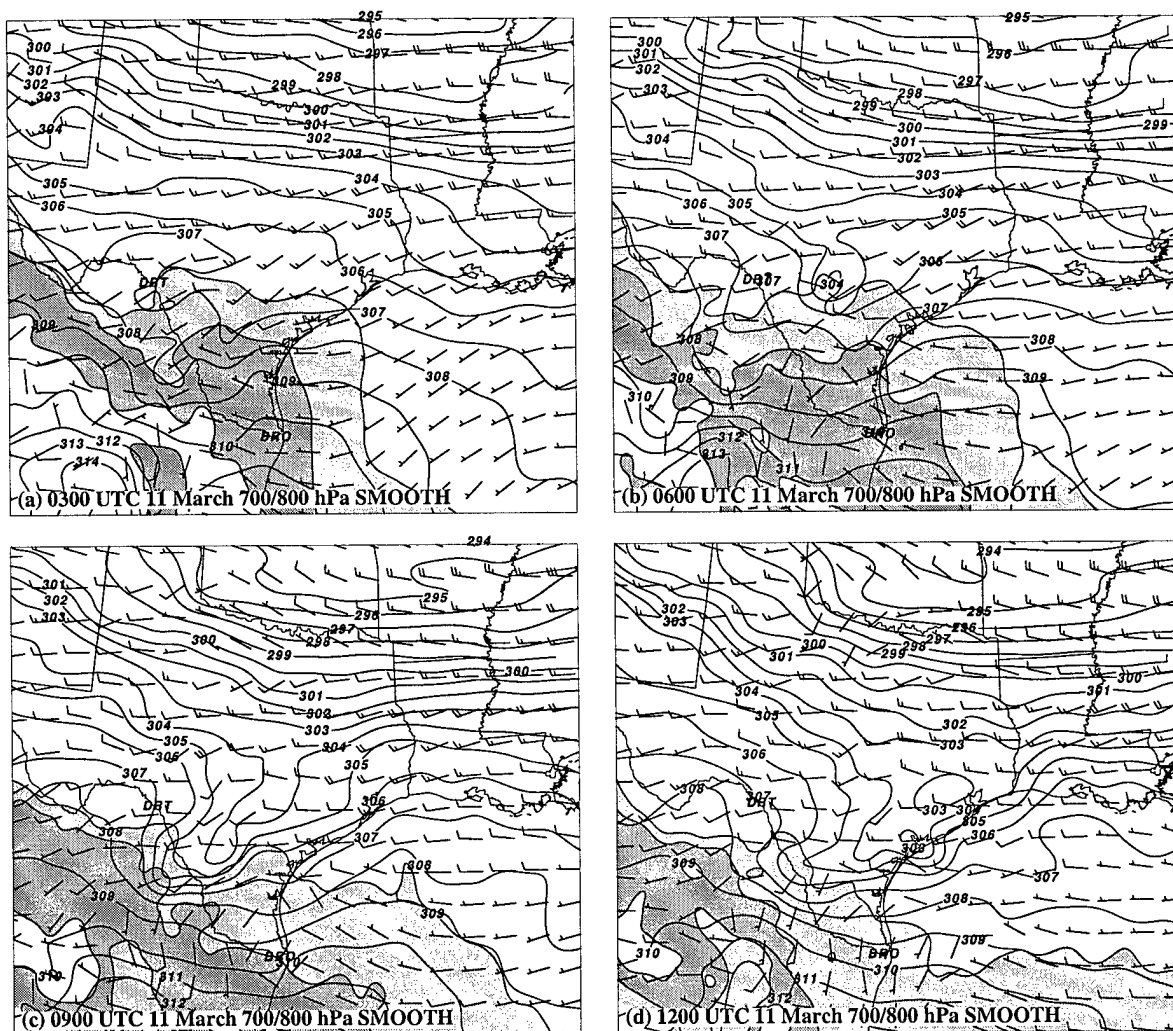


Figure 2.32: SMOOTH simulation 700 hPa standard wind vectors ( $\text{m s}^{-1}$ ), isentropes contoured every 1 K, and 800 hPa isentropes shaded from 302 to 304 K (light gray) and 304 to 306 K (dark gray), valid 11 March at (a) 0300 UTC, (b) 0600 UTC, (c) 0900 UTC, and (d) 1200 UTC.

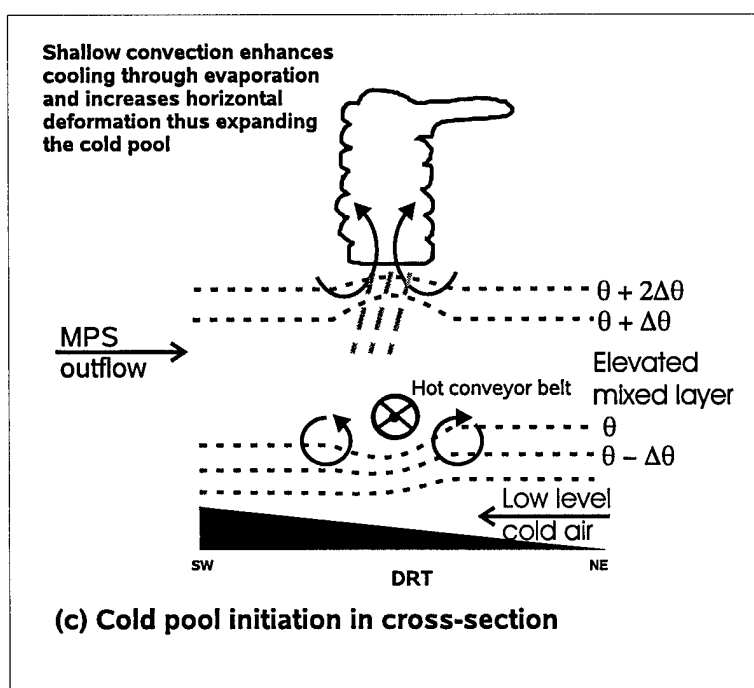
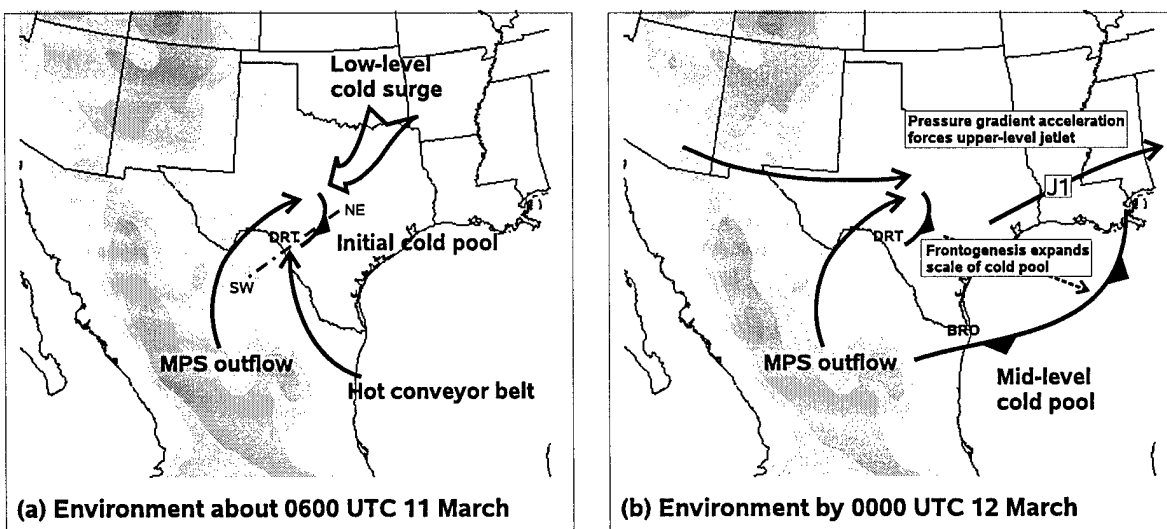


Figure 2.33: Summary of the development of the mid-level cold pool that is the locus of development early on 12 March. Schematics depict (a) initiation of the cold pool in the upper Rio Grande Valley early on 11 March, (b) frontogenesis and jetogenesis that condition the environment along the Gulf Coast for deep convection and (c) a cross-section view of the cold pool initiation with the plane indicated in (a).

## Chapter 3

# The Mesoscale Evolution of the March 1993 Storm of the Century. Part II: Initiation and maintenance of antecedent convection

### 3.1 Introduction

The March 1993 Storm of the Century (SOC93) devastated the United States with record-breaking snowfall amounts over an area far in excess of any previously recorded East Coast snowstorm (Kocin *et al.*, 1995). The event was heralded as a forecasting success because major operational models predicted a strong extratropical cyclone moving up the east coast of the U.S. in the period 13–14 March as early as 8 March, or about five days in advance (Uccellini *et al.*, 1995). This extraordinary storm, however, began as an explosively deepening surface cyclone in the western Gulf of Mexico evident at 1200 UTC 12 March as a 1000 hPa surface low (Fig. 3.1a). Sweeping across the northern Gulf of Mexico, the cyclone deepened by 16 hPa in 12 h, to 992 hPa at 1800 UTC (Fig. 3.1b) then to 984 hPa by 0000 UTC 13 March (Fig. 3.1c). The storm made landfall in northwest Florida at 979 hPa at about 0600 UTC 13 March (Fig. 3.1d). This crucial period of the storm's life cycle was not captured in *any* operational model and left forecasters with little indication of the storm's intensity at landfall (Uccellini *et al.*, 1995; Huo *et al.*, 1995; Dickinson *et al.*, 1997).

Several studies, notably those by Gilhousen (1994), Bosart *et al.* (1996), Dickinson *et al.* (1997) and Huo *et al.* (1998), have focused on the fundamental paradox of this remarkable

storm: *why did operational models that identified a major cyclone as early as five days in advance perform so poorly in simulating the initial cyclogenesis in the western Gulf of Mexico?* In Chapter 2 we proposed that the early cyclogenesis of SOC93 was driven by meso- $\beta$  scale (20 to 200 km) convection that was, in turn, organized by a sequence of dry and moist processes peculiar to the geography of southern Texas and northern Mexico. Our central hypothesis is that SOC93 evolved in three stages, detailed in Table. 3.1.

The purpose of this study is to document Stage I of SOC93, using observation and simulation datasets to reconstruct the sequence of events that created the mesoscale convective complex that forms the initial storm (Fig. 3.1a). From a simple perspective, atmospheric convection requires an instability to provide potential energy in the column and a triggering mechanism to realize this potential energy. Previous diagnostic studies of SOC93 have identified a mid-tropospheric front across the Texas Gulf Coast extending into northern Mexico early on 12 March along which the initial convection is triggered and organized (Kocin *et al.*, 1995; Huo *et al.*, 1995; Dickinson *et al.*, 1997). In Chapter 2, we demonstrated that this mid-level front develops early on 11 March near Del Rio (DRT), TX, then propagates to the Texas Gulf Coast by late on 11 March where it provides the potential energy for explosive development on 12 March.

In this chapter, we employ observation and simulation datasets to illustrate how this CAPE is realized as deep, organized convection that is sustained by and further modifies the upper-level flow. The resulting mesoscale convective complex (Fig. 3.1a) forms the kernel of the warm-core SOC93. A future study (Chapter 4) will address the over water (Stage II) development of the storm (Fig. 3.1b–d). Stage III describes the merger of strong PV anomalies over the eastern United States (Fig. 2.2), and is thoroughly documented in the comprehensive work of Bosart *et al.* (1996); the mechanisms that characterize this stage of storm development are similar to the case of the 1978 Cleveland Super Bomb documented in the work of Hakim *et al.* (1995).

The rest of this chapter is organized as follows: section 3.2 discusses the datasets used in the analysis, and offers a brief model verification; section 3.3 illustrates the physical sequence of events that initiates and sustains deep convection along the Texas Gulf Coast; and section 3.4 presents the concluding discussion.

## 3.2 Methodology and model verification

### 3.2.1 Observation and simulation datasets

The observation and numerical datasets used in this study are described in detail in Sec. 2.3 and are reviewed only briefly here. Uninitialized gridded analyses from the European Center for Medium-range Weather Forecasts (ECMWF) at  $1.125^\circ$  (T106) resolution were used for observational analysis and as initial and boundary condition fields for the numerical experiments. Additional surface meteorological data and sea-surface temperature (SST) data were obtained from the archives of the National Data Buoy Center (NDBC, reviewed in Gilhousen, 1994). These data were employed in observational analyses as well as in the construction of a synthetic SST field to correct deficiencies in operational analyses (Gilhousen, 1994). This SST field was used for model initialization in most of the numerical experiments conducted in this study and is described in detail in Sec. 2.3.

The Mesoscale Atmospheric Simulation System (MASS), version 5.12, was used for all of the numerical experiments. MASS is a hydrostatic, full-physics primitive equation model with fourth-order differencing (MESO Inc., 1993). In addition to the full-physics control experiment, several supporting experiments were conducted to evaluate the relative contributions of dry and moist diabatic processes and assess the relative importance of terrain to Stage I cyclogenesis. An adiabatic simulation (ADIABATIC) is employed to quantitatively assess the role of all diabatic processes in this early cyclogenesis. This assessment is further refined with two modified-physics experiments that separate moist and dry processes: a run in which the surface sensible heat flux is neglected (NOSFLX) and a run in which all latent heating is neglected (NOLATENT). To evaluate the importance of terrain, a smoothed-terrain run was conducted with resolution and physics matching the control simulation but with terrain suppressed with 50 passes through a nine-point smoother (full and smoothed-terrain fields are depicted in Fig. 2.6). Table 3.2 lists the numerical experiments conducted in this study.

### 3.2.2 Model verification

The storm central pressures (Fig. 3.2a) and track of the control experiment verify quite well with the observed storm based on the surface mesoanalysis of Kocin *et al.* (1995) (Fig. 3.2b). The mean central pressure error in the period of 1200 UTC 12 March to 1200 UTC 13 March is about +3.4 hPa, consistent with previous studies (e.g. Huo *et al.*, 1995, 1998). We must emphasize, however, that SOC93 modeling studies to date have only shown success by initializing at 1200 UTC 12 March or later, which is consistent with the gradual improvement of operational models as the fully-developed storm becomes an initialized, rather than model-developed, phenomenon (Caplan, 1995). In this study, the surface vortex at 1200 UTC 12 March is the product of 48 h of model integration, which gives us confidence that the key mesoscale signals are captured in this simulation dataset. A more detailed, three-dimensional verification of the control experiment is provided in Sec. 2.3.

## 3.3 Initiation and maintenance of the Stage I SOC93

### 3.3.1 Overview

Previous studies have observed that the initiation of SOC93 is linked to strong convection across northern Mexico early on 12 March (Kocin *et al.*, 1995; Huo *et al.*, 1995; Bosart *et al.*, 1996; Dickinson *et al.*, 1997; Huo *et al.*, 1998). Because this region is primed for convection on a large (meso- $\alpha$ ) scale, however, little attention has been given to the specific details regarding *how* the convection forms and *why* it forms in a particular location in northern Mexico. In this section, we present the sequence of events that initiates convection and maintains convection along the cold pool described in Chapter 2; it is this organized convective complex that subsequently produces the initial surface cyclone. We first illustrate the genesis of the crucial mesoscale convective complex in northern Mexico. We next explore the subsequent jetogenesis and development of the supporting upper-level environment. We then demonstrate how these elements phase to form the surface cyclone by 1200 UTC 12 March. We conclude with a brief sensitivity analysis.

### 3.3.2 Initiation of convection

We assert that the mesoscale convective complex that forms the kernel of SOC93 is initiated about 0600 UTC 12 March northeast of Monterey (MTY), Mexico. We hypothesize that the triggering mechanism for this early development is a deep column of ascent under powerful upper-level divergence created by the juxtaposition of intense MPS outflow and the left exit region of an approaching jet streak. Surface pressure falls under the core of the storm increase onshore flow and resupply the convective available potential energy, sustaining the continued development of the convective complex.

At 0000 UTC 12 March, the cold pool described in Chapter 2 is observed from the Texas Gulf Coast to just north of Tampico (TAM), Mexico (Fig. 3.3a), while the upper-level jetlet attendant to this cold pool is observed just east of the Texas Gulf Coast (identified as J1 in Fig. 3.3b). Daytime heating along the plateau is reflected in the strong thermal ridge at 700 hPa from southwest of TAM to extreme northwest Mexico, and the juxtaposition of this feature with the mid-tropospheric cold pool tightens the temperature gradient across the Sierra Madres approximately along a line from MTY to Ciudad Victoria (CVM) to TAM (Fig. 3.3a). The mountain-plains solenoid generated by the Altiplanicie Mexicana is the upper branch of a large, thermally-direct circulation extending to about 500 hPa, and the enhanced mid-level baroclinic zone along the terrain accelerates the southerly ageostrophic flow of the MPS proximal to MTY; this is substantiated, in part, by the observed increase in south-southwesterly flow at 700 hPa across northeastern Mexico by 0600 UTC (Fig. 3.4a).

An opposing, northerly ageostrophic flow is provided by the transverse circulation of the approaching subtropical jet streak (Fig. 3.4b), though the left exit region of this streak is strongly perturbed by the thermal ridge over the plateau (Fig. 3.4a). In a straight, quasi-balanced jet streak, the exit region transverse circulation is typically a thermally-indirect response to the deceleration of the parcel; that is, ascent in cold air in the cyclonic, left exit region and descent in the warm, anticyclonic right exit region construct a cross-stream pressure gradient force that increases the opposing, along-stream ageostrophy, thus decelerating parcels exiting the jet core (e.g. Keyser and Shapiro, 1986). As the STJ rotates over the Mexican plateau on the long-wave trough, the left exit region encounters a deep column of extremely hot air that disturbs the balanced exit region as parcels encounter an

increasing ageostrophy. This result, coupled with the natural curvature of the flow about the long wave trough, shifts the exit region poleward by 0600 UTC (Fig. 3.4b), thus increasing the upper-level divergence proximal to MTY.

Mesoscale simulations provide further evidence for this sequence of events. At 0000 UTC 12 March (36 h integration), the control simulation reproduces the 700 hPa thermal ridge along the plateau and the hyperbaroclinic zone extending from MTY to CVM (Fig. 3.5b). This thermal ridge is reflected in the mean sea-level pressure (PMSL) field as a meso- $\alpha$  scale trough along the plateau (Fig. 3.5a). Low-level convergence along the eastern edge of the Sierra Madres is driven at the subsynoptic scale by plateau heating and enhanced at the meso- $\beta$  scale by the 700 hPa cold pool, producing a weak inverted trough northeast of MTY, extending to Brownsville (BRO), Texas (Fig. 3.5a). At 700 hPa, the strongest southerly ageostrophy is indicated along the western edge of the hyperbaroclinic zone, confirming the local acceleration of the broader, southerly MPS along the plateau (Fig. 3.5b). The vertical penetration of the MPS is evident at 500 hPa as a strong southerly ageostrophic current west of MTY and CVM embedded in a large, quasi-adiabatic (316–318 K) pool of air consistent with the ascent and upfolding of the hot plateau boundary layer (Fig. 3.5c). At 300 hPa, the MPS appears as a relatively weak area of divergence just west of CVM, while a more significant divergence signal ( $> 0.5 \times 10^{-4} \text{ s}^{-1}$ ) is indicated over MTY (Fig. 3.5d). A vertical cross-section along the terrain further illustrates the breadth and depth of the MPS circulation as a deep core of strong ascent ( $< -40 \mu\text{bars s}^{-1}$ ) clearly tied to the deep penetration of the plateau boundary layer (Fig. 3.6a). The upper-level divergence near MTY is a hydrostatic response to the elevated heating along the mountain and low-level convergence below the mountain (Fig. 3.6b).

By 0300 UTC 12 March, the 700 hPa thermal ridge retreats southward (Fig. 3.7b) in the transition along the plateau to a nocturnal boundary layer<sup>1</sup>. The mesoscale frontal zone from MTY to CVM, however, sustains the strong southerly ageostrophy at 700 hPa (Fig. 3.7b) and southeasterly ageostrophy at 500 hPa (Fig. 3.7c). The more pronounced southeasterly ageostrophic current at 300 hPa is a signal of the perturbed exit region of the approaching STJ (Fig. 3.7d). This ageostrophic response accompanying the STJ forms a deep column of

<sup>1</sup>Texas and central Mexico are -6 h from UTC and local sunset in March 1993 occurred at approximately 0030 UTC.



ascent proximal to MTY (Figs. 3.8a and b) manifest as a strong ( $> 1 \times 10^{-4} \text{ s}^{-1}$ ) signal of divergence at 300 hPa (Fig. 3.7d). The height field at 300 hPa is perturbed just south of MTY by the MPS-induced thickness ridge thus producing a subsynoptic Laplacian of height just ahead of the STJ exit region. It is this interaction between the height perturbation and the STJ exit region which is crucial to increasing the divergence; note the extreme perturbation of the 9410 m isoheight at 300 hPa north of MTY (Fig. 3.7d). This is a highly unbalanced response as described in Koch and Dorian (1988) and more recently investigated in Kaplan *et al.* (1998).

This deep column of ascent *precedes* significant moist convection over MTY; both satellite (Fig. 3.3a) and model precipitation fields (Figs. 3.5a and 3.7a) show only light precipitation west of MTY by 0300 UTC. By 0600 UTC, however, the deep ascent over the midtropospheric cold pool has triggered significant convection over the base of the inverted surface trough anchored at MTY (Fig. 3.9a). Although the 700 hPa cold pool is weakening as the CAPE is realized in convection (Fig. 3.9b), the surface pressure falls and subsequent enhanced onshore flow transport warm, moist air into the developing storm, effectively maintaining the potential energy in the column about MTY (Fig. 3.9a). Warm plateau air, the residual of the MPS, feeds the warm core of the developing storm at mid-level (Fig. 3.9c) while helping to sustain the divergence aloft (Fig. 3.9d). A west-east cross-section through the lower Rio Grande Valley (normal to the Sierra Madres) indicates a deep, organized column of ascent ( $< -50 \mu\text{bar s}^{-1}$ ) over MTY (Fig. 3.10a). A south-north cross-section (approximately along the MPS) shows the deep warm core developing in this column as the latent heat release is reinforced by the warm, mid-level plateau air (Fig. 3.10b). These horizontal and vertical analyses confirm that the convective core of SOC93 is quickly becoming organized.

Another significant signal of upper-level divergence ( $> 3.0 \times 10^{-4} \text{ s}^{-1}$ ) is evident at 0600 UTC in the upper Rio Grande Valley near Del Rio (DRT), Texas (Fig. 3.9d). This region, also marked by observed (Fig. 3.4a) and simulated (Fig. 3.9a) moist convection, is forced by the left exit region of the approaching STJ where divergence is further enhanced by the increasing curvature of the synoptic-scale jet streak around the long-wave trough (Fig. 3.9d). This region, however, does not develop further and in fact the upper-level divergence proximal to DRT weakens after 0600 UTC. We contend that two unique features phase over MTY early on 12 March to initiate the convective core of SOC93: (1) the MPS and STJ act *in*

*concert* to develop and sustain sufficient upper-level divergence to trigger deep convection; and (2) the meso- $\alpha$  scale low-level convergence attendant to the mountain-plains solenoid is modulated at the meso- $\beta$  scale by the convection triggered under the strong divergence aloft, inducing surface pressure falls that enhance the onshore flow proximal to MTY. The low-level return branch circulation is enhanced by diabatically-forced outflow from the MPS and from moist convection. In the next section, we will demonstrate how this convective core modifies and is modified by the upper-level flow to produce an organizing jet streak in a short ( $< 6$  h) time period.

### 3.3.3 Jetogenesis in the supporting environment

In their classic study of convectively-driven weather systems, Fritsch and Maddox (1981a, 1981b) demonstrated that the outflow from meso- $\alpha$  scale convection can drive upper-level jetogenesis, particularly on the north or northwestern edge of the anticyclonic outflow where the ageostrophic current makes a positive contribution to the midlatitude synoptic-scale westerly momentum. Idealized studies of convective systems by Wolf and Johnson (1995) indicate that at the meso- $\beta$  scale, the latent-heating induced warm core can make an additional contribution to upper-tropospheric jetogenesis through the mass adjustment induced over this core. The jet streak supporting the initial SOC93 forms as the meso- $\alpha$  and meso- $\beta$  mechanisms described above act over deep convection initiated prior to 0600 UTC. These mechanisms operate in an environment already conditioned for jetogenesis by the jet streak created on 11 March by the formation of the mid-level cold pool (**J1**, described initially in Chapter 2), and enhanced by the southwesterly upper branch of the MPS circulation. In this section, we employ the observation datasets, control simulation and sensitivity experiments (Table 3.2) to investigate this upper-level jetogenesis and illustrate its importance to Stage I cyclogenesis.

Observation analyses indicate that explosive jetogenesis occurs in the lower Rio Grande Valley subsequent to the initiation of deep convection proximal to Monterey (MTY), Mexico about 0600 UTC. The jet streak that formed late on 11 March is observed in the 300 hPa ECMWF analysis at 0000 UTC 12 March (**J1** in Fig. 3.3b). Although this feature weakens in the 300 hPa analysis 6 h later (Fig. 3.4b), evidence of the jet streak is indicated by convection

along the southern Gulf Coast of Texas (Fig. 3.4a). By 1200 UTC, however, two jet streaks extending through central Texas and along the Texas Gulf Coast are an unambiguous signal of the developing storm (Fig. 3.11b). In the entrance region of these jet streaks is a broad area of strong ( $> 10^{-4} \text{ s}^{-1}$ ) divergence. This region, with a mean radius of 400 km or about 4 grid points in the ECMWF analysis, appears to have three lobes: a northern lobe near Del Rio (DRT), Texas, associated with the western jet streak along the northwestern edge of the mesoscale convective complex (Fig. 3.11a); a western lobe near Monterey (MTY), Mexico, proximal to the left exit region of the STJ that has been modified by plateau heating (note the 700 hPa thermal ridge in Fig. 3.11a); and an eastern lobe near Brownsville (BRO), Texas, in the entrance region of the eastern jet streak, associated most directly in time and space with the developing SOC93 (note collocation with the surface low indicated in Fig. 3.11a). The importance of the eastern lobe, and hence the primacy of the eastern jet streak, is supported by the observed 300 hPa vertical velocity field, with a relatively strong ( $> 16 \mu\text{bar s}^{-1}$ ) core of ascent over the surface low (Fig. 3.12). We contend that this meso- $\alpha$  scale jet streak is created rapidly as the entrance region of the old **J1** is reinforced by dry convection (the southwesterly MPS outflow) and moist convection in the period from about 0600 to 1200 UTC. It is this jet streak which organizes the continued development of the convective core of SOC93. To fully establish this sequence of events we employ mesoscale simulation results.

At 0600 UTC, the control simulation 300 hPa wind field (Fig. 3.13a) shows similar structure to the observed (ECMWF) analysis (Fig. 3.4b), though the jet streak along the Texas Gulf Coast is better resolved in the mesoscale simulation. The wind field in the adiabatic simulation reflects the turning of the STJ about the long wave trough (Fig. 3.13b); calculations show a minimum radius of curvature of about 300 km, which is consistent with the minimum radius computed from the observed (ECMWF) wind field (Fig. 3.4b). These results show that the synoptic-scale curvature in the wind field does not *by itself* induce significant divergence ( $> 0.5 \times 10^{-4}$ ) along the Rio Grande Valley.

We have established (Sec. 3.3.2) that the significant divergence ( $> 10^{-4} \text{ s}^{-1}$ ) in the entrance region of the jet streak along the Gulf Coast *initiates* the deep convection that is both observed (Fig. 3.4a) and simulated in the control experiment (Fig. 3.9a). We emphasize this point because a key component of our hypothesis and a unique aspect of this

study is that the moist convection crucial to the development of SOC93 is triggered in large part by substantial dry convection (the MPS outflow). Sustained divergence aloft, in turn, builds the entrance region of the organizing jet streak *while triggering* convection that also reinforces the existing jetlet along the Gulf Coast. The importance of the dry convection is highlighted by the NOLATENT simulation (surface sensible heat fluxes enabled, but all latent heating disabled), which still produces a weak divergence signal and jetlet *despite the complete absence of moist convection in the simulation* (Fig. 3.13c). With sensible surface heat fluxes disabled (NOSFLX, Fig. 3.13d), the Mexican plateau is no longer a source of elevated heating and can neither perturb the exit region of the approaching STJ nor induce a powerful southerly MPS outflow. Although moist convection is permitted in this simulation, no precipitation develops proximal to MTY (Fig. 3.14) because the divergence in the exit region of the STJ *working alone* is insufficient to trigger deep convection. These results provide further evidence that the dry convection attendant to the elevated heating along the Mexican plateau is a *necessary* ingredient to produce SOC93. With respect to the organizing jet streak, we conclude that the strong signal of divergence *precedes* the explosive jetogenesis along the Texas Gulf Coast.

In the period from 0600 to 0900 UTC, the dry convective outflow and subsequent moist convection along the lower Rio Grande Valley induce the organizing jet streak on the entrance region of the old J1, phasing the meso- $\alpha$  jetlet with the meso- $\beta$  convective complex; this phasing further focuses the development of the warm-core storm. By 0900 UTC, the control simulation indicates precipitation across much of central Texas (Fig. 3.15a), consistent with the satellite observation (Fig. 3.21a, to be discussed in Sec. 3.3.4). The convective core of SOC93 is indicated by the meso- $\beta$  scale inverted surface trough midway between MTY and BRO, located just north of the precipitation core of  $42 \text{ mm h}^{-1}$  (Fig. 3.15a). The warm meso- $\alpha$  scale MPS indicated by the southerly ageostrophy just west of BRO at 700 hPa (Fig. 3.15b) and just east of the line between MTY and CVM at 500 hPa (Fig. 3.15c) has been modulated by the deep, meso- $\beta$  scale convection triggered under the powerful and focused upper-level divergence ( $> 4 \times 10^{-4} \text{ s}^{-1}$  in Fig. 3.15d). This modulation of the MPS is deduced from the substantial warm core of the system in the triangle formed by MTY, BRO and CVM; at 700 hPa this appears as a warm pocket of 306 K (Fig. 3.15b) and at 500 hPa as a significant pool of 316 K air with an approximate radius of 150 km (Fig. 3.15c). We

assert that this warm core is a combination of the MPS *and* tremendous latent heat release because the scale of the warm air, particularly at 500 hPa, exceeds the scale of the deep convection by a factor of about three.

Direct comparisons between the full-physics (CONTROL) and sensitivity experiments at 0900 UTC further clarify the contributions of dry and moist diabatic processes to the explosive jetogenesis (Fig. 3.16, 3.17). These comparisons are constructed from the algebraic differences in the wind and height fields between the control experiment and sensitivity experiments; while this technique assumes a dominant linearity in the governing atmospheric processes, similar techniques have been employed in previous studies of rapid mesoscale cyclogenesis (e.g. Kuo *et al.*, 1995) and have been employed in diagnostic studies of SOC93 (Huo *et al.*, 1995). The jet streak forming on the outflow from the nascent storm appears at 300 hPa as a strong anticyclonic diabatic signal in the total wind field as well as a significant positive perturbation ( $> 60$  m) in the geopotential height field along the Rio Grande Valley (Fig. 3.16a), where we assume that the difference field represents a snapshot of the control simulation with the “background” adiabatic signal filtered out. The relative contribution from latent heating to this diabatic signal (CONTROL - NOLATENT, Fig. 3.16b) is slightly weaker than the contribution from surface heat fluxes (CONTROL - NOSFLX, Fig. 3.16c), consistent with our previous assertion that dry diabatic processes are crucial to Stage I cyclogenesis. Although it may seem unlikely that surface heat fluxes could so strongly perturb the upper-level flow, the mean terrain height across central Mexico is about 1500 m and daytime surface temperatures on 10–11 March reach 27°C, extending the boundary layer above 500 hPa (Fig. 3.6a). The momentum field between MTY and CVM in all three comparisons (Fig. 3.16) is directed into the approaching STJ (Fig. 3.15d). Although the dry diabatic forcing (Fig. 3.16c) is relatively stronger than the moist diabatic signal (Fig. 3.16b), both make a significant contribution by 0900 UTC to the imbalance in the left exit region of the approaching STJ, further enhancing the upper-level divergence over MTY (Fig. 3.15d).

Comparisons at 700 hPa demonstrate the organization of the incipient SOC93 under the meso- $\alpha$  jet streak by 0900 UTC. Diabatically-induced height falls and cyclonic inflow mark the storm just west of BRO (Fig. 3.17a). Latent heat release associated with the precipitation core (Fig. 3.15a) clearly contributes to the dramatic mid-level warming and attendant height falls (Fig. 3.17b). Residual warm air from the Mexican plateau, however,

continues to feed the rear inflow of the developing mesoscale convective complex (Fig. 3.17c). The thermally-direct acceleration over this warm core makes an additional contribution to the rapid jetogenesis along the Texas Gulf Coast, as indicated by the differential wind vectors north of BRO (Fig. 3.17a). We conclude that by 0900 UTC the mesoscale convective complex (MCC) initiated in the lower Rio Grande Valley has organized the upper-level flow in the form of a significant jet streak along the Texas Gulf Coast. The phasing of this jet streak with the warm core of the MCC guarantees the continued development of SOC93 by delivering a mechanism to sustain the upper-level divergence as the scale of the storm expands. In the next section we examine how the Stage I surface cyclone develops under this organized mesoscale convective system.

### 3.3.4 Transition to surface cyclogenesis

Bosart *et al.* (1996) and Dickinson *et al.* (1997) hypothesize that surface cyclogenesis along the Gulf Coast is triggered by the intrusion of PV anomaly C into northern Mexico early on 12 March; positions of PV anomaly C are indicated in Figs 3.5 (0000 UTC), 3.7 (0300 UTC), 3.9 (0600 UTC) and 3.15 (0900 UTC). In terms of potential vorticity thinking, surface cyclogenesis can occur when an upper-level PV anomaly approaches a low-level baroclinic zone; low-level warm advection ahead of the upper-level disturbance modulates the baroclinic zone, producing a warm anomaly that induces a surface cyclonic circulation that can reinforce the upper-level disturbance (Hoskins *et al.*, 1985, Sec. 7e). Moist diabatic processes intensify the coupling between upper and lower-level disturbances, thus contracting the time scale of development. While Dickinson *et al.* (1997) speculate that low-level warm advection ahead of PV anomaly C triggers the convective core of SOC93, we have demonstrated that the initiation of convection is more readily tied to the strong upper-level divergence in northern Mexico at the junction of the perturbed exit region of the STJ and the dry convective outflow of the mountain-plains solenoid. This divergence signal, with its attendant jet streak, is a mesoscale analog to the upper-level disturbance (PV anomaly) in the Hoskins *et al.* (1985) paradigm. In this section, we complete this mesoscale extension to classic IPV thinking by examining the low-level baroclinic zone and subsequent transition to surface cyclogenesis along this boundary that culminates in Stage I cyclogenesis.

To emphasize the time and space separation of PV signals, isentropic potential vorticity was calculated for both CONTROL and ADIABATIC simulations. The difference field (CONTROL - ADIABATIC) in the column from 316 K to 336 K (about 682 hPa to 367 hPa) at 0600 UTC reveals a significant pool of 0.25 PVU (following Hoskins *et al.*, 1985, where 1 PVU =  $\text{K m}^2 \text{ kg}^{-1} \text{ s}^{-1}$ ) redistributed by the dry diabatic outflow along the Sierra Madres (Fig. 3.18a). We contend that this pool is largely a signature of the MPS because it is coincident with the northward penetration of hot plateau air at 700 hPa (Fig. 3.9b) and 500 hPa (Fig. 3.9c) based on an analysis that masks the background (adiabatic) potential vorticity signal. A similar difference analysis at 0600 UTC 12 March shows similar structure among the CONTROL - NOSFLX (Fig. 3.19a) and CONTROL - NOLATENT (Fig. 3.19b) fields, with a diabatic pool of IPV between MTY and CVM at this time; we conclude that both dry and moist diabatic redistribution of IPV are active, though we have demonstrated that the dry forcing *precedes* the moist forcing. Computation of the Lagrangian Rossby number ( $Ro$ ), where

$$Ro = \left| \frac{\frac{DV}{Dt}}{fV} \right| \quad (3.3.1)$$

indicates that the pool of PV along the Sierra Madres is attendant to highly accelerating flow at 326 K (about 500 hPa). By 0900 UTC, this pool is reinforced by the redistribution of PV in the intense, moist convection proximal to MTY, and this pool is clearly separated in space by about 700 km from the upstream PV anomaly C (Fig. 3.18b). The acceleration of the mid-level flow in response to the increasing upper-level divergence is also marked by the increasing  $Ro$  ahead of the PV (Fig. 3.18b). The focused acceleration indicated in the  $Ro$  field at 0900 UTC (Fig. 3.18b) is further proof of the coupling by moist convection of the mid-level inflow from the MPS (Fig. 3.15b,c) to the upper-level outflow (Fig. 3.18d). We contend that dry and moist mesoscale processes along the eastern edge of the Mexican plateau *create* the upper-level disturbance diagnosed directly as the intense, coherent divergence signal over MTY (Fig. 3.9d, 3.15d). This disturbance is also manifest in the computation of the diabatically-redistributed IPV fields (Fig. 3.18a,b). It is this mesoscale ( $Ro \gg 1$ ) signature in the IPV field that marks the upper-level disturbance supporting the surface cyclone, as indicated by the IPV difference field at 1200 UTC 12 March (Fig. 3.18c).

The surface component of SOC93 forms under intense convection along on an inverted trough stretching from the lower Rio Grande Valley northeastward into the Gulf of Mexico (Fig. 3.20). This trough is a remnant of a stagnant surface boundary across eastern Texas, parallel to the coast, present since early 11 March. A Barnes (1964) objective analysis (OA) of the regional surface data illustrates the rapid development of the surface low along the Gulf Coast (Fig. 3.21). Convection dominates the western edge of this surface trough at 0900 UTC (Fig. 3.21a). We have demonstrated that the upper-level flow is sufficiently organized to sustain this deep convection, so that low-level convergence along the trough is enhanced, further dropping the surface pressure between MTY and BRO by about 3 hPa between 0900 and 1000 UTC (Fig. 3.21b). By 1100 UTC the surface cyclone appears as a 1003 hPa open low just east of BRO (Fig. 3.21c) that quickly matures as a closed circulation and is evident as the incipient SOC93 at 1200 UTC (Fig. 3.21d). Although the convection through this period is widespread and the trough is a meso- $\alpha$  feature at about 800 km along its major axis, the meso- $\beta$  focal point for the surface organization of the storm appears to be a relatively dry notch in the convection, evident just west of BRO at 0900 UTC (Fig. 3.21a). This notch corresponds in time and space with the simulated meso- $\beta$  inverted surface trough and precipitation-free region (Fig. 3.15a), and the penetration of the warm, dry MPS at 700 hPa (Fig. 3.15b) and at 500 hPa (Fig. 3.15c). This mid-level inflow corresponds vertically to the strong divergence signal at 300 hPa just southwest of BRO, which is the focal point for development. (Fig. 3.15d). From these results we infer that by 0900 UTC, the organizing upper-level jetlet and warm, rear inflow of the MPS are phased about the growing warm core, building the storm vertically over the effectively infinite supply of low-level moisture from the Gulf of Mexico.

Cross-sections through the developing storm make these relationships clearer. In a west-to-east vertical cross-section from MTY to BRO, the intense warm core of the storm is marked by a strong ( $< -100 \mu\text{bar s}^{-1}$  or  $> 1 \text{ m s}^{-1}$ ) updraft and a deep depression in the isentropes from about 600 to 300 hPa (Fig. 3.22a). The environment away from the storm shows weak vertical shear, which permits a nearly vertical updraft through this deep column. About 50 km west (left) of this deep column of ascent is evidence of a warm, low-level cyclonic circulation corresponding to the meso- $\beta$  surface trough (Fig. 3.15a); this circulation appears to extend from the surface to about 650 hPa (Fig. 3.22a). A south-to-



north vertical cross-section depicting rain water mixing ratio shows evidence of this low-level warm circulation north of the precipitation core (Fig. 3.22b). The extremely warm air in this circulation, marked by the deep depression in the isentropes from the surface to about 750 hPa, is dry and ascending; we infer that this low-level cyclonic circulation is part of the helical inflow of warm plateau air about the core of the storm (Fig. 3.22b). The warm surface circulation indicated in the west-east cross-section (Fig. 3.22a) is part of this same three-dimensional inflow into the convective core. From the ageostrophic circulation about the storm, we deduce that the warm MPS air, which was originally in the layer from 500 to 700 hPa (Fig. 3.15b,c), is entrained into the cool, moist downdrafts. The resulting evaporative cooling is overwhelmed by the dry, warm plateau air and the flow is wrapped back into the warm core of the storm. The lack of a surface mesohigh under the nearly upright, sustained precipitation is another indication that the cool downdrafts are being modified (Fig. 3.15a and 3.22b). In effect, the MPS circulation has become a large rear-inflow jet (e.g. Bluestein, 1993, p. 533) for the incipient SOC93.

The entrainment and transport of the warm plateau air builds the warm core of the storm downward, producing a 1004 hPa surface low in the control simulation just east of BRO by 1200 UTC (Fig. 3.23a). This is consistent in depth and location with the OA field (Fig. 3.21d) though about 4 hPa higher than the Kocin *et al.* (1995) mesoanalysis. The broad, warm core of the nascent SOC93 is evident at 500 hPa as a closed 318 K isentropes over BRO with a strong ageostrophic, cyclonic signature (Fig. 3.23c). The warm inflow at 700 hPa appears to follow the core of the storm (Fig. 3.23b), though more properly stated in cause-and-effect, the surface cyclone follows the penetration of this mid-level plateau air. The upper-level divergence at 300 hPa is focused in the right entrance region of the organizing jetlet (Fig. 3.23d), though the resolution of the mesoscale dataset allows for the discrimination of two significant jet streaks, with the more northerly jet streak developing on the convective outflow in the upper Rio Grande Valley (compare to Fig. 3.11b). A vertical cross-section oriented west-east along the path of the storm shows the column of the strongest ( $> 1 \text{ m s}^{-1}$ ) ascent extending down to 850 hPa, while the storm maintains its warm-core, vertical character (Fig. 3.24a). A similar south-north cross-section shows a deep, ascending cyclonic circulation about the storm's center, with the central rain water mixing ratio exceeding  $20 \text{ g kg}^{-1}$  (Fig. 3.24b). Cooler surface air to the south (Fig. 3.24b)

and west (Fig. 3.24a) of the storm are consistent with a weak mesohigh in the PMSL field southwest of the surface low (Fig. 3.23a). This is consistent with the growth of the storm to a large meso- $\beta$  feature. The vertical (Fig. 3.24) and horizontal (Fig. 3.23) structure of the initial warm-core vortex is very similar to the structure simulated by Zhang and Fritsch (1987) in their numerical study of the mesoscale convective complex responsible for the 1977 Johnstown Flood (compare to their Figs. 6 and 7). Redevelopment of MCCs is often associated with the transition to a nocturnal (low-friction) boundary layer (Maddox, 1983), though in this case the SOC93 has an even more favorable (and longer-lived) environment in the open waters of the Gulf of Mexico.

### 3.3.5 Sensitivity analysis

We have strongly implicated the MPS in the initiation and organization of the convective core. Comparisons with the smoothed-terrain (SMOOTH) sensitivity experiment provide further evidence for these claims by suppressing but not eliminating (as in the NOSFLX experiment) the MPS. The model terrain was run through 50 passes with a standard nine-point smoother; the resulting terrain field is depicted in Fig. 3.25b. Overall, suppressing the terrain and terrain gradients appears to shift the MPS signal further west. At 700 hPa at 0900 UTC 12 March, the acceleration over BRO in the control simulation (Fig. 3.15b) has been displaced in the smoothed-terrain run by about 200 km up the Rio Grande Valley, north of MTY (Fig. 3.25a). The SMOOTH simulation still produces a significant warm tongue at 500 hPa (note the warm tongue north of MTY in Fig. 3.25b), though the result appears to be the merging of two separate MPS signals that are more properly resolved in the control run (note the strong signal west of CVM and MTY and separate signal north of the line between MTY and BRO in Fig. 3.15c). The impact of this poorer resolution of the MPS is manifest as a still-significant but less focused signal of upper-level divergence in the lower Rio Grande Valley (compare Fig. 3.25c with Fig. 3.15d). The suppressed terrain also produces less impact on the STJ, indicated by the weaker cross-stream ageostrophy in the exit region (Fig. 3.25c). With these errors, the SMOOTH simulation still produces an initial vortex at 1200 UTC 12 March, but with a mean error of +4.8 hPa in the first 48 h of the simulation (Fig. 3.26a), and a much poorer track forecast (Fig. 3.26b) than the control track

(Fig. 3.2b). These results provide further evidence of the critical importance of dry diabatic forcing along the Altiplanicie Mexicana to the early development of this storm.

The failure of operational models to capture the early cyclogenesis in the western Gulf of Mexico has been attributed in part to deficiencies in the initialized sea-surface temperature (SST) (e.g. Gilhousen, 1994). These deficiencies are assumed to have contributed to the poor representation of the coastal baroclinicity along the Texas Gulf Coast early on 12 March (Huo *et al.*, 1995; Bosart *et al.*, 1996; Dickinson *et al.*, 1997). In Chapter 2, we determined that the strong coastal baroclinicity was actually an aspect of the mid-level cold pool created in the upper Rio Grande Valley. To compensate for the observed weaknesses in the National Hurricane Center (NHC) SST analysis, the control run employed an SST field synthesized from the original NHC analysis, NDBC buoy data and satellite data (Fig. 2.3). An additional numerical experiment was executed, however, with the original NHC SST field to assess the relative importance of this parameter to the overall development of the storm. The NHCSST experiment produces surface fields that strongly resemble the control experiment in the transition to surface cyclogenesis. At 0900 UTC, the NHCSST run develops a weaker inverted surface trough between MTY and BRO (compare Fig. 3.27a to Fig. 3.15a), though the large-scale inverted trough along the Gulf Coast is well-represented. This experiment does indeed produce the incipient SOC93 as a closed, 1004 hPa surface low close to the forecast position in the control experiment (compare Fig. 3.27b to Fig. 3.23a); not surprisingly, the forecast position of the two experiments more closely resemble each other than the observed (Kocin *et al.*, 1995) position. We conclude that the mechanisms that trigger and organize the initial warm-core vortex (Stage I) are relatively insensitive to the sea-surface temperature field. We should not conclude, though, that the entire life-cycle of SOC93 is insensitive to the SST field. After 1200 UTC 12 March, as the storm develops over the Gulf, the mean error in simulated central pressure is -4.9 hPa (Fig. 3.28a) in the NHCSST experiment, with a much poorer forecast of the surface storm track (Fig. 3.28b). In Chapter 4 we will revisit this sensitivity experiment in regard to over water (Stage II) development.

### 3.4 Summary and concluding discussion

The key processes of Stage I of SOC93 are depicted in Fig. 3.29. The mid-level cold pool, described in detail in Chapter 2, propagates to the Gulf Coast of Texas late on 11 March and is aligned east of and parallel to the coast by early on 12 March. The tail end of this cold pool moves southward along the front range of the Sierra Madres, while daytime heating along the plateau tightens the mid-level baroclinic zone in this region of northern Mexico between Monterey (MTY) and Ciudad Victoria (CVM). The southerly MPS is accelerated over this region of mesoscale mid-tropospheric frontogenesis, while the exit region of the approaching synoptic-scale subtropical jet (STJ) streak provides an opposing northerly ageostrophic current. The exit region of this STJ is building ahead of the synoptic-scale propagation of the jet streak because of the intense heating along the Mexican plateau. The thermally-indirect circulation that should be decelerating parcels exiting the streak is strongly perturbed by the ridge above the hot pool in the left (ascending) quadrant, displacing the entire exit region poleward. The juxtaposition of the strong southerly MPS and northerly  $V_{age}$  in the exit region of the STJ creates a strong divergence signal aloft proximal to MTY; this signal originates from *dry* diabatic forcing along the Altiplanicie Mexicana. This dry convective outflow triggers deep, moist convection. Outflow from both moist and dry convection rapidly builds a jet streak on the entrance region of an old jetlet attendant to the mid-level cold pool formed on 11 March (Chapter 2). The organizing jetlet phases with the deepening warm core that grows from both latent heat release and the continued inflow of warm MPS air into the southern flank of the developing storm. The sustained, organized convection induces surface pressure falls along an existing inverted coastal trough, the product of a stagnant surface boundary in eastern Texas; the isallobaric response increases onshore flow, replenishing the potential energy for moist convection in northern Mexico and southern Texas. Warm MPS air, entrained into the moist downdrafts of the nearly vertical precipitation core, builds the warm core of the cyclone downward, producing a closed surface low by 1200 UTC as the storm moves over the open water of the western Gulf. These results depart significantly from previous studies in two important ways.

First, while the early mesoscale convection in the western Gulf of Mexico has been recog-

nized as important to the overall development of SOC93 (e.g. Kocin *et al.*, 1995; Huo *et al.*, 1995), little attention has been given to the mesoscale details of this period, particularly in the critical 36 h prior to 1200 UTC 12 March. In this chapter, we have established that the triggering mechanism for this convection was a strong upper-level divergence created at the opposing junction of the southerly MPS outflow and the northerly ageostrophic circulation in the exit region of the subtropical jet. This finding is in contrast to previous speculation that enhanced low-level warm advection ahead of PV anomaly C triggered the widespread convection (Dickinson *et al.*, 1997). This does not diminish the importance of the background synoptic-scale flow: the interaction of the MPS and STJ are crucial to the sustained divergence that focuses the convective core. We contend, however, that dry diabatic forcing is very important both to triggering and organizing this extraordinary storm.

A second important finding is that the transition to surface cyclogenesis is a warm-core process driven by deep, upright convection sustained by powerful divergence aloft and organized in part by the rear inflow jet formed by the residual MPS air over the Gulf of Mexico. Rapid cyclogenesis is generally assumed to require a significant component of moist convection to more strongly couple the upper and lower disturbances (e.g. Hoskins *et al.*, 1985). In a numerical study of the rapid, mesoscale cyclogenesis of 28–29 March 1984, Gyakum *et al.* (1995) demonstrate a similar multi-stage process for an intense, large meso- $\beta$  scale storm that produced numerous tornadoes in the southeastern U.S. These investigators identify a low-level warm anomaly, attributed to organized mesoscale precipitation and strong sensible surface heat flux, as a precursor signal of rapid cyclogenesis; rapid extratropical (cold-core) cyclogenesis ensues when an upper-level PV anomaly overtakes this warm-core cyclone, dropping surface pressure by 11 hPa in 3 h over a well-organized center of circulation with a radius of approximately 120 km (Gyakum *et al.*, 1995). In the case of SOC93, we contend that the period of warm-core development is prolonged by the Gulf of Mexico and the continued penetration of warm, MPS air into the rear quadrant of the storm (Stage II cyclogenesis). Recent work by Rozumalski (1997) provides further insight into the 28–29 March 1984 event by connecting the mid-tropospheric circulation that organizes the initial mesoscale precipitation to the inflow of warm air from the Mexican plateau; this signal of the MPS travels over the Gulf of Mexico and penetrates the southeastern U.S. in less than 18 h (Rozumalski, 1997).

The implications for understanding Stage I of the March 1993 Storm of the Century extend well beyond this case study. In an early study of Texas-West Gulf cyclones, Saucier (1949) analyzed 388 storms in the period 1899–1938, for a mean of 9.7 winter cyclones per year. In a more recent study, Johnson *et al.* (1984) analyzed extratropical cyclogenesis in the western Gulf in the period 1972–1982 and found an average of 10.4 winter cyclones per year. Dickinson *et al.* (1997) presented a brief study of cool-season (November–April) storms in the Gulf of Mexico from 1957–1989, finding 206 deep storms (storms with central pressures  $\leq 1000$  hPa). Although this is a cursory analysis, we can at least infer that *significant cyclogenesis in the western Gulf of Mexico is not a rare event.*

We speculate that the high percentage of strong cyclogenesis events is due in part to the unique topography of the Mexican plateau and its attendant diabatic and terrain-driven circulations, coupled with a ready moisture source in the Gulf of Mexico. In this study we have presented several mechanisms that, independently, could produce significant, organized convection. We contend that the uniqueness of Stage I of SOC93 lies in the phasing of these circulations to trigger, organize and sustain the initial warm-core cyclone. In Chapter 4, we will investigate the life-cycle of this warm-core storm across the Gulf of Mexico and its subsequent transformation into an extratropical (cold-core) system early on 13 March.

Stage	Period	Characteristics
<b>I</b>	0000 UTC 11 March to 1200 UTC 12 March	A sequence of mesoscale processes constructs a warm-core surface cyclone.
<b>II</b>	1200 UTC 12 March to 0600 UTC 13 March	The storm develops as a warm-core low then is transformed into an extratropical (cold-core) system.
<b>III</b>	0600 UTC 13 March to 0000 UTC 14 March	The storm intensifies again as strong PV anomalies merge over the southeastern U.S. The storm then matures over the northeastern U.S.

Table 3.1: Summary of the SOC93 three-stage evolution.

Experiment ID	Horizontal Resolution	Physics	Initialization
CONTROL	12 km	Full model physics	ECMWF 1.125° Synthetic SST field
SMOOTH	12 km	Full model physics	ECMWF 1.125° Synthetic SST field Smoothed model terrain
ADIABATIC	12 km	Adiabatic physics No PBL or cumulus scheme	ECMWF 1.125° Synthetic SST field
NOLATENT	12 km	PBL physics enabled Latent heating enabled	ECMWF 1.125° Synthetic SST field
NOSFLX	12 km	Surface sensible heat flux disabled Latent heating enabled	ECMWF 1.125° Synthetic SST field
NCEP	12 km	Full model physics	NCEP 2.5° Synthetic SST field
NHCSST	12 km	Full model physics	ECMWF 1.125° NHC SST field

Table 3.2: Numerical experiments. All simulations initialized at 1200 UTC 10 March.

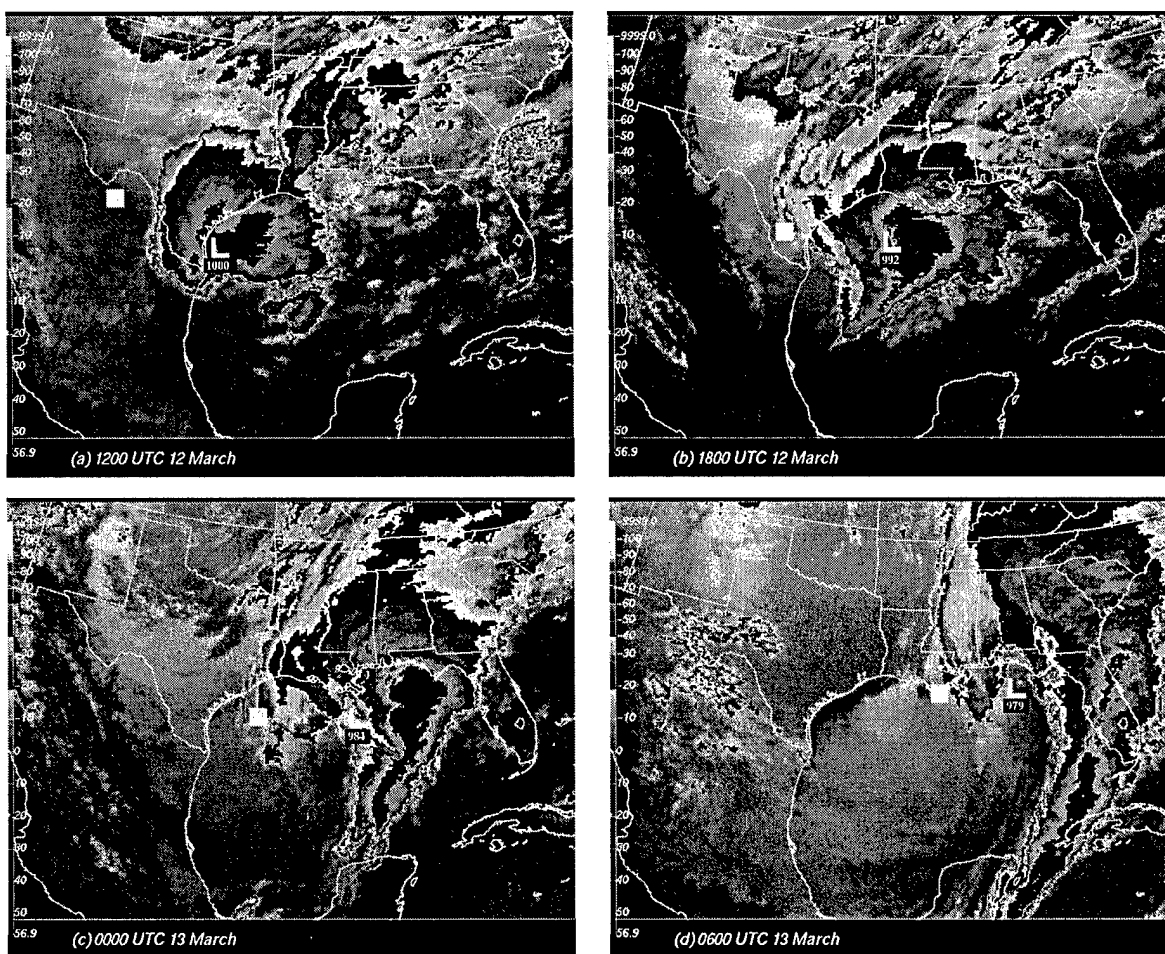


Figure 3.1: GOES-7 IR imagery with superimposed storm positions from the mesoanalysis of Kocin et al. (1995), valid (a) 1200 UTC 12 March (1000 hPa), (b) 1800 UTC 12 March (992 hPa), (c) 0000 UTC 13 March (984 hPa), and (d) 0600 UTC 13 March (979 hPa). Position of Bosart et al. (1996) PV anomaly C, discussed in the text, is indicated by the filled square.



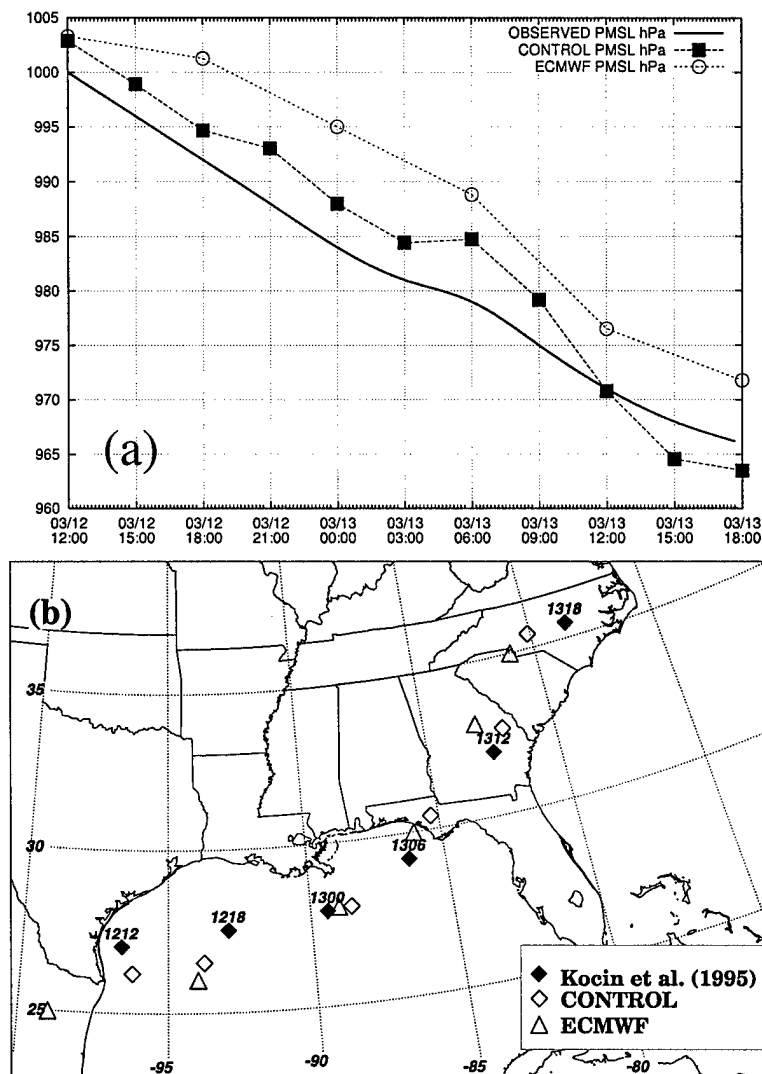


Figure 3.2: Track of the SOC93 surface cyclone in the mesoanalysis of Kocin et al. (1995), the CONTROL simulation and the ECMWF analysis. Depicted are comparisons of (a) storm central pressures and (b) storm position, where the mesoanalysis is indicated by a filled diamond, the CONTROL simulation is indicated by a hollow diamond, and the ECMWF analysis is indicated by the hollow triangle. Times in (b) are of the form *DDHH* (e.g. 1218 = 1800 UTC 12 March).

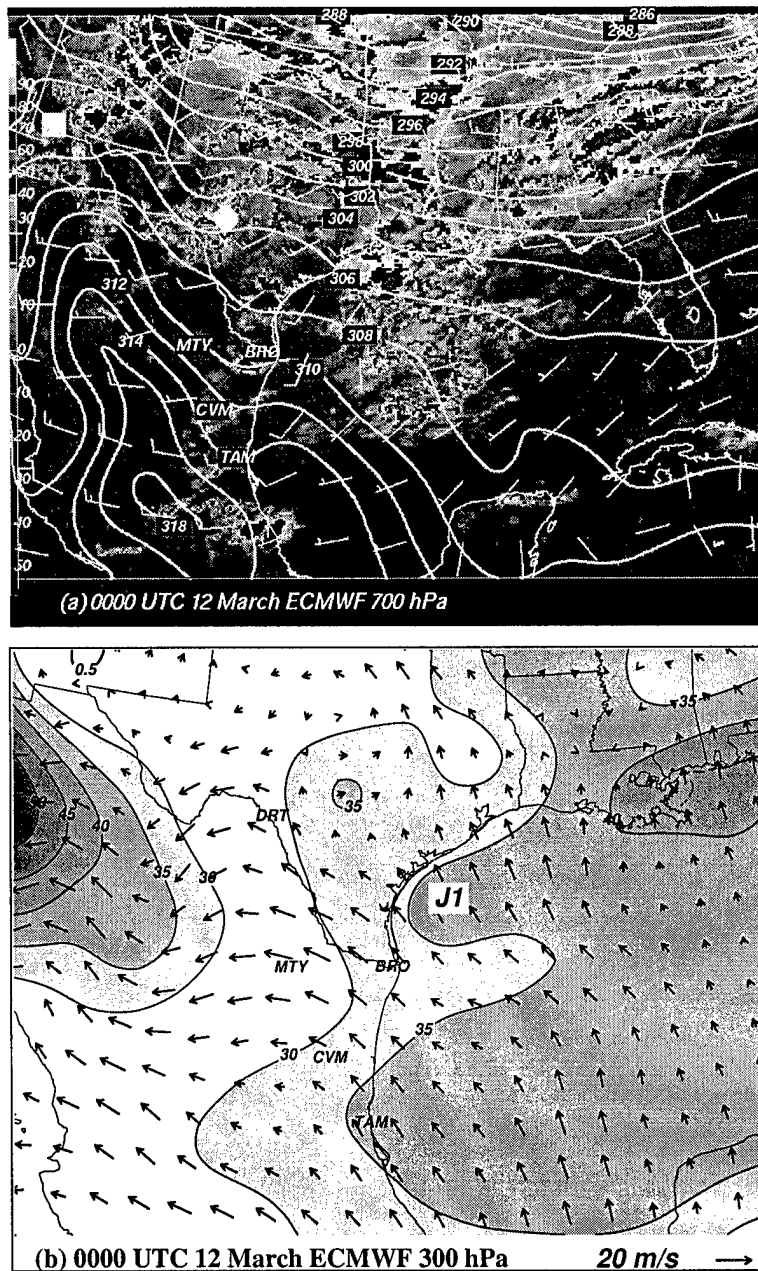


Figure 3.3: Observation analyses valid 0000 UTC 12 March, depicted are (a) ECMWF 700 hPa analysis, potential temperature contoured every 2 K and standard wind vectors in  $\text{m s}^{-1}$ , with GOES-7 IR imagery, and (b) ECMWF 300 hPa analysis, ageostrophic wind vectors (reference vector in lower right) and total wind isotachs contoured and shaded over  $35 \text{ m s}^{-1}$ ; horizontal divergence contoured every  $0.5 \times 10^{-4} \text{ s}^{-1}$  with heavy lines.

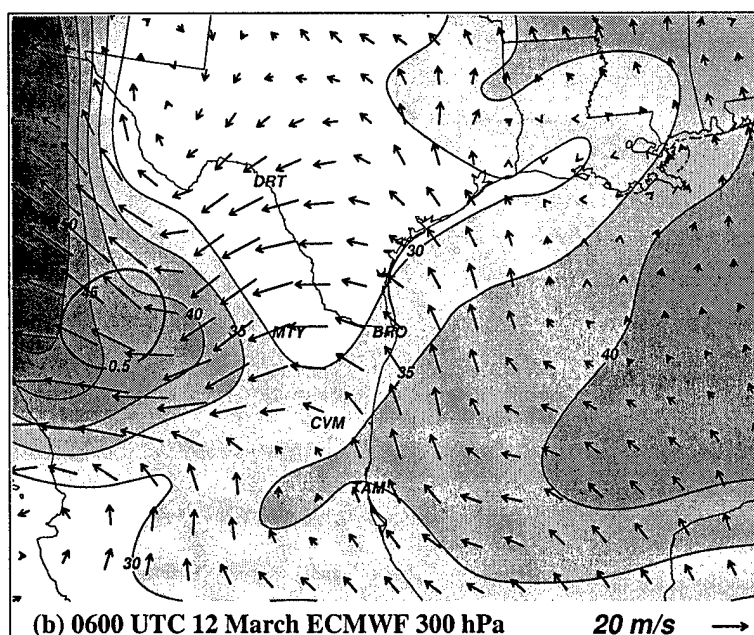


Figure 3.4: As in Fig. 3.3 except for 0600 UTC 12 March.

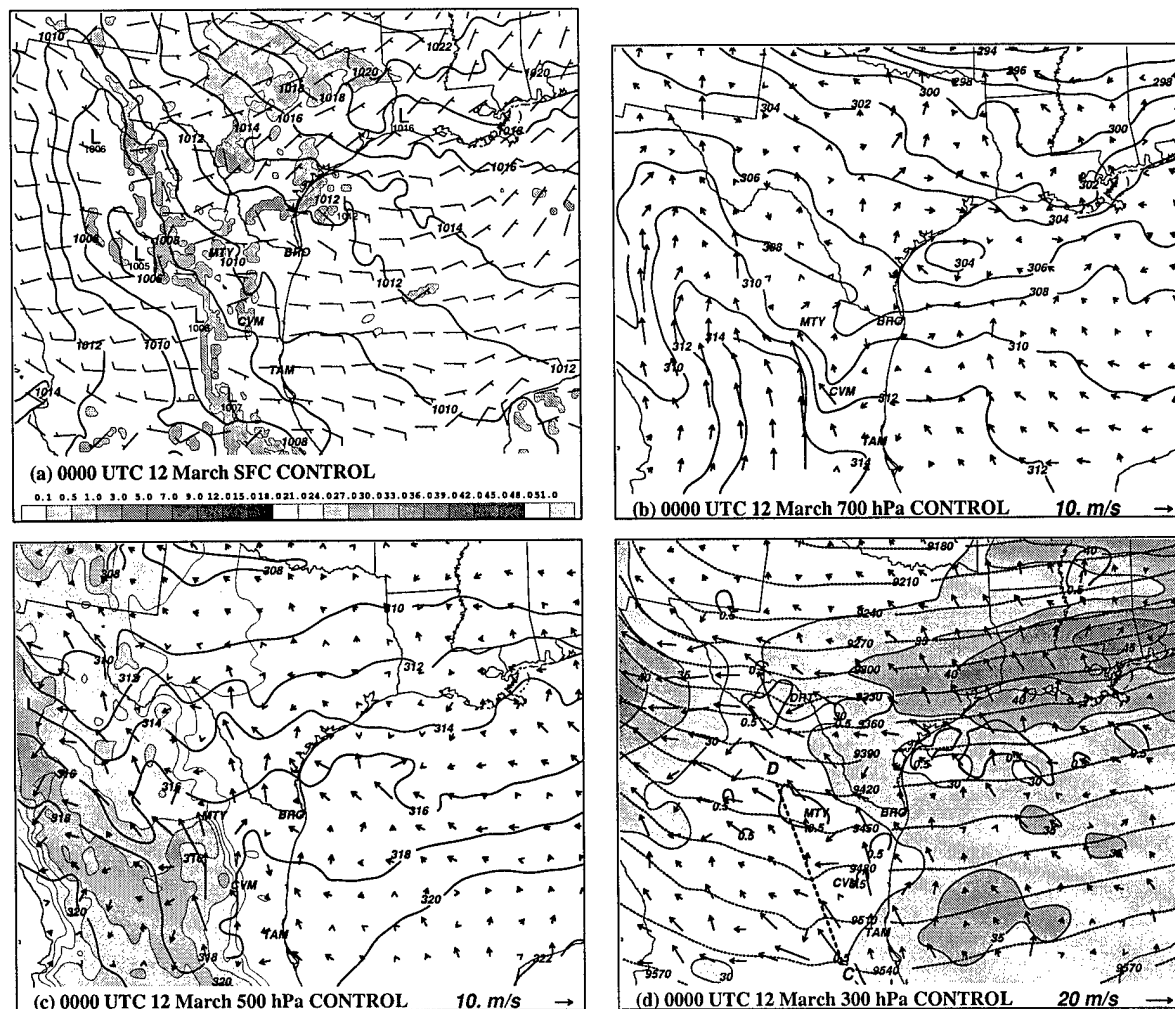


Figure 3.5: CONTROL simulation fields valid 0000 UTC 12 March. Depicted are (a) Mean sea-level pressure (PMSL) contoured every 2 hPa, surface wind vectors ( $\text{m s}^{-1}$ ) and simulated hourly precipitation ( $\text{mm h}^{-1}$ ); (b) 700 hPa potential temperature contoured every 2 K and ageostrophic wind vectors; (c) 500 hPa potential temperature contoured every 2 K, ageostrophic wind vectors, and terrain shaded every 500 m; (d) 300 hPa isotachs (shaded  $> 35 \text{ m s}^{-1}$ ), geopotential height contoured with dashed lines every 30 m, horizontal divergence contoured in heavy black lines contoured at  $0.5 \times 10^{-4} \text{ s}^{-1}$  and every  $1.0 \times 10^{-4} \text{ s}^{-1}$  thereafter. Reference vectors for ageostrophic wind plots are in the lower right corner of the respective panels.

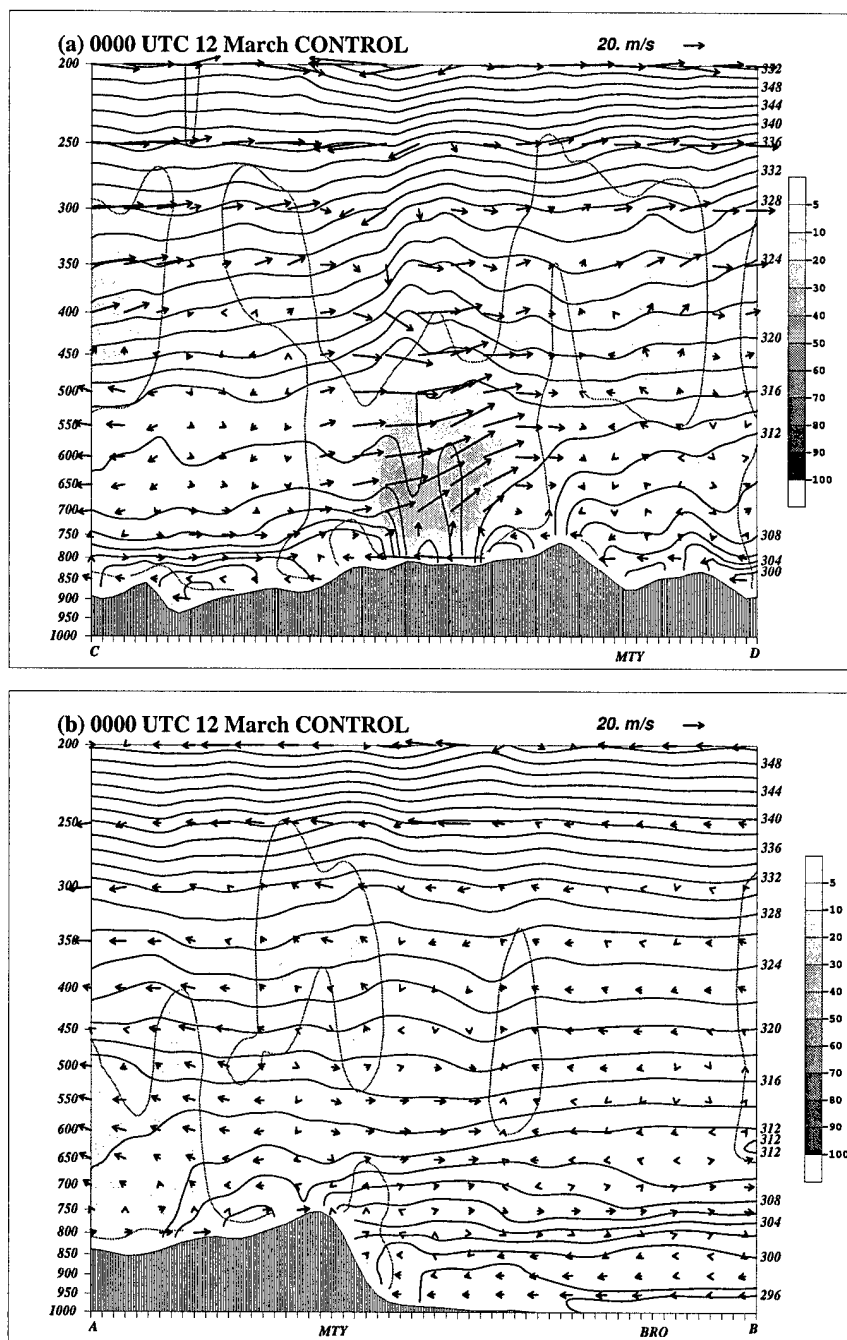


Figure 3.6: CONTROL simulation cross-sections valid 0000 UTC 12 March oriented (a) approximately parallel to the Sierra Madres (along MPS) and (b) normal to the Sierra Madres. Depicted are isentropes contoured every 2 K, ageostrophic circulation vectors, and vertical velocity shaded every  $-5 \mu\text{bar s}^{-1}$ . Planes of the cross-sections are indicated in Fig. 3.5d, and 3.7d.

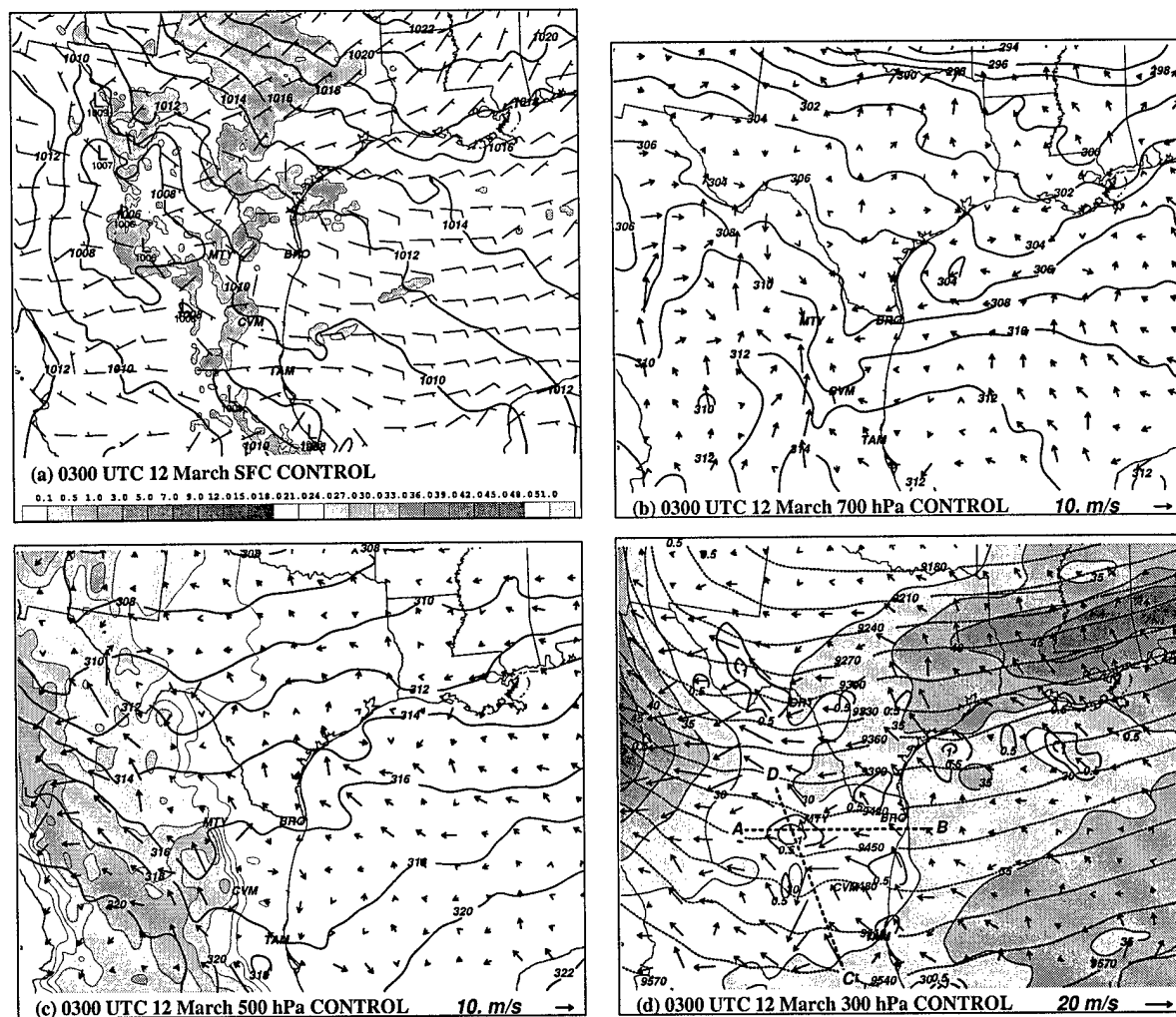


Figure 3.7: As in Fig. 3.5, except for 0300 UTC 12 March.

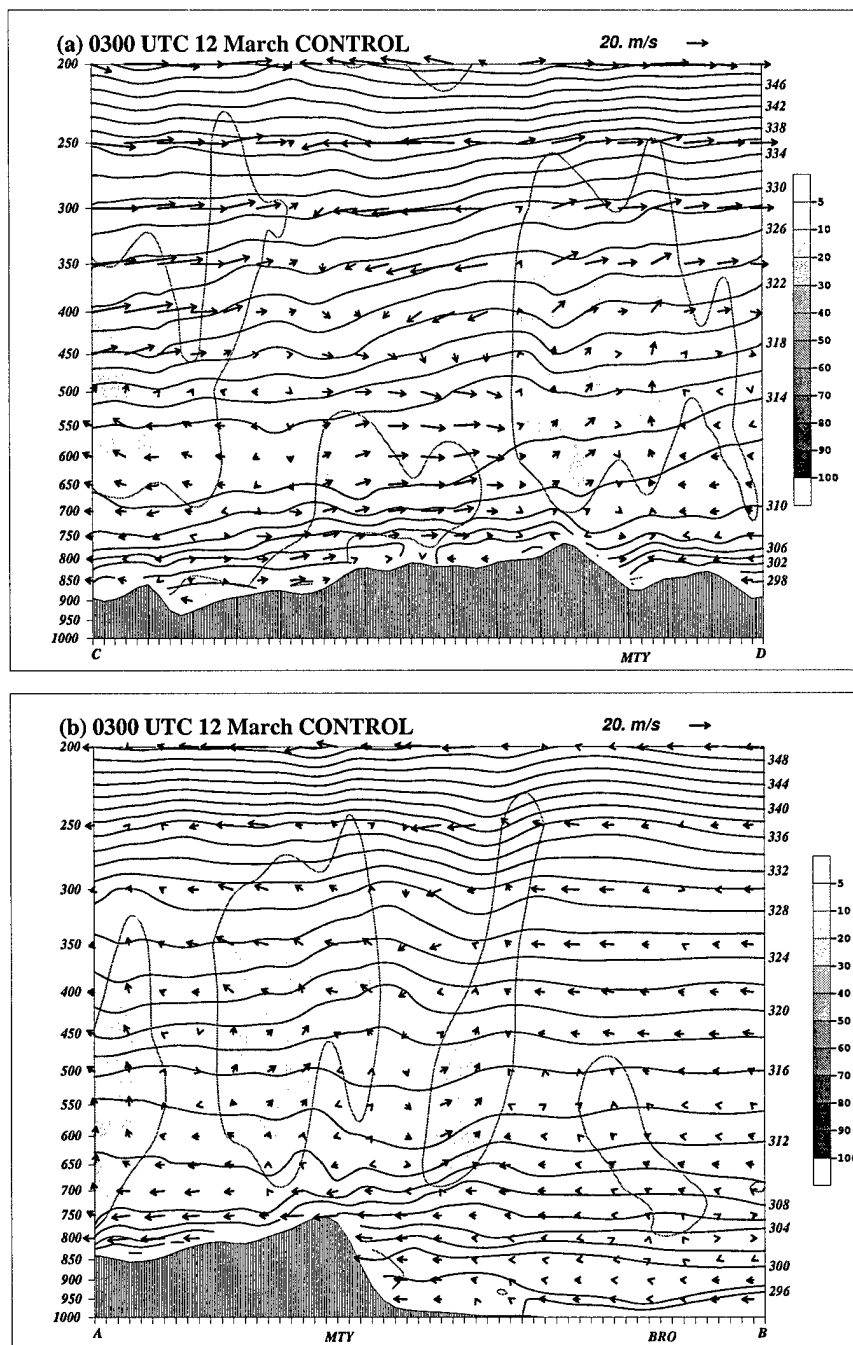


Figure 3.8: CONTROL simulation cross-sections valid 0300 UTC 12 March oriented (a) approximately parallel to the Sierra Madres (along MPS) and (b) normal to the Sierra Madres, parameters as in Fig. 3.6. Planes of the cross-sections are indicated in Fig. 3.7d.

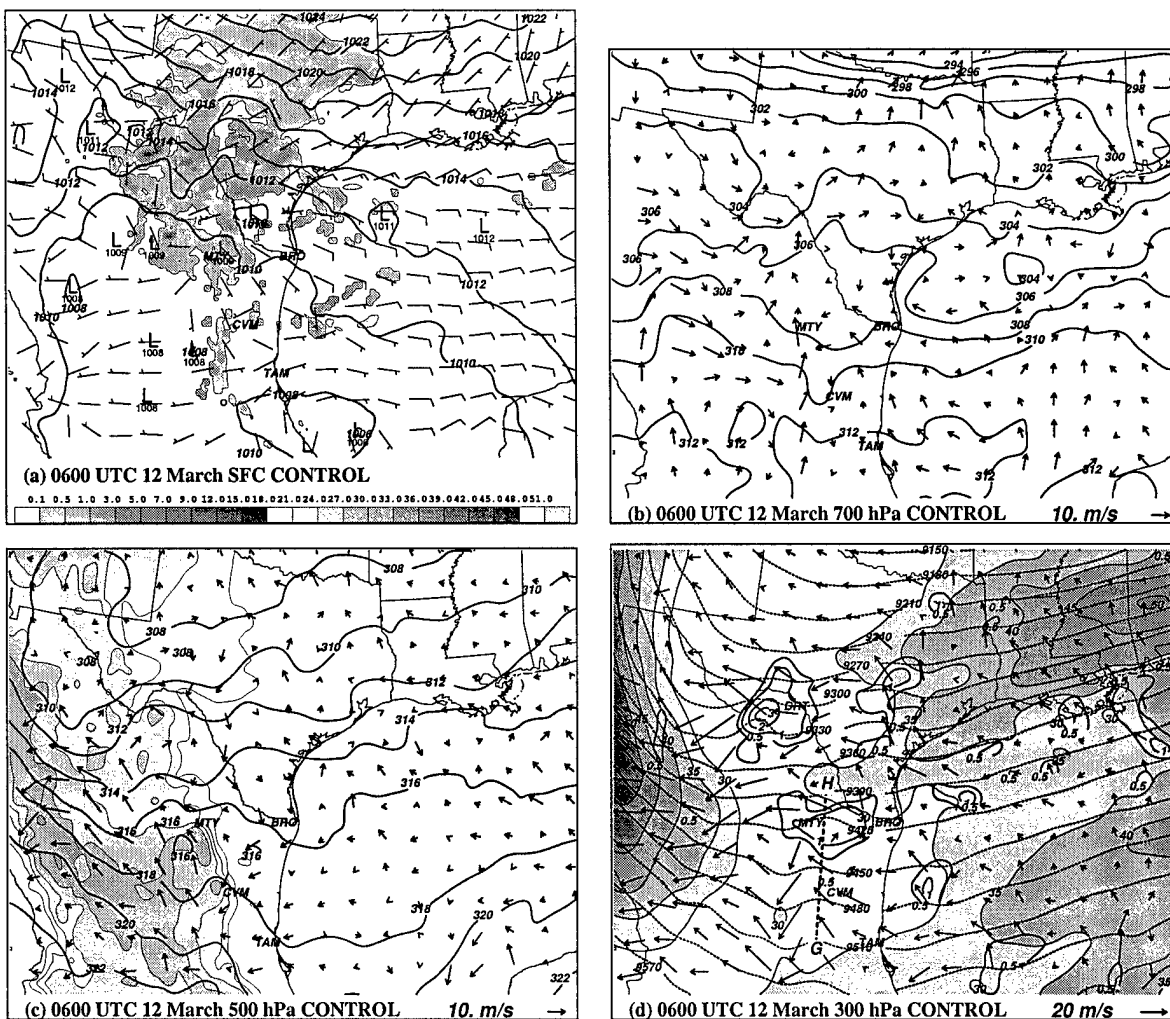


Figure 3.9: As in Fig. 3.5, except for 0600 UTC 12 March.



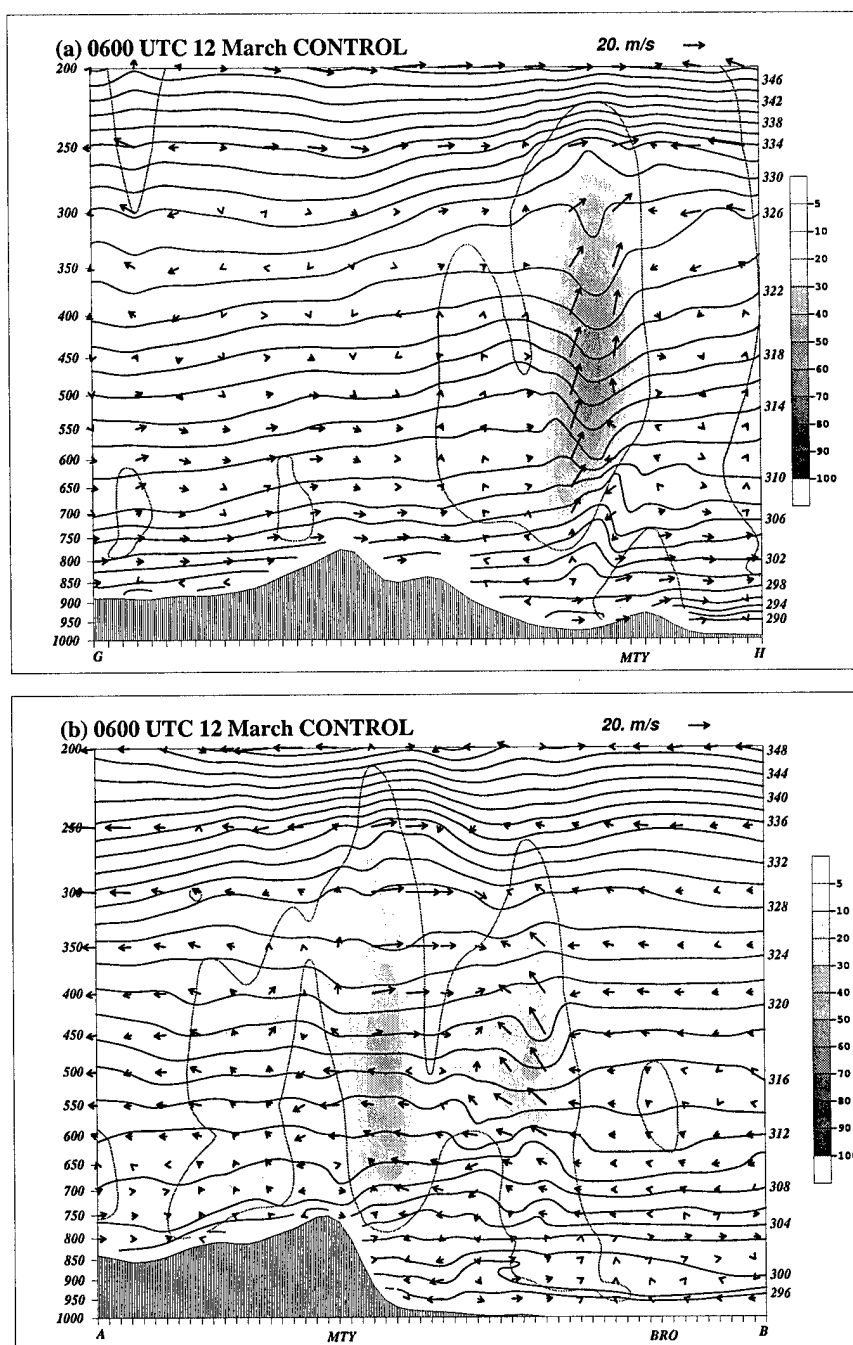


Figure 3.10: CONTROL simulation cross-sections valid 0600 UTC 12 March oriented (a) approximately parallel to the Sierra Madres (along MPS) and (b) normal to the Sierra Madres, parameters as in Fig. 3.6. Planes of the cross-sections are indicated in Fig. 3.7d and 3.9d.

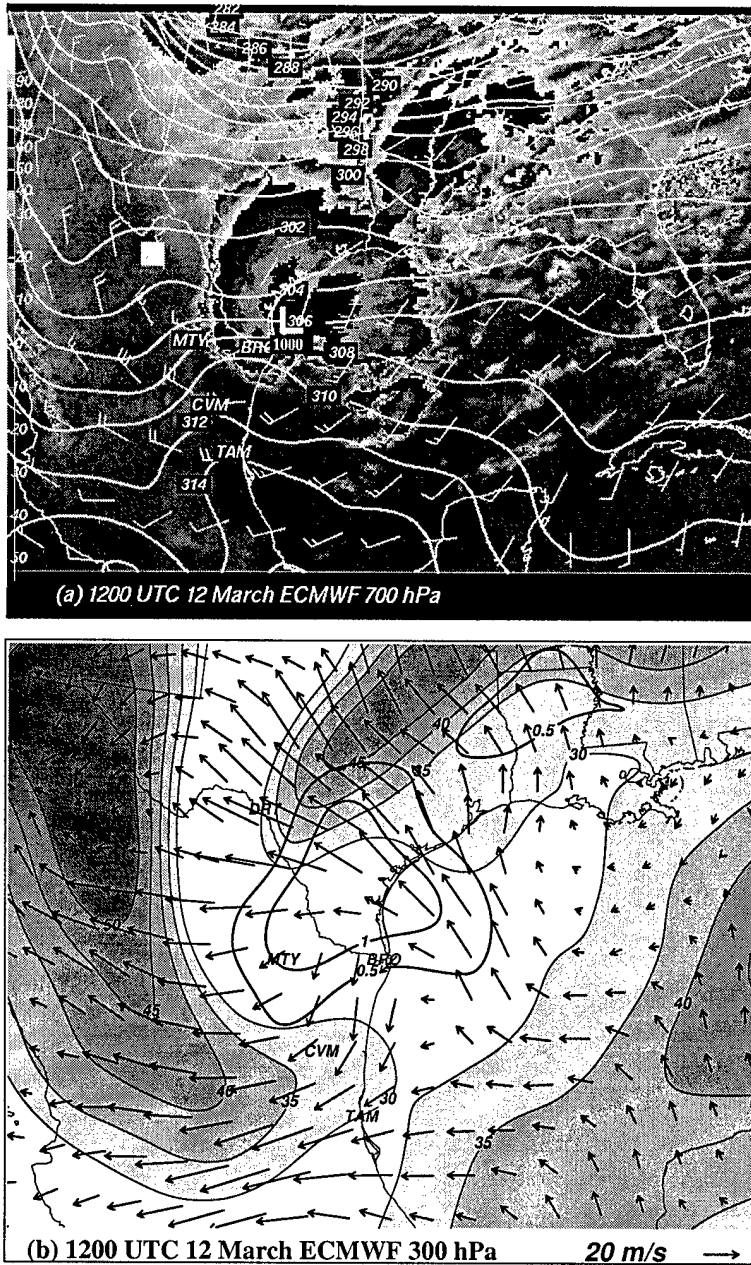


Figure 3.11: Same as Fig. 3.3 except for 1200 UTC 12 March.

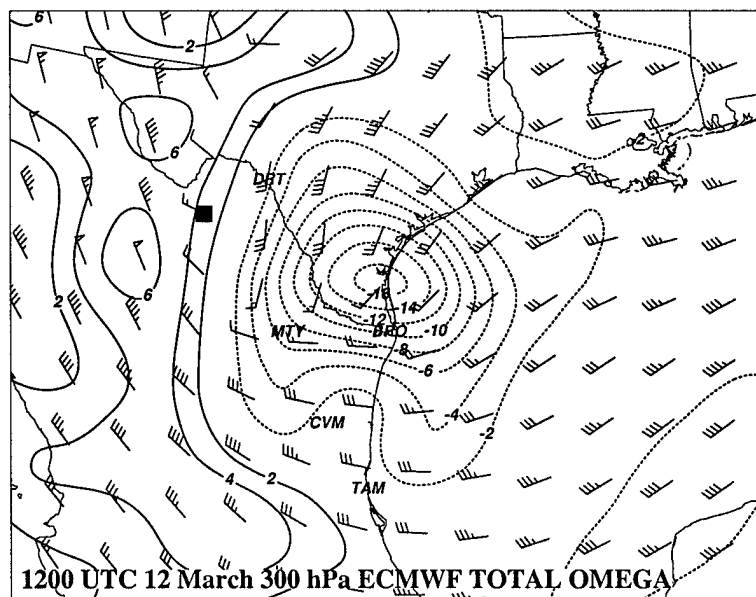


Figure 3.12: ECMWF 300 hPa analysis of vertical velocity, contoured every  $1 \mu\text{bar s}^{-1}$  (negative or ascent is dashed), valid 1200 UTC 12 March. Also depicted are standard wind vectors in  $\text{m s}^{-1}$ .

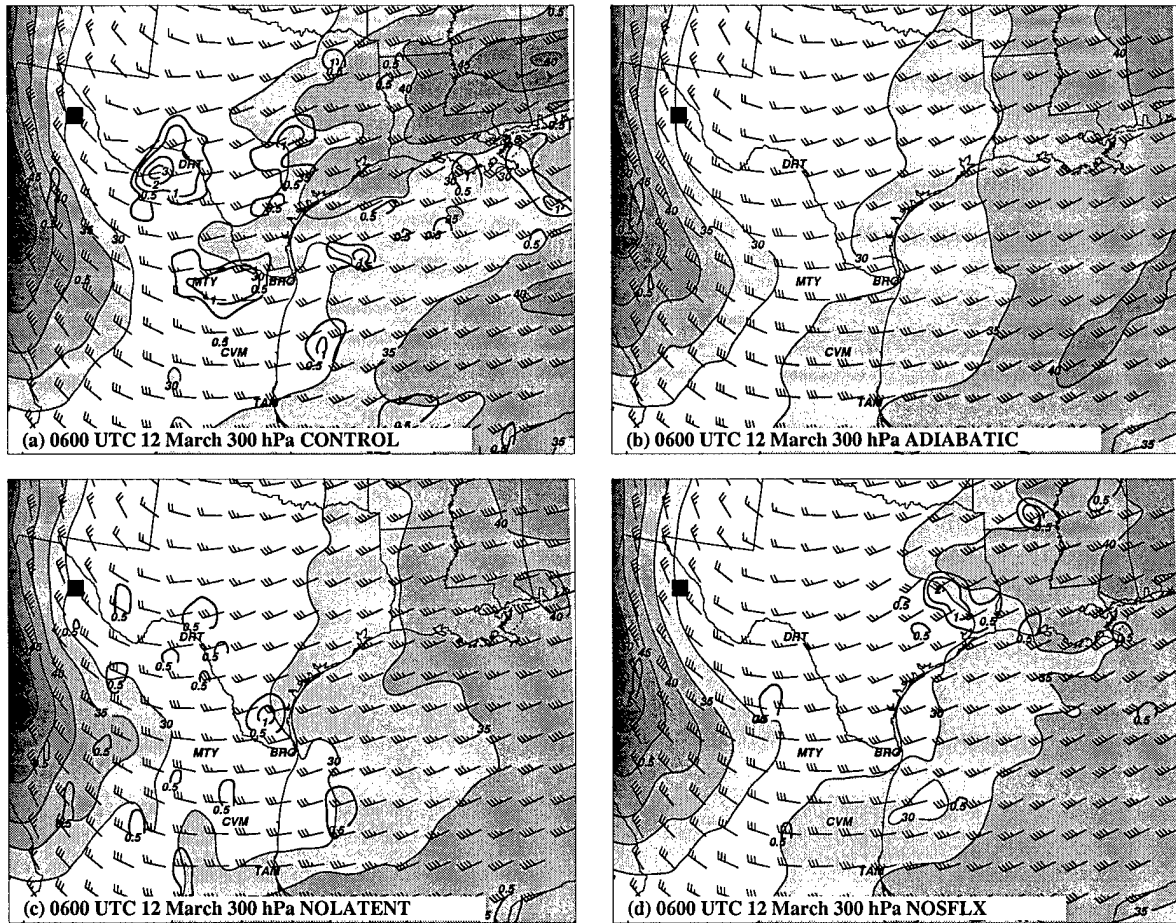


Figure 3.13: Comparison of 300 hPa simulation results, valid 0600 UTC 12 March. Depicted are standard wind vectors ( $\text{m s}^{-1}$ ), isotachs (shaded  $> 35 \text{ m s}^{-1}$ ), and divergence (thick solid lines at  $0.5 \times 10^{-4} \text{ s}^{-1}$  and every  $1.0 \times 10^{-4} \text{ s}^{-1}$  thereafter), from the (a) CONTROL, (b) ADIABATIC, (c) NOLATENT, and (d) NOSFLX simulations.

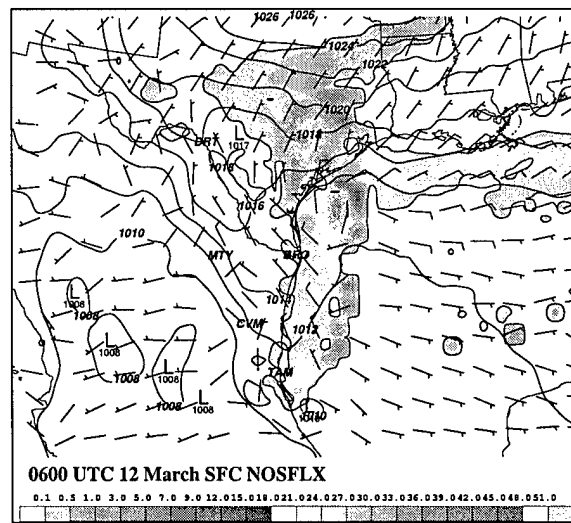


Figure 3.14: NOSFLX simulation at 0600 UTC 12 March, mean sea-level pressure (PMSL) contoured every 2 hPa, surface wind vectors ( $\text{m s}^{-1}$ ) and simulated hourly precipitation ( $\text{mm h}^{-1}$ ).

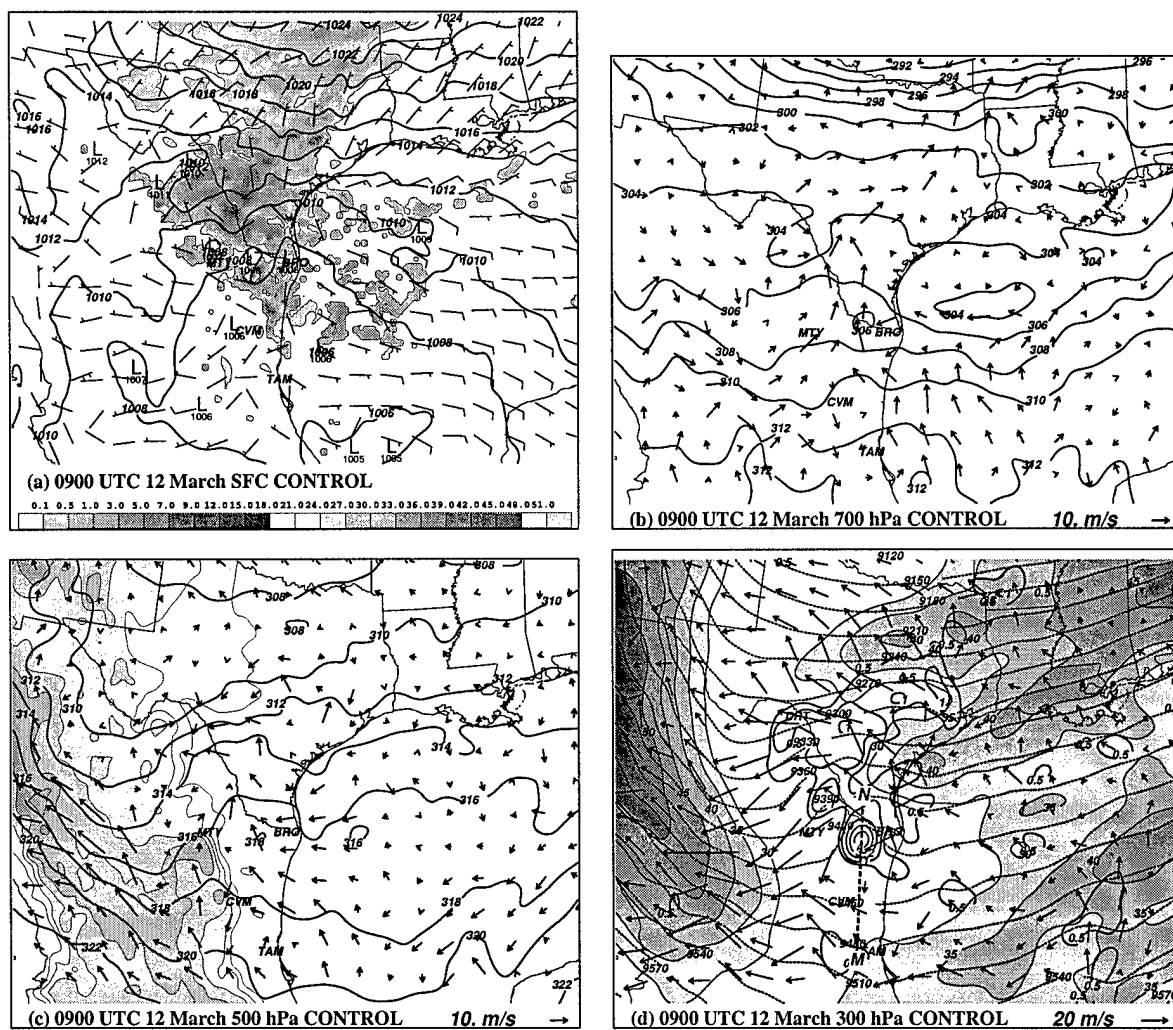


Figure 3.15: As in Fig. 3.5, except for 0900 UTC 12 March.

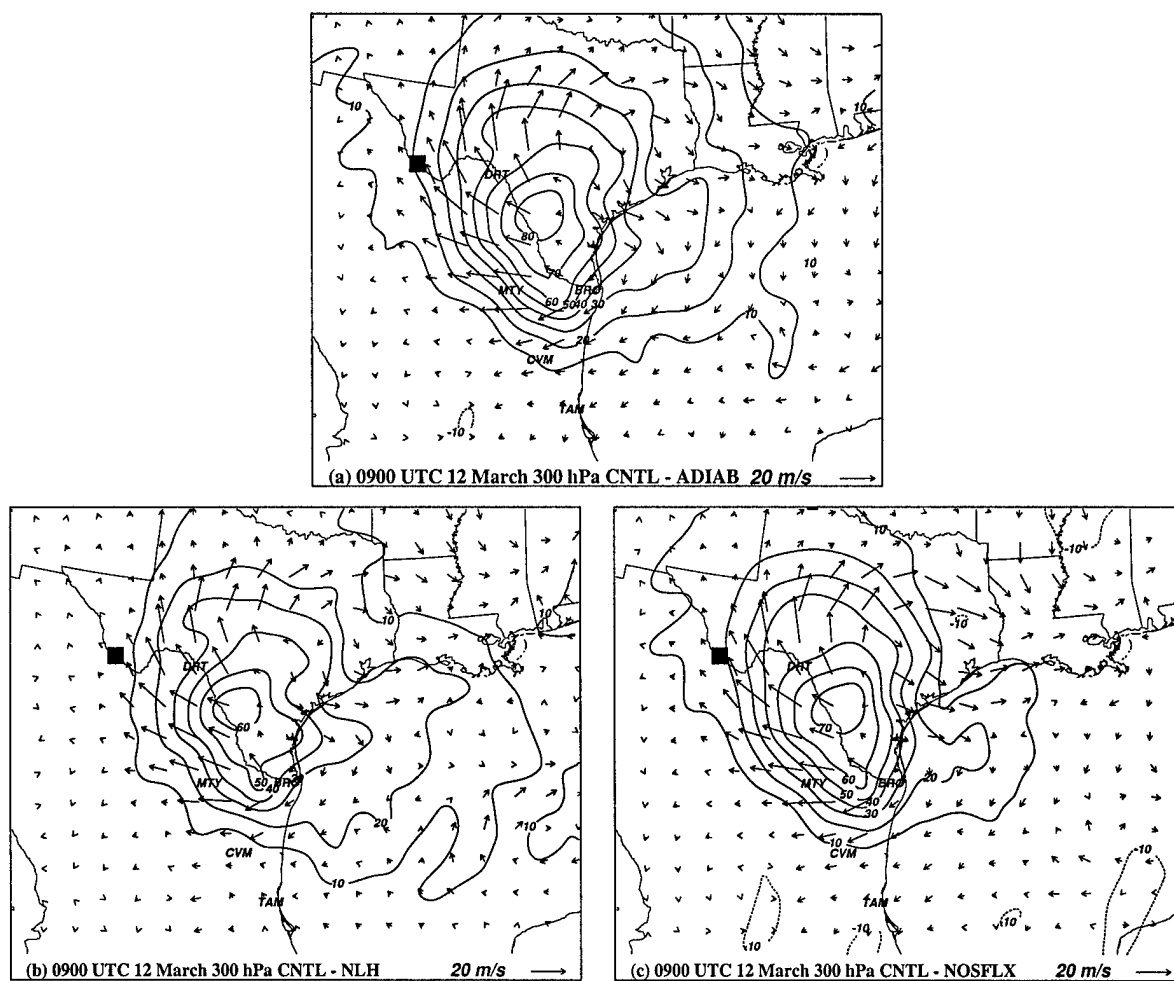


Figure 3.16: 0900 UTC 12 March 300 hPa difference fields between the CONTROL simulation and (a) ADIABATIC simulation, (b) NOLATENT simulation, and (c) NOSFLX simulation. Depicted are the vector difference in the total wind field (reference vector lower right corner of each panel) and difference in geopotential height field contoured every 10 m (negative dashed).

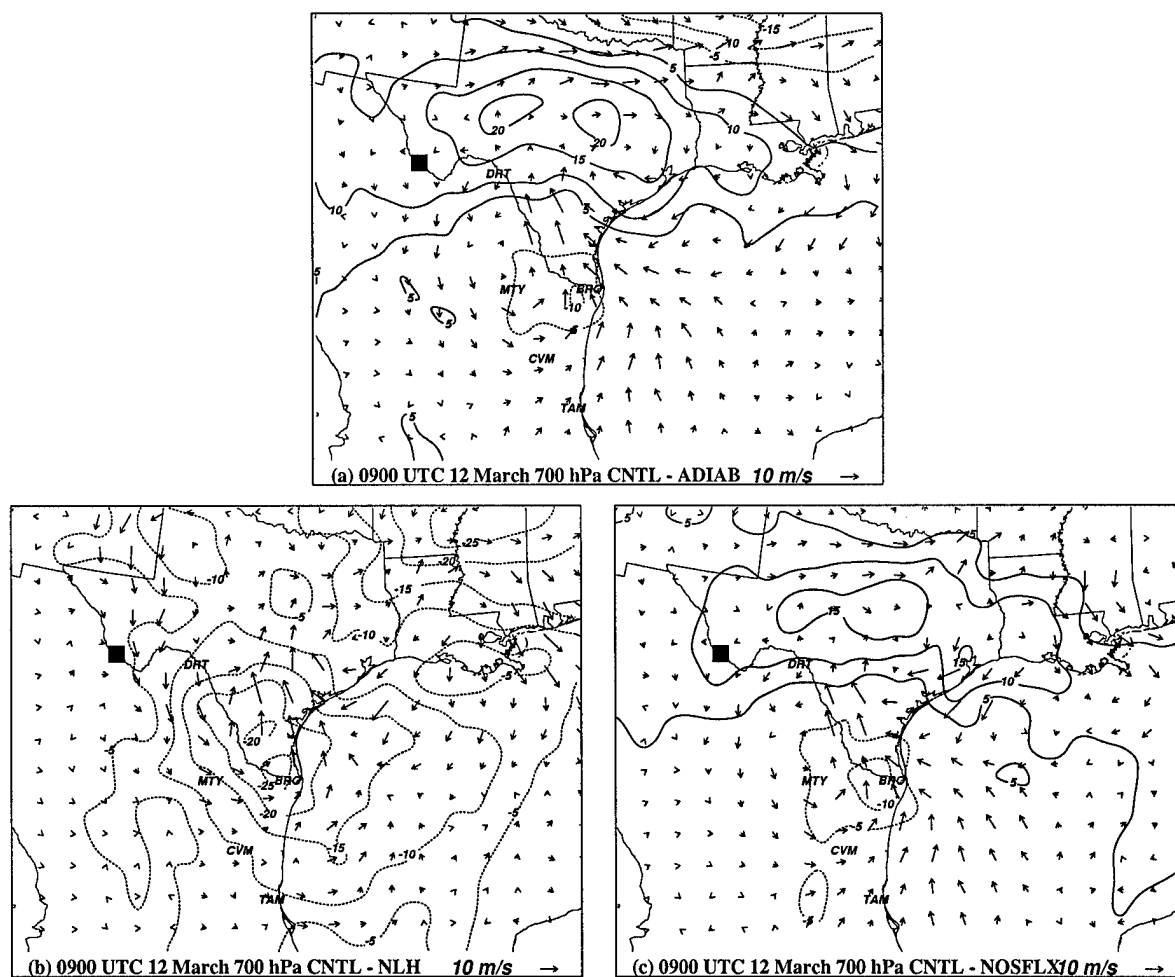


Figure 3.17: 0900 UTC 12 March 700 hPa difference fields between the CONTROL simulation and (a) ADIABATIC simulation, (b) NOLATENT simulation, and (c) NOSFLX simulation. Depicted are the vector difference in the total wind field (reference vector lower right corner of each panel) and difference in geopotential height field contoured every 5 m (negative dashed).



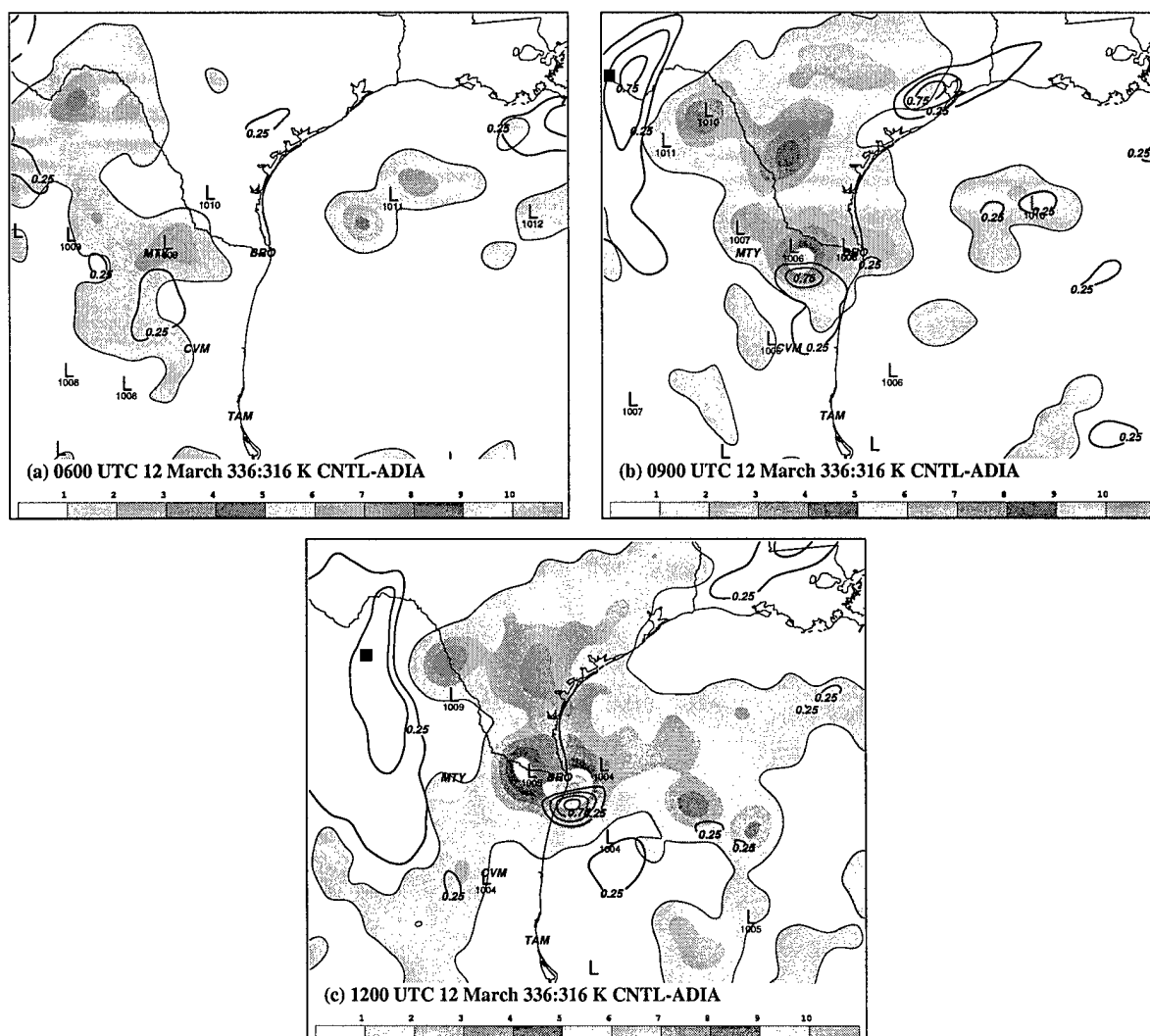


Figure 3.18: Isentropic potential vorticity difference fields, CONTROL - ADIABATIC, in the column from 336 K to 316 K, contoured every 0.25 PVU; and Lagrangian Rossby number ( $Ro$ ) from the CONTROL simulation at 326 K, valid (a) 0600 UTC, (b) 0900 UTC, and (c) 1200 UTC 12 March. Also shown are surface pressure centers from the CONTROL PMSL field. Positions of Bosart et al. (1996) PV anomaly C are indicated by the filled square.

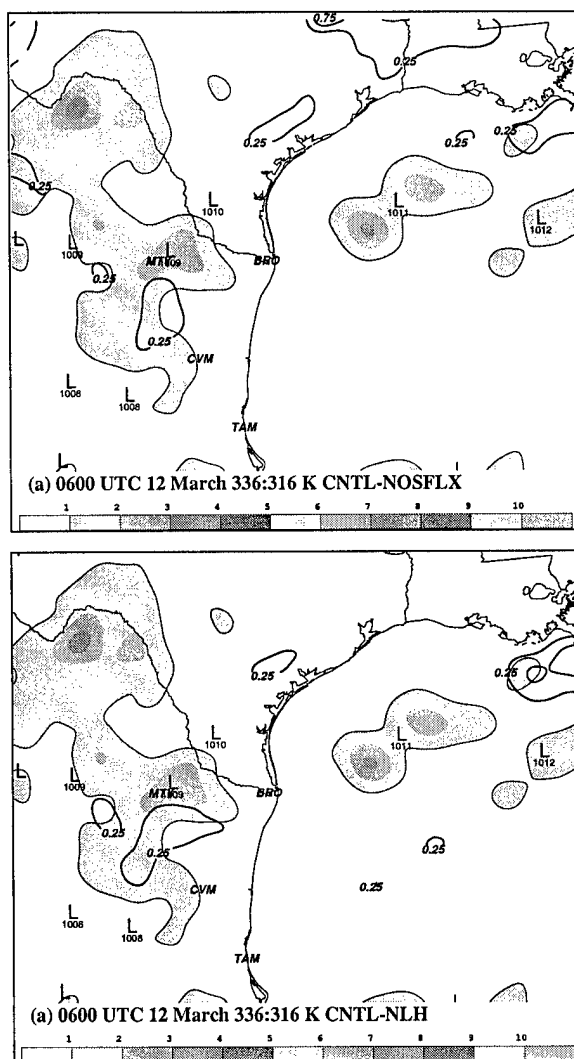


Figure 3.19: Isentropic potential vorticity difference fields, in the column from 336 K to 316 K, contoured every 0.25 PVU; and Lagrangian Rossby number ( $Ro$ ) from the CONTROL simulation at 326 K, valid 0600 UTC 12 March for the (a) CONTROL - NOSFLX and (b) CONTROL - NOLATENT. Also shown are surface pressure centers from the CONTROL PMSL field. Positions of Bosart et al. (1996) PV anomaly C are indicated by the filled square.



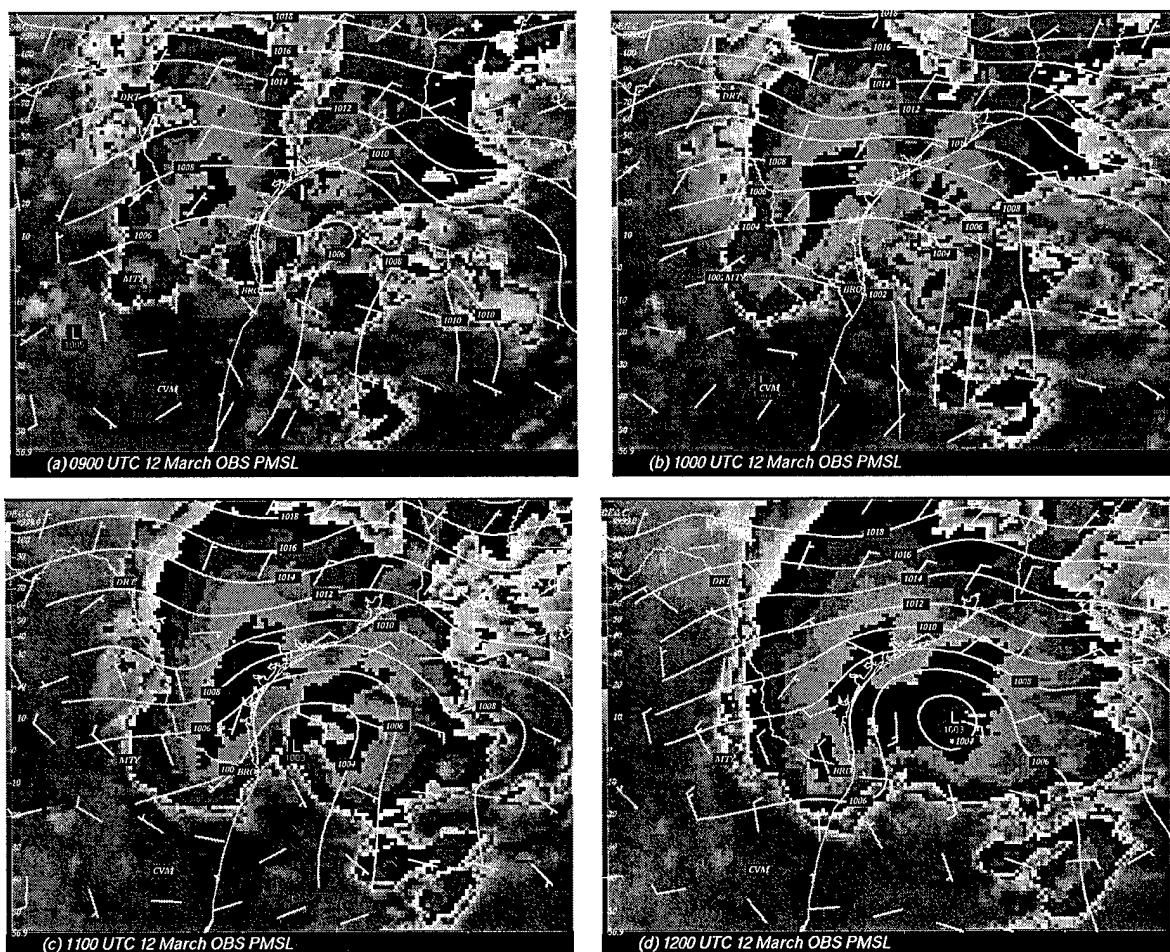


Figure 3.21: GOES-7 satellite imagery and a Barnes objective analysis of available PMSL (contoured every 2 hPa) and wind data (standard wind vectors in  $\text{m s}^{-1}$ ), valid (a) 0900, (b) 1000, (c) 1100, and (d) 1200 UTC 12 March.

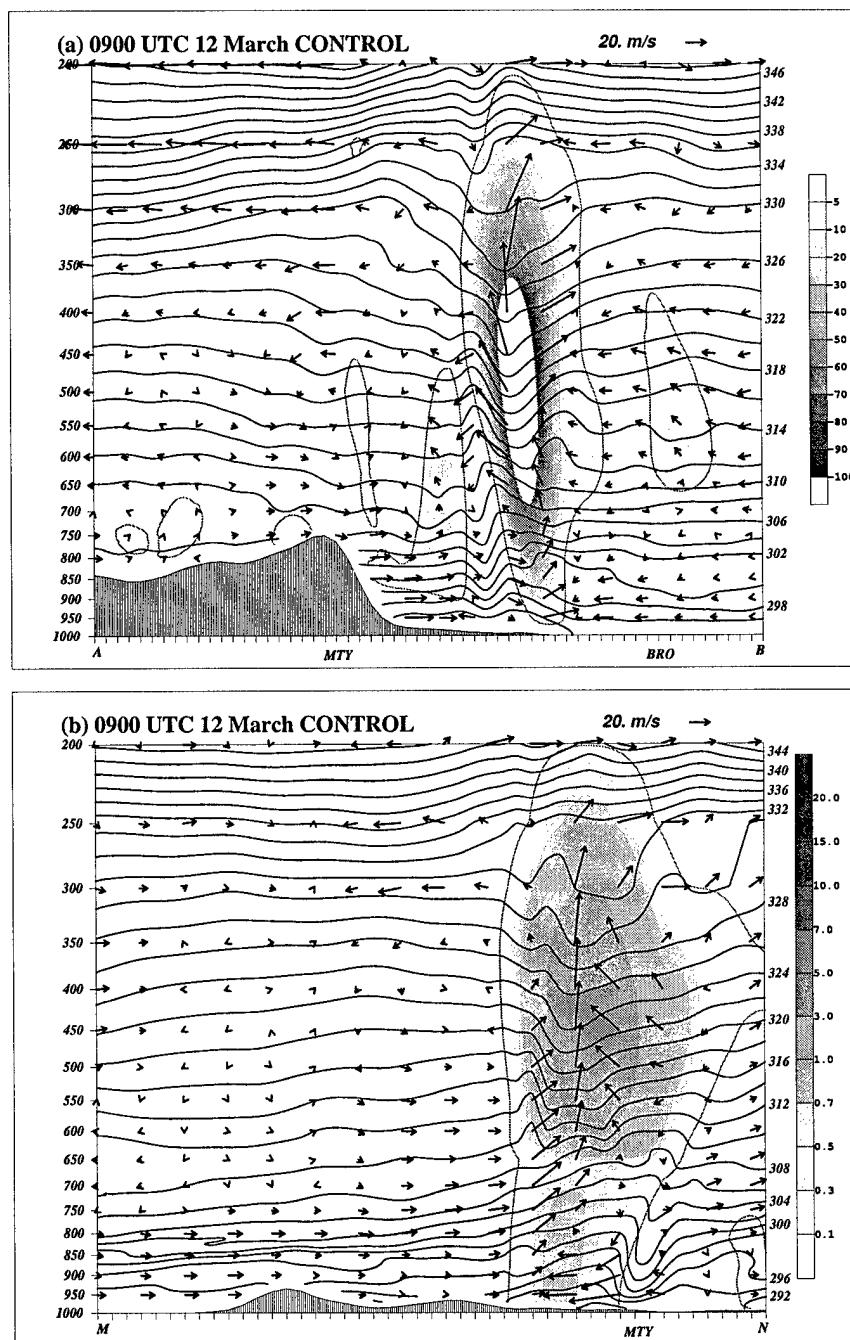


Figure 3.22: CONTROL simulation cross-sections at 0900 UTC 12 March, (a) west to east, plane indicated in Fig. 3.7d, depicting isentropes contoured every 2 K, ageostrophic circulation vectors, and vertical velocity shaded every  $-5 \mu\text{bar s}^{-1}$ , (b) south to north, plane indicated in Fig. 3.15d, depicting isentropes and circulation vectors as in (a), with rain water mixing ratio (shaded in  $\text{g kg}^{-1}$ ). Positions of MTY and BRO are indicated; for (b), MTY and BRO are projected into the same position in the south-north plane.

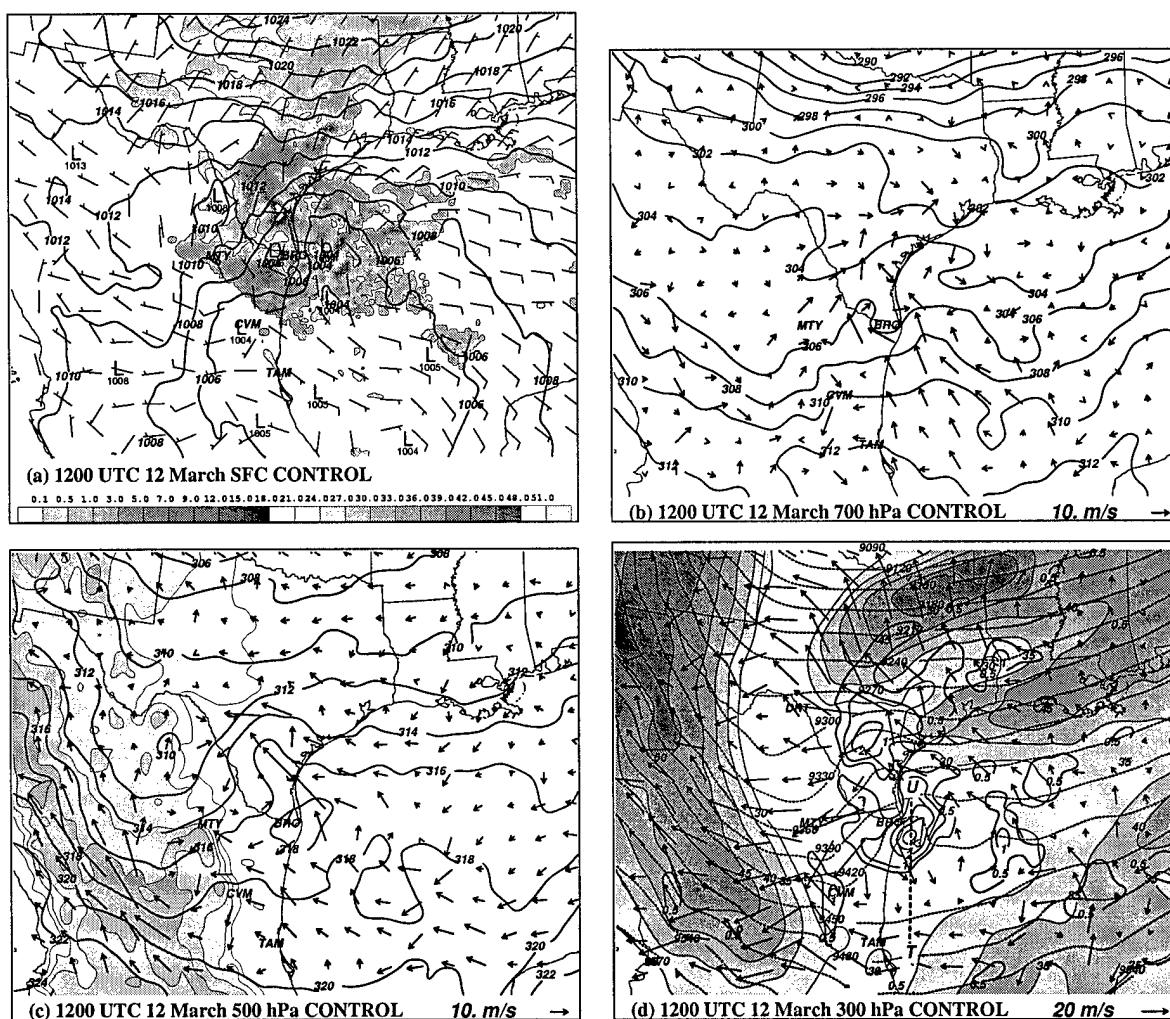


Figure 3.23: CONTROL simulation fields, as in Fig. 3.5, valid 1200 UTC 12 March.

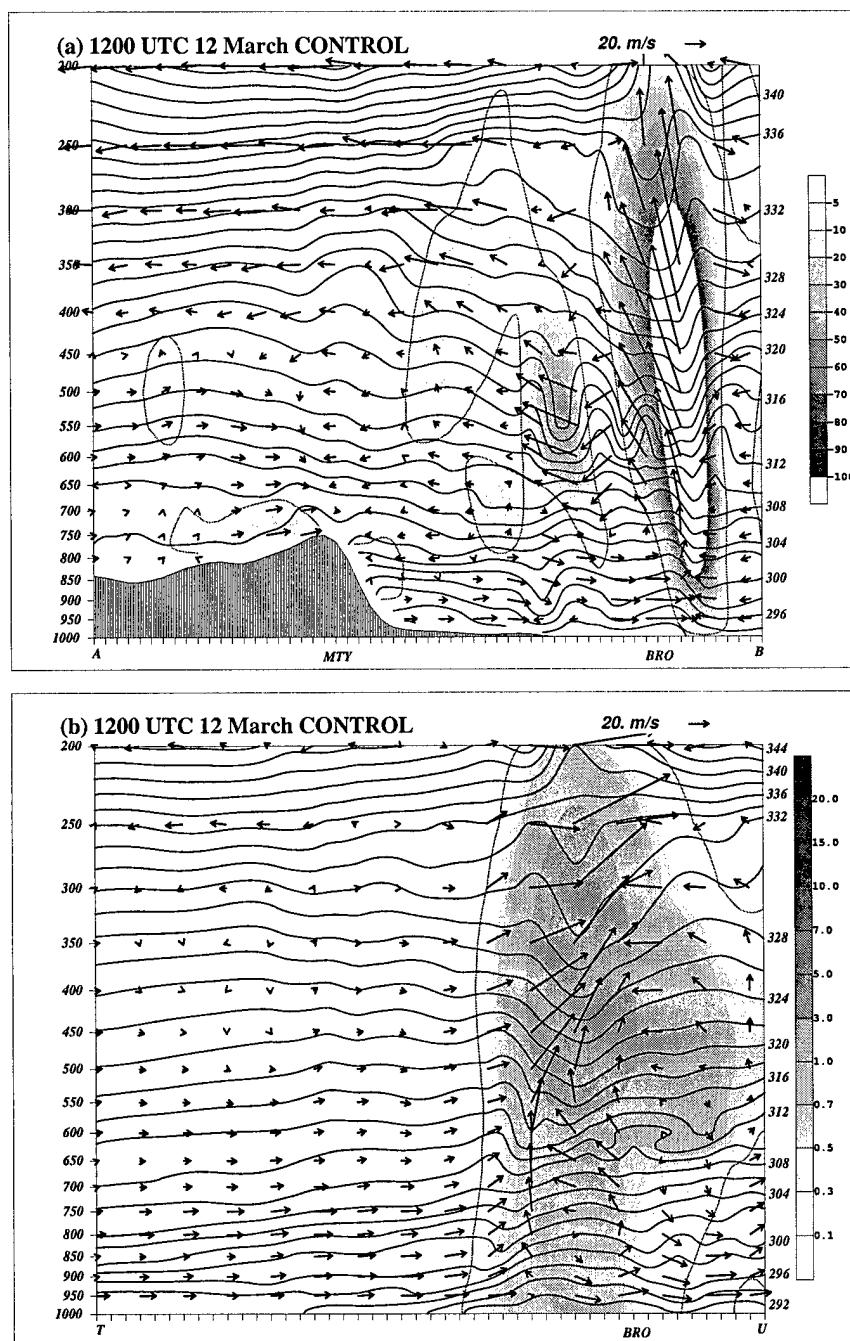


Figure 3.24: CONTROL simulation cross-sections at 1200 UTC 12 March, as in Fig. 3.22. Plane of (a) is indicated in Fig. 3.7d, and plane of (b) is indicated in Fig. 3.23d. The positions of MTY and BRO relative to the plane of the cross-section are indicated.

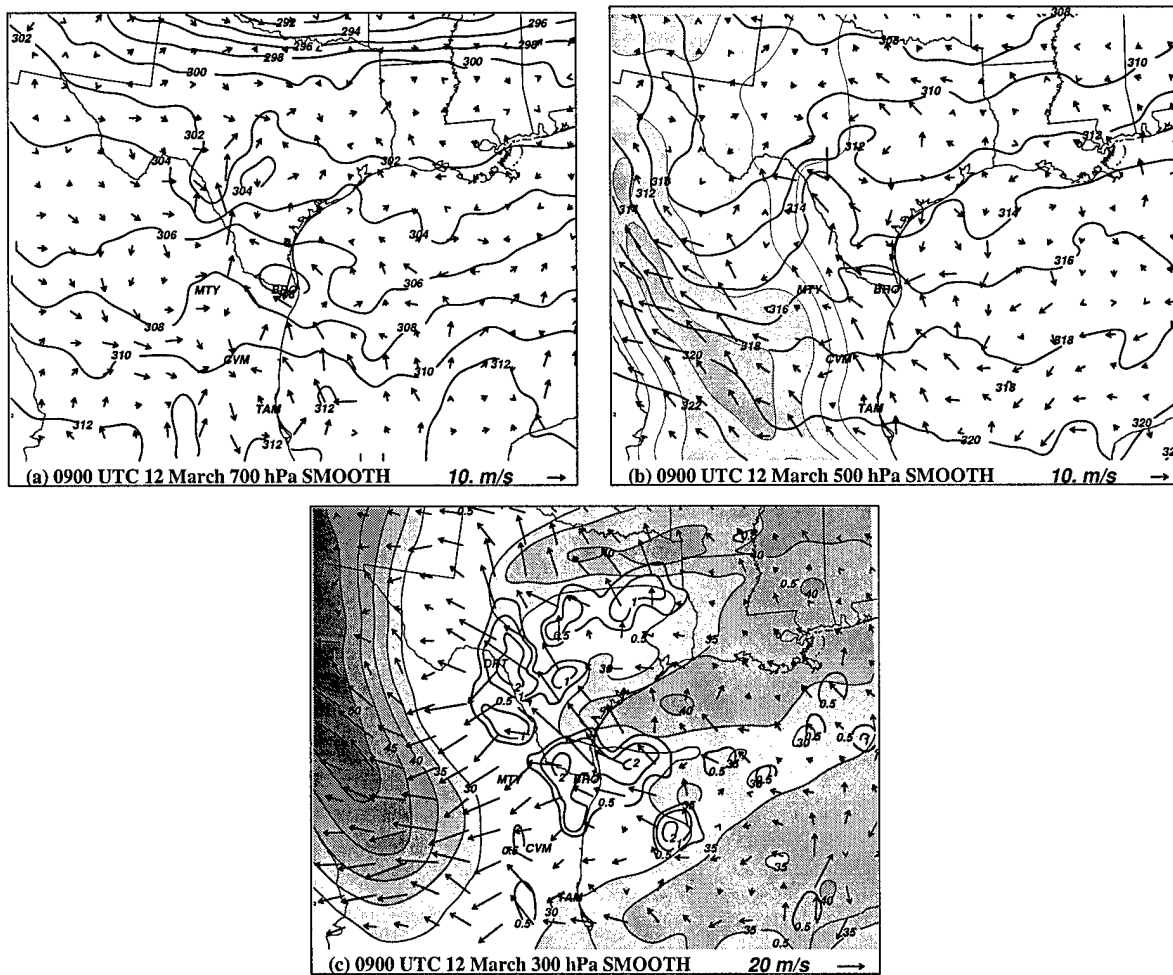


Figure 3.25: SMOOTH simulation comparisons at 0900 UTC 12 March, (a) 700 hPa potential temperature contoured every 2 K and ageostrophic wind vectors; (b) 500 hPa potential temperature contoured every 2 K, ageostrophic wind vectors, and terrain shaded every 500 m; and (c) 300 hPa isotachs (shaded  $> 35 \text{ m s}^{-1}$ ), geopotential height contoured with dashed lines every 30 m, horizontal divergence contoured in heavy black lines contoured at  $0.5 \times 10^{-4} \text{ s}^{-1}$  and every  $1.0 \times 10^{-4} \text{ s}^{-1}$  thereafter. Reference vectors for ageostrophic wind plots are in the lower right corner of the respective panels.



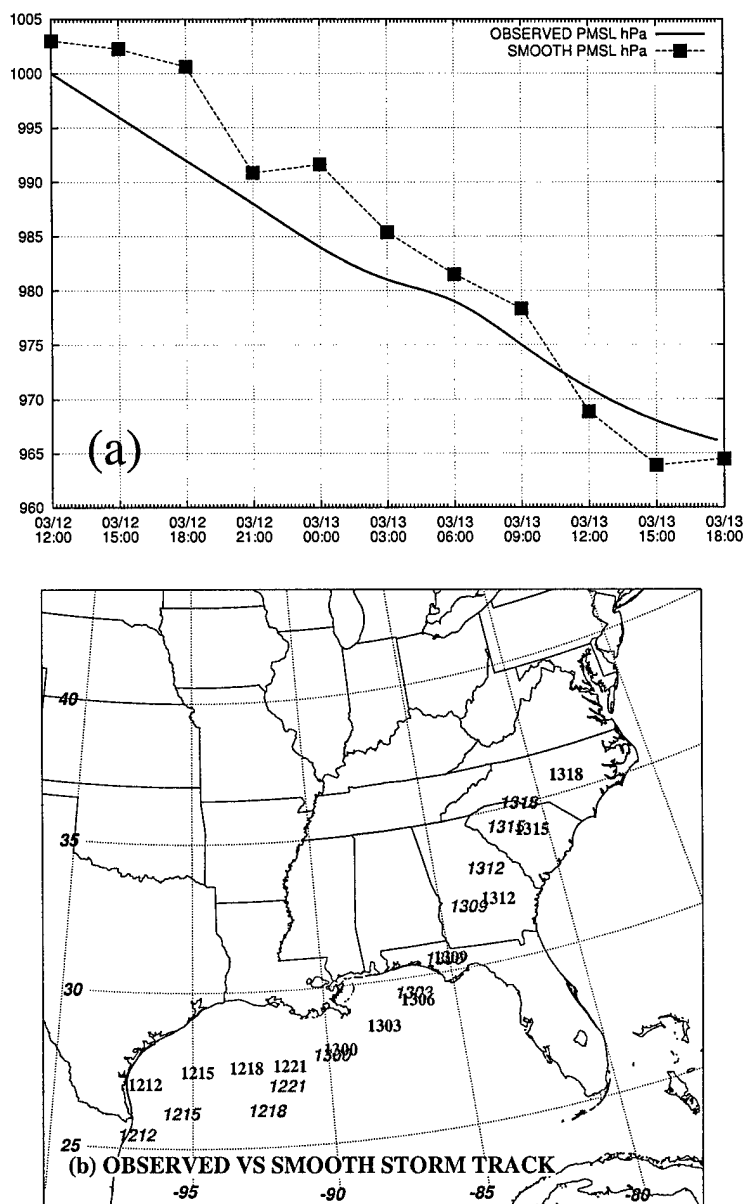


Figure 3.26: Verification of the SMOOTH simulation against the mesoanalysis of Kocin et al. (1995). Depicted are (a) storm central pressures and (b) storm track, indicating times (e.g. 1215 = 1500 UTC 12 March) and positions, observed track in normal black type, SMOOTH track in italicized dark gray type.

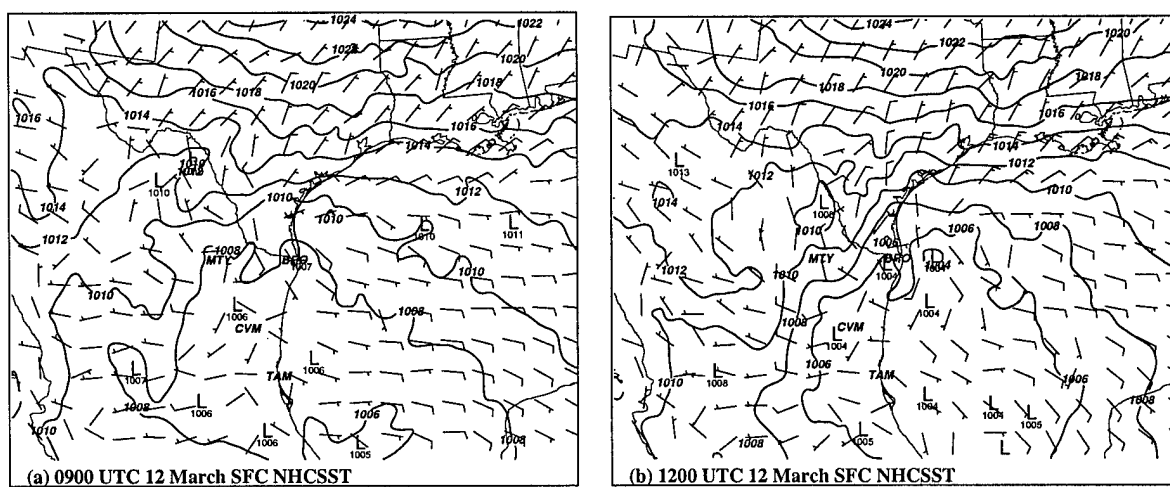


Figure 3.27: NHC SST simulation results, valid (a) 0900 UTC and (b) 1200 UTC 12 March. Depicted are PMSL contoured every 2 hPa and surface wind vectors in  $\text{m s}^{-1}$ .

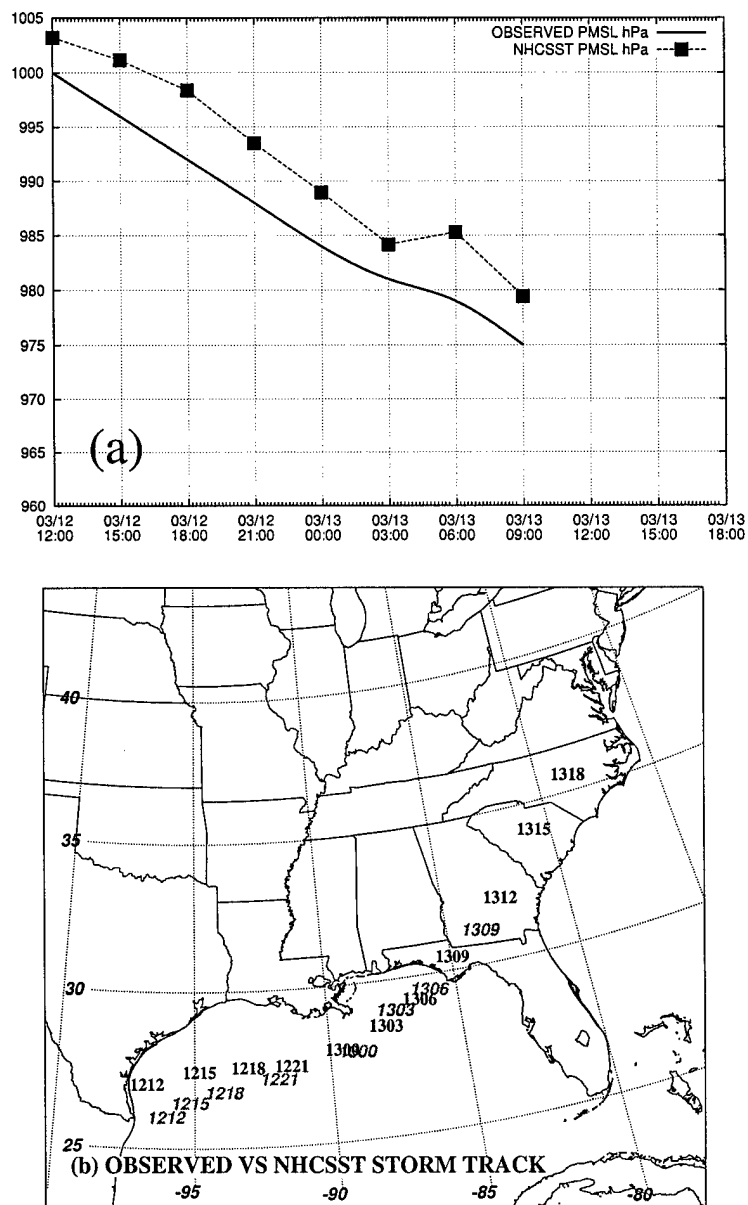


Figure 3.28: Verification of the NHCSST simulation against the mesoanalysis of Kocin et al. (1995), as in Fig. 3.26.

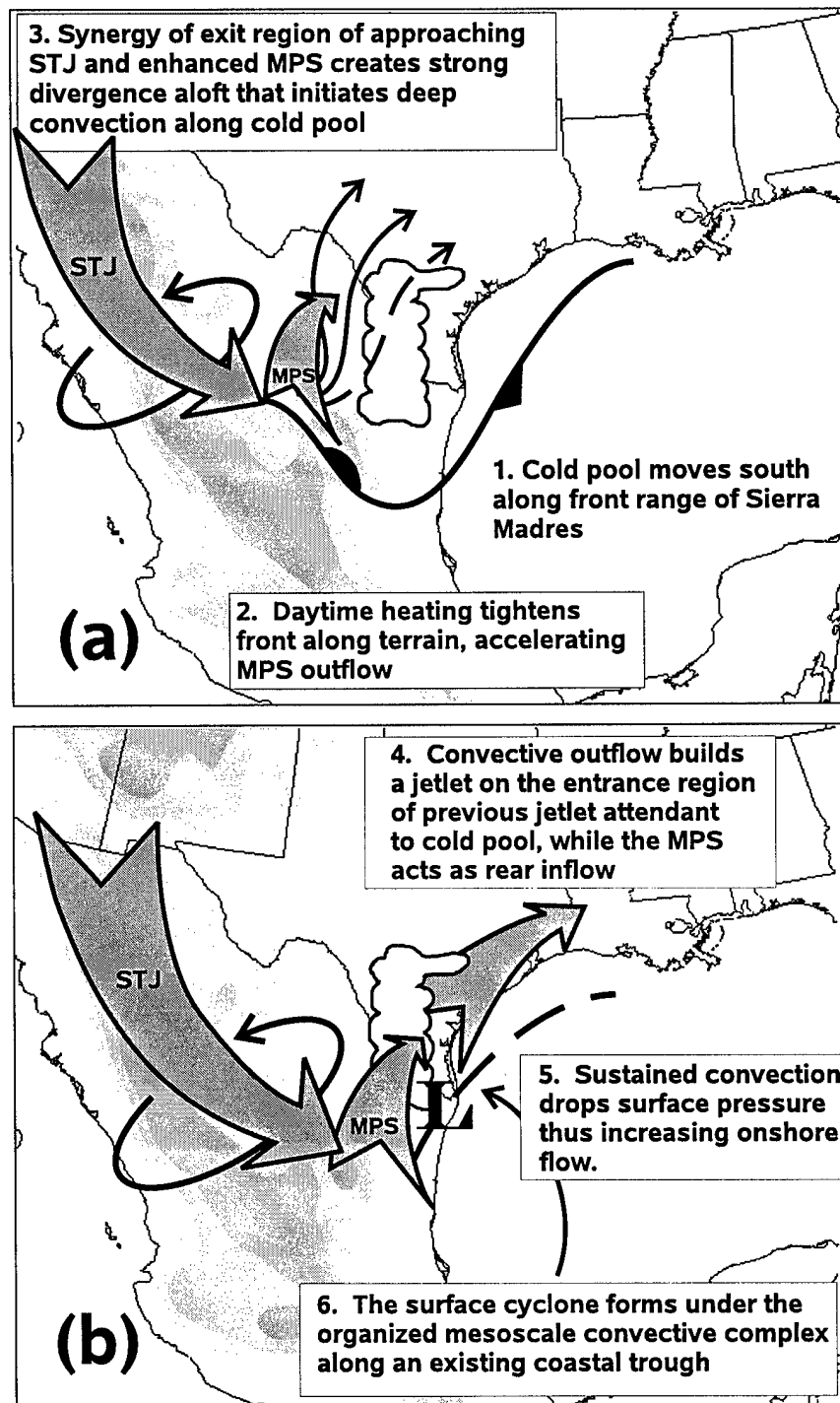


Figure 3.29: Schematic summarizing the sequence of events on 12 March that (a) initiates deep convection and (b) organizes the convection and upper-level flow, triggering surface cyclogenesis.

## Chapter 4

# The Mesoscale Evolution of the March 1993 Storm of the Century. Part III: Transition from warm-core to cold-core cyclogenesis

### 4.1 Introduction

The March 1993 Storm of the Century (SOC93) was initiated in the northwest Gulf of Mexico early on 12 March, diagnosed in the mesoanalysis of Kocin *et al.* (1995) as a 1000 hPa surface low (Fig. 4.1a). Over the next nine hours, the storm deepened by 12 hPa while moving eastward across the Gulf at about  $58 \text{ km h}^{-1}$  ( $16 \text{ m s}^{-1}$ ) (Fig. 4.1b). The paucity of observations over the Gulf coupled with poor model solutions at this time gave forecasters little insight into this period of SOC93 (Uccellini *et al.*, 1995; Caplan, 1995). Gale warnings along the Gulf Coast were not upgraded to storm warnings until an hour before the 2100 UTC observation at South Marsh Island, LA (7R8), indicated sustained  $42 \text{ m s}^{-1}$  winds (Gilhousen, 1994). As the storm made landfall in northwest Florida early on 13 March (Fig. 4.1c), a coastal flood watch for Apalachee Bay was not upgraded to a warning until a 4-m storm surge was in progress (Gilhousen, 1994); 13 deaths are directly attributed to this flooding (NWS, 1994). As SOC93 drove northeastward across the panhandle of Florida (Fig. 4.1c) into southeast Georgia (Fig. 4.1d), an intense pre-frontal squall line caused extensive damage to western Cuba, with 10 fatalities and economic losses approaching U.S. \$1 billion (Alfonso and Naranjo, 1996). In the U.S., as this same squall line crossed Florida it produced 11

confirmed tornadoes which were responsible for seven fatalities (Kocin *et al.*, 1995).

This period of over-water development and subsequent landfall represents a significant and largely unforecast portion of the storm's overall impact. In total, 79 deaths are directly attributed to SOC93, and of these 28 occurred in Florida (NWS, 1994). Of the approximately \$2.7 billion in economic impact in the U.S., about \$1.6 billion was assessed in Florida (NWS, 1994). The storm matured to a minimum central pressure of 960 hPa in New Jersey at about 0000 UTC 14 March, having deepened 40 hPa in 36 h (Kocin *et al.*, 1995); fully half of this deepening (about 21 hPa) took place in the over-water period from 1200 UTC 12 March to about 0600 UTC 13 March and directly preceded some of the most devastating phenomena attendant to this storm.

In previous chapters we have proposed that SOC93 evolved in three stages, outlined in Table. 4.1. These chapters focused on Stage I, which is the initiation and organization of deep convection early on 12 March in the northwest Gulf of Mexico. **Stage II**, the focus of this chapter, is the over-water development period. Studies by Bosart *et al.* (1996) and Dickinson *et al.* (1997) have suggested that this early cyclogenesis is dominated by an upper-level potential vorticity (PV) anomaly strongly coupled through moist convective feedback to a mid-level baroclinic zone along the Texas Gulf Coast. This upper-level synoptic feature is identified as PV anomaly C, indicated in Fig. 4.1. Using simulation datasets, we will illustrate the *mesoscale* details of this crucial stage in the evolution of SOC93 and clarify the role of this PV anomaly in the early development of the storm. Specifically, we contend that in this period SOC93 undergoes an intense, *sustained* warm-core development, then is transformed into an extratropical (cold-core) storm with the penetration of synoptic-scale cold air into the western flank of the storm shortly before landfall on 13 March. We hypothesize that prior to the penetration of this cold air SOC93 develops largely independently of the *upper-level* PV distribution and is more directly affected by the rear inflow of mid-level warm air from the Mexican plateau, which represents a diabatic redistribution of PV at mid-level. This is a logical extension of our previous work demonstrating that the initiation and maintenance of the antecedent convection (Fig. 4.1a) is strongly tied to the mountain-plains solenoid (MPS) attendant to the Altiplanicie Mexicana (Chapters 2 and 3).

The rest of this paper is organized as follows: section 4.2 discusses the observation and simulation datasets used in the analysis, including a brief model verification; section 4.3

presents preliminary evidence of three key periods in the over-water evolution (Stage II) of SOC93; sections 4.4–4.6 present a detailed discussion of each of these periods; section 4.7 briefly discusses these results from a potential vorticity perspective; and section 4.8 presents a summary and concluding discussion.

## 4.2 Methodology

For this study, we employed the observation and numerical datasets used in our earlier analysis of Stage I; we review these data only briefly here. European Center for Medium-range Weather Forecasts (ECMWF) uninitialized gridded analyses at  $1.125^\circ$  (T106) resolution were used for analysis and as initial and boundary conditions for all simulations. A synthetic sea-surface temperature (SST) field was constructed from National Data Buoy Center (NDBC) observations and the Advanced Very High Resolution Radiometer (AVHRR) Pathfinder satellite observations; this modified SST field corrects deficiencies in operational products discussed in Gilhousen (1994); further details are given in Chapter 2.

Simulations were executed with the Mesoscale Atmospheric Simulation System (MASS, version 5.12). MASS is a hydrostatic, full-physics primitive equation model with fourth-order differencing (MESO Inc., 1993). The control experiment was supported by several sensitivity experiments to evaluate the relative contribution of moist and dry diabatic processes, terrain, and SST on the cyclogenesis of SOC93. These experiments were executed on a  $260 \times 220 \times 45$  grid at 12 km horizontal resolution. Table 4.2 provides a detailed list of the numerical experiments. Grid boundaries for these experiments are depicted in Fig. 4.2.

All numerical experiments were initialized at 1200 UTC 10 March, or about 48 h prior to the appearance of the initial surface vortex at 1200 UTC 12 March (Kocin *et al.*, 1995). In the period 1200 UTC 12 March to 1200 UTC 13 March, the CONTROL surface storm verifies well against the mesoanalysis of Kocin *et al.* (1995), with a mean central pressure error of +3.4 hPa (Fig. 4.3a) and a mean position error of 110 km (Fig. 4.3b). These errors are consistent with previous numerical studies (e.g. Huo *et al.*, 1995, 1998) that *initialized* at 1200 UTC 12 March or later. A more extensive three-dimensional verification of the CONTROL experiment is given in Sec. 2.3.

### 4.3 Evolution of the surface cyclone

We first present an overview of Stage II cyclogenesis and offer preliminary evidence for three key periods in this overwater development: an early, warm-core period from about 1200 to 1800 UTC 12 March; a secondary cyclogenesis from about 1500 UTC 12 March to 0000 UTC 13 March; then a transition to a dominant cold-core system after about 0000 UTC 13 March. The subsequent sections will provide a detailed discussion of each of these three key periods.

Stage I cyclogenesis culminates in a surface cyclone in the western Gulf of Mexico about 1200 UTC 12 March (Fig. 4.4a), and we take this as our starting point for the analysis of Stage II. The control experiment simulates the nascent storm as a 1003 hPa surface low that correlates well with intense convection in the GOES-7 IR imagery (Fig. 4.4b). The storm forms along a quasi-stationary surface front extending from northern Mexico to central Florida (Fig. 4.4a). The simulated feature verifies well with the observed surface boundary: observed temperatures along the Florida panhandle range from about 48°F to 54°F (9 to 11°C, Fig. 4.4a), while simulated temperatures in this region are about 10°C (Fig. 4.4b). As described in diagnostic studies of SOC93 (Huo *et al.*, 1995; Kocin *et al.*, 1995; Bosart *et al.*, 1996), this surface front is the locus of further development across the Gulf. In this early period, the storm-relative flow appears quasi-circular with the surface low immediately under the strongest convection (Fig. 4.4b). In Sec. 4.4, we will demonstrate that this early period of Stage II is characterized by warm-core dynamics associated with the growth of this MCC.

A surface trough intensifies ahead of the initial, warm-core storm, extending southward from the initial development at 1500 UTC in both observed (Fig. 4.5a) and simulated (Fig. 4.5b) mean sea-level pressure (PMSL) fields. Secondary cyclogenesis is underway by 1800 UTC, evident as a surface low (1002 hPa) at the head of this trough and along the old surface boundary extending northeastward from the initial surface storm (995 hPa) (Fig. 4.6b); this surface trough also verifies in the NCEP analysis (Fig. 4.6a). The simulated secondary low, however, is not well-positioned with respect to the convection (Fig. 4.6b) and is likely about 100 km west-northwest of its simulated position, consistent with the observed surface development (Fig. 4.6a). The buoy observation of 66°F (19°C) just west of



the observed storm verifies well with the 20°C region west of the simulated storm, indicating that the western flank of the storm is still relatively warm (Fig. 4.6b). The relatively weak baroclinicity proximal to the center has been noted in Kocin *et al.* (1995) and is consistent with the early stages of marine cyclogenesis (Shapiro and Keyser, 1990, Sec. 10.4.1).

Simulated secondary cyclogenesis is corroborated by the NCEP analysis at 2100 UTC, which indicates a separation of SOC93 into the initial western (990 hPa) surface cyclone and a developing eastern (989 hPa) cyclone (Fig. 4.7a), consistent with the separation of the simulated storm into the initial (994 hPa) and the developing (997 hPa) surface low (Fig. 4.7b). The secondary low is the focus of renewed convection on the eastern edge of the storm (Fig. 4.7b) in contrast to the early period characterized by the nearly vertical alignment of convection with the surface cyclone (Fig. 4.4b).

By 0000 UTC 13 March, the storm develops a structure similar to the Phase II “frontal fracture” described in the marine cyclogenesis study of Neiman and Shapiro (1993), (Fig. 4.8a, and attendant comma cloud in Fig. 4.8b). Although the pressure trace of the CONTROL storm center appears smooth in this period at about 1 hPa h<sup>-1</sup> (Fig. 4.3a), the deepening of the secondary cyclone in this period is about 3 hPa h<sup>-1</sup>, dropping from 997 hPa at 2100 UTC (Fig. 4.7b) to 988 hPa at 0000 UTC 13 March (Fig. 4.8b). In Sec. 4.5, we will provide more detailed evidence of this secondary cyclogenesis and document our hypothesis as to its origin.

The penetration of cold air into the western flank of the surface storm marks the beginning of the transformation of SOC93 into an extratropical system. This transformation is complete by 0600 UTC 13 March as the storm makes landfall in northwest Florida (Fig. 4.9). In the period from 0300 to 0600 UTC 13 March, the deepening rate decreases for both the observed and simulated storm, though more dramatically in the case of the simulated phenomenon where the surface storm fills slightly; after 0600 UTC, however, the storm begins to deepen at a about 1 hPa h<sup>-1</sup> as it advances into the southeastern U.S. (Fig. 4.3a). We speculate that this renewed development after 0600 UTC 13 March occurs as an upper-level PV anomaly (Dickinson *et al.*, 1997, PV anomaly C, see their Fig. 2a) phases with the extratropical SOC93. This is consistent with the synoptic-scale signal of development early on 13 March discernible in operational models as early as 8 March (Uccellini *et al.*, 1995; Caplan, 1995). In Sec. 4.6, we will document this transition to a cold-core structure in the final phase of

overwater development.

## 4.4 Early warm-core development

Long-lived MCCs have been documented previously; in particular, the convective system that triggered the 1977 Johnstown Flood has been the subject of detailed observational study (Bosart and Sanders, 1981) and numerical investigation (Zhang and Fritsch, 1987). This system was initiated in South Dakota then propagated eastward, developing a structure resembling a young tropical storm while crossing the open water of the Great Lakes (Bosart and Sanders, 1981). Using mesoscale simulation datasets, Zhang and Fritsch (1987) found that this stage of the storm was characterized by a deep warm core and a nearly uniform equivalent potential temperature structure and horizontal momentum field proximal to the storm center. In this section, we document similar structures in the early overwater development of SOC93.

### 4.4.1 Warm-core characteristics and mid-tropospheric structure

Diabatic heating was calculated from the CONTROL simulation in the isentropic column from 336 K (about 350 hPa) to 316 K (about 650 hPa); details of the computation are given in Appendix A. At 1500 UTC 12 March, the simulated surface low (998 hPa) and local maximum in diabatic heating ( $> 22 \text{ K h}^{-1}$ ) are well-correlated with the strongest convection indicated in GOES-7 IR imagery (Fig. 4.10). The latent-heating signal attendant to this convection corresponds to a hot pool ( $> 321 \text{ K}$ ) and sharp meso- $\beta$  ridge at 500 hPa extending northwest of the surface low (Fig. 4.11). Outflow from the deep convection is evident as a leftward acceleration of the flow about the core; flow in the northeast quadrant of the storm is dominated by this isallobaric response to the mass-flux divergence in the column (Fig. 4.11). The latent-heating hot pool is embedded in a poleward tongue of warm air extending from the northern Mexican Gulf Coast to the central Gulf (Fig. 4.11). The larger signal of the warm pool is associated with air originating along the elevated plateau of central Mexico and in the marine boundary layer of the southern Gulf (Fig. 4.12a). While latent heating makes a local contribution to the broad signal of warming at 500 hPa, we note that the

tongue extends about 100 km west and about 200 km south, or upstream, of the convection (Fig. 4.11).

Representative parcel trajectories computed through the storm center at 1500 UTC confirm the transport of warm air directly from the plateau (Fig. 4.12b) and indirectly from the coastal plain once displaced eastward from the plateau (Fig. 4.12c). The plateau airstream (Fig. 4.12b) is significantly drier than the coastal plain airstream (Fig. 4.12c), reflected in their originating  $\theta_e$  values. The confluence of these airstreams along the northern coast of Mexico yields a warm, moist inflow to the initial SOC93 penetrating at about 500 hPa (Fig. 4.12b,c). Parcels originating along the southern coast of Mexico (Fig. 4.12d) and Yucatan Peninsula (Fig. 4.12e) penetrate beneath this plateau airstream at about 850 to 900 hPa but with somewhat higher  $\theta_e$  consistent with the longer fetch over the Gulf. All of these parcels appear to quickly ascend through the storm then exit on approximately the same  $\theta_e$  surface (336 K to 338 K), which is consistent with the warm core development of this system.

The vertical structure of potential temperature through the storm reveals this deep warm core extending from about 300 hPa to the surface and nearly vertically aligned with the surface low, as well as a cold mesohigh above about 250 hPa (Fig. 4.13a), consistent with structures discerned in the observational studies of Maddox (1983). Strong low-level convergence is indicated at the base of a deep column of ascent ( $< 100 \mu\text{bar s}^{-1}$  or approximately  $> 1 \text{ m s}^{-1}$ ) coincident with the warm core (Fig. 4.13a). The column is also characterized by a nearly uniform equivalent potential temperature ( $\theta_e$ ) and deep moisture convergence (Fig. 4.13b). Low-level moisture appears to enter the convective complex primarily from the south and west, consistent with the parcel trajectories (Fig. 4.12a). The  $\theta_e$  structure northeast of the storm reveals an elevated cool, dry layer ( $\theta_e < 312 \text{ K}$ ) atop the marine boundary layer (Fig. 4.13b).

This cool, dry layer originates in the continental cold air associated with the old surface front (e.g. Fig. 4.4a) and its elevated penetration into the Gulf is consistent with the observed low-level cold air “damming” along the northern Gulf Coast noted in Kocin *et al.* (1995). The  $\theta_e$  structure on the 800 hPa surface (Fig. 4.14) clarifies this baroclinic zone extending across the central Gulf as a boundary between dry continental and maritime air; the potential temperature structure at 800 hPa (not shown) indicates little baroclinicity over the Gulf.

Similarly, surface fields indicate this region as more of a convergence zone (e.g. Fig. 4.4b, 4.6b) with only weak temperature contrast over the open water. In terms of the early, warm-core development of SOC93, this baroclinic zone and its attendant vertical shear are in the far field of initial development. Thus, the low-level momentum field proximal to the storm is driven largely by the organized convection, as indicated by the convergent inflow below about 650 hPa (Fig. 4.13a).

#### 4.4.2 Local jet structure

While the low-level flow supplies available potential energy to the warm-core development, the upper-level flow sustains the convection through divergence attendant to upper-level jet streaks. Bosart *et al.* (1996) note that a unique aspect of the SOC93 development is the amplification of planetary flow prior to the explosive subsynoptic development of SOC93. As a consequence of this amplification, strong jet streaks from both the subtropical (STJ) and polar front (PFJ) jets are proximal to the initial storm, evident in the large-scale ECMWF 250 hPa analysis at 1200 UTC 12 March (Fig. 4.15). The jet streak along the plateau of central Mexico is the southern extension of a confluence of the STJ and PFJ over the Rocky Mountains (Fig. 4.15); following Bosart *et al.* (1996), we will refer to this as an STJ streak or the western jet streak. The jet streak along the southeastern U.S. (Fig. 4.15) is part of the PFJ attendant to the old surface boundary across the northern Gulf Coast (Fig. 4.4a). A jet streak associated with the STJ stretches from southern Mexico across the Yucatan Peninsula to southern Florida (Fig. 4.15). At 1500 UTC, CONTROL results indicate that the surface cyclone is supported by strong upper-level divergence ( $> 5 \times 10^{-4} \text{ s}^{-1}$ ) in the right entrance region of the PFJ streak (Fig. 4.16). This is in contradistinction to typical extratropical cyclogenesis, wherein the preferred region for surface cyclogenesis is typically in left exit region of an approaching upper-level jet streak (e.g. Hoskins *et al.*, 1985; Petterssen and Smebye, 1971). The cyclone is proximal to the left exit region of the western STJ, and this does appear to make a contribution to the divergence signal; however, the strongest ageostrophy driving this divergence appears to be the transverse acceleration of the PFJ (Fig. 4.16).

We claim that the early SOC93 is largely a warm-core system, and so we are compelled

to clarify the relationship between the surface cyclone and the upper-level jet streaks. The ADIABATIC simulation reproduces the synoptic-scale jet streaks but with significant differences in the subsynoptic (meso- $\alpha$ ) structure (Fig. 4.17a). In the full-physics simulation, the PFJ extends westward to central Texas with a sharp gradient of wind speed along the entrance region (Fig. 4.16), while this jet streak propagates eastward in the adiabatic run with a significantly weaker gradient of wind speed marking the entrance region along the Texas-Louisiana border (Fig. 4.17a). Uccellini and Johnson (1979) have noted that the strength of a jet streak's ageostrophic transverse circulation is more directly related to the along-stream variation in speed than to the strength of the jet core; this is consistent with the stronger simulated ageostrophy in the full-physics run (Fig. 4.16) despite the relative similarity in core strength to the adiabatic PFJ (Fig. 4.17a).

The convective outflow from the initial SOC93 fortifies the entrance region of the PFJ, building the jet streak eastward and restructuring the upper atmosphere in a way that supports further development of the surface cyclone. This process begins with convection initiated in the lower Rio Grande Valley in the period from 0600 to 0900 UTC 12 March (Chapter 3) and continues in a positive feedback through the early development of the storm: the intensifying PFJ streak provides a mechanism for ventilation of the convection through upper-level divergence, which supports further convection through a meso- $\beta$  scale deep column of ascent (Fig. 4.13a) and drives further surface pressure falls. A direct comparison between the vector wind fields of the CONTROL and ADIABATIC simulations gives a qualitative sense of this rapid development. The anticyclonic outflow from the convective complex supporting SOC93 is the dominant signal in this wind field, though the vectors should not be interpreted as the first-order diabatic signal (Fig. 4.17b). This large meso- $\alpha$  outflow extends from about southern Missouri to eastern Mexico, about 2000 km in diameter, and represents the net result of a strong interaction between meso- $\beta$  convection (Fig. 4.10) and a favorable upper-level environment (Fig. 4.16). The convective outflow tightens the wind speed gradients in both the entrance region of the PFJ and the exit region of the western STJ (compare Fig. 4.16 to Fig. 4.17a), yielding opposing transverse circulations oriented approximately 90° to one another. The concomitant divergence at the vertex sustains the deep, organized convection that further intensifies these circulations (Fig. 4.16).

### 4.4.3 Summary

We conclude that the early overwater SOC93 exhibits the thermodynamic structure and lower-tropospheric dynamics of a warm-core cyclone. This is supported by the deep warm core (Fig. 4.13a) coincident with a local maximum in diabatic heating (Fig. 4.10), but extending to the surface and vertically aligned over the surface cyclone. The nearly uniform equivalent potential temperature structure through the storm is another indication of significant warm-core development and the simulated structure (Fig. 4.13b) strongly resembles the observed structure in early tropical development (e.g. Hakwins and Imbembo, 1976, for Hurricane Inez, September 1966). Although there is significant baroclinicity above the marine boundary layer (Fig. 4.14), the lower-tropospheric momentum field proximal to the storm center is dominated by cyclonic inflow (Fig. 4.4b, 4.14) and strong low-level convergence (Fig. 4.13a). The upper-level flow, however, appears atypical of warm-core development because of the number and strength of nearby synoptic-scale jet streaks (Fig. 4.16). We next examine how these jet streaks interact with the lower-tropospheric baroclinicity to produce the rapid, secondary cyclogenesis.

## 4.5 Secondary cyclogenesis

The initial warm-core storm and warm plume from the MPS establish a low-level deformation field that supports deep convection in the central Gulf *ahead* of the initial storm and in an upper-level environment already conditioned to support explosive development by the first convective event. The secondary surface cyclone appears as early as 1600 UTC 12 March in a broad region of precipitation centered about a 1004 hPa surface low (Fig. 4.18a); this development occurs along a surface trough (Fig. 4.5b) induced in part by the mid-level ascent attendant to the MPS propagating ahead of the initial storm (Fig. 4.11). This secondary storm quickly deepens by 1800 UTC as the surface flow accelerates along this broad trough that encompasses both the original storm (998 hPa) and the rapidly developing secondary cyclone (1002 hPa); by this time a significant precipitation core ( $> 40 \text{ mm h}^{-1}$  over about 50 km) has developed northwest of the secondary low (Fig. 4.18b). By 2100 UTC, the precipitation about the primary cyclone (993 hPa) appears to weaken in favor of the convective

complex supporting the secondary low (997 hPa) which has rotated northward to just east of the initial storm (Fig. 4.18c). The transition to the secondary cyclone is complete by 2300 UTC, as the secondary low (990 hPa) rotates northeast and to within about 100 km of the initial low (993 hPa, Fig. 4.18d). In this period, the secondary system overtakes the primary by deepening at a rate of about  $2 \text{ hPa h}^{-1}$ , compared to the primary low which deepens at about  $1 \text{ hPa h}^{-1}$  and stagnates in the period from 2100 to 2300 UTC 12 March. The storm appears to “jump” to the secondary low, which becomes the focus of development for the rest of the overwater period. In this section, we examine the conditioning of this region for secondary cyclogenesis and the primary mechanisms of this development: convection, jetogenesis and rapid frontogenesis.

#### 4.5.1 Pre-cyclogenesis environment

The warm, moist southerly flow feeding the initial cyclone (Sec. 4.4.1) extends well east of this storm and into the central Gulf. Representative parcel trajectories through the secondary storm at 1600 UTC 12 March (Fig. 4.19a) indicate a rear inflow very similar to the initial system (Fig. 4.12a), with air clearly originating along the plateau (Fig. 4.19b) and coastal plain (Fig. 4.19c) capping a moist flow from the marine boundary layer (Fig. 4.19d,e). This warm plume conditions the region southeast of the initial storm for further convective development by inducing a broad region of lower-tropospheric ascent, evident at 700 hPa at 1200 UTC 12 March (Fig. 4.20a), which is approximately along the surface trough leading the primary storm (Fig. 4.4a). Weak convection southeast of the main MCC is evident in satellite imagery and is consistent with this region of ascent (Fig. 4.4b). The circulation about the primary storm necessarily makes a contribution to the northerly transport of this warm plume; however, the depth of this plume is enhanced by an interaction with the broad entrance region of the southern STJ (Fig. 4.20b). A cross-section along this region indicates that the northward transport *and ascent* of the warm MPS plume perturbs the weak STJ entrance region (Fig. 4.21). In effect, the thermally-direct circulation of the northbound MPS extends the STJ downward in a process that occurs largely *independently* of the development of the initial storm. In the absence of the meso- $\alpha$  signal from the primary surface cyclone, there would still be a southerly (leftward-directed) ageostrophic component to the MPS

outflow, and even in this case we note that the extension of the STJ to 400 hPa is evident as early as 1200 UTC (Fig. 4.21). The MPS plume in Fig. 4.21 is identifiable in the weak moist adiabatic lapse rate (weak  $\partial\theta_e/\partial p$ ) from about 324 K to 328 K or about 600 hPa to 400 hPa; parcels originating from the plateau at about 1200 UTC travel in the layer from about 560 hPa (Fig. 4.19b) to 670 hPa (Fig. 4.19c) on the  $\theta_e = 326$  K surface.

The action of the MPS circulation on the STJ helps to connect the entrance regions of the northern PFJ and southern STJ (Fig. 4.21), inducing a broad thermally-direct circulation over the central Gulf; the low-level return branch from this flow enhances the southerly transport of cool air from the continent into the northern Gulf, evident in the lower troposphere in the northern (left-hand) portion of Fig. 4.21 and as a cool southerly intrusion east of the warm tongue at 700 hPa (Fig. 4.20a). By 1400 UTC, the primary storm advances eastward, enhancing the 700 hPa baroclinicity (Fig. 4.22a). The region of 700 hPa ascent marking the northern edge of the MPS (Fig. 4.22a) is reflected as a stronger cross-stream ageostrophy in the southern STJ (Fig. 4.22b). This more pronounced leftward-directed ageostrophy is consistent with the well-defined, thermally-direct circulation whose upper branch extends from about the Louisiana Gulf Coast to the Yucatan Peninsula (Fig. 4.23); The lower branch of this circulation brings cool air southward, increasing the depth of the baroclinic zone in the central Gulf; this zone is comprised of cool, continental air to the north and warm MPS air to the south (Fig. 4.23). We next demonstrate how convection is triggered along this baroclinic zone.

### 4.5.2 Early convection and jetogenesis

Meso- $\beta$  convection is initiated about 1600 UTC 12 March along the deep lower-tropospheric convergence formed by the deceleration of warm, moist southerly flow against the dome of cool, dry continental air penetrating into the northeast Gulf above the marine boundary layer (Fig. 4.18a). This significant convergence occurs along a southwest-northeast axis evident in the moist adiabatic ( $\theta_e$ ) structure at 800 hPa (Fig. 4.24). As previously discussed (Sec. 4.5.1) the cool, dry air originates north of the stationary surface front across the Gulf (e.g. Fig. 4.5a) while the warm, moist air originates from the Mexican plateau and southern Gulf (Fig. 4.19); this boundary is better defined in the  $\theta_e$  field than the potential temperature



( $\theta$ ) field (not shown); this is consistent with the weak baroclinicity in the surface temperature field at about this time (e.g. Fig. 4.5b).

The depth of this boundary is evident in the significant ascent ( $< 50 \mu\text{bar s}^{-1}$ ) at 500 hPa along the eastern edge of the warm MPS outflow (Fig. 4.25). The advance of synoptic-scale cold air into the initial cyclone at about 500 hPa is also indicated on the western edge of this warm tongue, marked as well by broad ascent ( $< 10 \mu\text{bar s}^{-1}$ ) at the boundary between this cold air and the western edge of the warm tongue. This cold surge into the Gulf is a meso- $\alpha$  aspect of the large-scale, equator ward surge of cold air along the the Rocky Mountains and Sierra Madres, documented in Schultz *et al.* (1997) and associated with PV anomaly C (Bosart *et al.*, 1996). We will examine the potential vorticity structure in detail in Sec. 4.7.

Vertical cross-sections along the 800 hPa  $\theta_e$  axis through the secondary cyclone (Fig. 4.24) indicate a weak warm core extending from about 250 hPa to 650 hPa coincident with a deep column of ascent that extends to the surface (Fig. 4.26a). The upper branch of the large, thermally-direct circulation through the central Gulf is evident north of the developing secondary storm and is indicative of the coupling of PFJ and STJ entrance regions (left-hand side of Fig. 4.26a). The vertical structure of  $\theta_e$  through the secondary cyclone indicates a nearly uniform region of equivalent potential temperature from about 400 to 600 hPa (Fig. 4.26b) and resembles the structure of the initial surface cyclone (Fig. 4.13b). Unlike the initial cyclone, however, the cool, dry continental air makes a significant penetration into the base of the secondary storm; the juxtaposition of this air mass over the relatively warm, moist marine boundary layer provides a ready source of convective available potential energy to support the secondary development (Fig. 4.26b). Calculations along this axis indicate  $\text{CAPE} > 1400 \text{ J kg}^{-1}$  northeast of the developing surface low.

This new convection taps an upper-level momentum field already conditioned by the initial cyclone. The coupling of PFJ and STJ entrance regions is initiated by the MPS (Sec. 4.5.1), though moist convection from the initial cyclone and nascent secondary cyclone quickly reinforce this circulation; this reinforcement appears to broaden the entrance region of the PFJ streak located across the northern Gulf Coast Fig. 4.27a). The subsequent strong southeasterly ageostrophy aloft connects the outflow from the secondary cyclone to the entrance region of the PFJ (Fig. 4.27a), which accelerates development under significant divergence ( $> 1 \times 10^{-4} \text{ s}^{-1}$ ) vertically aligned over the surface low (Fig. 4.27a). A vertical

cross-section through entrance region of the PFJ clarifies the relationship among the primary cyclone, secondary cyclone and this jet streak. The primary cyclone acts to extend eastward the thermally-direct circulation in the entrance region of the PFJ, enhancing both low-level convergence and mid to upper-tropospheric divergence on the western flank of the secondary storm (Fig. 4.27b). Convective outflow attendant to the secondary development reinforces the upper-level circulation initiated by the coupling of the STJ and MPS prior to 1200 UTC, establishing a distinct entrance region to the PFJ proximal to the secondary storm; this is evident in the enhanced wind speed gradient at 250 hPa northeast of the secondary cyclone (Fig. 4.27a).

The intense convection at 1800 UTC (Fig. 4.18b) produces a strong along-stream ageostrophy evident at 400 hPa (Fig. 4.28a) and extending to 250 hPa (Fig. 4.28b), while the somewhat slower adjustment in the entrance region of the PFJ produces a strong cross-stream ageostrophy, maximizing divergence proximal to the secondary cyclone (Fig. 4.28b). The secondary storm develops under the ascending branch of the strengthening thermally-direct circulation associated with the PFJ (Fig. 4.29). The subsequent divergence signal ( $> 4 \times 10^{-4} \text{ s}^{-1}$ ) is focused and significantly stronger than the signal ( $> 2 \times 10^{-4} \text{ s}^{-1}$ ) supporting the initial cyclone (Fig. 4.28b). This is consistent with increasing low-level cold advection ahead of the cold surge (Schultz *et al.*, 1997) into the western flank of the initial cyclone (Fig. 4.6b) damping the supporting convection (994 hPa low in Fig. 4.18b); this is further evidence that development of the secondary storm is overtaking the initial cyclone. The ECMWF analysis at 1800 UTC corroborates the simulated structure at 250 hPa, with significant divergence ( $> 2 \times 10^{-4} \text{ s}^{-1}$ ) supporting the surface storm aligned under the entrance region of the PFJ streak (Fig. 4.30). The secondary low is not detected in the ECMWF dataset, but this is expected given that the grid spacing ( $1.125^\circ$  or about 125 km) would only allow about  $3\delta x$  to cover the 330 km between the simulated initial and secondary storms (e.g. Fig. 4.28b); the strong wind speed gradients marking the secondary entrance region to the PFJ (east of the initial storm) are supported in this analysis, however, and provide further observational evidence of the secondary cyclogenesis (Fig. 4.30).

The strengthening thermally-direct circulation in the northern Gulf (Fig. 4.29) and convective outflow produce a substantial jet streak at 400 hPa by 1800 UTC (Fig. 4.28a) which strengthens significantly by 2100 UTC (Fig. 4.31a) and appears as a distinct feature on the

PFJ entrance region (proximal to 997 hPa surface low in Fig. 4.31b). The strengthening entrance region circulation is due in part to the increasing baroclinicity of the lower troposphere, which is itself due in part to the southward transport of cool continental air along the lower branch of this circulation (Fig. 4.32). Opposing the cool northerly flow is the warm, southerly MPS flow entrained in the surface storm circulation (southeastern or right-hand side of Fig. 4.32). The resulting deep baroclinicity is evident as deep jetogenesis that extends from the tropopause down to about 900 hPa, where flow within about 60 km of the storm center exceeds  $30 \text{ m s}^{-1}$  (Fig. 4.32); we note that the position of the simulated surface low (997 hPa) is about 50 km southeast of South Marsh Island, LA, (indicated in Fig. 4.1b) where a buoy recorded sustained winds of  $42 \text{ m s}^{-1}$  (Gilhousen, 1994).

Significant along-stream subgeostrophy is indicated southwest of SOC93 as the exit region of the western STJ advances around the long-wave trough into the Gulf of Mexico. Blocking of the planetary-scale flow (discussed in Bosart *et al.*, 1996) closes the distance between the synoptic-scale western jet streak and the developing SOC93 system, and the eastern surge of cold air into the Gulf (Fig. 4.31a) attendant to this jet streak further enhances the baroclinicity in the Gulf. This sudden intrusion of mid to lower-tropospheric cold air on the western flank of the system produces a broad divergence ( $> 1 \times 10^{-4} \text{ s}^{-1}$ ) at 250 hPa southwest of the secondary storm (Fig. 4.31b); in the next section we will examine further this cold intrusion and subsequent rapid frontogenesis.

In the period from 2100 to 2300 UTC 12 March, SOC93 undergoes a dramatic scale contraction as the secondary surface cyclone becomes the nexus of overwater development. This transition is marked by a rapid jetogenesis in the mid-troposphere attendant to the explosively deepening ( $7 \text{ hPa } 2 \text{ h}^{-1}$ ) surface cyclone (Fig. 4.33a). The exit region of the upper-level western jet streak (Fig. 4.33b) and attendant cold air (Fig. 4.33a) make a significant intrusion into the Gulf in this two-hour period and are indicated just southwest of the developing surface storm. The opposing ageostrophic circulations of the western STJ exit region and northern PFJ entrance region appear to dominate the upper-level divergence supporting the storm (Fig. 4.33b). The vertical structure of SOC93 at this time has elements of both warm and cold-core development. The momentum field on the southern flank of the storm strongly resembles a warm-core system similar to a strong tropical phenomenon: a narrow band of  $35 \text{ m s}^{-1}$  winds extend from 250 hPa to about 800 hPa through a core marked

by moist adiabatic ascent from the surface to about 400 hPa (right-hand side of Fig. 4.34). The northern flank of the storm, however, is marked by a westward tilt toward cooler, drier air originating over the southern U.S. and more closely resembles an extratropical storm (left-hand side of Fig. 4.34).

Although the interaction of synoptic jet streaks is important to the secondary cyclogenesis, we assert that the convective storm and its attendant mid-level jetogenesis (Fig. 4.33a) are connecting mechanisms for these synoptic circulations. Comparison of the CONTROL fields (Fig. 4.33a) to ADIABATIC results (Fig. 4.35a) confirm that the mid-tropospheric jetogenesis is induced primarily by the diabatic signal attendant to the storm. The western jet streak advancing through the long-wave trough does induce an adiabatic jetogenesis at 400 hPa, though without the diabatic signal from early SOC93 there is only weak evidence of the PFJ at 400 hPa (Fig. 4.35a) and hence no coupling of the PFJ to this western jet streak. The resulting upper-level flow is significantly curved consistent with the planetary flow but with weaker along-stream wind speed gradients, subsequently inducing weaker ageostrophic flow; this is confirmed in the unremarkable upper-level divergence (everywhere  $< 1 \times 10^{-4} \text{ s}^{-1}$ ) in the ADIABATIC results (Fig. 4.35b).

### 4.5.3 Rapid frontogenesis

In their observational study of SOC93, Kocin *et al.* (1995) note that the surface front northeast of the storm appears to strengthen from 1800 UTC 12 March to 0000 UTC 13 March though the front appears to retreat southward in this period. We have demonstrated with simulation results that the boundary upon which the secondary storm develops is better defined in a southward penetration of cool, dry continental air into the Gulf at about 800 hPa (Fig. 4.14, 4.24, and 4.26b). In this section we examine the role of this lower tropospheric baroclinicity in the secondary cyclogenesis.

Moist frontogenesis can be computed, using  $\theta_e$  as the thermodynamic variable, with (e.g. Bluestein, 1993, Eq. 2.3.8):

$$\mathcal{F} = \frac{1}{|\nabla_p \theta_e|} \left[ - \left( \frac{\partial \theta_e}{\partial x} \right)^2 \frac{\partial u}{\partial x} - \frac{\partial \theta_e}{\partial x} \frac{\partial \theta_e}{\partial y} \frac{\partial v}{\partial x} - \frac{\partial \theta_e}{\partial x} \frac{\partial \theta_e}{\partial y} \frac{\partial u}{\partial y} - \left( \frac{\partial \theta_e}{\partial y} \right)^2 \frac{\partial v}{\partial y} \right] \quad (4.5.1)$$

Simulation results at 1800 UTC show three frontal boundaries: a cold boundary west of the

initial cyclone oriented along the Texas Gulf Coast, associated with the deep, synoptic-scale cold air over the Southern Plains (indicated in the NCEP analysis, Fig. 4.6a), a cool boundary extending southwest of the initial cyclone to northeast Mexico, and a warm boundary that connects the initial and secondary cyclones (Fig. 4.36). The cool and warm boundaries form on the western and eastern edges (respectively) of the warm, southerly intrusion of the composite airstream formed by the elevated mixed layer from the Mexican plateau moistened by the marine boundary layer (Fig. 4.12).

Cross-sections through the secondary cyclone at 1800 UTC indicate a large thermally-direct circulation northeast of the storm (Fig. 4.37a), which is consistent with the extended entrance region of the PFJ streak across the southeastern U.S. (Fig. 4.28). The lower branch of this ageostrophic circulation contributes to the relative frontogenesis at 800 hPa by holding in place the cool, dry continental air (Fig. 4.37b). The penetration of this elevated cool air into the northeast quadrant of the storm increases the CAPE for further convective development of the secondary cyclone; additionally, the depth of the cool air proximal to the ascending branch of the circulation accelerates the flow at mid-level (Fig. 4.37a). The resulting vertical shear disrupts the warm-core circulation of the secondary cyclone, evident in the low-level deformation of the  $\theta_e$  surfaces (Fig. 4.37b). While convection is crucial to the secondary cyclogenesis, the highly baroclinic lower troposphere is an important distinction between this event and the initial cyclogenesis.

By 2100 UTC, the southerly warm tongue and attendant cool boundary along the western edge have propagated to the central Gulf (Fig. 4.38). The warm boundary coincident with the secondary cyclone continues to merge with the cool boundary along the northeast Gulf Coast (Fig. 4.38). The northward penetration of the warm tongue is coincident with the mid-tropospheric jetogenesis induced by the curvature of the western STJ streak about the long-wave trough (Fig. 4.31a). A cross-section through the secondary cyclone clarifies this relationship, indicating a large, thermally-indirect circulation induced by the exit region of the western jet streak (Fig. 4.39a). The ascending column of this circulation initiates new convection on the southern flank of the secondary cyclone (Fig. 4.18c) and the developing synergy of the northern and western jet streaks induces the broad region of significant divergence ( $> 1 \times 10^{-4} \text{ s}^{-1}$ ) southwest of the secondary cyclone (Fig. 4.31b).

A warm seclusion (Neiman and Shapiro, 1993) appears to form behind the dominant

secondary cyclone at 2300 UTC (Fig. 4.40) as the scale of the surface storm further contracts and the focus of development shifts to the secondary storm. A significant column of ascent ( $< 100 \mu\text{bar s}^{-1}$  or  $> 1 \text{ m s}^{-1}$ ) supports the surface cyclone and a warm core is evident in the  $\theta$  structure of this column (Fig. 4.41a). There is a significant penetration of cooler air into the southwest quadrant of the storm, consistent with the cutoff of the initial warm-core storm in the seclusion (rightmost portion of Fig. 4.41a,b); Kocin *et al.* (1995) note in their surface mesoanalysis that a bent-back warm front appears to form at about this time, which is consistent with the nascent seclusion (Neiman and Shapiro, 1993). The vertical  $\theta_e$  structure indicates a hybrid system with a residual warm-core associated with the secondary system that is undergoing significant modification by the deep shear attendant to the increasing baroclinicity in the lower troposphere (Fig. 4.40, 4.41a). This is consistent with the meso- $\alpha$  jetogenesis at 400 hPa (Fig. 4.33a) and directly precedes the intense squall line (Fig. 4.8b) that sweeps across Florida and Cuba.

In an observational study of this squall line and its passage through Cuba, Alfonso and Naranjo (1996) note that the deep transport of hot, dry Mexican plateau air into the central Gulf increases the convective instability of the lower troposphere prior to the initiation of the pre-frontal squall line; this transport is corroborated by our simulation results (e.g. Fig. 4.12). The antecedent front results from the rapid ( $< 12 \text{ h}$ ) deformation of this warm tongue by the meso- $\alpha$  SOC93 circulation; the plateau air forms the warm sector for the incipient front, with the warm boundary forming in the northeast quadrant of the surface cyclone and the cold boundary forming on the western flank of the warm pool with the intrusion of synoptic-scale cold air into the Gulf (e.g. Fig. 4.38). This squall line forms on the anticyclonic (eastern) flank of the mid-tropospheric jet streak (Fig. 4.33a), indicating that the line convection was likely triggered by inertia-gravity waves (IGWs) generated by inertial instability. A profile of absolute vorticity through the center of the secondary cyclone (Fig. 4.42) confirms this diagnosis. At 1800 UTC, the storm is characterized by strong ( $> 80 \times 10^{-5} \text{ s}^{-1}$ ) cyclonic vorticity at mid-level; the vorticity decreases with height, consistent with the outflow of the convective development (Fig. 4.42). The vortex descends to about 700 hPa by 2100 UTC (Fig. 4.42) as the convection intensifies (Fig. 4.18c); the concomitant outflow aloft also intensifies. The abrupt penetration of the western jet streak southwest of the storm is indicated at 2300 UTC as a uniform acceleration of the flow in the column from 700 to 300

hPa and accompanies an intensification of the low-level cyclonic vortex (Fig. 4.42). Above the storm vortex the absolute vorticity decreases sharply, forming a region of  $\zeta + f < 0$  at about 400 hPa. The large scale of jetogenesis at this level (Fig. 4.33a) coupled with strong negative absolute vorticity strongly implies IGW generation on the eastern flank of the jetlet (e.g. Holton, 1992, Sec. 7.5.2).

#### 4.5.4 Summary

In the period from 1200 to 2300 UTC 12 March, SOC93 evolves from its primary, warm-core circulation to a hybrid, secondary storm that has a similar convection-driven (warm-core) structure although it develops in an increasingly baroclinic lower troposphere. The penetration of the western STJ streak into the Gulf of Mexico and attendant cold surge introduces a deep, thermally-indirect circulation southwest of the secondary development which accelerates frontogenesis in the central Gulf of Mexico. The convective outflow from the meso- $\alpha$  storm aloft and low-level cold surge act to connect the thermally-indirect exit region of this western jet streak to the thermally-direct entrance region of the northern PFJ streak. The subsequent divergence at the juxtaposition of these circulations increases the scale of the already significant upper-level divergence supporting the surface cyclone, forcing an adjustment in the mid-troposphere that induces a strong jetlet with substantial anticyclonic shear on its eastern flank. The resulting inertial instability triggers an intense, pre-frontal squall line responsible for over \$1 billion in damage in western Cuba (Alfonso and Naranjo, 1996); this long-lived phenomenon preceded landfall of SOC93 in northwest Florida and produced 11 tornadoes across the state (Kocin *et al.*, 1995). We next examine the structure of the cyclone at landfall.

### 4.6 Transition to dominant cold-core development

After 2300 UTC 12 March, large-scale forcing by the cold dome and attendant jet streak begins to modify significantly the warm-core structure of the early SOC93, and by 0600 UTC 13 March the storm more closely resembles classic extratropical (cold-core) development. In this section, we briefly examine the evolution of the storm in this final phase of the overwater

development.

#### 4.6.1 Precipitation and surface development

The diffuse surface circulation composed of the initial and secondary cyclones contracts between 0000 UTC (Fig. 4.43a) and 0300 UTC 13 March (Fig. 4.43b) into a single surface low (984 hPa). The 0000 UTC simulated squall line verifies well with satellite imagery (compare Fig. 4.43a to Fig. 4.8b) though the simulated feature is about 100 km west of the observed phenomenon; this is consistent with the mean error in surface features (Sec. 4.2). Although intense convection persists in the northeast quadrant of the storm, the transition to a cold-core development is marked by the displacement of the surface circulation from the strongest precipitation core (Fig. 4.43c). The deepening of the storm slows down as the meso- $\beta$  convection moves ahead of the surface circulation: in the period from 0300 (Fig. 4.43b) to 0600 UTC 13 March (Fig. 4.43c) the simulated storm actually fills by about 0.5 hPa. This decrease in deepening rate is corroborated by the mesoanalysis of Kocin *et al.* (1995), which indicates that in the period from 1200 UTC 12 March to 0300 UTC 13 March the observed storm deepened by about  $1.27 \text{ hPa h}^{-1}$ , while in the period from 0300 to 0600 UTC this rate slowed to  $0.67 \text{ hPa h}^{-1}$ .

#### 4.6.2 Frontal evolution

The lower tropospheric front strengthens along the cold boundary south of the surface low at 0300 UTC 13 March, with the sharp  $\theta_e$  gradient marked by a nearly  $90^\circ$  poleward turn in the 800 hPa flow (Fig. 4.44). The lower moistened boundary of the plateau air forms a narrow warm sector ahead of this front (indicated by the southerly plume of  $\theta_e$  332 – 336 K, Fig. 4.44) and is wrapped north of the surface cyclone into the strong convection ahead of the storm (Fig. 4.43b). Although a thorough gravity wave analysis is beyond the scope of this work, we speculate that the convective instability inherent to this warm sector is released by the inertia-gravity waves triggered about 2300 UTC 12 March. This is at least consistent with the rapid development of the pre-frontal squall line along this plume and its acceleration *away* from the lower tropospheric front (Kocin *et al.*, 1995). The warm core that marks the initial stage of both the primary (Fig. 4.13a) and secondary (Fig. 4.26a)



cyclones is significantly modified by the intrusion of cold air into the western flank of the storm (Fig. 4.45a). The displacement of the latent-heating warm core from the surface circulation is evident in the weakened and more shallow columns of ascent proximal to the surface storm (Fig. 4.45a). The deep frontal boundary is better defined in the vertical  $\theta_e$  structure (Fig. 4.45b), with a sharp moisture gradient separating the warm-core circulation from the intruding cold air.

At 0600 UTC 13 March, the simulated 800 hPa front (Fig. 4.46) verifies well with the NCEP-analyzed surface feature (Fig. 4.9a), to include the southwest displacement of the frontal triple-point relative to the surface low. This appears to be similar to the bent-back warm front described by Neiman and Shapiro (1993), with its western protrusion of the warm boundary into the polar airstream; by 0900 UTC, the surface low does migrate westward along this boundary (not shown) as the storm re-intensifies over land. The cold dome, extending from the surface to about 300 hPa, appears to dominate the left flank of the storm and induce the westward tilt typical of extratropical cyclogenesis (Fig. 4.47a). There is little evidence of the warm core at this stage, and the ascent that marks the leading edge of development is shallow but significant ( $< 100 \mu\text{bar s}^{-1}$ ), with the cold air capping this column in a mesohigh at about 500 hPa (Fig. 4.47a). Although there is still significant convection attendant to the storm circulation at 0600 UTC (Fig. 4.43c), the dissociation of the warm core is a signal of the shift to broader, stratiform precipitation proximal to the storm. The weakened warm core is evident in the  $\theta_e$  structure through the storm, along with the large-scale transport of Gulf moisture into the developing cold-core storm (Fig. 4.47b).

### 4.6.3 Mid and upper-tropospheric development

At 0300 UTC a significant 400 hPa jetlet connects the exit region of the highly curved western jet streak and the right entrance region of the northern PFJ streak (Fig. 4.48a). The concomitant divergence at the junction of these circulations is significant but *displaced eastward* ahead of the surface cyclone (Fig. 4.48b) and coincident with the strongest convective core (Fig. 4.43b). In effect, once the convective outflow has initiated the process of connecting the two synoptic-scale jet streaks (Fig. 4.35, discussed in Sec. 4.54.5.2) the subsequent synoptic signals quickly supplant the original warm-core outflow.

This connection is firmly established by 0600 UTC 13 March as the surface storm makes landfall in northwest Florida under strong southwesterly jetlet extending from 400 to 250 hPa (Fig. 4.49). A broad signal of upper-level divergence supports the surface cyclone at this point as indicated by the opposing ageostrophy at the juxtaposition of the synoptic-scale jet streaks, though the wind speed gradient and concomitant divergence are weaker proximal to the storm (Fig. 4.49b). The transition to cold-core cyclogenesis is a geostrophic adjustment that establishes the dominance of synoptic-scale forcing in the further development of the storm. Rossby number calculations, using

$$Ro = \left| \frac{\frac{DV}{Dt}}{fV} \right| \quad (4.6.1)$$

make this relationship clearer.  $Ro$  is a measure of the importance of inertial acceleration ( $fV$ ) in the overall acceleration of the flow ( $DV/Dt$ ); inertial acceleration is relatively large for synoptic-scale processes, with  $Ro \sim 0.1$  typically equated with synoptic-scale motions, while  $Ro \sim 1$  is typical of a subsynoptic or meso- $\alpha$  phenomenon (e.g. Orlanski, 1975). At 0300 UTC at 250 hPa, the highly divergent flow along the mid-tropospheric jetlet yields  $Ro > 5$  proximal to the surface storm (Fig. 4.50a); south along the squall line,  $Ro > 7$  just west of Cuba. By 0600 UTC, the adjustment local to SOC93 reduces  $Ro < 2$ , which is consistent with the transformation of the storm from a large meso- $\beta$  convective system to a more balanced, subsynoptic cyclone (Fig. 4.50b). Along the squall line, significant divergence persists with  $Ro \sim 10$  west of Florida and north of Cuba (Fig. 4.50b).

#### 4.6.4 Summary

The final period of overwater development of SOC93 is characterized by the upscale growth of the surface vortex as the warm core is almost completely supplanted by a cold-core circulation. This transformation is most evident in the developing westward tilt of the storm with height (Fig. 4.47a) and the rapid upper-level adjustment to a quasi-balanced state at the subsynoptic scale (Fig. 4.50b). After 0600 UTC 13 March, synoptic-scale cold air (Fig. 4.46) and attendant jet streak circulations (Fig. 4.49) control the further development of the storm.

## 4.7 Potential vorticity structure

We have connected the western jet streak (Fig. 4.16, PFJ/STJ along the Mexican plateau) to the rapid frontogenesis in the central Gulf of Mexico and the subsequent transformation of the early, warm-core storm into a strong extratropical cyclone. This jet streak is associated with the upper-level PV anomaly C, diagnosed in Bosart *et al.* (1996). These authors suggest that the early, overwater development of SOC93 is strongly influenced by this PV anomaly (Bosart *et al.*, 1996). In this section, we examine the PV structure to further clarify the role of this synoptic-scale feature in Stage II.

Isentropic potential vorticity (IPV) was computed on simulation fields with

$$PV = -g \left( \frac{\partial \theta}{\partial p} \right) (\zeta_\theta + f) \quad (4.7.1)$$

where  $g$  is gravitational acceleration,  $\zeta_\theta$  is the vertical component of relative vorticity in isentropic coordinates and  $f$  is the Coriolis parameter. This formulation yields units of  $\text{K m}^2 \text{ kg}^{-1} \text{ s}^{-1}$ , and a common notational shorthand is to establish that 1 potential vorticity unit (PVU) =  $10^{-6} \text{ K m}^2 \text{ kg}^{-1} \text{ s}^{-1}$  (Hoskins *et al.*, 1985). A column-weighted average PV was analyzed from 336 K (about 375 hPa) to 316 K (about 650 hPa), to approximate the 350:675 hPa column used in the QGPV analysis of Bosart *et al.* (1996)

PV anomaly C is well-simulated at 1200 UTC 12 March and appears as a lobe of isentropic potential vorticity (IPV) extending from western Texas south along the Rio Grande Valley (Fig. 4.51a). The incipient SOC93 (1003 hPa surface low) is supported by a pool of IPV ( $> 1$  PVU) that appears distinct from PV anomaly C and its attendant positive IPV advection (Fig. 4.51a). We have established previously that the proximity of the initial SOC93 and PV anomaly C is not a simple cause-and-effect relationship: the mesoscale convective complex that supports the initial warm-core cyclone (Fig. 4.1a) is triggered by a strong upper-level divergence created at the juxtaposition of the western jet streak (attendant to PV anomaly C) and dry convective outflow from the Mexican plateau. This is a clarification of previous speculation by Bosart *et al.* (1996) and Dickinson *et al.* (1997) that warm advection ahead of PV anomaly C triggers the initial MCC; we contend that this PV anomaly (through its attendant jet streak) is important to the early convection, though the warm signal in this process is largely a product of the Mexican plateau (Chapter 3).

The separation of the nascent SOC93 from the upper-level PV feature is more evident at 1800 UTC 12 March (Fig. 4.51b) with weak to negative IPV advection separating the synoptic-scale feature from the warm-core cyclone (994 hPa) and the evolving secondary storm (1002 hPa). Significant pools of IPV ( $> 1$  PVU) support both cyclones, however, and indicate the redistribution of potential vorticity from the lower and mid-troposphere. As the western jet streak advances around the long-wave trough (Fig. 4.33b), positive IPV advection attendant to PV anomaly C begins to overtake the weakening primary cyclone (Fig. 4.51c), concomitant with the transformation of the early warm-core storm to a larger-scale cold-core system. By 0600 UTC 13 March, the amplifying PV anomaly is a signal of the amplifying cold air that is dominating the surface development (Fig. 4.51d). The significant region of negative IPV advection south of the surface low indicates that there is still a significant pool of potential vorticity intrinsic to the original warm-core storm; from this we infer that the transformation, though well underway, is not complete by 0600 UTC 13 March (Fig. 4.51d).

These results are consistent with the numerical sensitivity studies of Huo *et al.* (1999b). Using PV inversion (Davis and Emanuel, 1991), these investigators altered the initial potential vorticity distribution, to include removal of PV anomaly C (characterized in the study as the southern trough); strong surface cyclogenesis in the Gulf occurs even without this upper-level feature (Huo *et al.*, 1999b). We should note that in this study the numerical experiments were initialized at 1200 UTC 12 March, with the meso- $\beta$  storm vortex (Fig. 4.4a) intrinsic to the first-guess fields. From these results and the findings of Huo *et al.* (1999b) we infer that upper-level PV anomaly C is relatively unimportant to the much of the overwater (Stage II) development of SOC93. PV anomaly C becomes increasingly important as the storm transitions from a meso- $\alpha$ , convectively-driven storm into a synoptic-scale extratropical cyclone after landfall on 13 March. This PV perspective is equivalent to the previous analysis of upper-level jets proximal to the secondary development (Sec. 4.54.5.2). The rapid ( $\sim 3$  h) penetration of the western cold surge and western jet streak exit region introduce strong baroclinicity and a favorable frontogenetical circulation on the southwest flank of the developing storm; the subsequent adjustment to this circulation is responsible for the transformation of SOC93 to a larger-scale, cold-core system.

## 4.8 Concluding discussion

The March 1993 Storm of the Century challenged operational models with a rapid cyclogenesis in the Gulf of Mexico that accounted for fully half the deepening in the complete evolution of the storm. This research was motivated to elucidate the mesoscale details of this early cyclogenesis. Previous chapters have established the mechanisms that initiated and organized the deep convection in the western Gulf early on 12 March (Fig. 4.1a). This chapter has focused on the development of this warm-core system over the Gulf and its subsequent transformation into a cold-core storm about the time of landfall early on 13 March.

These results clarify the relationship among the synoptic-scale jet streaks proximal to the Gulf and the convective outflow jetlet attendant to the early SOC93. Kocin *et al.* (1995), among others, have noted the interaction of polar and subtropical jet streaks in the post-landfall (after 0600 UTC 13 March) storm. In a study of snowstorms in the southeastern U.S., Mote *et al.* (1997) *excluded* SOC93 from their sample because this jet streak interaction was more characteristic of heavy east coast snowstorms (e.g. Kocin and Uccellini, 1990). We have demonstrated, however, that significant convective outflow from the early overwater storm *connects* these synoptic-scale jet streaks. Although previous studies have speculated on the importance of convection to the storm (e.g. Dickinson *et al.*, 1997), particularly as the focus of mesoscale cyclogenesis early in the development, the *role* of this convection in restructuring the upper-level flow has not been documented.

An additional, though not independent, finding is that the upper-level potential vorticity anomaly attendant to the western jet streak is relatively unimportant to the development of SOC93 in much of the overwater period. This clarifies the synoptic-scale analyses of Bosart *et al.* (1996) and provides an additional perspective on the numerical studies of Huo *et al.* (1999b). This is consistent with our hypothesis that the early storm undergoes a *sustained* warm-core development in the Gulf of Mexico. This represents a significant advancement in understanding the complete evolution of SOC93: this early, convection-driven development is precisely the period (about 1200 UTC 12 March to 0600 UTC 13 March) that was so poorly captured in operational models (Caplan, 1995).

The preeminence of warm air from the Mexican plateau in the overall development of SOC93 represents, perhaps, the most important finding of this work. Previously, we have

established the importance of the dry, diabatically-forced mountain-plains solenoid (MPS) to the creation of a substantial pool of convective available potential energy off the Texas Gulf Coast (Chapter 2). This potential energy is then realized under a strong upper-level divergence created at the junction of the MPS outflow and the approaching western jet streak, triggering the initial MCC that supports the early surface storm (Chapter 3). In this chapter, we have demonstrated that this warm plateau air, moistened by the marine boundary layer and coupled to the entrance region of a subtropical jet streak, focuses moisture convergence in the lower troposphere along an axis with residual cool air along the northern Gulf coast, triggering deep convection and a secondary warm-core cyclogenesis in the central Gulf. With the advance of cold air into the western flank of the surface storm, this plateau air becomes the warm sector of the developing cold-core system. The geostrophic adjustment concomitant to this transformation induces a mid-tropospheric jetogenesis that, in turn, triggers an inertial instability created on the anticyclonic flank of the jetlet; the subsequent inertia-gravity waves trigger a strong squall precisely along this warm plateau air. Additional research at the mesoscale could demonstrate that many of these mechanisms related to the MPS are ubiquitous to cool-season (Nov – Apr) cyclogenesis events in the eastern U.S.

Stage	Period	Characteristics
<b>I</b>	0000 UTC 11 March to 1200 UTC 12 March	A sequence of mesoscale processes constructs a warm-core surface cyclone.
<b>II</b>	1200 UTC 12 March to 0600 UTC 13 March	The storm develops as a warm-core low then is transformed into an extratropical (cold-core) system.
<b>III</b>	0600 UTC 13 March to 0000 UTC 14 March	The storm intensifies again as strong PV anomalies merge over the southeastern U.S. The storm then matures over the northeastern U.S.

Table 4.1: Summary of the SOC93 three-stage evolution.

Experiment ID	Horizontal Resolution	Physics	Initialization
CONTROL	12 km	Full model physics	ECMWF 1.125° Synthetic SST field
SMOOTH	12 km	Full model physics	ECMWF 1.125° Synthetic SST field Smoothed model terrain
ADIABATIC	12 km	Adiabatic physics No PBL or cumulus scheme	ECMWF 1.125° Synthetic SST field
NOLATENT	12 km	PBL physics enabled Latent heating enabled	ECMWF 1.125° Synthetic SST field
NOSFLX	12 km	Surface sensible heat flux disabled Latent heating enabled	ECMWF 1.125° Synthetic SST field
NCEP	12 km	Full model physics	NCEP 2.5° Synthetic SST field
NHCSST	12 km	Full model physics	ECMWF 1.125° NHC SST field

Table 4.2: Numerical experiments. All simulations initialized at 1200 UTC 10 March.

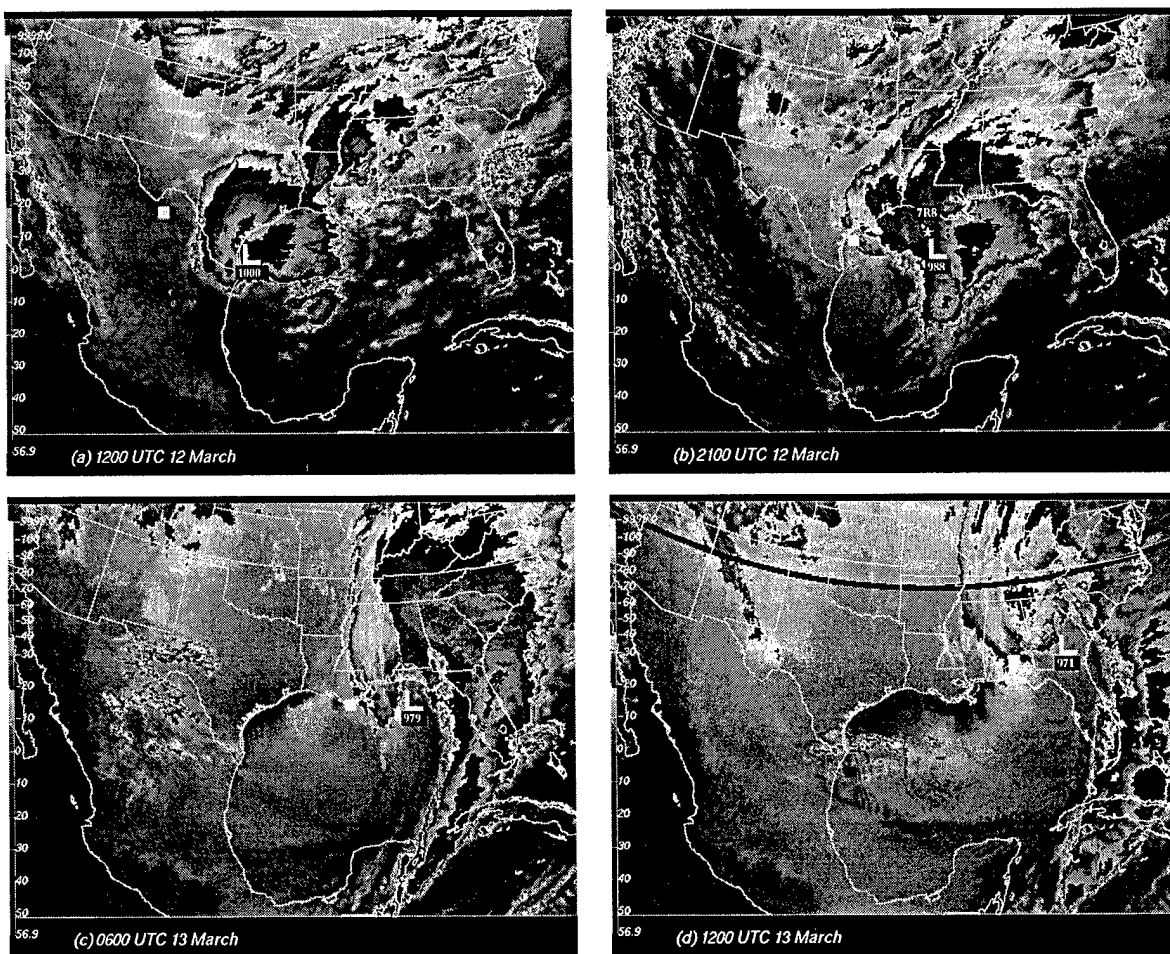


Figure 4.1: GOES-7 IR imagery with superimposed storm positions from the mesoanalysis of Kocin et al. (1995), valid (a) 1200 UTC 12 March (1000 hPa), (b) 2100 UTC 12 March (988 hPa), (c) 0600 UTC 13 March (979 hPa), and (d) 1200 UTC 13 March (971 hPa). The position of PV anomaly C (Bosart et al., 1996), discussed in the text, is indicated by the filled square. South Marsh Island, LA (7R8) is indicated by the star in (b).



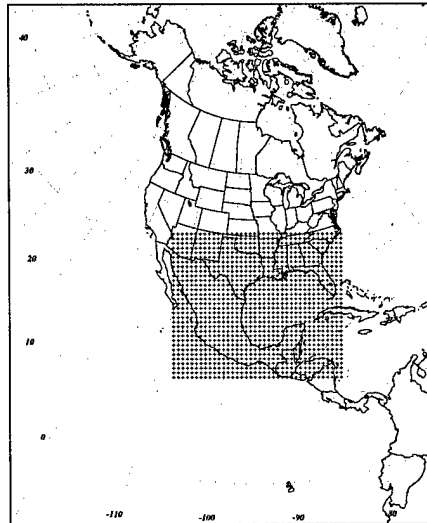


Figure 4.2: Grid boundaries for the 12 km simulations; every sixth grid point is displayed.

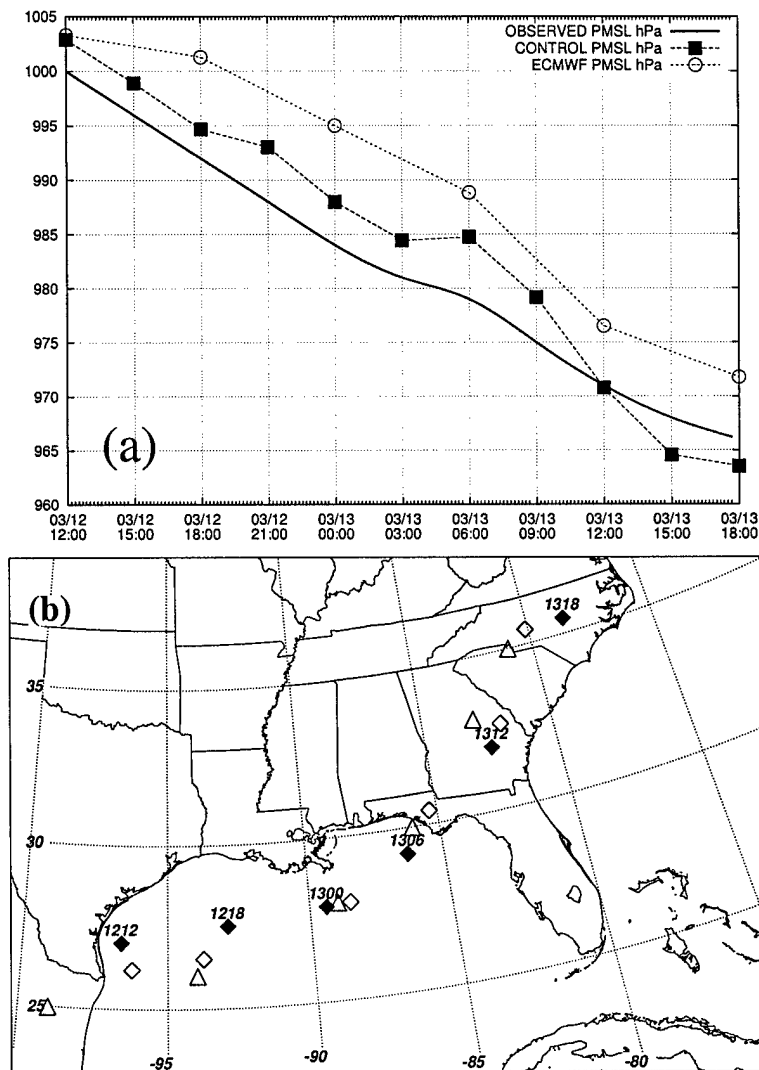


Figure 4.3: Track of the SOC93 surface cyclone in the mesoanalysis of Kocin et al. (1995), the CONTROL simulation and the ECMWF analysis. Depicted are comparisons of (a) storm central pressures and (b) storm position, where the mesoanalysis is indicated by a filled diamond, the CONTROL simulation is indicated by a hollow diamond, and the ECMWF analysis is indicated by the hollow triangle. Times in (b) are of the form DDHH (e.g. 1218 = 1800 UTC 12 March).

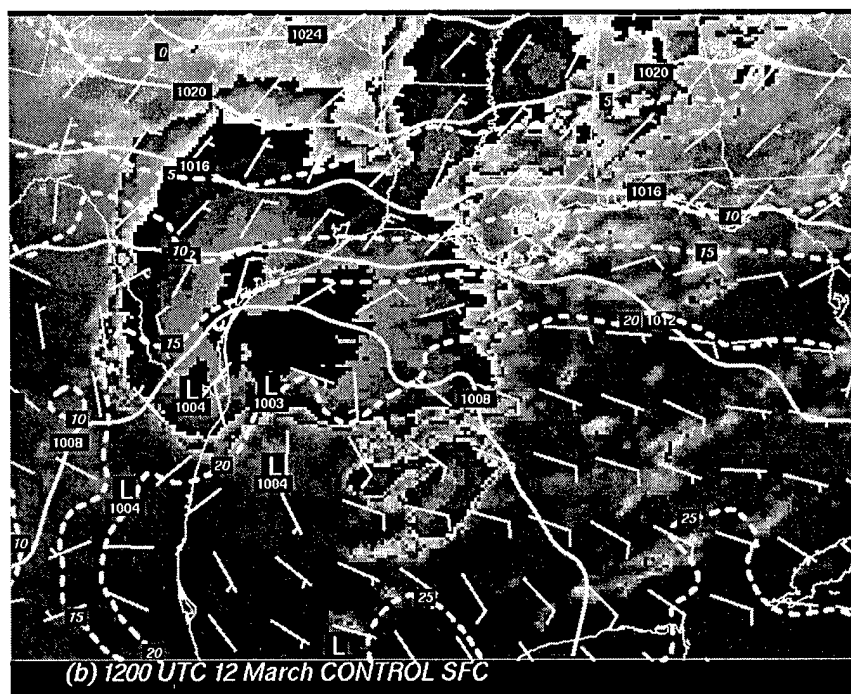
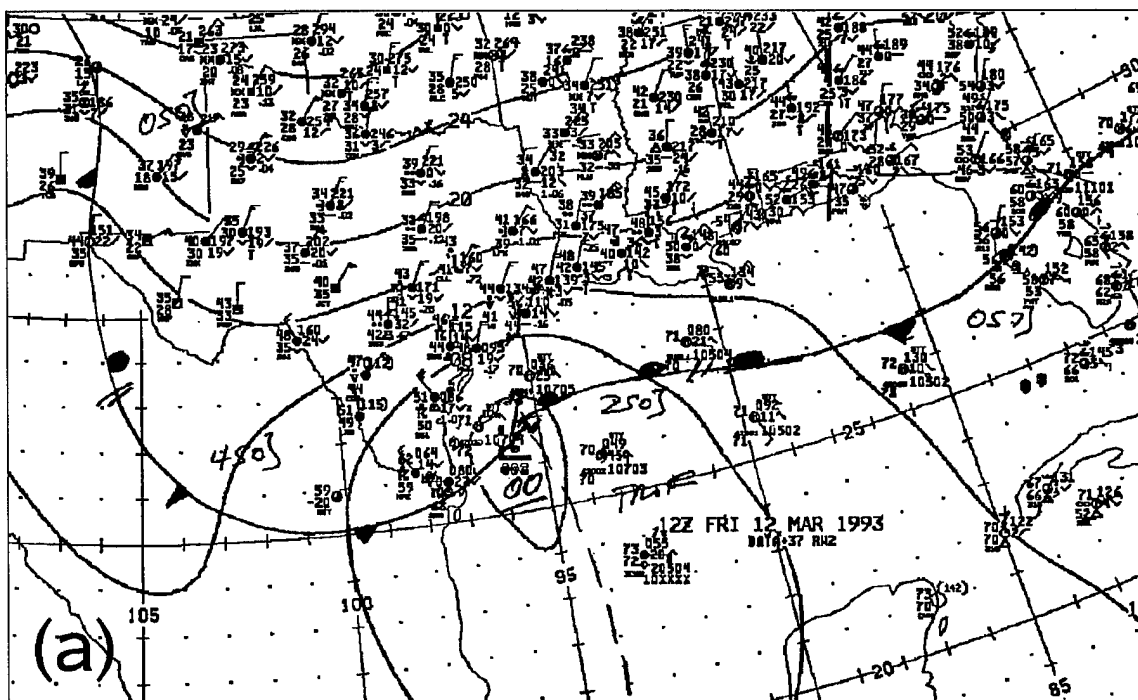


Figure 4.4: Observed and simulated surface fields at 1200 UTC 12 March. (a) NCEP surface analysis and (b) CONTROL surface fields on GOES-7 IR imagery, depicting PMSL (solid every 4 hPa), surface temperature (dashed every 5 C), and total wind vectors (in  $\text{m s}^{-1}$ ).

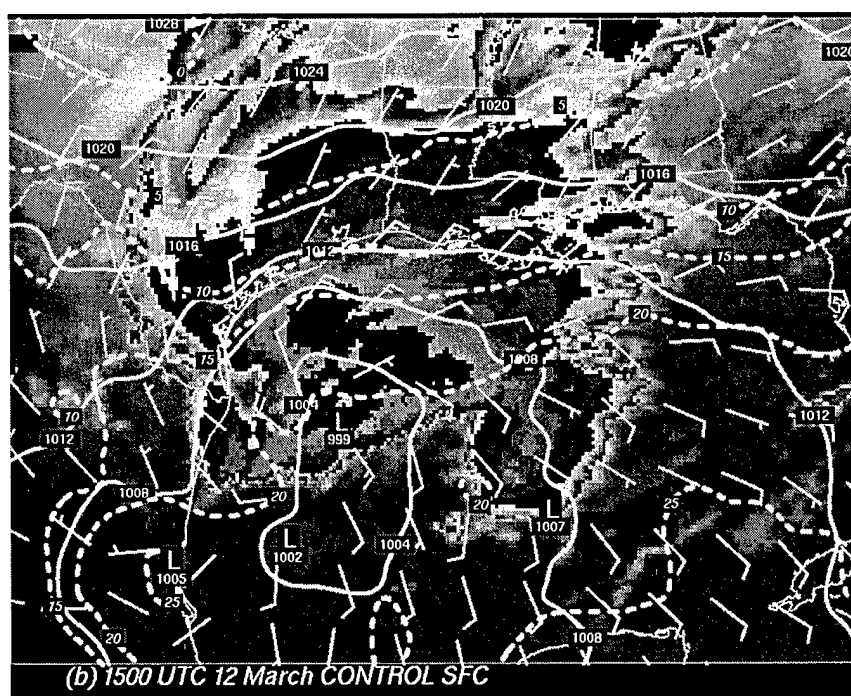
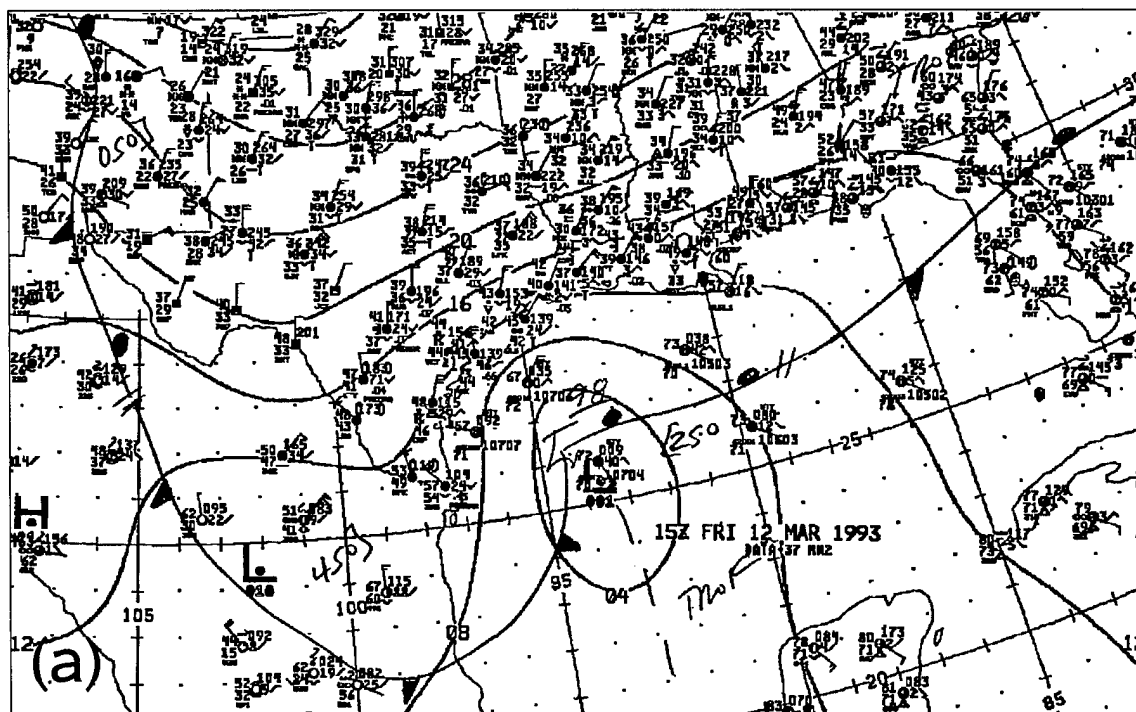


Figure 4.5: Observed and simulated surface fields at 1500 UTC 12 March. (a) NCEP surface analysis and (b) CONTROL surface fields on GOES-7 IR imagery, depicting PMSL (solid every 4 hPa), surface temperature (dashed every 5 C), and total wind vectors (in  $\text{m s}^{-1}$ ).

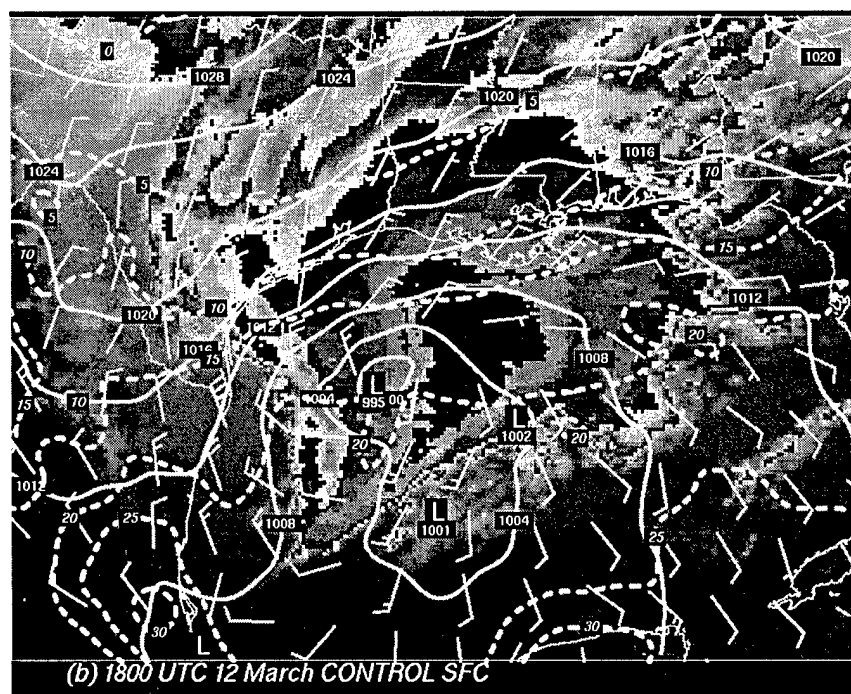
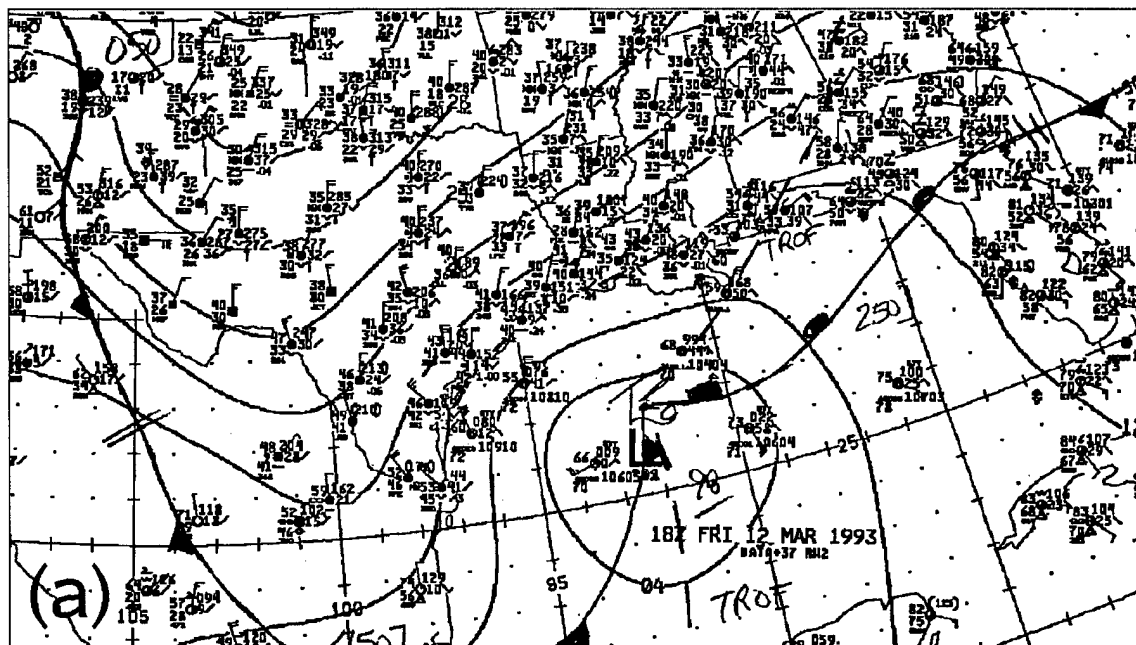


Figure 4.6: Observed and simulated surface fields at 1800 UTC 12 March, as in Fig. 4.4.

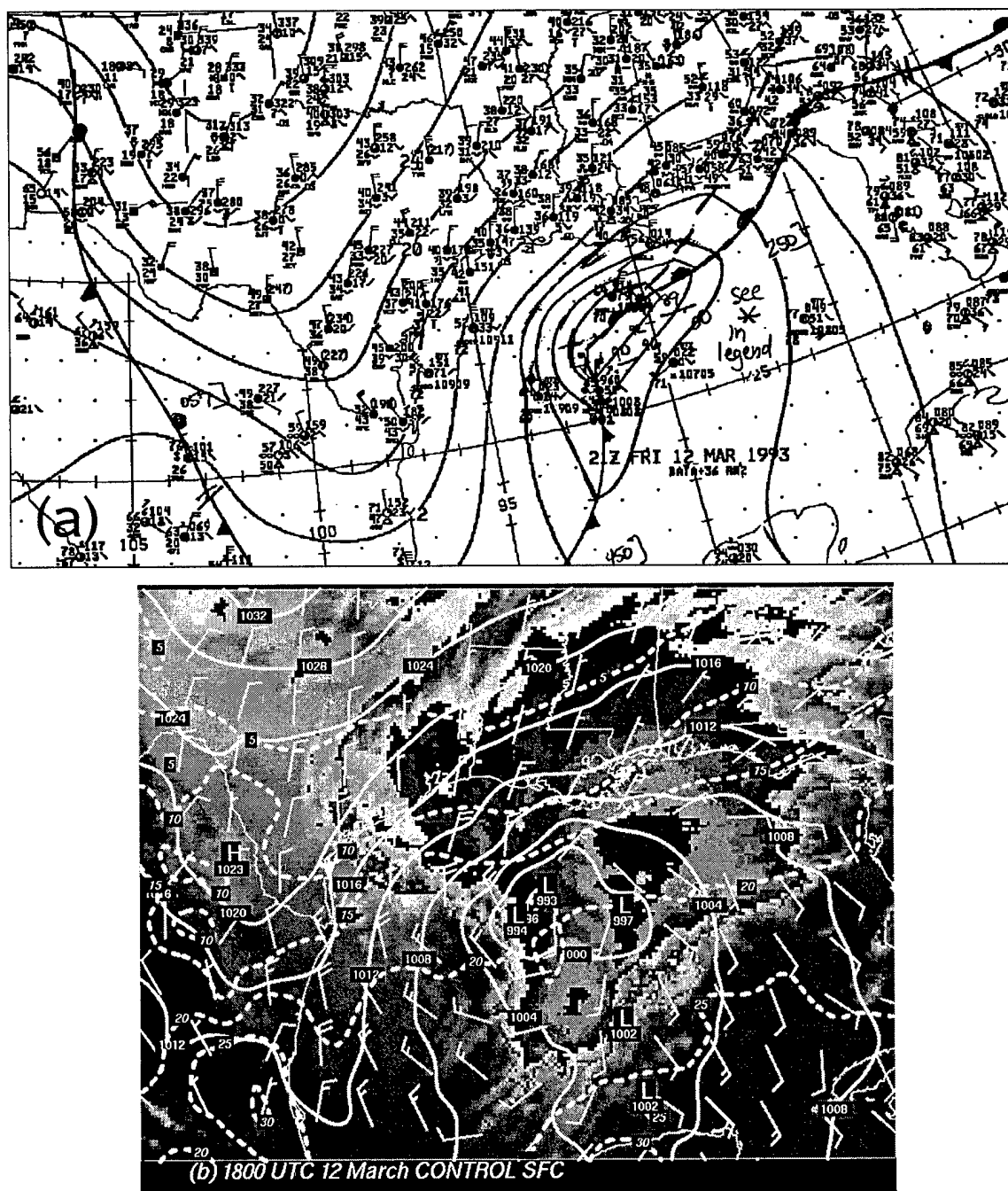


Figure 4.7: Observed and simulated surface fields at 2100 UTC 12 March, as in Fig. 4.4.

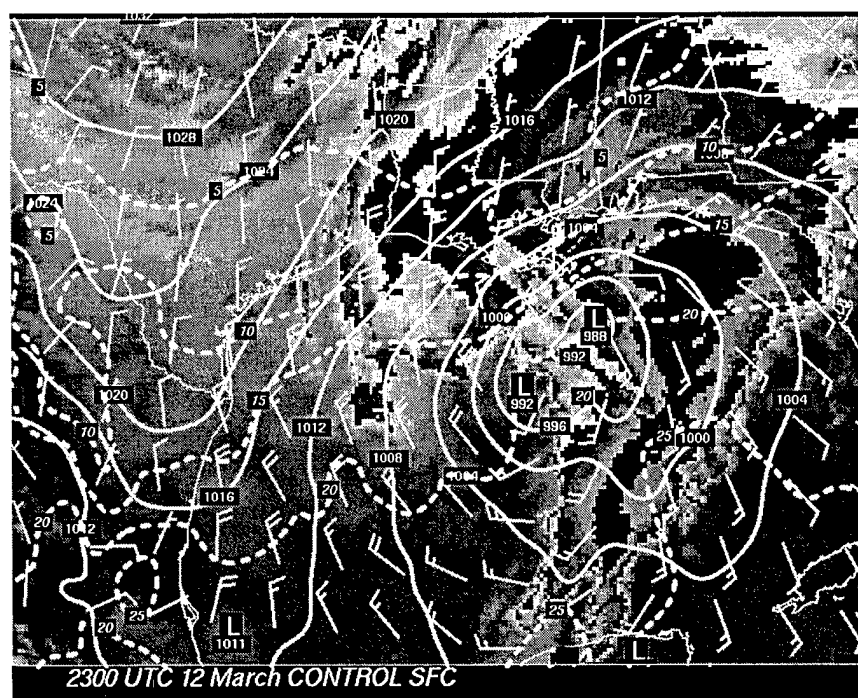
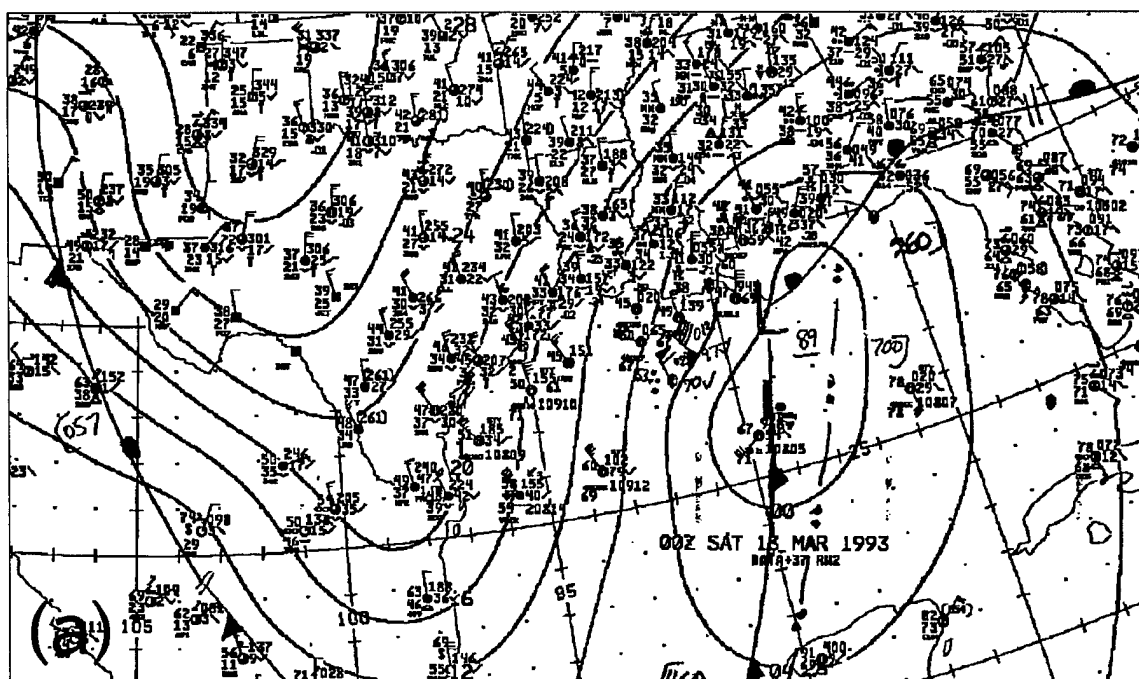


Figure 4.8: Observed and simulated surface fields at 0000 UTC 13 March, as in Fig. 4.4.

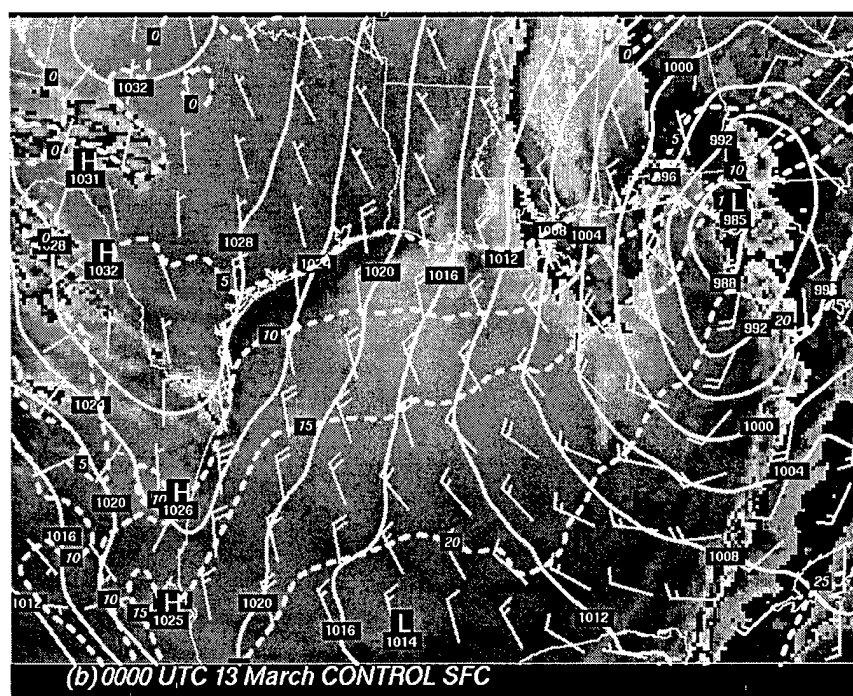
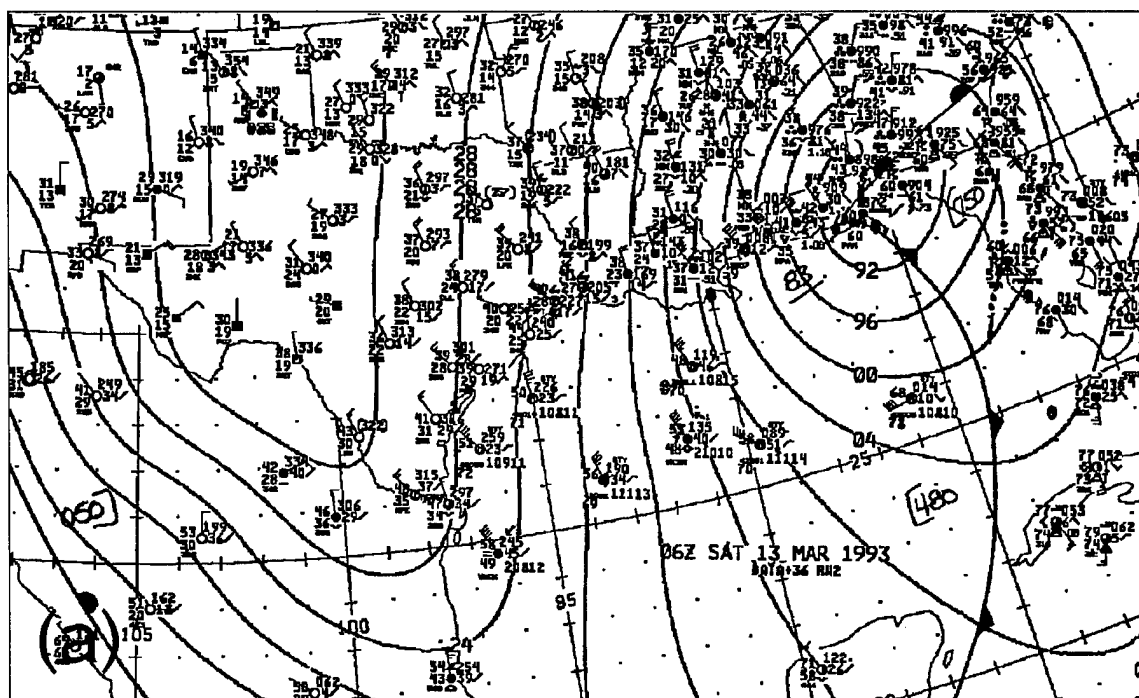


Figure 4.9: Observed and simulated surface fields at 0600 UTC 13 March, as in Fig. 4.4.



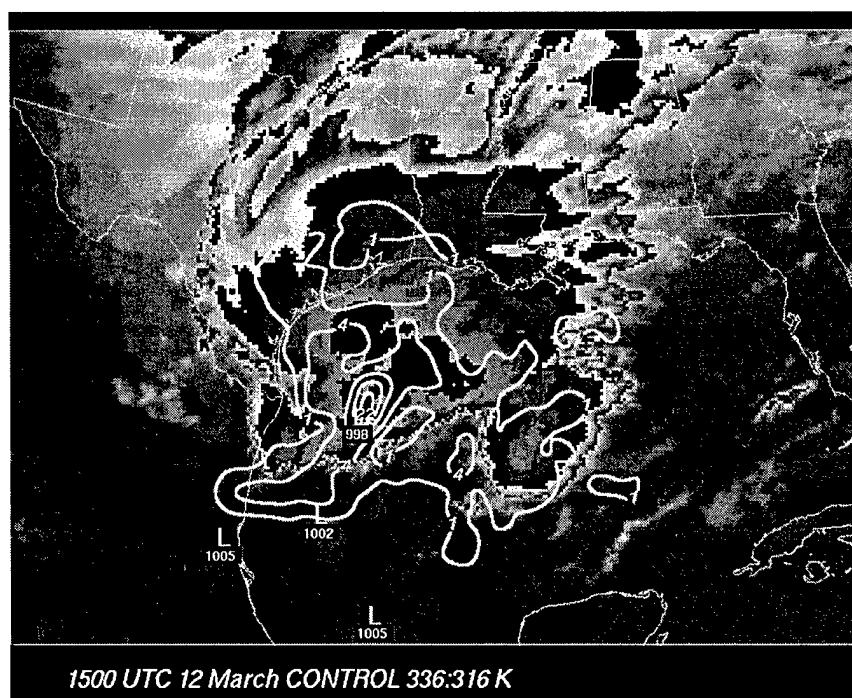


Figure 4.10: CONTROL simulation at 1500 UTC 12 March. Vertically integrated instantaneous diabatic heating from 336 K (350 hPa) to 316 K (650 hPa) contoured at 1, 4, 10, 16, and 22  $\text{K h}^{-1}$ , and layer-averaged wind field in the column 336:316 K, superimposed on GOES-7 IR.

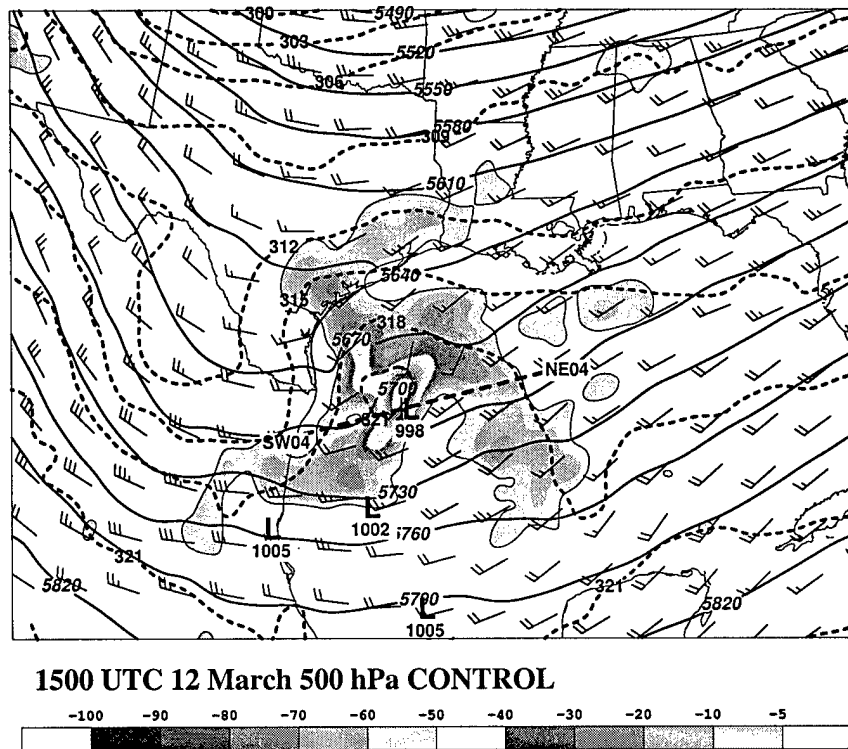
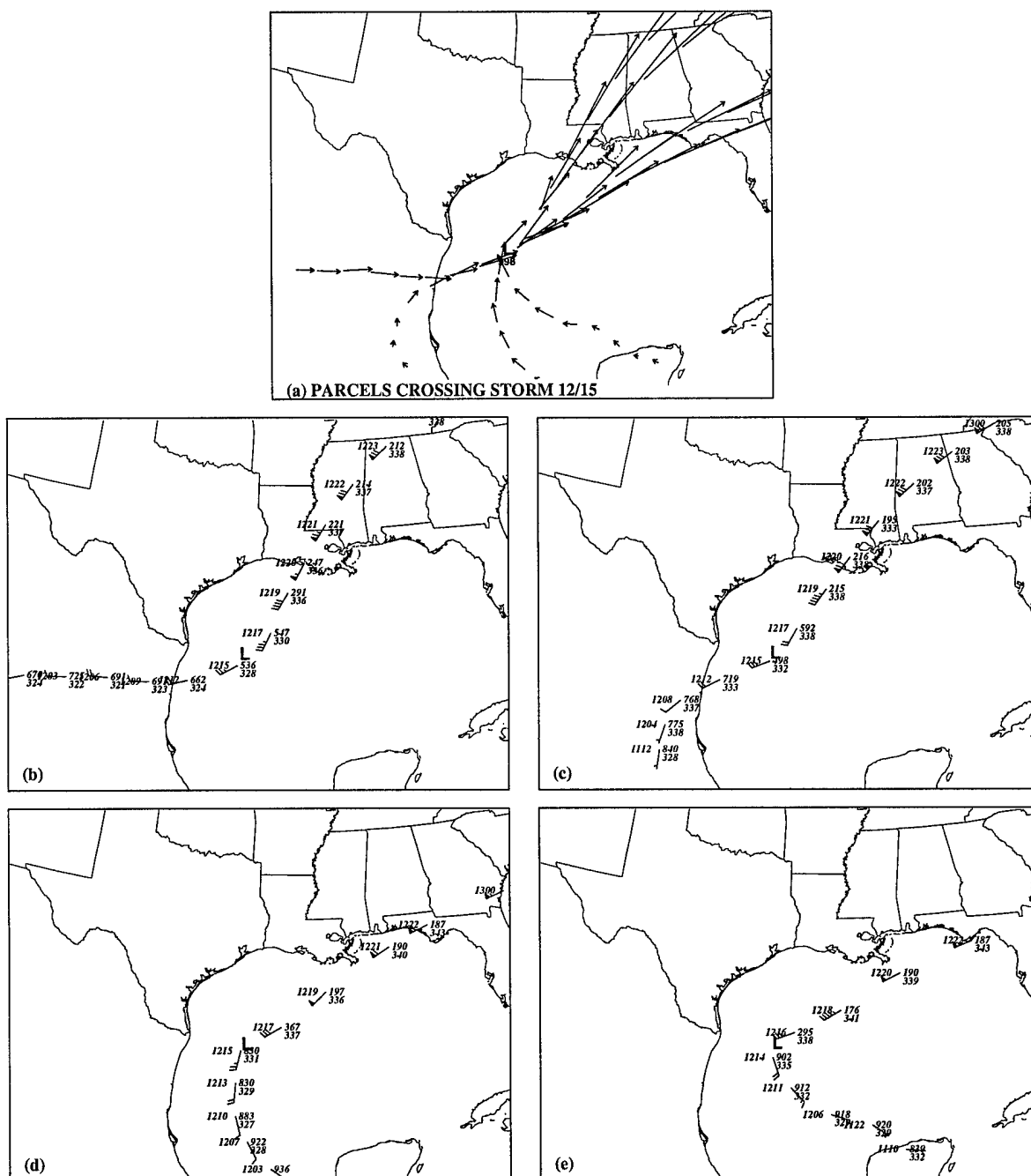


Figure 4.11: CONTROL 500 hPa fields at 1500 UTC 12 March. Depicted are geopotential height (contoured every 30 m), isentropes (contoured every 3 K), standard wind vectors (in  $\text{m s}^{-1}$ ), and vertical velocity (shaded in  $\mu\text{bar s}^{-1}$ ). Surface low pressure centers are indicated.



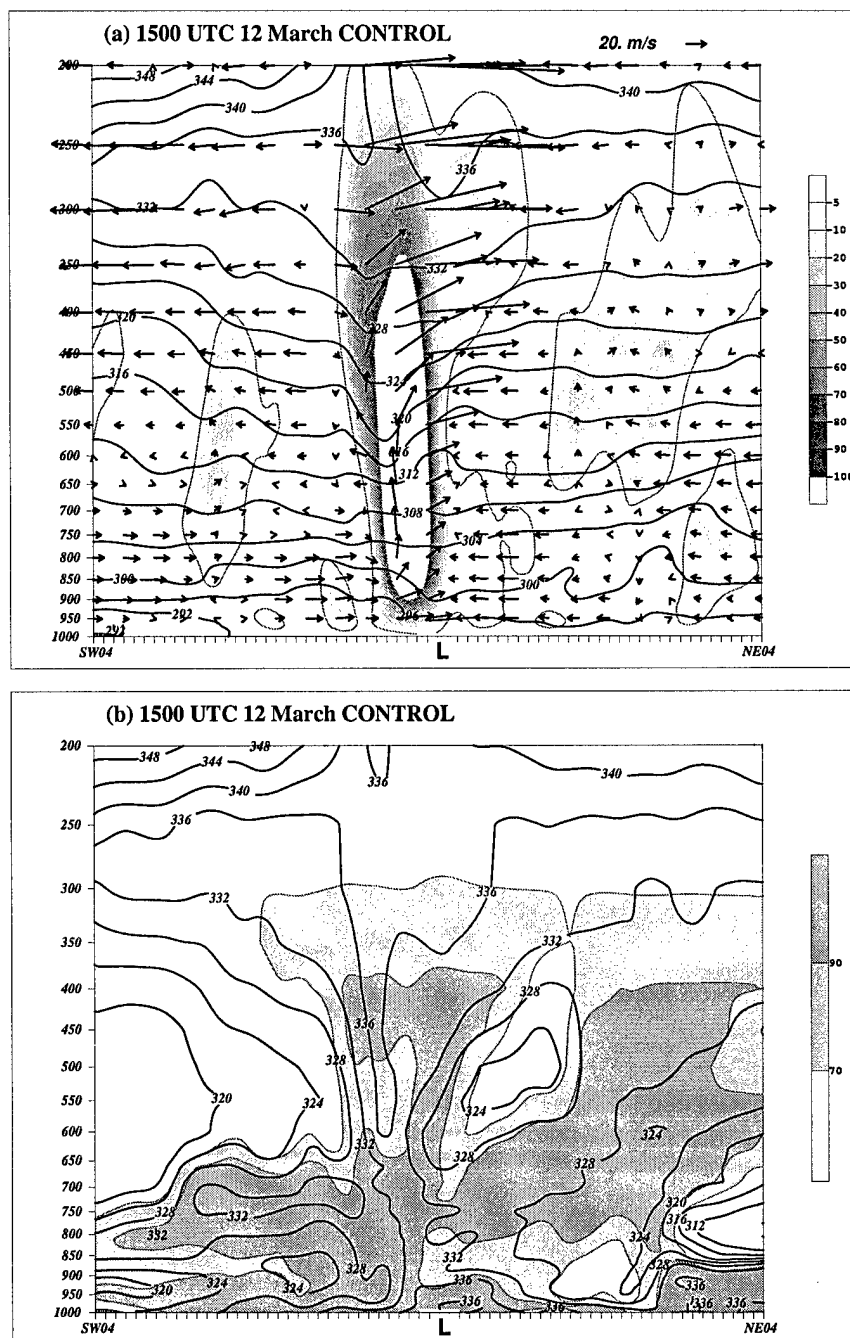


Figure 4.13: CONTROL cross-sections along the path of the storm at 1500 UTC 12 March, depicting (a) potential temperature (contoured every 2 K), ageostrophic circulation vectors, and vertical velocity (shaded in  $\mu\text{bar s}^{-1}$ , ascent only shown); and (b) equivalent potential temperature (contoured every 4 K) and relative humidity (shaded at 70% and 90%). Plane of the cross-section is indicated in Fig. 4.11.

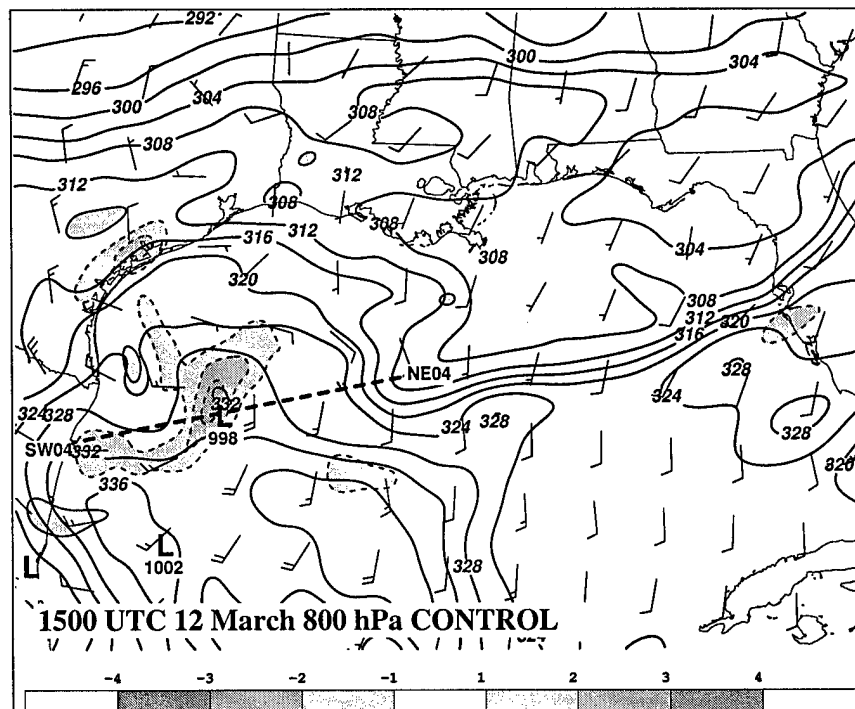


Figure 4.14: CONTROL 800 hPa fields at 1500 UTC 12 March. Depicted are equivalent potential temperature ( $\theta_e$ ) contoured every 4 K, divergence shaded and contoured every  $1 \times 10^{-4} \text{ s}^{-1}$  (negative dashed contour), and standard wind vectors in  $\text{m s}^{-1}$ . Surface low pressure centers and the plane of the cross-section in Fig. 4.13 are indicated.

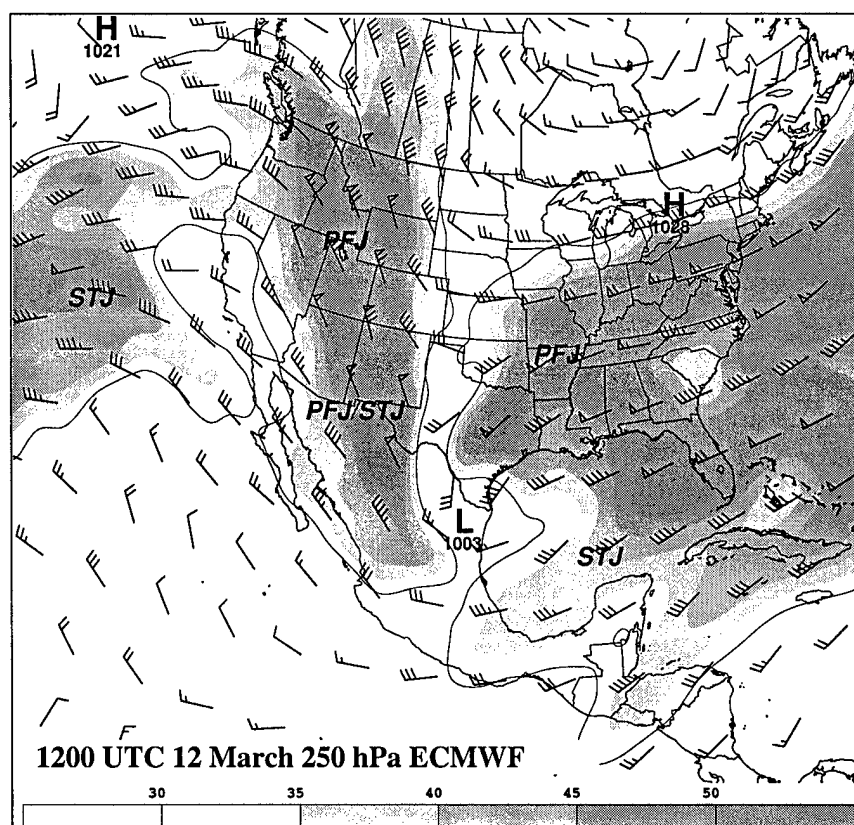


Figure 4.15: ECMWF 250 hPa jet analysis at 1200 UTC 12 March. Depicted are standard wind vectors (in  $\text{m s}^{-1}$ ) and isotachs (shaded  $> 35 \text{ m s}^{-1}$ ).

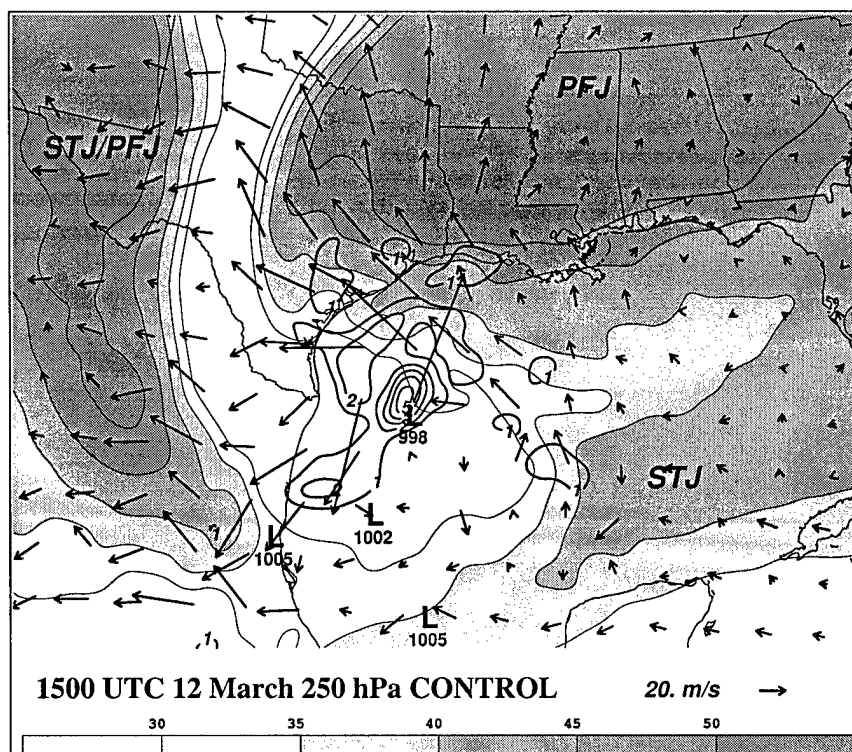


Figure 4.16: CONTROL 250 hPa fields at 1500 UTC 12 March. Depicted are total wind speed ( $> 35 \text{ m s}^{-1}$  shaded), ageostrophic wind vectors (reference vector in lower right of panel) and horizontal divergence (contoured every  $1 \times 10^{-4} \text{ s}^{-1}$ ).

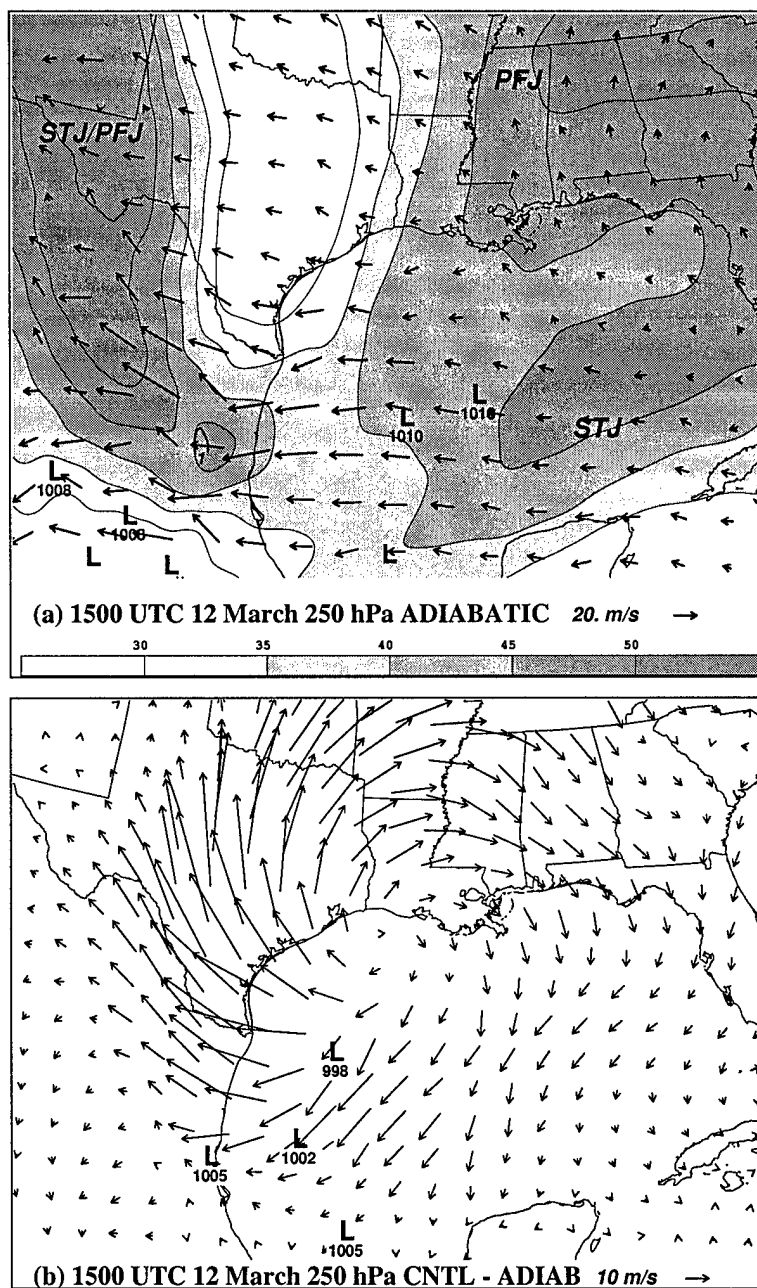


Figure 4.17: ADIABATIC comparisons at 250 hPa, 1500 UTC 12 March. (a) total wind speed ( $> 35 \text{ m s}^{-1}$  shaded), ageostrophic wind vectors (reference vector in lower right of panel) and horizontal divergence (contoured every  $1 \times 10^{-4} \text{ s}^{-1}$ ); and (b) vector subtraction of total wind ( $V_{CNTL} - V_{ADIA}$ ), reference vector in lower right of panel. Surface low pressure centers from the ADIABATIC simulation are indicated in (a); centers from the CONTROL simulation are indicated in (b).



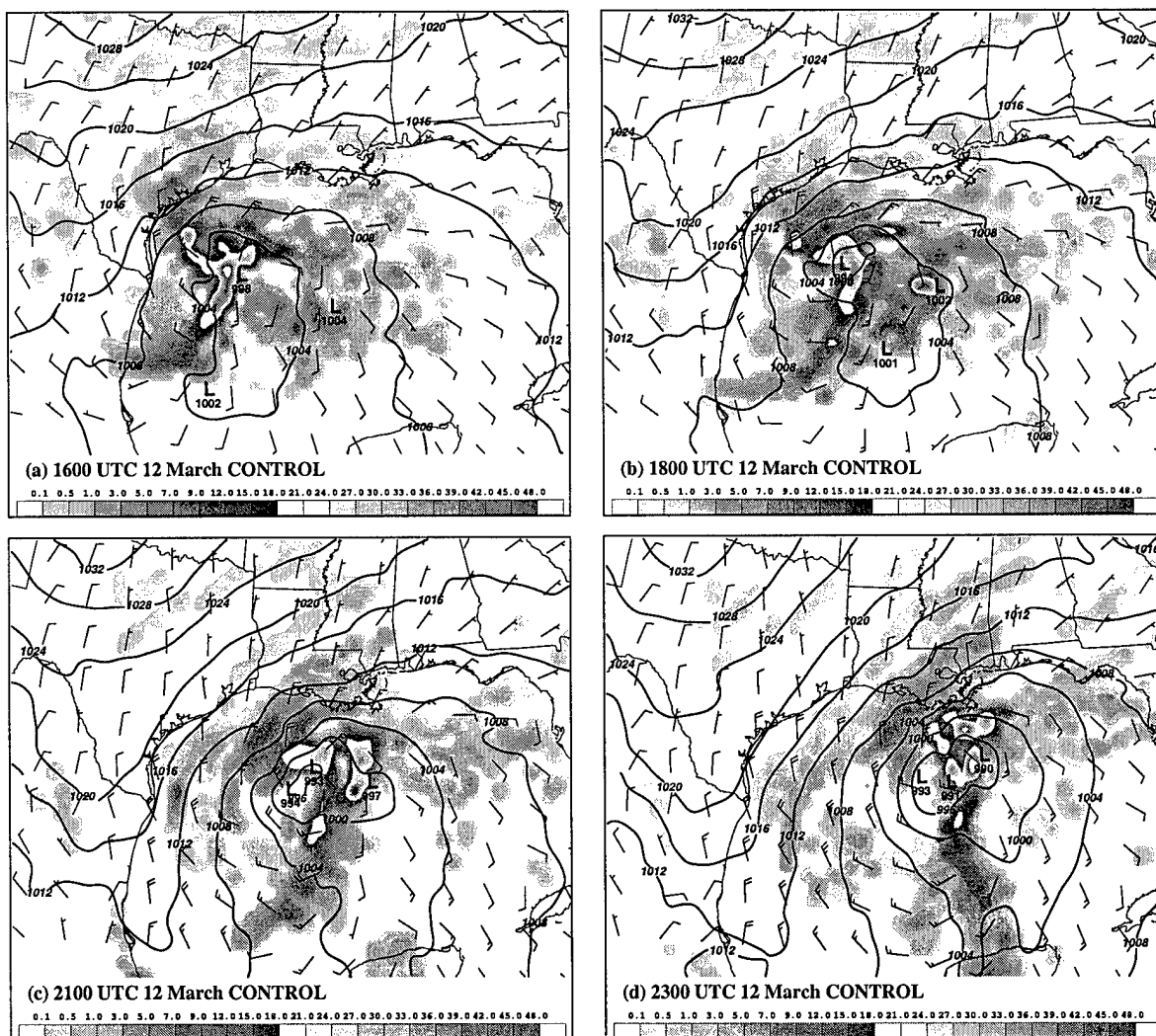


Figure 4.18: CONTROL surface fields, depicting PMSL (contoured every 4 K), surface wind vectors (in  $\text{m s}^{-1}$ ), and total precipitation (shaded in  $\text{mm h}^{-1}$ ), valid (a) 1600 UTC, (b) 1800 UTC, (c) 2100 UTC, and (d) 2300 UTC 12 March.

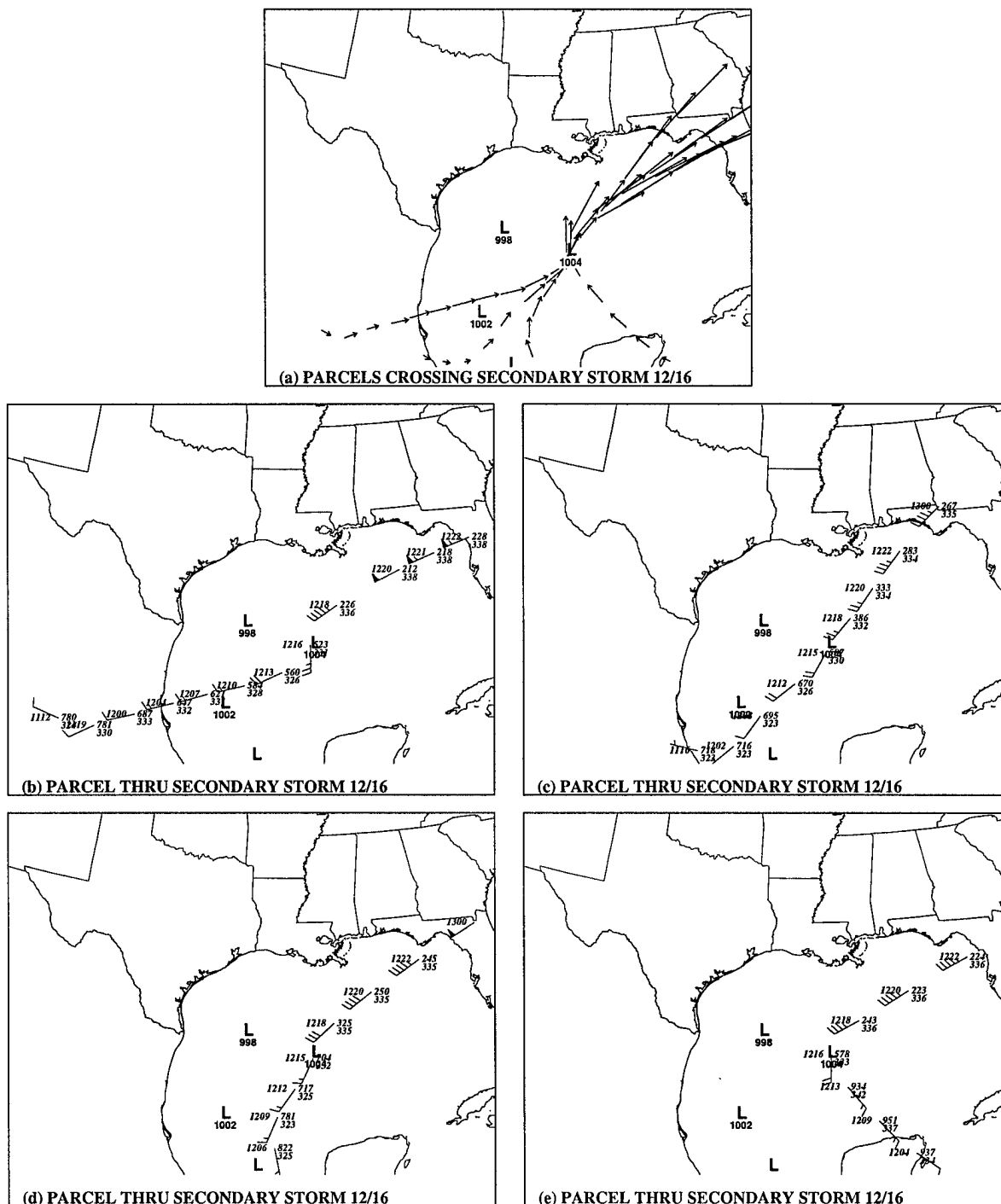
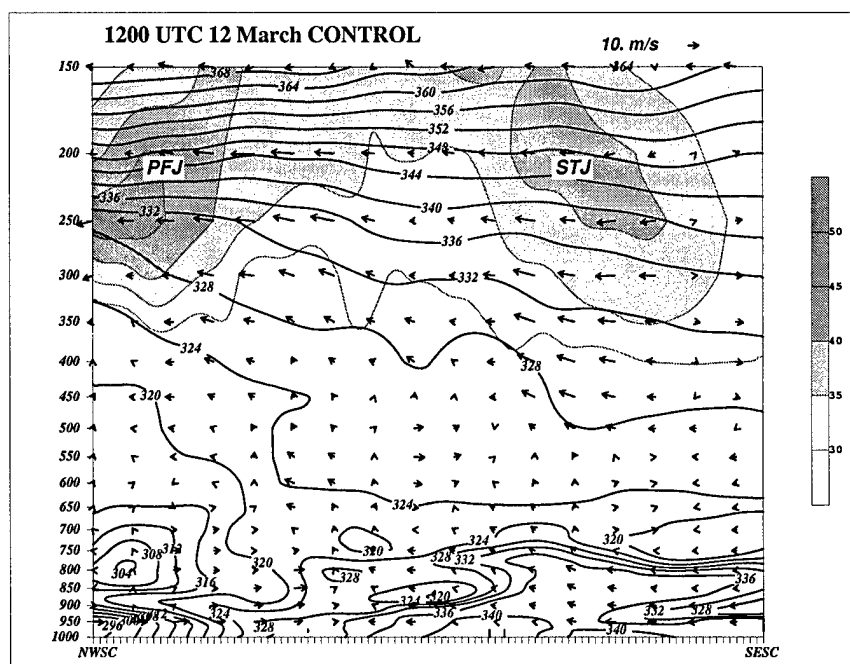


Figure 4.19: CONTROL parcel trajectories crossing the secondary storm at 1600 UTC 12 March. Depicted are (a) a composite of four representative trajectories, with arrows representing wind speed; and (b)-(e), individual trajectories following the plot model: standard wind vector in  $\text{m s}^{-1}$ , DDHH (e.g. 1215 = 1500 UTC 12 March) in the upper left, parcel pressure (hPa) at upper right and equivalent potential temperature ( $\theta_e$ , in K) at lower right.





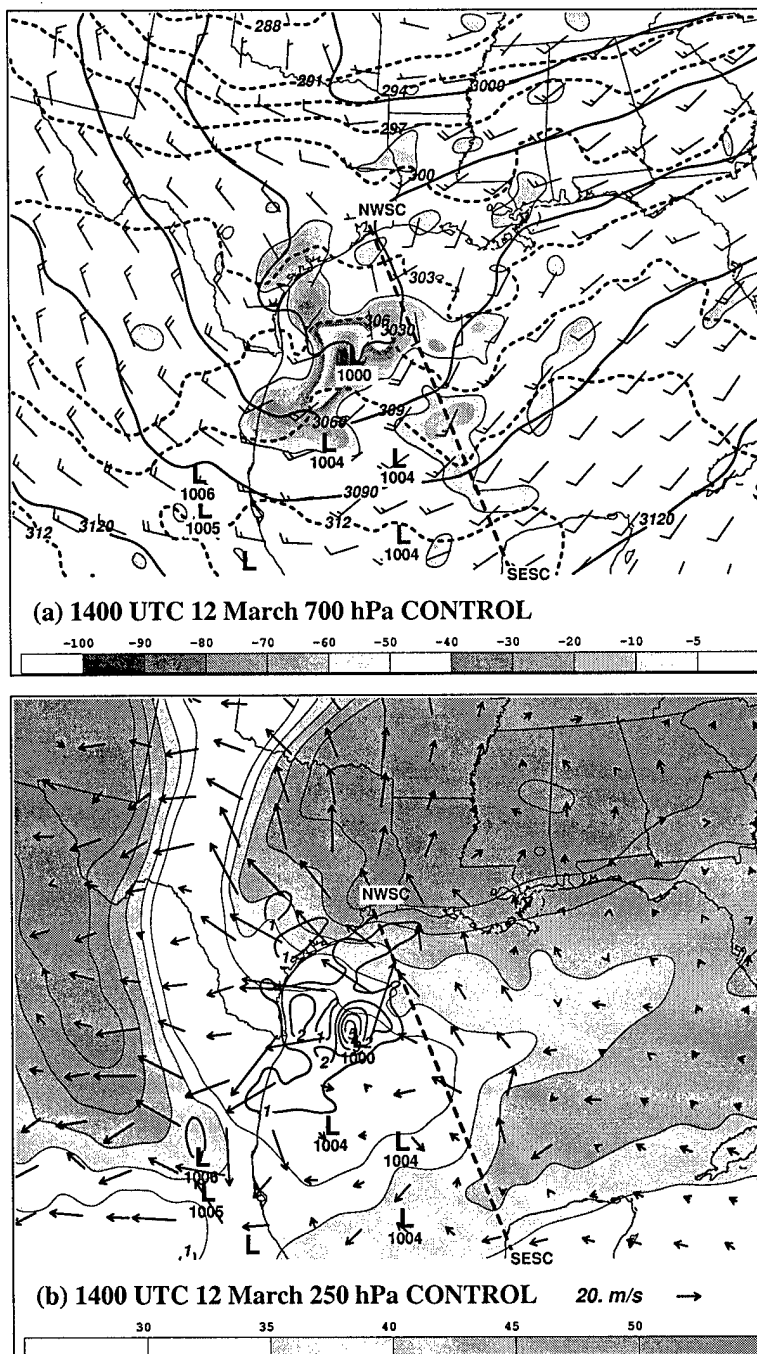


Figure 4.22: CONTROL analysis at 1400 UTC 12 March, as in Fig. 4.20.

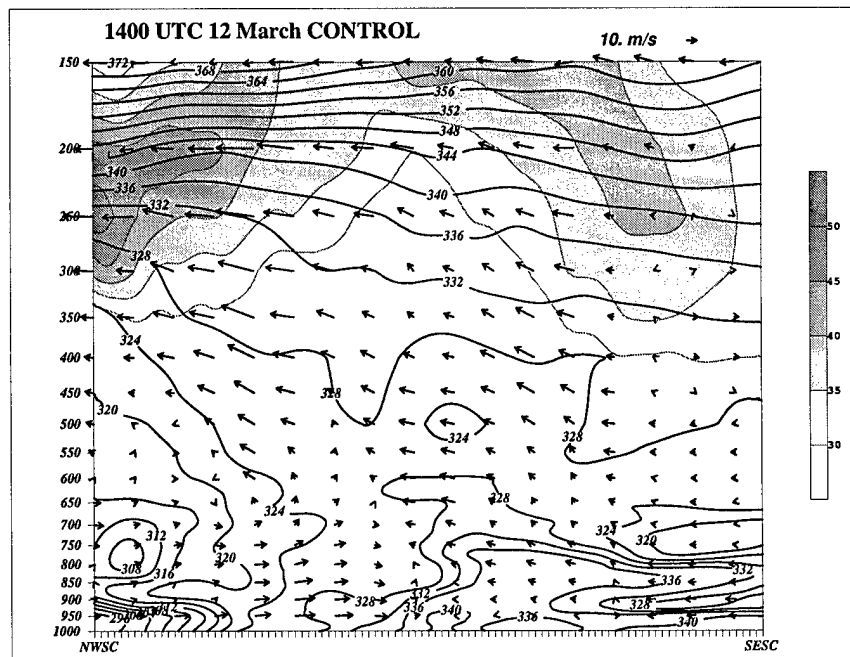


Figure 4.23: CONTROL cross-section at 1400 UTC 12 March along the plane indicated in Fig. 4.22, parameters as in Fig. 4.21.

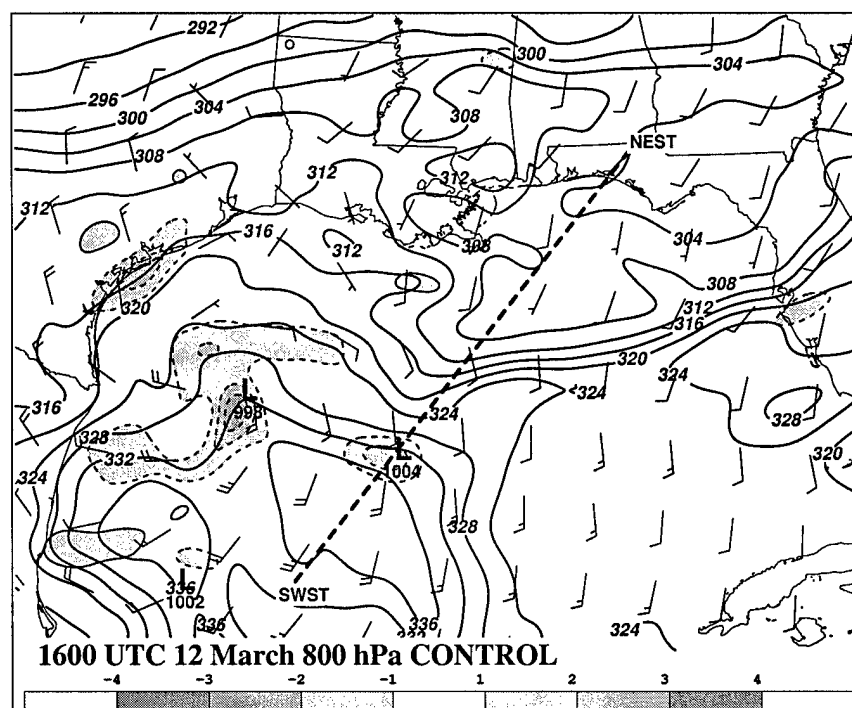


Figure 4.24: CONTROL 800 hPa fields at 1600 UTC 12 March, depicting equivalent potential temperature ( $\theta_e$ ) contoured every 4 K, standard wind vectors (in  $\text{m s}^{-1}$ ) and divergence (shaded every  $1 \times 10^{-4}$ , negative dashed). Positions of surface lows are indicated.

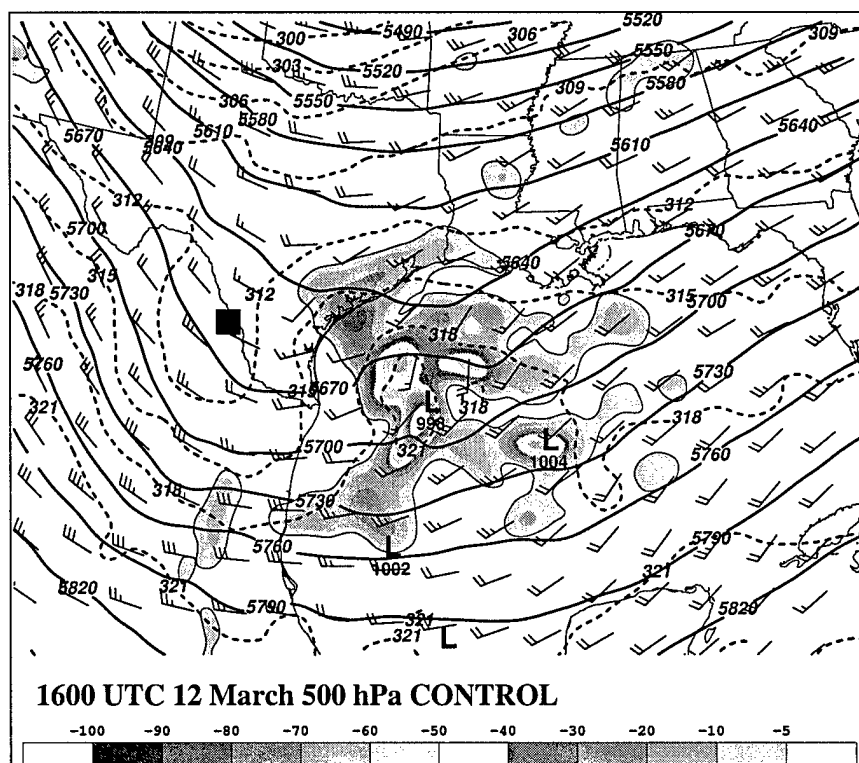


Figure 4.25: CONTROL 500 hPa fields at 1600 UTC 12 March. Depicted are potential temperature ( $\theta$ ) contoured every 3 K, standard wind vectors (in  $\text{m s}^{-1}$ ) and vertical velocity (shaded in  $\mu\text{bar s}^{-1}$ ). The position of PV anomaly C (Bosart et al., 1996) is indicated.



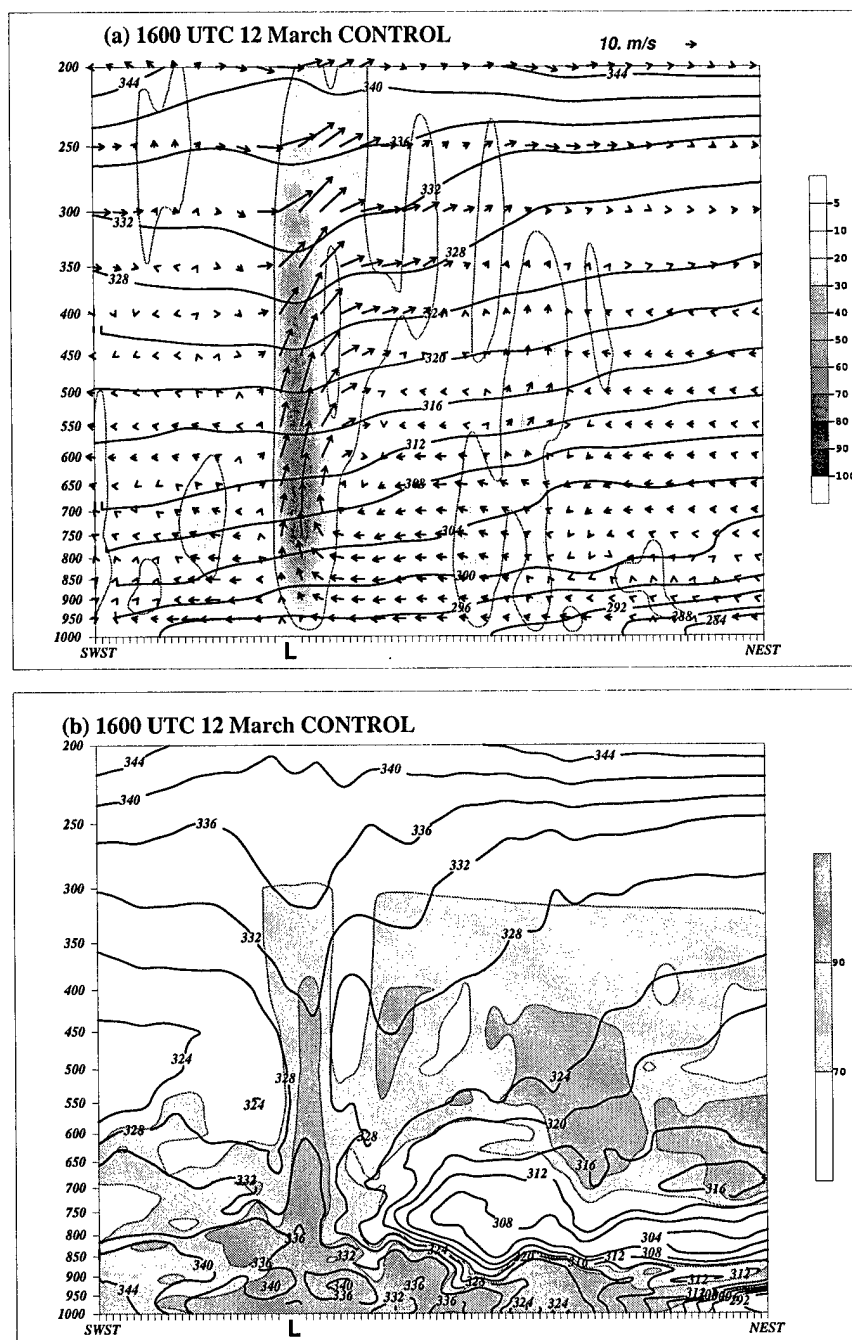


Figure 4.26: CONTROL cross-sections through the secondary cyclone at 1600 UTC 12 March, depicting (a) potential temperature (contoured every 4 K), ageostrophic circulation vectors, and vertical velocity (shaded in  $\mu\text{bar s}^{-1}$ , ascent only shown); and (b) equivalent potential temperature (contoured every 4 K) and relative humidity (shaded at 70% and 90%). Plane of the cross-section is indicated in Fig. 4.24.

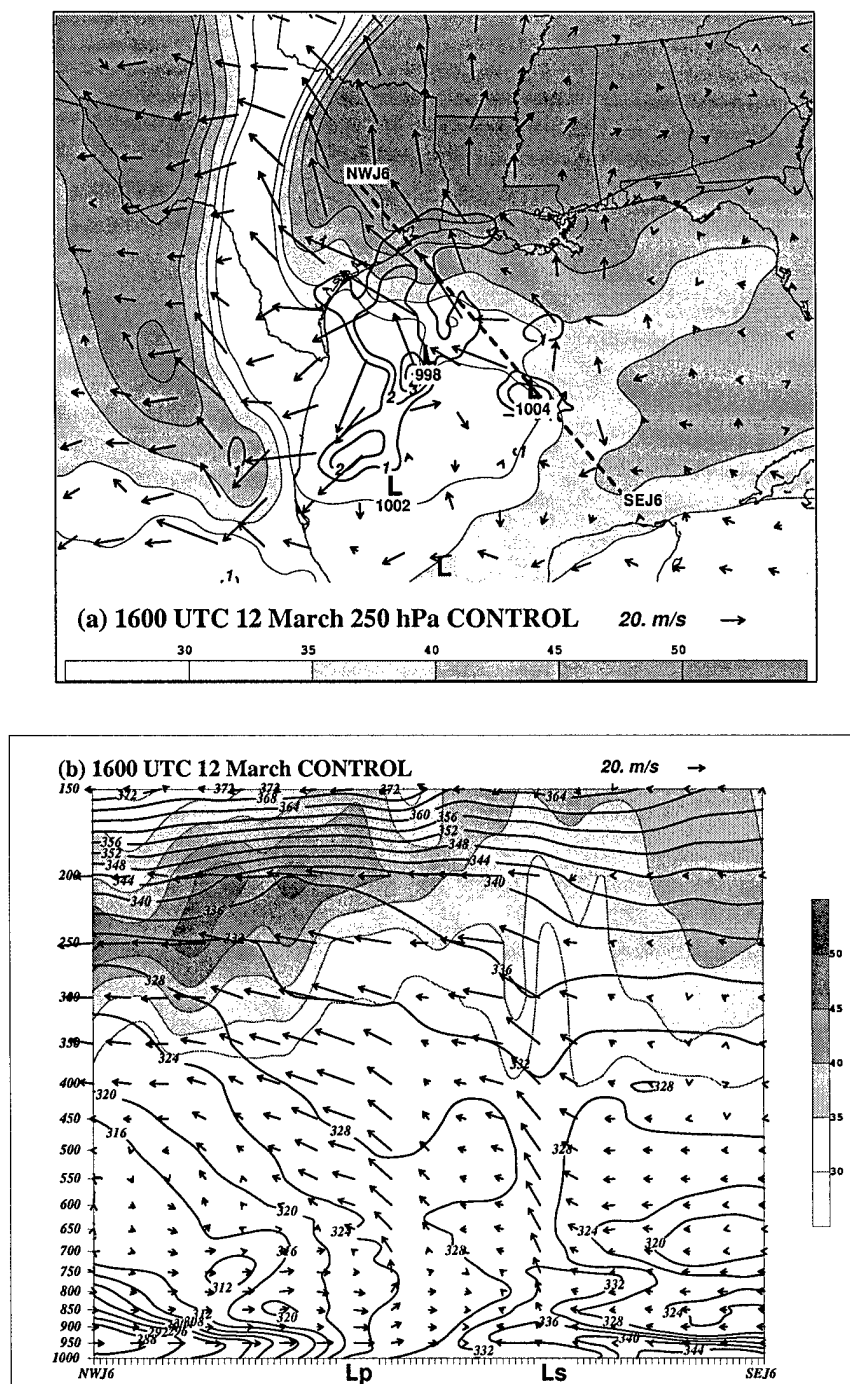


Figure 4.27: CONTROL jet structure at 1600 UTC 12 March, depicting (a) 250 hPa ageostrophic wind vectors (reference vector in lower right of panel), divergence (contoured every  $1 \times 10^{-4}$ ), and total isotachs (shaded  $> 35 \text{ m s}^{-1}$ ); and (b) cross-section through the PFJ and STJ entrance regions; ageostrophic circulation vectors, isotachs (shaded  $> 35 \text{ m s}^{-1}$ ), and equivalent potential temperature (contoured every 4 K). Plane of the cross-section is indicated in (a). Positions of the primary (Lp) and secondary (Ls) low are indicated relative to the plane of the cross-section.

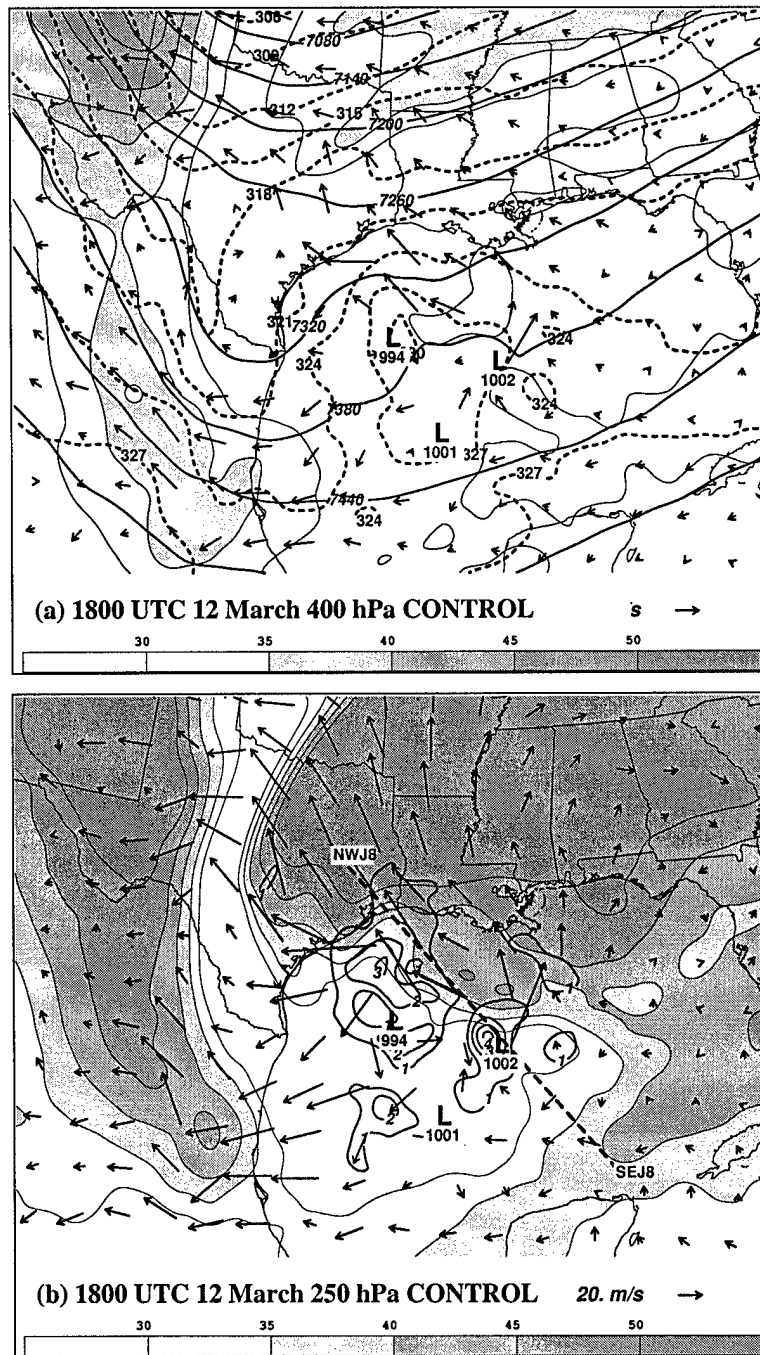


Figure 4.28: CONTROL jet structure at 1800 UTC 12 March, depicting (a) 400 hPa ageostrophic wind vectors (reference vector in lower right of panel), isotachs (shaded > 30 m s<sup>-1</sup>), geopotential height (contoured every 60 m), and potential temperature (contoured every 3 K); and (b) 250 hPa ageostrophic wind vectors (reference vector in lower right of panel), isotachs (shaded > 30 m s<sup>-1</sup>), and divergence (contoured at 1 × 10<sup>-4</sup> s<sup>-1</sup>).

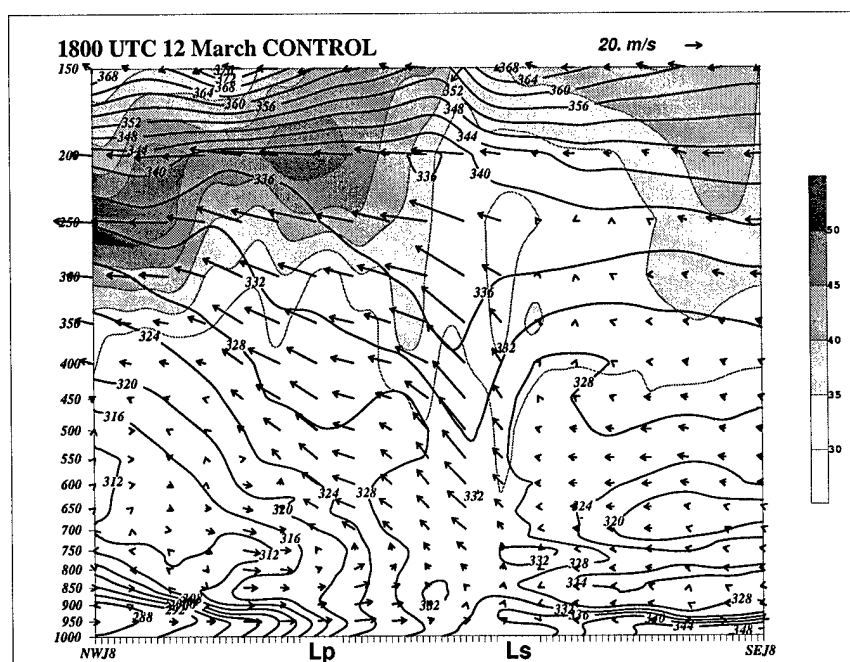


Figure 4.29: CONTROL cross-section at 1800 UTC 12 March along the plane indicated in Fig. 4.28, parameters as in Fig. 4.21.

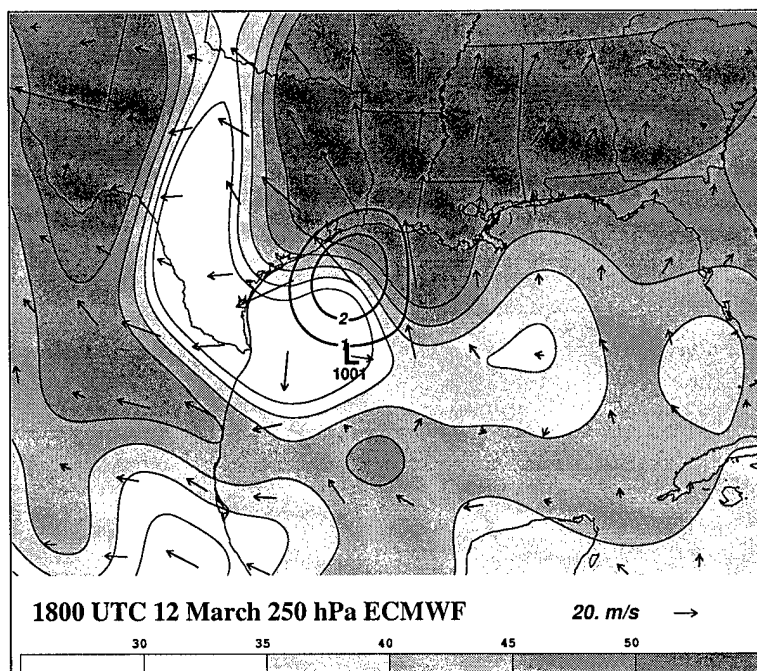


Figure 4.30: ECMWF 250 hPa jet structure at 1800 UTC 12 March, depicting ageostrophic wind vectors (reference vector in lower right of panel), isotachs (shaded  $> 30 \text{ m s}^{-1}$ ), and divergence (contoured at  $1 \times 10^{-4} \text{ s}^{-1}$ ).

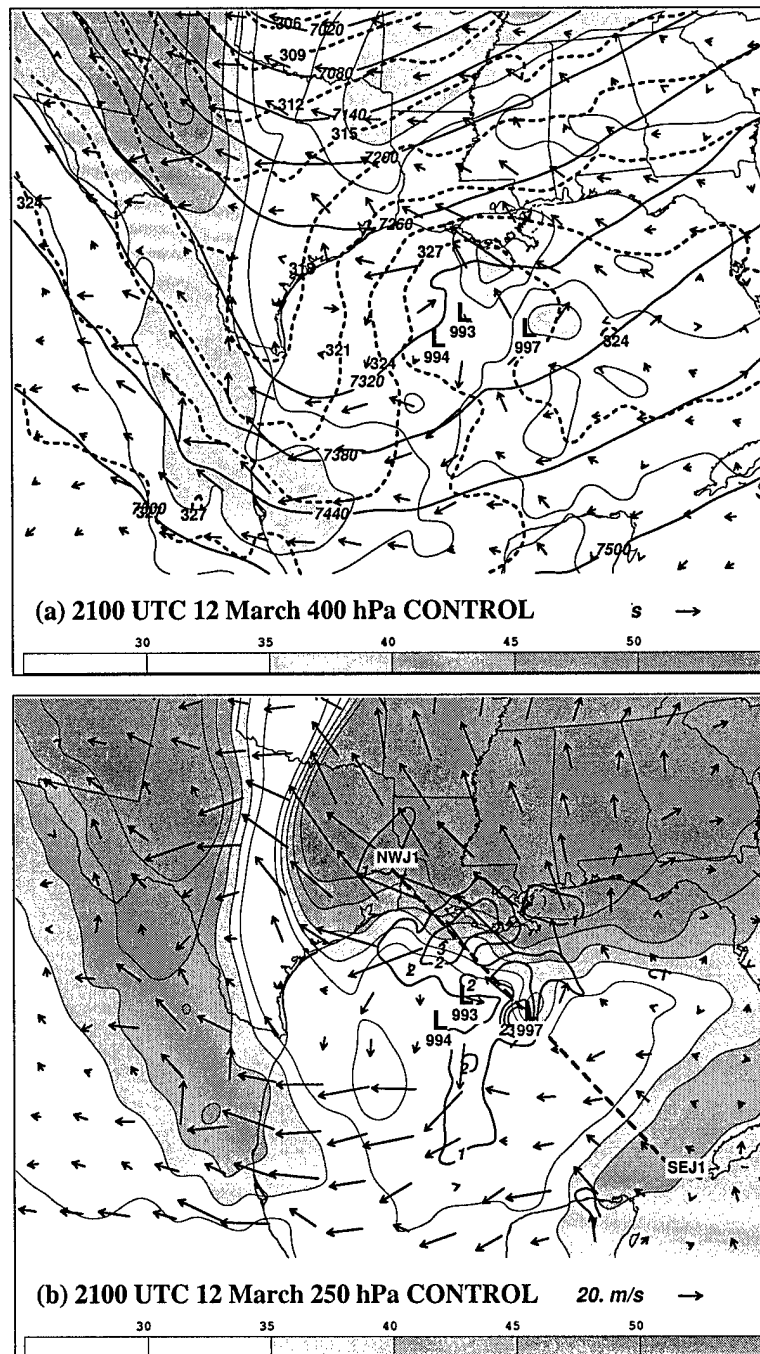


Figure 4.31: CONTROL jet structure at 2100 UTC 12 March, as in Fig. 4.28.

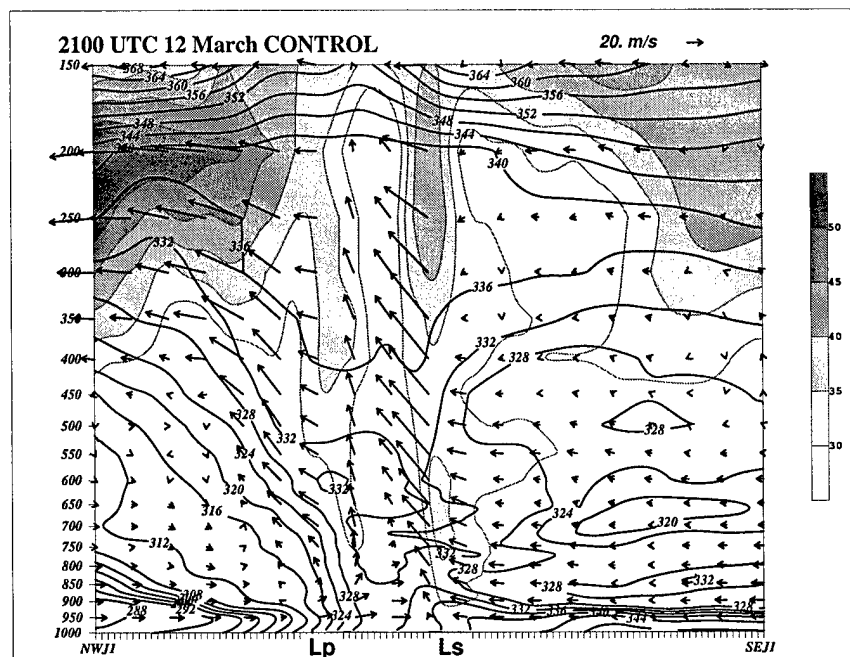


Figure 4.32: CONTROL cross-section at 2100 UTC 12 March along the plane indicated in Fig. 4.31, parameters as in Fig. 4.21.

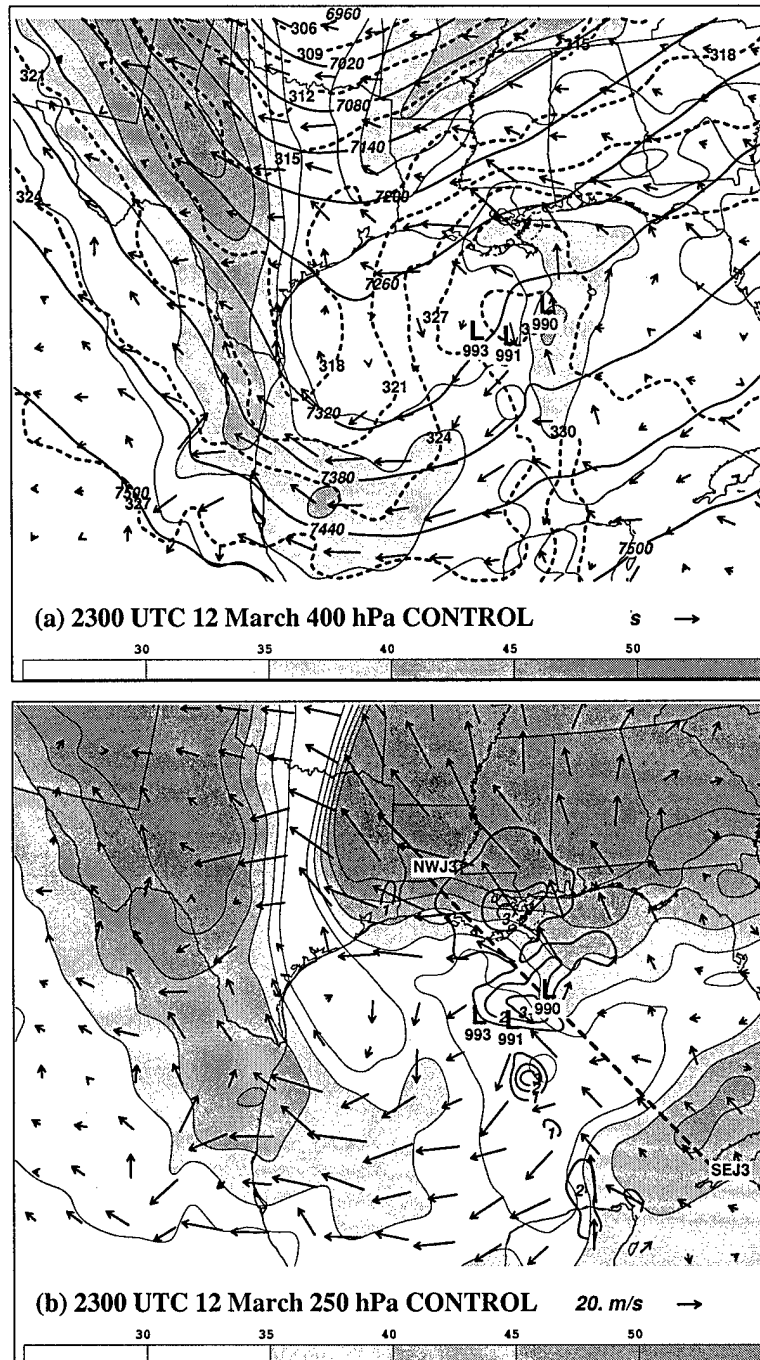


Figure 4.33: CONTROL jet structure at 2300 UTC 12 March, as in Fig. 4.28.



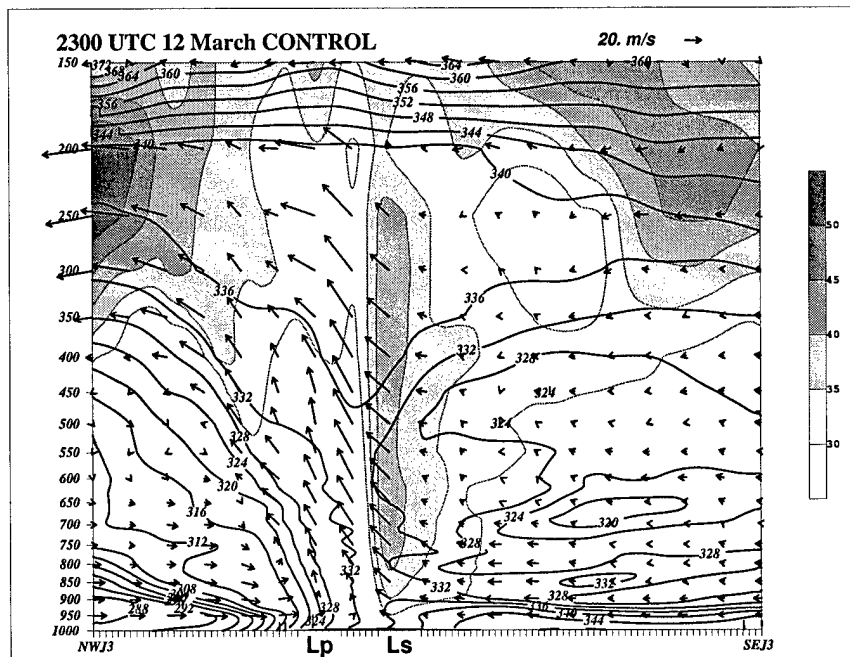


Figure 4.34: CONTROL cross-section at 2300 UTC 12 March along the plane indicated in Fig. 4.33, parameters as in Fig. 4.21.

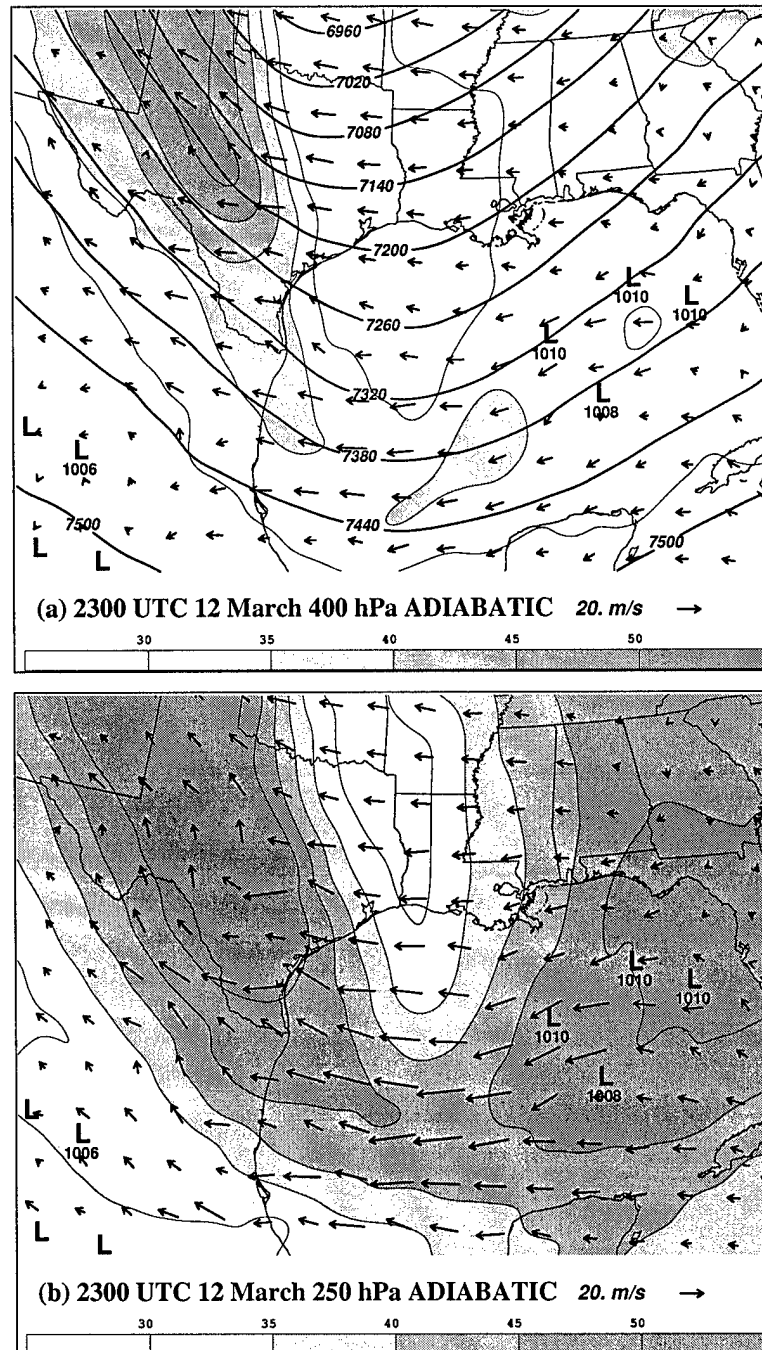


Figure 4.35: ADIABATIC jet structure at 2300 UTC 12 March, as in Fig. 4.28.

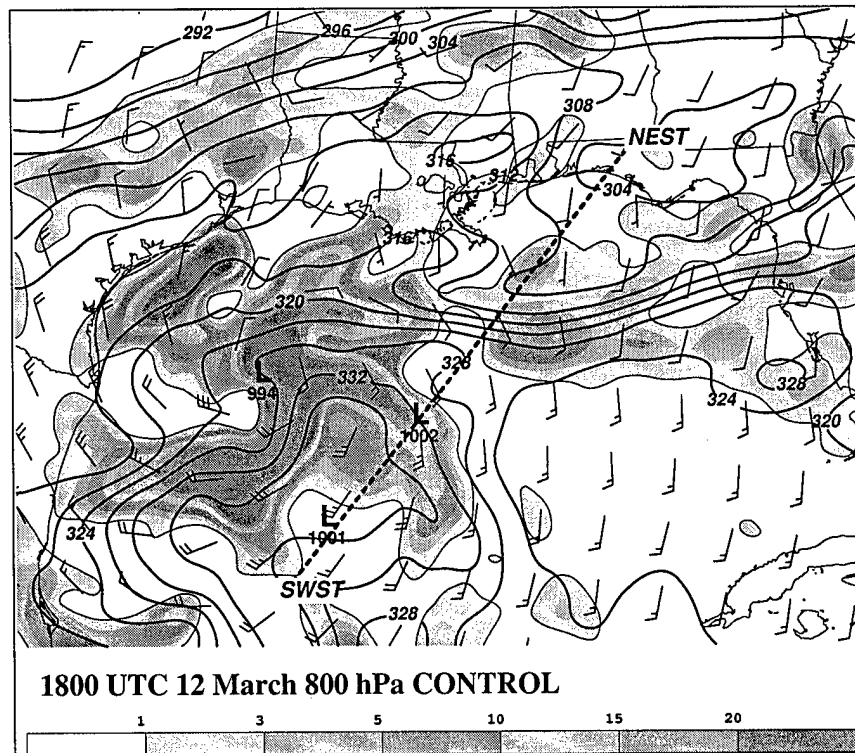


Figure 4.36: CONTROL 800 hPa fields at 1800 UTC 12 March, depicting equivalent potential temperature ( $\theta_e$ ) contoured every 4 K, standard wind vectors (in  $\text{m s}^{-1}$ ), and horizontal frontogenesis on  $\theta_e$  (shaded  $> 1 \text{ K } 100 \text{ km}^{-1} \text{ 3 h}^{-1}$ ). Positions of surface lows are indicated.

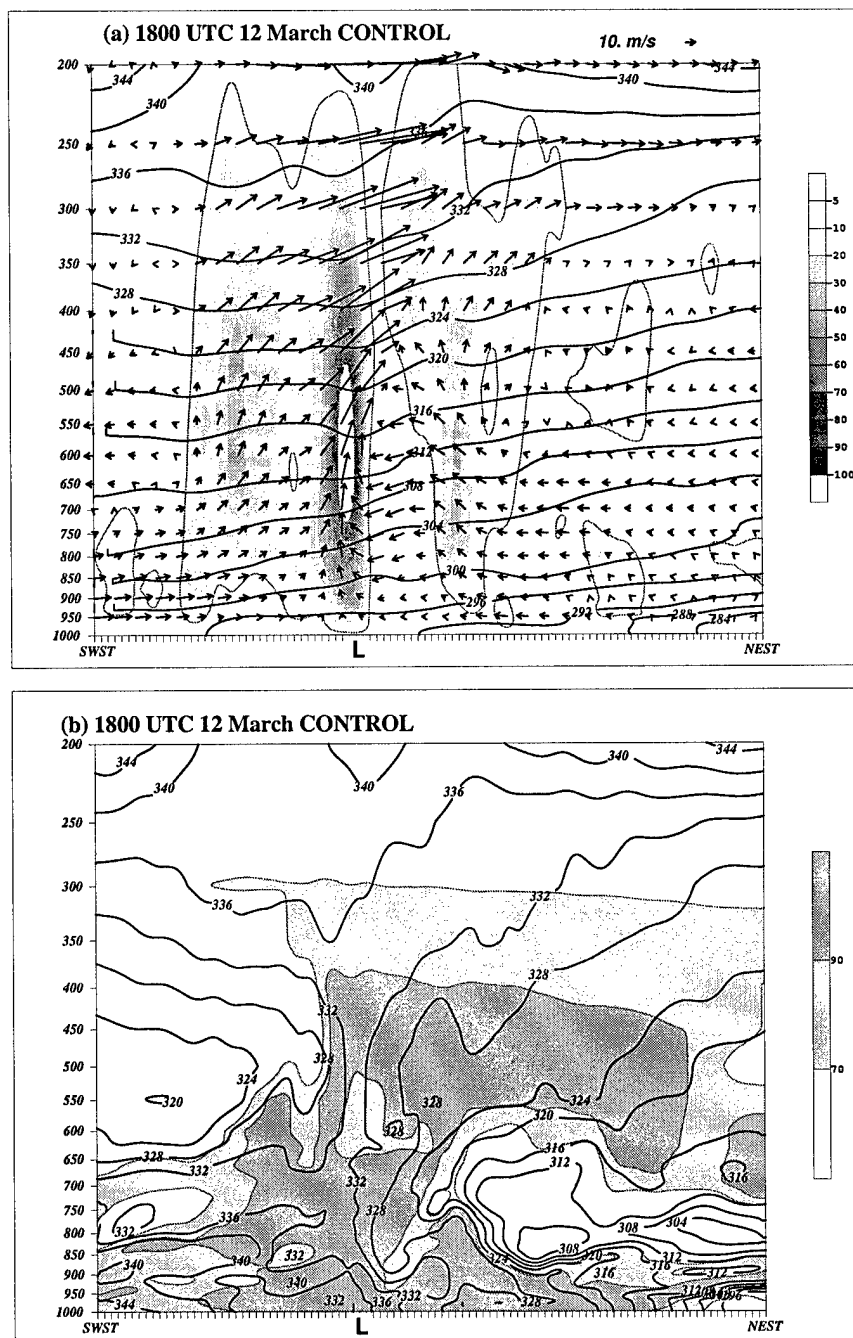


Figure 4.37: CONTROL cross-sections through the secondary cyclone at 1800 UTC 12 March, depicting (a) potential temperature (contoured every 4 K), ageostrophic circulation vectors, and vertical velocity (shaded in  $\mu\text{bar s}^{-1}$ , ascent only shown); and (b) equivalent potential temperature (contoured every 4 K) and relative humidity (shaded at 70% and 90%). Plane of the cross-section is indicated in Fig. 4.36.

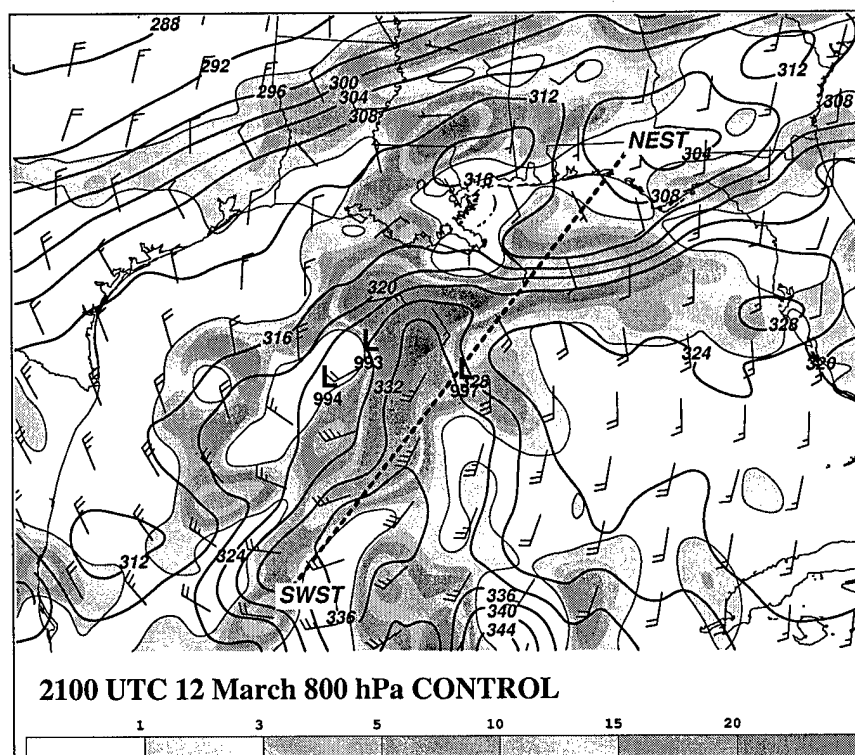


Figure 4.38: CONTROL 800 hPa fields at 2100 UTC 12 March, as in Fig. 4.36.

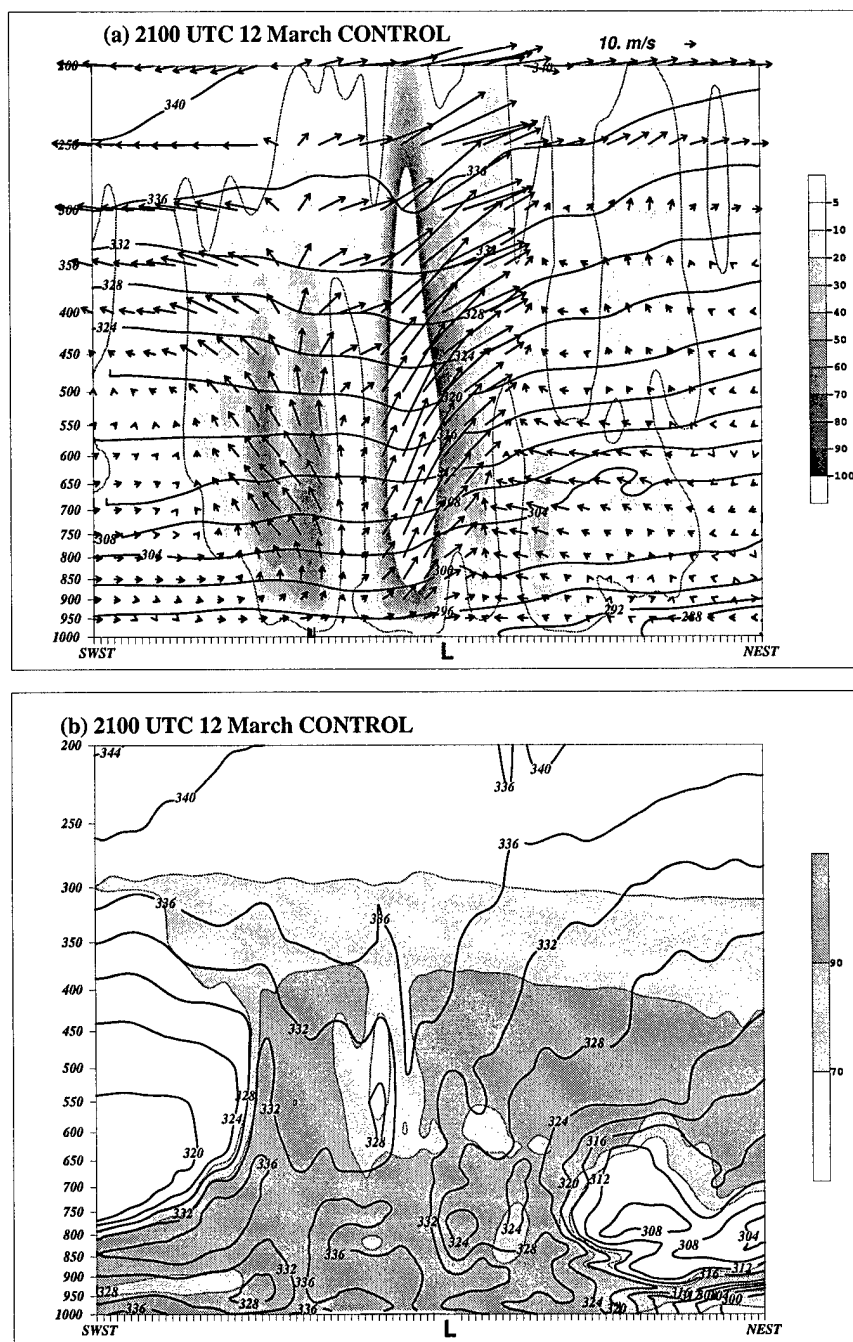


Figure 4.39: CONTROL cross-sections through the secondary cyclone at 2100 UTC 12 March, as in Fig. 4.37.

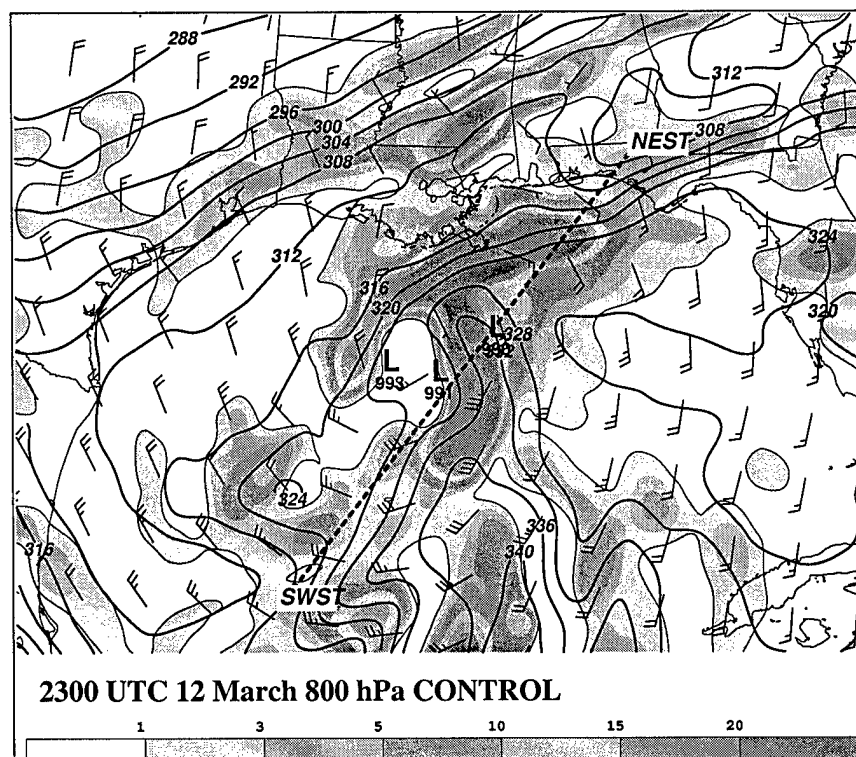


Figure 4.40: CONTROL 800 hPa fields at 2300 UTC 12 March, as in Fig. 4.36.

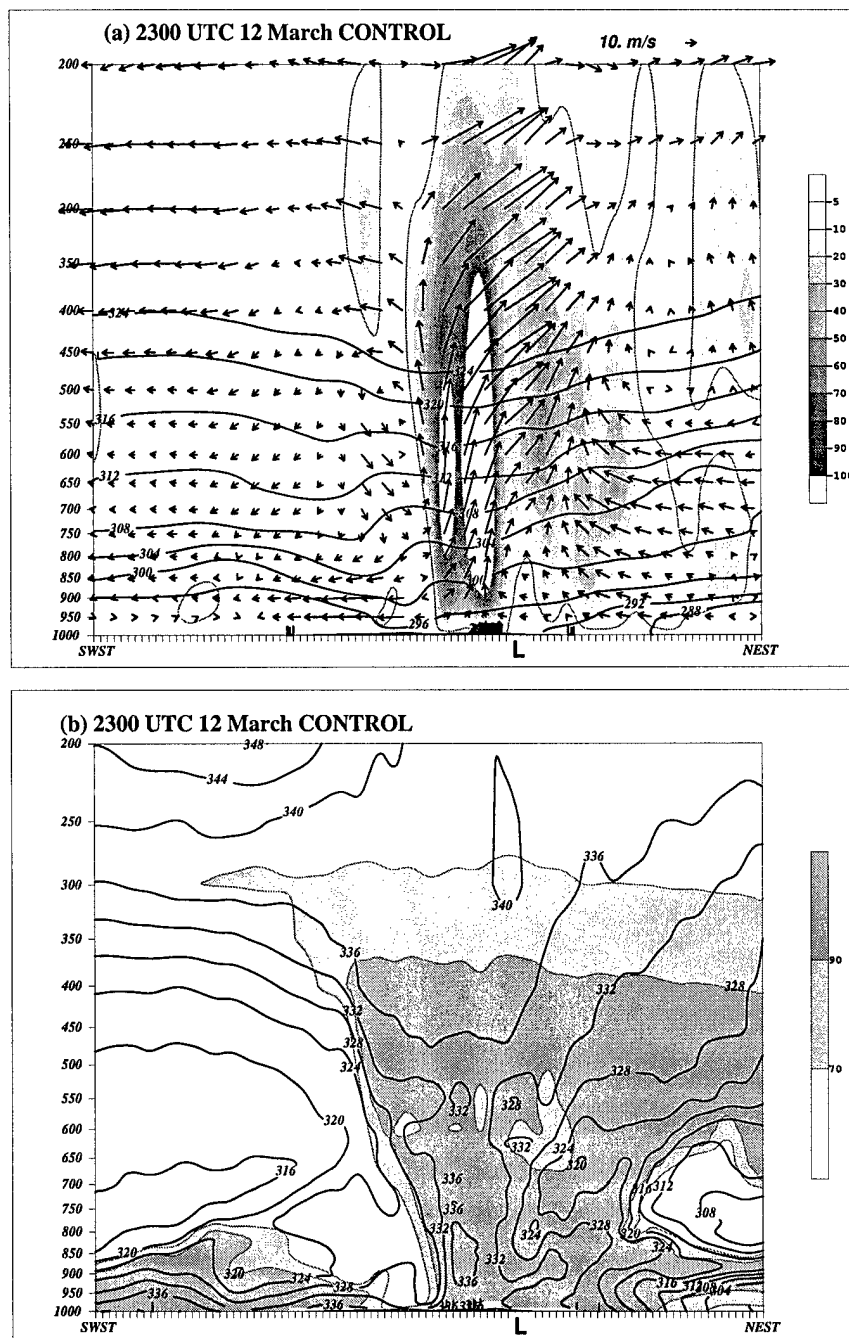


Figure 4.41: CONTROL cross-sections through the secondary cyclone at 2300 UTC 12 March, as in Fig. 4.37.



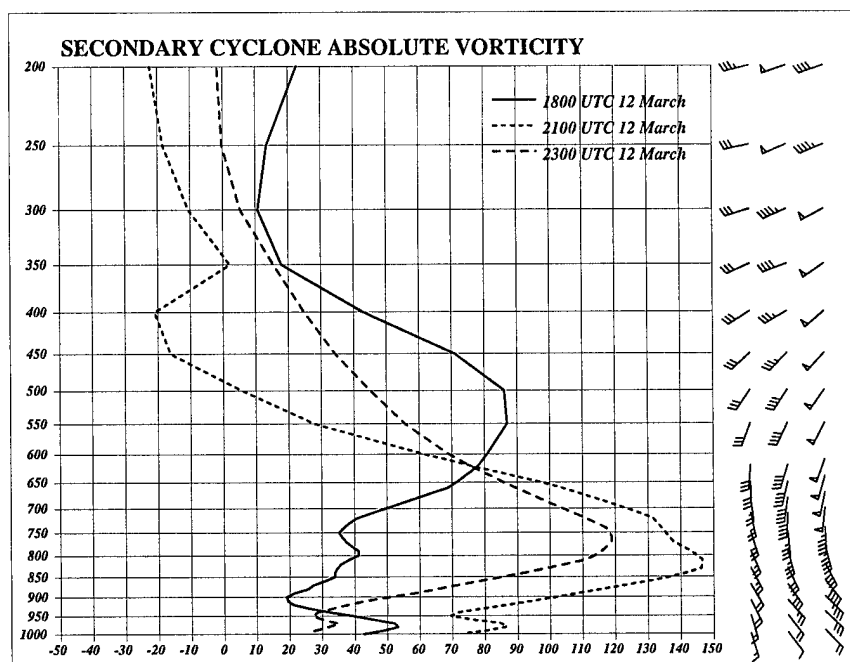


Figure 4.42: CONTROL absolute vorticity profile through center of secondary cyclone, at 1800, 2100 and 2300 UTC 12 March. Vorticity is scaled by  $10^{-5} \text{ s}^{-1}$ , and wind vectors (in  $\text{m s}^{-1}$ ) are depicted at right.

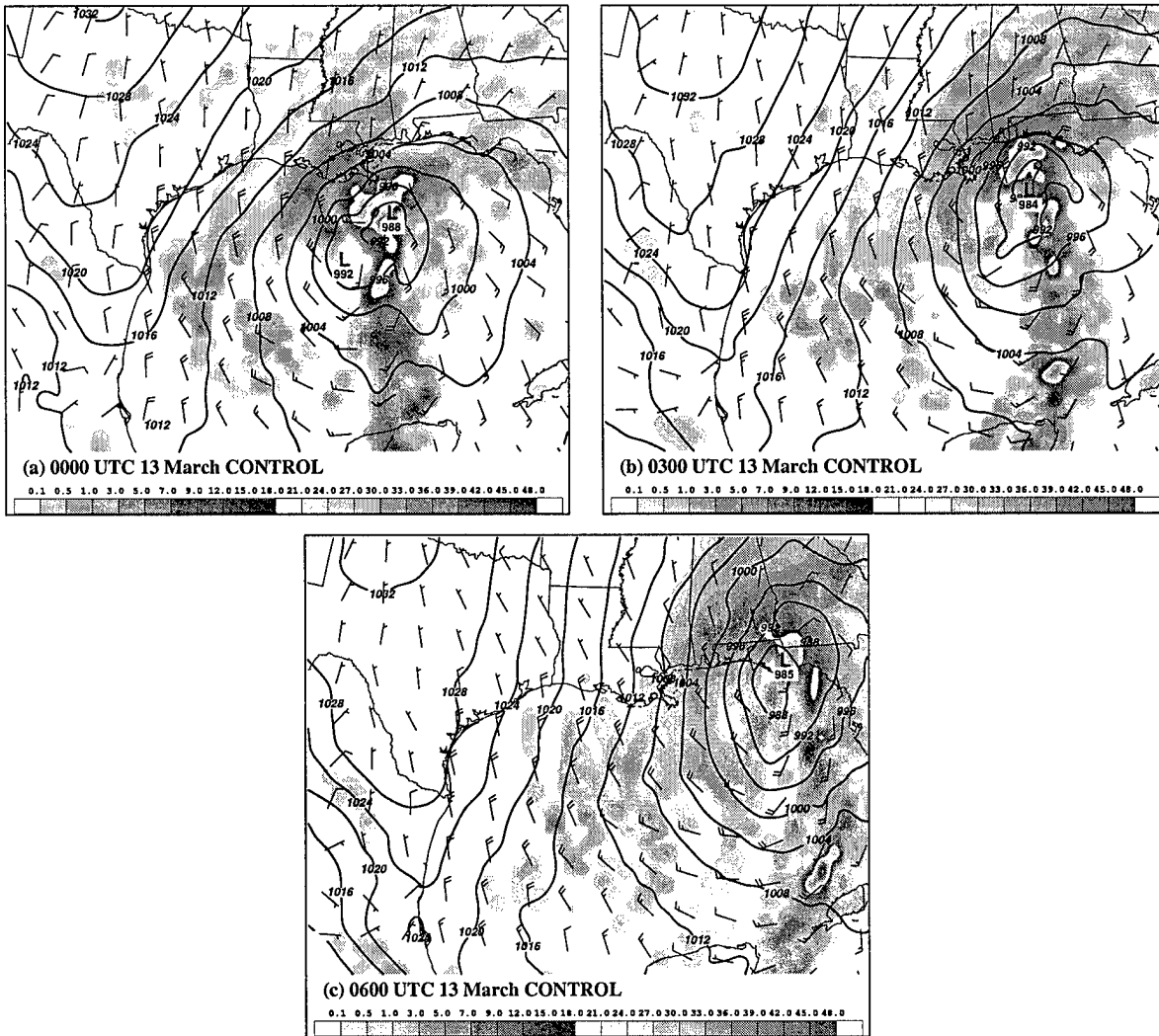


Figure 4.43: CONTROL surface fields, depicting PMSL (contoured every 4 K), surface wind vectors (in  $\text{m s}^{-1}$ ), and total precipitation (shaded in  $\text{mm h}^{-1}$ ), valid (a) 0000 UTC, (b) 0300 UTC, and (c) 0600 UTC 13 March.

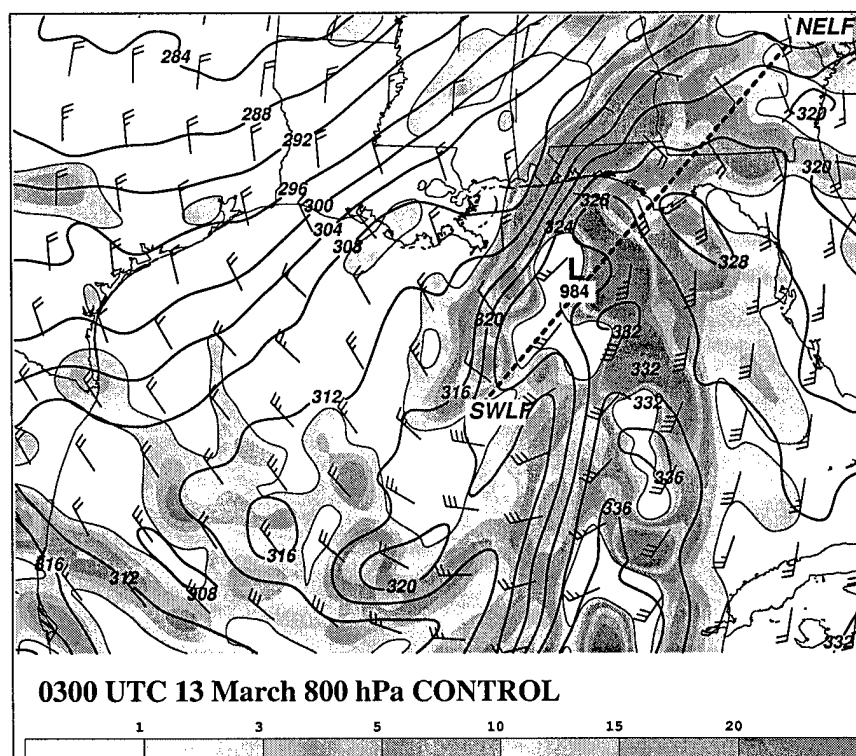


Figure 4.44: CONTROL 800 hPa fields at 0300 UTC 13 March. Depicted are equivalent potential temperature ( $\theta_e$ ) contoured every 4 K, divergence shaded and contoured every  $1 \times 10^{-4} \text{ s}^{-1}$  (negative dashed contour), and standard wind vectors in  $\text{m s}^{-1}$ . Surface low pressure centers and the plane of the cross-section in Fig. 4.45 are indicated.

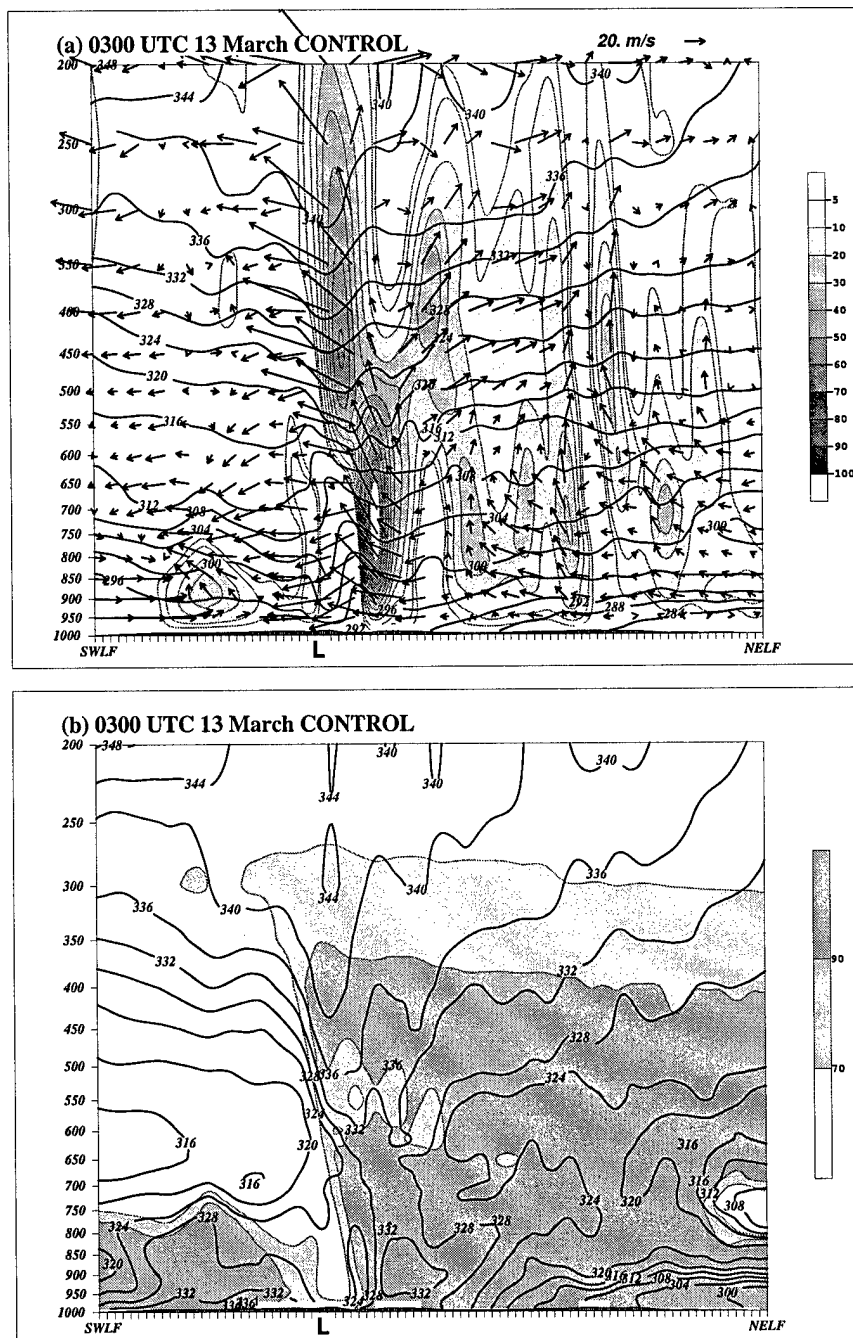


Figure 4.45: CONTROL cross-sections through the secondary cyclone at 0300 UTC 13 March, depicting (a) potential temperature (contoured every 2 K), ageostrophic circulation vectors, and vertical velocity (shaded in  $\mu\text{bar s}^{-1}$ , ascent only shown); and (b) equivalent potential temperature (contoured every 4 K) and relative humidity (shaded at 70% and 90%). Plane of the cross-section is indicated in Fig. 4.44.

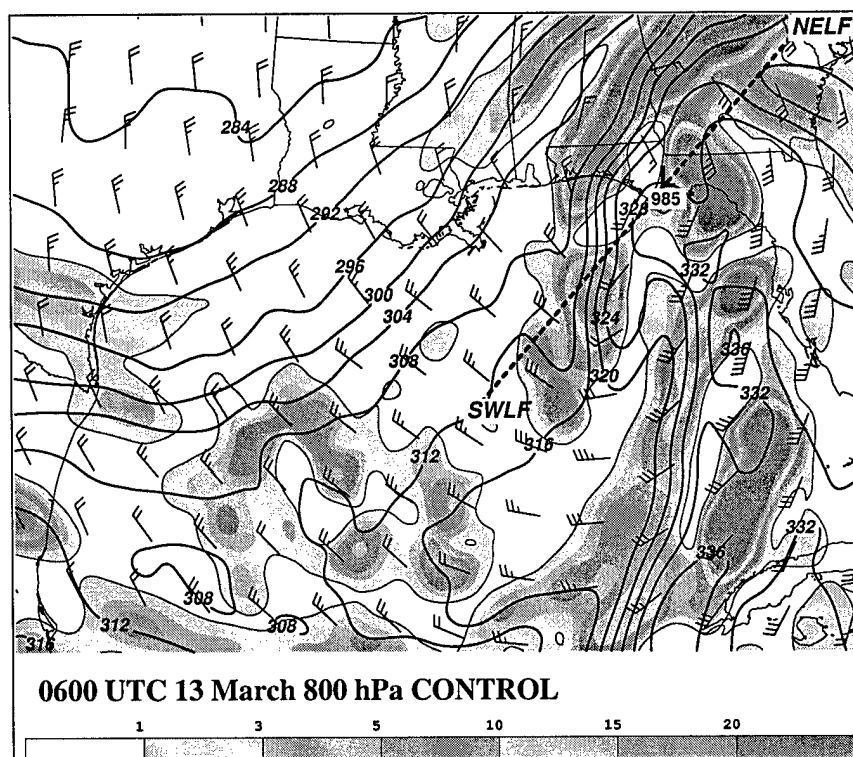


Figure 4.46: CONTROL 800 hPa fields at 0600 UTC 13 March, as in Fig. 4.44.

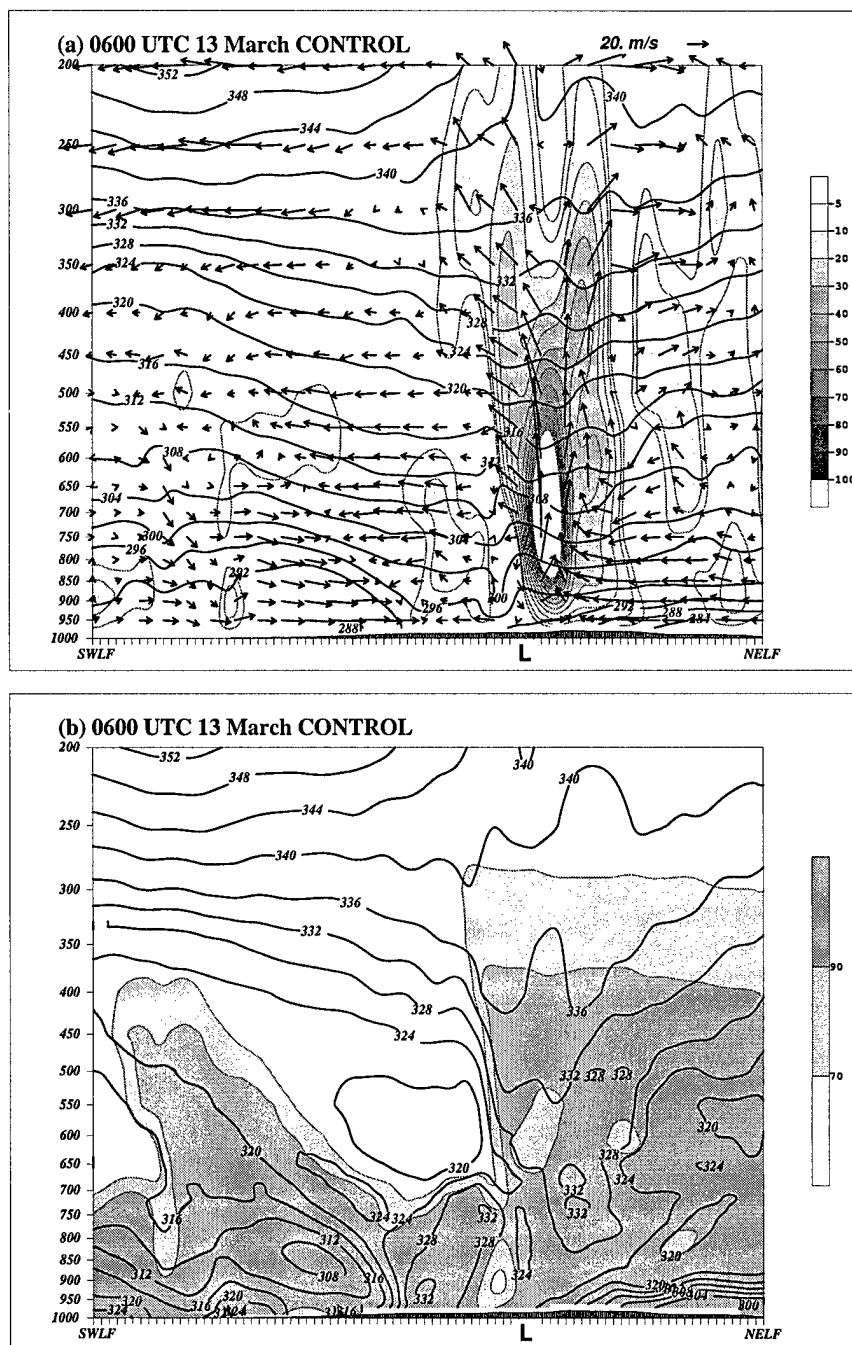


Figure 4.47: CONTROL cross-sections through the secondary cyclone at 0600 UTC 13 March, as in Fig. 4.45.

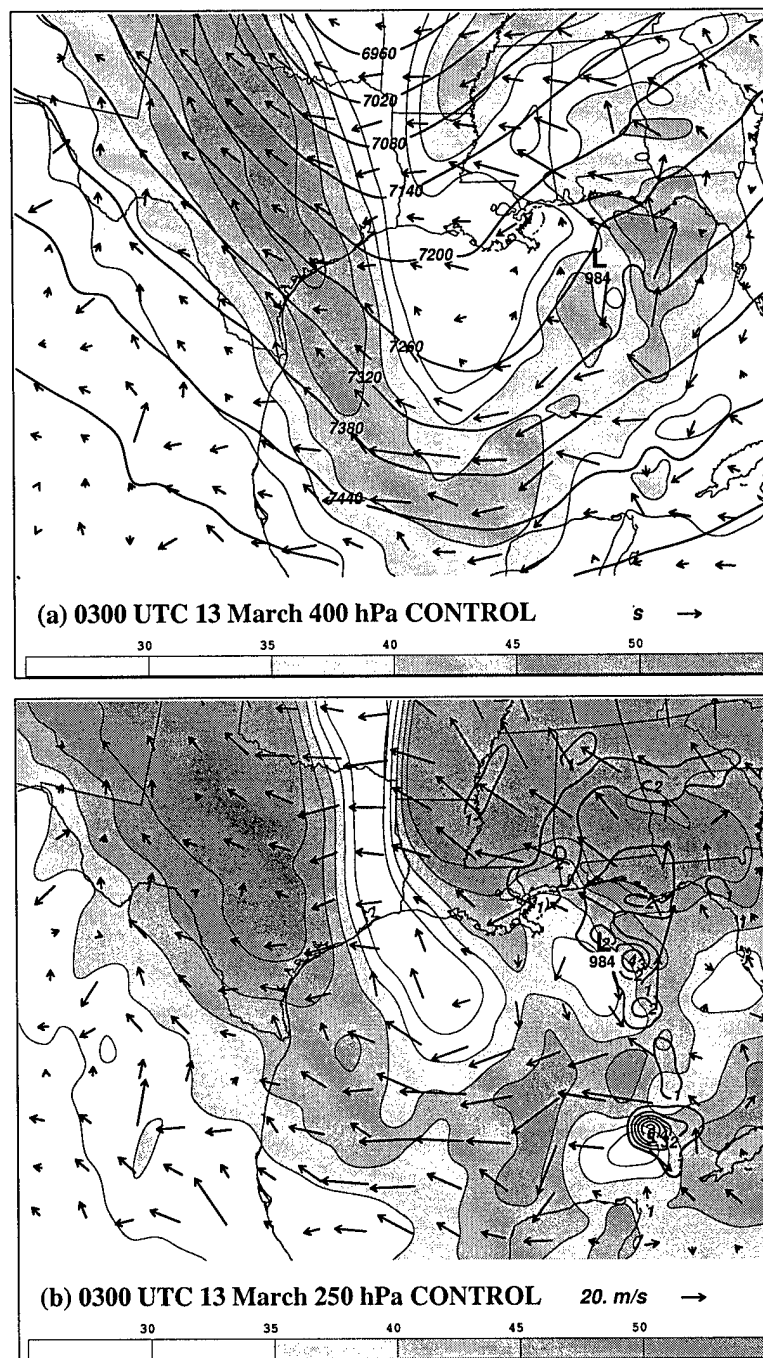


Figure 4.48: CONTROL jet structure at 0300 UTC 13 March, depicting (a) 400 hPa ageostrophic wind vectors (reference vector in lower right of panel), isotachs (shaded  $> 30 \text{ m s}^{-1}$ ), and geopotential height (contoured every 60 m); and (b) 250 hPa ageostrophic wind vectors (reference vector in lower right of panel), isotachs (shaded  $> 30 \text{ m s}^{-1}$ ), and divergence (contoured at  $1 \times 10^{-4} \text{ s}^{-1}$ ).

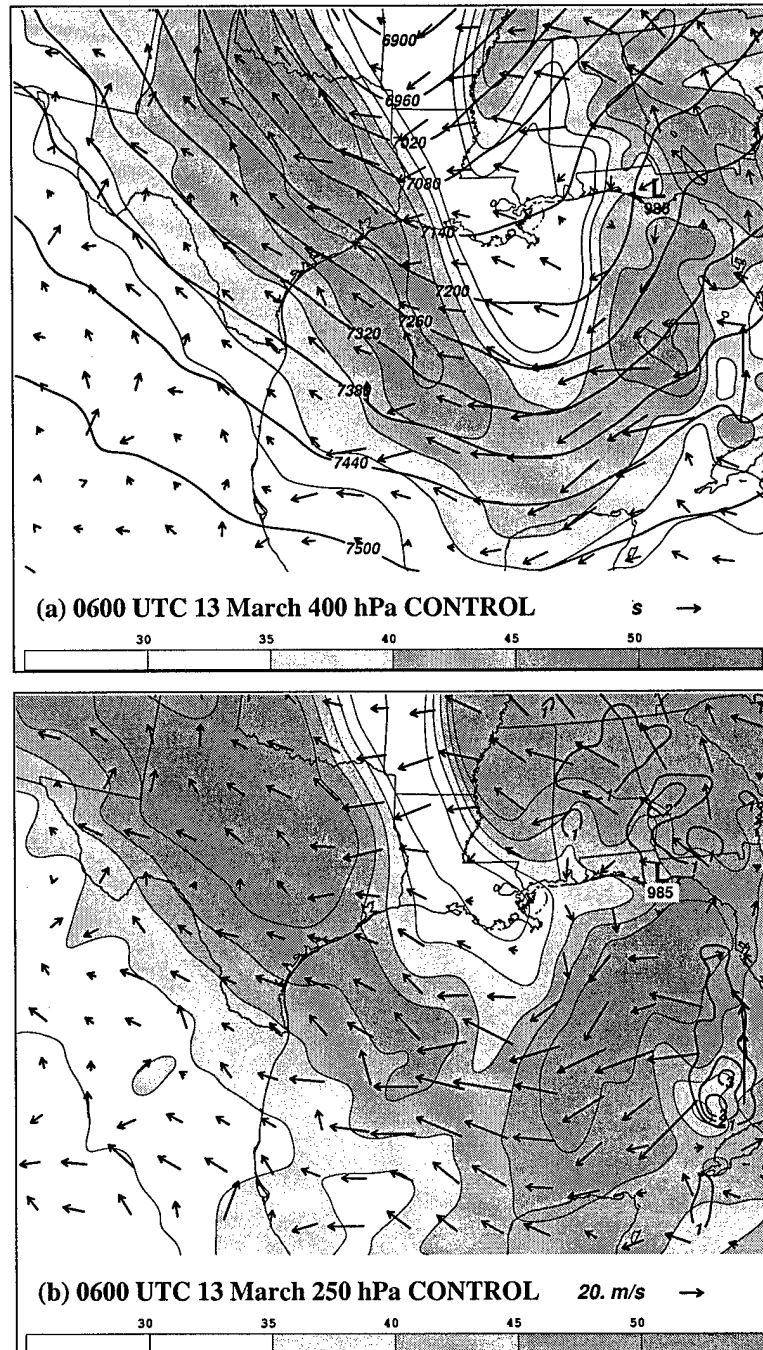
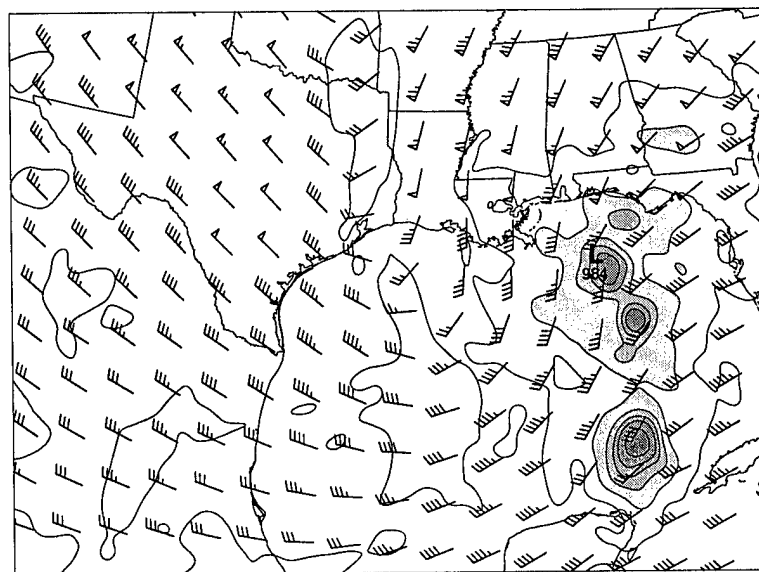
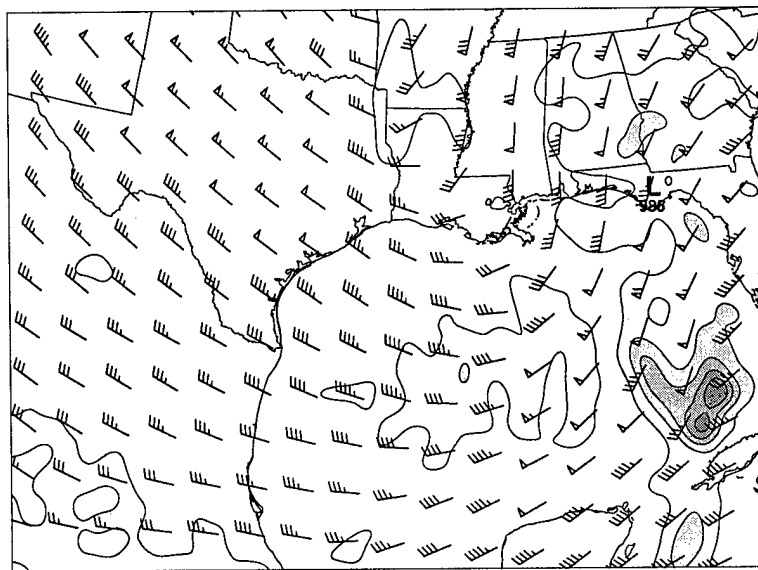
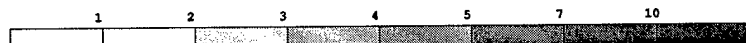


Figure 4.49: CONTROL jet structure at 0600 UTC 13 March, as in Fig. 4.48.





(a) 0300 UTC 13 March 250 hPa CONTROL



(b) 0600 UTC 13 March 250 hPa CONTROL

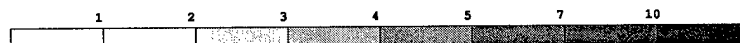


Figure 4.50: CONTROL 250 hPa Lagrangian Rossby number (shaded) and total wind vectors (in  $\text{m s}^{-1}$ ), valid (a) 0300 UTC and (b) 0600 UTC 13 March.

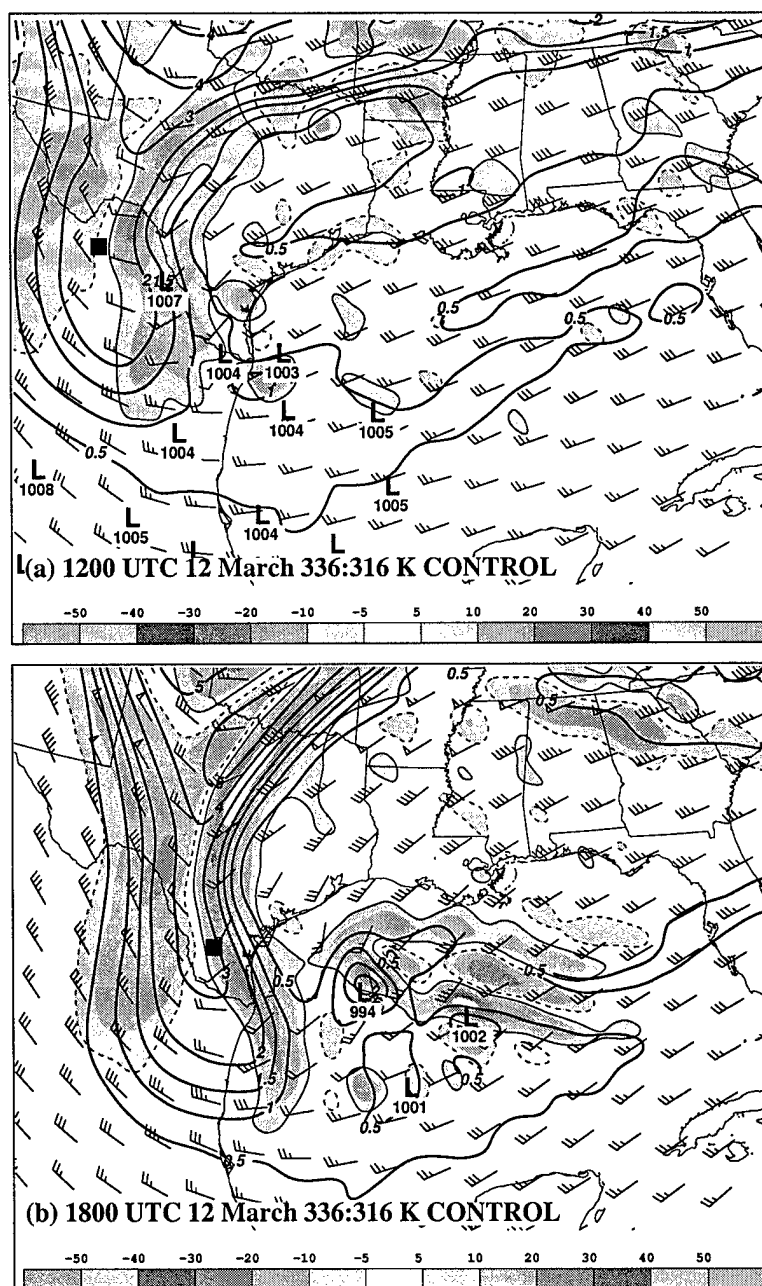
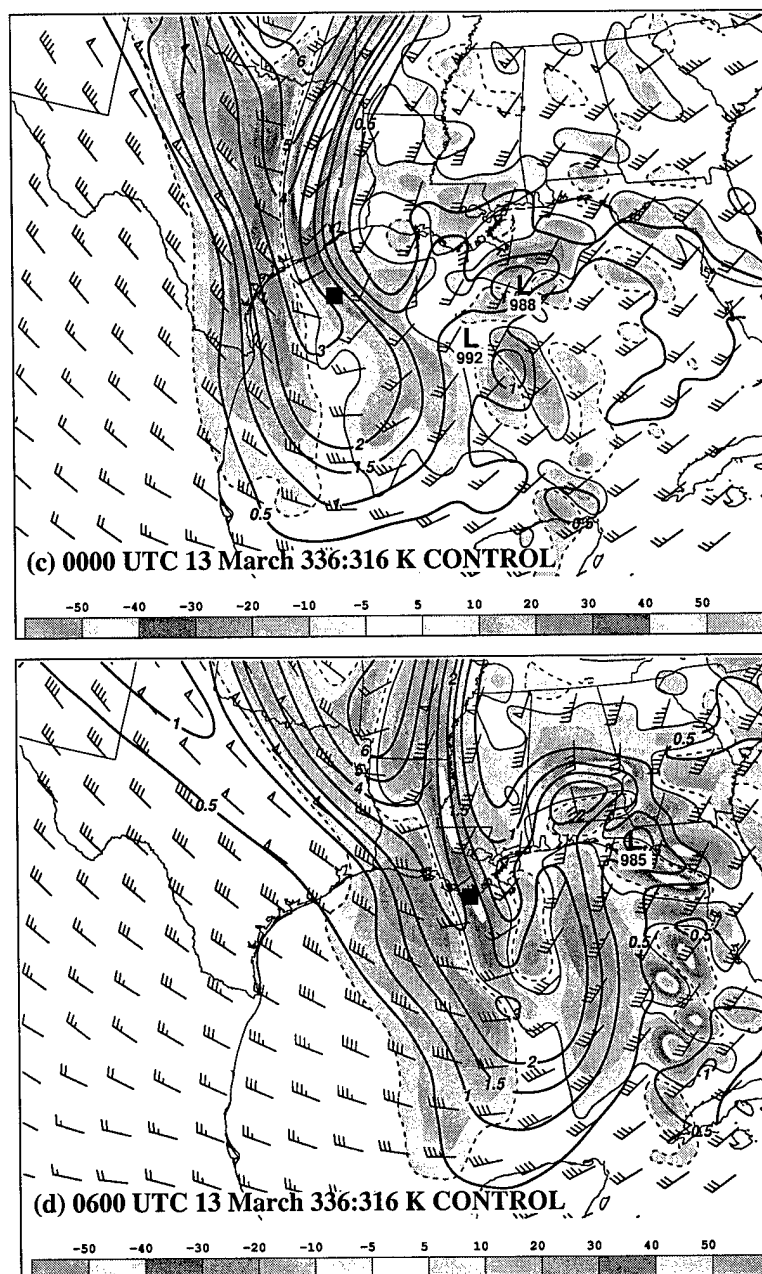


Figure 4.51: CONTROL IPV analysis in the column from 336 K to 316 K, with IPV contoured at 0.5 PVU and every 1.0 PVU thereafter, IPV advection ( $-\mathbf{V} \bullet \nabla IPV$ ) shaded at 5 PVU day<sup>-1</sup> and every 10 PVU day<sup>-1</sup> thereafter (negative dashed contour outline), and layer-averaged wind vectors (in m s<sup>-1</sup>). Valid (a) 1200 UTC 12 March, (b) 1800 UTC 12 March, (c) 0000 UTC 13 March, and (d) 0600 UTC 13 March.

Figure 4.51: *Continued.*

# Chapter 5

## Summary and Conclusions

The early cyclogenesis of the March 1993 Storm of the Century (SOC93) challenged operational synoptic-scale models because mesoscale processes crucial to this development could not be resolved. We have presented a conceptual model of the life-cycle of SOC93 as a three-stage evolution:

- I. Early on 11 March to 1200 UTC 12 March, a sequence of mesoscale processes initiates and organizes deep convection in the western Gulf of Mexico.
- II. From 1200 UTC 12 March to early on 13 March, the storm develops initially as a warm-core system, then is transformed into a cold-core storm in the central Gulf prior to landfall in northwest Florida.
- III. 0600 UTC 13 March to late on 14 March, the storm intensifies, then matures, as a classic extratropical cyclone.

This research has focused on illuminating the mesoscale details of **Stage I**, the initiation of cyclogenesis in the western Gulf of Mexico early on 12 March (Fig. 2.1), and of **Stage II**, the overwater development prior to landfall in northwest Florida early on 13 March (Fig. 4.1).

### 5.1 Stage I: Conditioning of environment

Simulation results show that the environment along the Texas Gulf Coast is conditioned for deep convection early on 12 March by a mid-level cold pool originating in the upper

Rio Grande Valley east of Del Rio, TX, early on 11 March. This cold pool develops at the junction of terrain-driven circulations (the MPS aloft and hot conveyor belt below) over a near-surface cold surge ahead of a synoptic-scale cold front (Fig. 2.33a). Shallow convection, confined between the near-surface cold air and elevated mixed layer from the Mexican plateau, deposits evaporationally-cooled air at the top of a layer that is destabilized from below by the intense southeasterly warm advection from the hot conveyor belt; this positive feedback cools and expands the mid-level feature (Fig. 2.33b). As the terrain-induced hot conveyor belt is displaced eastward by nocturnal cooling along the Mexican plateau, the mid-level cold pool begins to propagate eastward, reaching the Texas Gulf Coast early on 12 March (Fig. 2.33c). The baroclinic zone formed by this mid-level cold air and warm air attendant to the MPS to the southwest drives a mesoscale northward-directed pressure gradient force that accelerates the upper-level flow, forming a meso- $\alpha$  scale 300 hPa jet streak (Fig. 2.33c). The environment along the Gulf Coast of southern Texas is thus conditioned for deep, organized convection by the potential energy of the elevated cold pool and the significant upper-level jetlet attendant to this cold pool.

These results clarify previous SOC93 studies; in particular, we note that the dissipation of PV anomaly D over central Texas late on 11 March (Bosart *et al.*, 1996) occurs *after* the cold pool is in place along the Gulf Coast early on 12 March and *long after* the cold pool is established in the upper Rio Grande Valley. Strong coastal baroclinicity noted in Gilhousen (1994), Huo *et al.* (1995), Bosart *et al.* (1996) and Dickinson *et al.* (1997) is relatively unimportant to the *initiation* of convection early on 12 March.

## 5.2 Stage I: Initiation of organized convection

The antecedent mesoscale convective complex that supports the initial SOC93 forms under a deep column of ascent induced by upper-level divergence at the juxtaposition of opposing ageostrophic circulations (Fig. 3.29a). Northerly ageostrophy is induced along the plateau by the upper branch of the transverse circulation attendant to the exit region of the approaching synoptic-scale jet streak (Fig. 3.29a); the transverse circulation is skewed from the idealized, four-cell pattern in a balanced, straight jet streak (e.g. Keyser and Shapiro, 1986) in part because the elevated heating along the plateau changes the balance

in this exit region. The typical thermally-indirect exit region circulation should decelerate parcels by converting the kinetic energy of the jet core to potential energy in the lower troposphere (enhancing baroclinicity); the elevated heating of the plateau actually drives a thermally-direct circulation which would *accelerate* parcels in the exit region, increasing along-stream divergence and further contributing to the upper-level signal in the lower Rio Grande Valley. Southerly ageostrophy is induced by the upper branch of the mountain-plains solenoid, which is accelerating over the mid-level cold pool created on 11 March (Fig. 3.29a). The subsequent, substantial signal of upper-level divergence in northern Mexico is largely the product of *dry* diabatic forcing along the Altiplanicie Mexicana. Under this divergence, concomitant ascent triggers deep, moist convection in a region rich in convective available potential energy; subsequent convective outflow reinforces the upper-level jetlet formed in response to the mid-level cold pool (Fig. 3.29a). The coupled system of upper-level jetlet and mesoscale convective complex develop a deepening warm core that grows from both latent heat release and the continued inflow of warm MPS air into the southern flank of the developing storm. The sustained convection induces surface pressure falls along an inverted surface trough along the coast; this trough is an artifact of the stationary surface front in eastern Texas. The isallobaric response to the organized convection enhances onshore flow which replenishes the potential energy for continued moist convection in northern Mexico and southern Texas (Fig. 3.29b). Latent heating augmented by the mid-level penetration of warm MPS air builds the warm core surfaceward, culminating in a well-defined surface cyclone by 1200 UTC 12 March, as the storm moves over the Gulf (Fig. 3.1a).

These results shed considerable light on the mesoscale processes that trigger deep, organized convection in the crucial 36 h period prior to 1200 UTC 12 March. The importance of diabatic forcing along the Mexican plateau, particularly *dry* diabatic forcing, is a significant clarification of previous speculation that enhanced low-level warm advection ahead of PV anomaly C triggered the widespread convection early on 12 March (Dickinson *et al.*, 1997). These results do not diminish the importance of the background synoptic-scale flow: the interaction of the meso- $\alpha$  MPS and synoptic-scale STJ are key to the sustained divergence in northern Mexico; the amplification of planetary flow is certainly important to sustaining this interaction. We assert, however, that the significant *dry* diabatic processes in this early period have heretofore received little attention.

### 5.3 Stage II: Overwater development

Once over the Gulf, the Stage II SOC93 evolves through three phases: an early, warm-core period; a secondary cyclogenesis that exhibits features of both warm and cold-core development; and a transition to a dominant cold-core (extratropical) system about the time of landfall in northwest Florida. The upscale growth of a mesoscale convective complex (Fig. 4.1a) has been documented in many other cases (e.g. Bosart and Sanders, 1981; Zhang and Fritsch, 1986) though *not* in the case of SOC93 prior to this research. This warm-core period is quickly supplanted by a secondary cyclogenesis in the central Gulf of Mexico in an environment preconditioned for cyclogenesis by the initial cyclone *and by the eastward propagation of warm, mid-level air from the Mexican plateau under the entrance region of a subtropical jet streak*. The secondary system resembles the initial warm core storm but develops in an increasingly baroclinic environment; an existing synoptic-scale boundary is intensified from below by the northward intrusion of the warm MPS and from above by an intensifying polar front jet structure invigorated by the initial, convectively-driven surface cyclone. A meso- $\alpha$  cold surge (documented in Schultz *et al.*, 1997) and coupled western jet streak enhance this secondary cyclogenesis and contribute to the rapid development of significant surface baroclinicity in the central Gulf late on 12 March, marking the transition of the now-dominant secondary storm to a hybrid system with a lower-tropospheric warm-core under an increasingly westward-tilted upper-level structure typical of mid-latitude extratropical storms. After approximately 0600 UTC 13 March, the landfalling SOC93 largely resembles an extratropical (cold-core) system as the available potential energy of the large-scale baroclinicity is tapped for further development.

Previous investigators (e.g. Kocin *et al.*, 1995) have noted the importance of jet streak interactions in the post-landfall period (after 0600 UTC 13 March). In this study, however, we have demonstrated that the connection of these jet streaks begins with the initiation of convection in the western Gulf of Mexico; the subsequent cyclogenesis and organized convective outflow act to *connect* these synoptic-scale jet streaks. This gives a qualitative insight as to why operational models, failing to capture the storm in the early period over the Gulf, also yielded poor initial solutions for the landfalling storm (Caplan, 1995).

## 5.4 Future research

Previous investigators have noted that the western Gulf of Mexico is climatologically favored for cyclogenesis (e.g. Hsu, 1993). In a synoptic-dynamic study of Texas-West Gulf cyclones, Saucier (1949) found 388 such storms in the period 1899–1938, for a mean of 9.7 winter cyclones per year originating in this region. A more recent study by Johnson *et al.* (1984) of the period 1972–1982 found a similar average of 10.4 winter cyclones per year originating in the western Gulf. Dickinson *et al.* (1997) motivated their study of SOC93 by reviewing cool-season (November–April) storms in the Gulf of Mexico from 1957–1989, finding 206 deep storms (storms with central pressures  $\leq 1000$  hPa), or about 6.2 cyclones per year. From a cursory analysis of these combined results, we infer that significant cyclogenesis in the western Gulf of Mexico is not rare and often leads to deep storms. A more comprehensive (and current) synoptic-dynamic climatology of extratropical cyclogenesis in this region could yield additional insight into the predisposition of the western Gulf to significant cool-season events.

We speculate that the western Gulf is climatologically favored for deep cyclogenesis in part because of the unique topography of the Mexican plateau and attendant diabatic and terrain-driven circulations. In the case of SOC93, elevated heating along the plateau coupled to the subtropical jet was important in initiating early cyclogenesis (in the exit region of the western jet streak) and later in initiating secondary cyclogenesis in the central Gulf (in the entrance region of the southern jet streak). In a recent modeling study of the 28–29 March 1984 case of rapid continental cyclogenesis in the southeastern U.S., Rozumalski (1997) found that the rear inflow of warm air from the Mexican plateau helped to organize the mesoscale precipitation and subsequent explosive cyclogenesis. This signal of the MPS traveled over the Gulf of Mexico and penetrated the southeastern U.S. in less than 18 h (Rozumalski, 1997). Egentowich *et al.* (2000a, 2000b, 2000c) used mesoscale simulations to demonstrate a precursor signal of plateau heating in the subtropical jet that produced a significant tornado outbreak in November 1988 in the southeastern U.S.; the F4 Raleigh (NC) tornado was part of this outbreak. Additional research at the mesoscale may demonstrate that circulations from the Altiplanicie Mexicana are ubiquitous to cool-season cyclogenesis events in the eastern U.S.



# Appendix A

## Computation of diabatic forcing

In an isentropic framework ( $D\theta/Dt$ ) can be inferred from the vertical motion on isentropic surfaces; that is, a parcel cannot cross a  $\theta$ -surface without some diabatic forcing. MASS model fields are integrated on  $\sigma_p$  surfaces (MESO Inc., 1993), then postprocessed to pressure surfaces for analysis. In isobaric coordinates, vertical velocity is given by  $\omega = Dp/Dt$ ; a parcel ascends (descends) in an isobaric framework to a lower (higher) parcel pressure or higher (lower) isobaric surface. We can relate isentropic and isobaric coordinate systems by noting that (e.g. Bluestein, 1992, Eq. 5.3.12)

$$\omega = \left( \frac{\partial p}{\partial t} \right)_\theta + \mathbf{V} \cdot \nabla_{\theta p} + \frac{\partial p}{\partial \theta} \frac{D\theta}{Dt} \quad (\text{A.0.1})$$

which means that, given model fields on isentropic surfaces with isobaric vertical velocities, we can compute the diabatic forcing with

$$\begin{array}{ccccccc} \frac{D\theta}{Dt} & = & \left( \frac{\Delta\theta}{\Delta p} \right) & [ & \omega & - & \left( \frac{\Delta p}{\Delta t} \right)_\theta & - & \mathbf{V} \cdot \nabla_{\theta p} & ] \\ & & \text{Term 1} & & \text{Term 2} & & \text{Term 3} & & \text{Term 4} & \end{array} \quad (\text{A.0.2})$$

In a practical sense, the diabatic forcing ( $D\theta/Dt$ ) is that portion of the local change in potential temperature that cannot be explained by either quasi-horizontal advection or adiabatic expansion.

Model fields were interpolated to isentropic surfaces at 2 K intervals, yielding a mean separation of about 20 hPa between  $\theta$ -surfaces below 700 hPa. Centered finite differences were used for the local time derivative ( $\Delta t = 2$  h) and space derivatives on the interior; one-step differences in space were used at the boundaries.

## References

- Alfonso, A. P. and L. R. Naranjo, 1996: The 13 March 1993 severe squall line over western Cuba. *Wea. Forecasting*, **11**, 89–102.
- Barnes, S. L., 1964: A technique for maximizing details in numerical weather map analysis. *J. Appl. Meteor.*, **3**, 396–409.
- Bluestein, H. B., 1992: *Synoptic-Dynamic Meteorology in Midlatitudes*, vol. I: Principles of Kinematics and Dynamics. Oxford University Press.
- Bluestein, H. B., 1993: *Synoptic-Dynamic Meteorology in Midlatitudes*, vol. II: Observations and Theory of Weather Systems. Oxford University Press.
- Bosart, L. F., G. J. Hakim, K. R. Tyle, M. A. Bedrick, M. J. Dickinson, and D. M. Schultz, 1996: Large-scale antecedent conditions associated with the 12–14 March 1993 cyclone (“Superstorm 93”) over eastern North America. *Mon. Wea. Rev.*, **124**, 1865–1891.
- Bosart, L. F. and F. Sanders, 1981: The Johnstown flood of July 1977: A long-lived convective storm. *J. Atmos. Sci.*, **38**, 1616–1642.
- Caplan, P. M., 1995: The 12–14 March 1993 Superstorm: Performance of NCEP Global Medium Range Model. *Bull. Amer. Meteor. Soc.*, **76**, 202–212.
- Davis, C. A. and K. A. Emanuel, 1991: Potential vorticity diagnostics of cyclogenesis. *Mon. Wea. Rev.*, **119**, 1929–1953.
- Dickinson, M. J., L. F. Bosart, W. E. Bracken, G. J. Hakim, D. M. Schultz, M. A. Bedrick, and K. R. Tyle, 1997: The March 1993 Superstorm cyclogenesis: Incipient phase synoptic- and convective-scale flow interaction and model performance. *Mon. Wea. Rev.*, **125**, 3041–3072.
- Egentowich, J. M., M. L. Kaplan, Y.-L. Lin, and A. J. Riordan, 2000a: Mesoscale simulations of dynamical factors discriminating between a tornado outbreak and nonevent over the southeast U.S. Part I: 84–48 hour precursors. *Meteorol. Atmos. Phys.*, **74**, 129–157.

- Egentowich, J. M., M. L. Kaplan, Y.-L. Lin, and A. J. Riordan, 2000b: Mesoscale simulations of dynamical factors discriminating between a tornado outbreak and nonevent over the southeast U.S. Part II: 48–6 hour precursors. *Meteorol. Atmos. Phys.*, **74**, 159–187.
- Egentowich, J. M., M. L. Kaplan, Y.-L. Lin, and A. J. Riordan, 2000c: Mesoscale simulations of dynamical factors discriminating between a tornado outbreak and nonevent over the southeast U.S. Part III: 6 hour precursors. *Meteorol. Atmos. Phys.*, **74**, 189–215.
- Fritsch, J. M. and C. F. Chappell, 1980: Numerical prediction of convectively driven mesoscale pressure systems. Part I: Convective parameterization. *J. Atmos. Sci.*, **37**, 1722–1733.
- Fritsch, J. M. and R. A. Maddox, 1981a: Convectively driven mesoscale weather systems aloft Part I: Observations. *J. Appl. Meteor.*, **20**, 9–19.
- Fritsch, J. M. and R. A. Maddox, 1981b: Convectively driven mesoscale weather systems aloft Part II: Numerical simulations. *J. Appl. Meteor.*, **20**, 20–26.
- Gilhousen, D. B., 1994: The value of NDBC observations during March 1993's Storm of the Century. *Wea. Forecasting*, **9**, 255–264.
- Gyakum, J. R., Y.-H. Kuo, Z. Guo, and Y.-R. Guo, 1995: A case of rapid continental mesoscale cyclogenesis. Part II: Model and observational diagnosis. *Mon. Wea. Rev.*, **123**, 998–1024.
- Hakim, G. J., L. F. Bosart, and D. Keyser, 1995: The Ohio Valley wave merger cyclogenesis event of 25–26 January 1978. Part I: multiscale case study. *Mon. Wea. Rev.*, **123**, 2663–2692.
- Hakwins, H. F. and S. M. Imbembo, 1976: The structure of a small, intense hurricane, Inez 1966. *Mon. Wea. Rev.*, **104**, 418–442.
- Holton, J. R., 1992: *An Introduction to Dynamic Meteorology*. Academic Press.
- Hoskins, B. J., M. E. McIntyre, and A. W. Robertson, 1985: On the use and significance of isentropic potential vorticity maps. *Quart. J. Roy. Meteor. Soc.*, **111**, 877–946.

Hsu, S. A., 1993: The Gulf of Mexico – A breeding ground for winter storms. *Mar. Wea. Log*, **37**(2), 4–11.

Huo, Z., D.-L. Zhang, and J. Gyakum, 1995: A diagnostic analysis of the Superstorm of March 1993. *Mon. Wea. Rev.*, **123**, 1740–1761.

Huo, Z., D.-L. Zhang, and J. Gyakum, 1998: An application of potential vorticity inversion to improving the numerical prediction of the March 1993 Superstorm. *Mon. Wea. Rev.*, **126**, 424–436.

Huo, Z., D.-L. Zhang, and J. R. Gyakum, 1999a: Interaction of potential vorticity anomalies in extratropical cyclogenesis. Part I: Static piecewise inversion. *Mon. Wea. Rev.*, **127**, 2546–2561.

Huo, Z., D.-L. Zhang, and J. R. Gyakum, 1999b: Interaction of potential vorticity anomalies in extratropical cyclogenesis. Part II: Sensitivity to initial perturbations. *Mon. Wea. Rev.*, **127**, 2563–2575.

Igau, R. C. and J. W. Nielsen-Gammon, 1998: Low-level jet development during a numerically simulated return flow event. *Mon. Wea. Rev.*, **126**, 2972–2990.

Johnson, G. A., E. A. Meindl, E. G. Mortimer, and J. S. Lynch, 1984: Features associated with repeated strong cyclogenesis in the western Gulf of Mexico during the winter of 1982–83. In *Third Conf. on Meteorology of the Coastal Zone*, pp. 110–117. Amer. Meteor. Soc., Miami, FL.

Kaplan, M. L., S. E. Koch, Y.-L. Lin, R. P. Weglarz, and R. A. Rozumalski, 1997: Numerical simulations of a gravity wave event over CCOPE. Part I: the role of geostrophic adjustment in mesoscale jetlet formation. *Mon. Wea. Rev.*, **125**, 1185–1211.

Kaplan, M. L., Y.-L. Lin, J. J. Charney, K. D. Pfeiffer, D. B. Ensley, D. S. DeCroix, and R. P. Weglarz, 2000: A terminal area PBL prediction system at Dallas-Fort Worth and its application in simulation diurnal PBL jets. *Bull. Amer. Meteor. Soc.*, **81**, 2179–2204.

- Kaplan, M. L., Y.-L. Lin, D. W. Hamilton, and R. A. Rozumalski, 1998: A numerical simulation of an unbalanced jetlet and its role in the Palm Sunday 1994 tornado outbreak in Alabama and Georgia. *Mon. Wea. Rev.*, **126**, 1867–1886.
- Keyser, D. and M. A. Shapiro, 1986: A review of the structure and dynamics of upper-level frontal zones. *Mon. Wea. Rev.*, **114**, 452–499.
- Koch, S. E. and P. B. Dorian, 1988: A mesoscale gravity wave event observed during CCOPE. Part III: Wave environment and probable source mechanisms. *Mon. Wea. Rev.*, **116**, 2570–2592.
- Kocin, P. J., P. N. Schumacher, R. F. Morales, and L. W. Uccellini, 1995: Overview of the 12–14 March 1993 Superstorm. *Bull. Amer. Meteor. Soc.*, **76**, 165–182.
- Kocin, P. J. and L. W. Uccellini, 1990: *Snowstorms Along the Northeastern Coast of the United States: 1955 to 1985*. Amer. Meteor. Soc.
- Kuo, Y.-H., J. R. Gyakum, and Z. Guo, 1995: A case of rapid continental mesoscale cyclogenesis. Part I: Model sensitivity experiments. *Mon. Wea. Rev.*, **123**, 970–997.
- Lanicci, J. M. and T. T. Warner, 1991a: A synoptic climatology of the elevated mixed-layer inversion over the southern Great Plains in Spring. Part I: Structure, dynamics and seasonal evolution. *Wea. Forecasting*, **6**, 181–197.
- Lanicci, J. M. and T. T. Warner, 1991b: A synoptic climatology of the elevated mixed-layer inversion over the southern Great Plains in Spring. Part II: The life cycle of the lid. *Wea. Forecasting*, **6**, 198–213.
- Lanicci, J. M. and T. T. Warner, 1991c: A synoptic climatology of the elevated mixed-layer inversion over the southern Great Plains in Spring. Part III: Relationship to severe-storms climatology. *Wea. Forecasting*, **6**, 214–226.
- Maddox, R. A., 1983: Large-scale meteorological conditions associated with midlatitude, mesoscale convective complexes. *Mon. Wea. Rev.*, **111**, 1475–1493.
- MESO Inc., 1993: *MASS Version 5.8 Reference Manual*. (Available from MESO Inc., 185 Jordan Road, Troy, NY 12180).

- Mote, T. L., D. W. Gamble, S. J. Underwood, and M. L. Bentley, 1997: Synoptic-scale features common to heavy snowstorms in the southeast United States. *Wea. Forecasting*, **12**, 5–23.
- Neiman, P. and M. Shapiro, 1993: The life cycle of an extratropical marine cyclone. Part I: Frontal-cyclone evolution and thermodynamic air-sea interaction. *Mon. Wea. Rev.*, **121**, 2153–2176.
- NWS, 1994: Superstorm of March 1993: March 12–14 1993. Natural disasters survey report, NWS, U.S. Dept. of Commerce, 152 pp.
- Orlanski, I., 1975: A rational subdivision of scales for atmospheric processes. *Bull. Amer. Meteor. Soc.*, **56**, 527–530.
- Petterssen, S. and S. J. Smebye, 1971: On the development of extratropical cyclones. *Quart. J. Roy. Meteor. Soc.*, **97**, 457–482.
- Rozumalski, R. A., 1997: *The role of jet streak regeneration forced by a deepening continental planetary boundary layer in the explosive surface cyclogenesis of 28 March 1984*. Ph.D. thesis, North Carolina State University.
- Sanders, F. and J. R. Gyakum, 1980: Synoptic-dynamic climatology of the “bomb”. *Mon. Wea. Rev.*, **108**, 1589–1606.
- Saucier, W. J., 1949: Texas-West Gulf cyclones. *Mon. Wea. Rev.*, **77**, 219–231.
- Schultz, D. M., W. E. Bracken, L. F. Bosart, G. J. Hakim, M. A. Bedrick, M. J. Dickinson, and K. R. Tyle, 1997: The 1993 Superstorm cold surge: Frontal structure, gap outflow, and tropical impact. *Mon. Wea. Rev.*, **125**, 5–39.
- Schultz, D. M. and W. J. Steenburgh, 1999: The formation of a forward-tilting cold front with multiple cloud bands during Superstorm 1993. *Mon. Wea. Rev.*, **127**, 1108–1124.
- Shapiro, M. and D. Keyser, 1990: Fronts, jet streams and the tropopause. In *Extratropical Cyclones: The Erik Palmén Memorial Volume* ( C. W. Newton and E. O. Holopainen, eds.), chap. 10, pp. 167–192. American Meteorological Society.

- Uccellini, L. W. and D. R. Johnson, 1979: The coupling of upper and lower tropospheric jet streaks and implications for the development of severe convective storm. *Mon. Wea. Rev.*, **107**, 682–703.
- Uccellini, L. W., P. J. Kocin, R. S. Schneider, P. M. Stokels, and R. A. Dorr, 1995: Forecasting the 12–14 March Superstorm. *Bull. Amer. Meteor. Soc.*, **76**, 183–199.
- Wolf, B. J. and D. R. Johnson, 1995: The mesoscale forcing of a midlatitude upper-tropospheric jet streak by a simulated convective system. Part I: Mass circulation and ageostrophic processes. *Mon. Wea. Rev.*, **123**, 1059–1087.
- Zhang, D. L. and R. A. Anthes, 1982: A high resolution model of the planetary boundary layer: Sensitivity tests and comparisons with SESAME-79 data. *J. Appl. Meteor.*, **21**, 1594–1609.
- Zhang, D.-L. and J. M. Fritsch, 1986: Numerical simulation of the meso-beta scale structure and evolution of the 1977 Johnstown flood, Part I: Model description and verification. *J. Atmos. Sci.*, **43**, 1913–1943.
- Zhang, D.-L. and J. M. Fritsch, 1987: Numerical simulation of the meso-beta scale structure and evolution of the 1977 Johnstown flood, Part II: Inertially stable warm-core vortex and the mesoscale convective complex. *J. Atmos. Sci.*, **44**, 2593–2612.